PhD Thesis

Application of Multibody Dynamics Techniques to the Analysis of Human Gait

Rosa Pàmies i Vilà

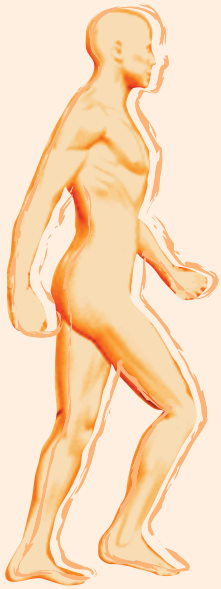

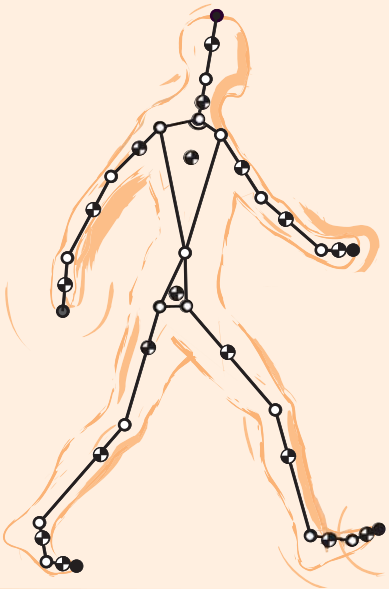

Universitat Politècnica de Catalunya
Departament d'Enginyeria Mecànica

UNIVERSITAT POLITÈCNICA DE CATALUNYA

Biomedical Engineering Doctoral Programme

APPLICATION OF MULTIBODY DYNAMICS TECHNIQUES TO THE ANALYSIS OF HUMAN GAIT

by Rosa Pàmies Vilà

A thesis submitted for the degree of Doctor for the Universitat Politècnica de Catalunya

Supervised by Dr. Josep Maria Font Llagunes

Department of Mechanical Engineering (DEM)

Barcelona, December 2012

A tu, pare.

Agraïments

Han sigut moltes les persones que m'han ajudat i recolzat perquè aquesta tesi hagi tirat endavant. Per això, m'agradaria especialment donar les gràcies

Al director, Dr. Josep Maria Font Llagunes, per haver confiat sempre amb mi, per haver-me esperonat en els moments més difícils i foscos i haver-me ajudat a créixer, donant-me sempre la mà, en el fascinant món científic. Pels reptes que hem compartit i per l'amistat que des del respecte sempre ens quedarà.

Als companys del Departament d'Enginyeria Mecànica de l'Escola Tècnica Superior d'Enginyeria Industrial de Barcelona: Daniel, Quim, Lluïsa, Joan, Miquel, Jordi, Salvador, Enrique, Pau, Ana, Joaquim, Tània, Laia, Ayoub, Matteo i Bruno, pel seu recolzament i pels molt bons moments que ens han anat portant aquests quatre anys.

Als investigadors del *Laboratorio de Ingeniería Mecánica* (LIM) de la Coruña: Amelia, Roland, Fran, Alberto, Daniel, Emilio, Javier, Jairo i Miguel, per no fer-me sentir gens estranya a Ferrol. En especial al Dr. Javier Cuadrado, per introduir-me al món de la dinàmica multisòlid i posar-me totes les facilitats per l'estada a Galícia. I un agraïment especial perquè el model biomecànic no hagués estat possible sense les llibreries del Daniel ni el treball que hem compartit amb l'Urbano, qui sempre ha estat disposat a ajudar-me i a respondre qualsevol pregunta que li he fet sobre programació i sobre el funcionament del laboratori.

Als companys del *Departamento de Ingeniería Mecánica, Energética y de los Materiales* de la *Universidad de Extremadura*, al Javier Alonso i al Francisco Romero, per poder compartir juntament amb els companys del LIM l'aventura de participar en un projecte nacional coordinat entre les tres universitats.

Als revisors externs, pels seus comentaris i suggeriments.

Finalment, també vull agrair el suport d'aquells que han estat al meu costat: A la mare, per ser-hi sempre; al pare, per fer-me costat de lluny estant; a la Montserrat per posar-se fins i tot a entendre la formulació Lagrangiana i pels seus retocs montserratins; a la meva família, per preguntar-me si ja teníem l'ortesi a punt; als amics que han fet l'esforç d'entendre que la tesis no em deixava temps lliure, i al Cesc, per aguantar les llargues nits al departament sense queixar-se mai i per la il·lusió que sempre ha mostrat en aquesta tesi.

I a totes aquelles persones que m'heu encoratjat a seguir endavant donant-me suport durant aquests últims anys:

"...Sempre hi ha Algú que em crida fort des de la sorra,
és una veu que em parla al cor quan tot s'enfonsa
i em diu que tiri mar endins...
Torna-ho a intentar!"

CTF

Acknowledgements

There have been many people who have helped me during this enjoyable experience. I would like to give my sincerely thanks to them, to only some of whom it is possible to give particular mention here.

First of all, I would like to thank to my PhD advisor, Dr. Josep Maria Font Llagunes for the good advice, support and friendship that has been invaluable on both academic and personal level. He has been very patiently supervising me and always guiding me in the right direction. I have learned a lot from him, without his help this thesis would not have met an end.

I would like to acknowledge my colleagues in the *Departament d'Enginyeria Mecànica* in ETSEIB: Daniel, Quim, Lluïsa, Joan, Miquel, Jordi, Salvador, Enrique, Pau, Ana, Joaquim, Tània, Laia, Ayoub, Matteo and Bruno, for their support and for the great time we have shared these four years.

I acknowledge with gratitude the support from the researchers of the *Laboratorio de Ingenieria Mecánica* (LIM) in La Coruña: Amelia, Roland, Urbano, Fran, Alberto, Daniel, Emilio, Javier, Jairo and Miguel, for offering me an ideal work environment in Ferrol. Special thanks go to Dr. Javier Cuadrado, for introducing me the multibody dynamic's world and offering all the facilities for my research visiting in Galicia. Very particular thanks go to Daniel, the biomechanical model would not have been possible without his libraries, and to Urbano, I know that I could always ask him for advice and opinions on lab related issues.

I would also like to express my gratitude to the colleagues Francisco Javier Alonso and Francisco Romero from the *Departamento de Ingeniería Mecánica, Energética y de los Materiales* at *Universidad de Extremadura.* We have shared, also with colleagues of the LIM, the adventure of participating in a spanish national research project.

I would like to thank the reviewers for their comments which have been very useful to improve the quality of the thesis.

Finally, I owe my heartfelt thanks to my close people. I am very grateful for my mother, her understanding encouraged me to work hard. I specially appreciate knowing that my father is near, I miss him. Special thanks go to my sister Montserrat, for transmiting me her happiness and for trying to understand even the Lagrangian formulation. Thanks to my family who always ask for the state of the orthosis, and also thanks to my friends, who have made the effort to understand that PhD does not let me have so much free time. Last but not least, I want to thank Cesc, his love and support without any complaint or regret have enabled me to complete this PhD project.

Contents

Abstract

This thesis presents the kinematic and dynamic study of human motion by means of multibody system dynamics techniques. For this purpose, two biomechanical models are used: a 2D model formed by 11 segments with 14 degrees of freedom, and a 3D model that consists of 18 segments with 57 degrees of freedom. The multibody formulation has been developed in mixed coordinates (natural and relative).

The movement of the subject is recorded in the laboratory using a motion capture system that provides the position along time of 37 markers attached on the body of the subject. Position data are filtered using an algorithm based on singular spectrum analysis (SSA) and the natural coordinates of the model are calculated using algebraic relations between the marker positions. Afterwards, a procedure ensures the kinematic consistency and the data processing continues with the approximation of the position histories using B-spline curves and obtaining, by analytical derivation, the velocity and acceleration values.

In an inverse dynamic analysis (IDA) of human motion, body segment parameters (geometric and inertial), kinematic data and force plate measurements are usually used as input data. Differing to most published works, in this thesis the force plates measurements are not used directly as inputs of the analysis, they are used to solve the contact wrench sharing problem during the double support phase. In this phase, both feet contact the ground and kinematic measurements are insufficient to determine the individual wrench at each foot. One of the contributions of the thesis is a new strategy that is proposed to solve this indeterminacy (called corrected force plate sharing method, CFP). Using this method, a set of two contact wrenches dynamically consistent with the moviment are obtained with no need neither to add residual forces and torques nor to modif the original motion.

Also in the IDA field, the sensitivity of the joint torques to errors in the anthropometric parameters, in the force plate measurements and to errors committed during the kinematic data processing is studied. The analysis shows that the results are very sensitive to errors in force measurements and in the kinematic processing, being the errors in the body segment parameters less influential.

The thesis also presents a new 3D foot-ground contact model based on sphere-plane contact. Its parameters are estimated using two different approaches based on optimization techniques. The model is used as an alternative method to solve the mentioned sharing problem during the double support phase and it is also used, in a forward dynamic analysis, to estimate the contact forces between the biomechanical model and its environment. The forward dynamic simulation requires the implementation of a controller that is based, in this case, on the extended Kalman filter.

The most important contributions of the thesis in IDA are focused on the method to solve the problem of the distribution of contact forces during the double support phase, making a comparison of the results obtained via different methods including CFP and the contact model. Regarding the analysis of the influence of errors in input data on the inverse dynamics results, the statistical modelling of the uncertainties together with the perturbation of more than one parameter at same time (remaining height and weight as constant parameters) is also new in the literature.

Moreover, the presented foot-ground contact model is also original. In the current state of the art, there are no models that use real data captured in the laboratory to solve the contact wrench sharing problem during the double support phase. Furthermore, there are few studies simulating the foot-ground interaction in a forward dynamic analysis using a continuous foot-ground contact model.

Finally, developing a model that is used for both forward and inverse dynamic analysis is a relevant aspect of the methodology used. Although the two approaches separately are common research topics in the field of biomechanics, a small number of studies prove the validity of the obtained results. In this thesis, the results of the inverse dynamics are used as input data for the forward dynamic analysis, and the results of the latter (the motion) have been compared with the motion capture in the laboratory (input of the inverse dynamics analysis). Thus, the circle has been closed which allows us to validate the accuracy of both the models and the obtained results.

Resum

La tesi que es presenta tracta l'estudi cinemàtic i dinàmic de la marxa humana mitjançant tècniques de dinàmica de sistemes multisòlid. Per a aquest propòsit, s'utilitzen dos models biomecànics: un model pla format per 11 segments i 14 graus de llibertat i un model tridimensional format per 18 segments i 57 graus de llibertat. La formulació dinàmica multisòlid ha estat desenvolupada en coordenades mixtes (naturals i relatives).

La marxa de l'individu s'enregistra al laboratori utilitzant un sistema de captura del moviment mitjançant el qual s'obté la posició de cadascun dels 37 marcadors situats sobre el cos del subjecte. Les dades de posició es filtren utilitzant un algorisme basat en el *singular spectrum analysis* (SSA) i les coordenades naturals del model es calculen mitjançant relacions algebraiques entre les posicions dels marcadors. Posteriorment, un procés de consistència cinemàtica assegura les restriccions de sòlid rígid. El processament cinemàtic continua amb l'aproximació de les posicions mitjançant corbes B-spline d'on se n'obtenen, per derivació analítica, els valors de velocitat i acceleració.

En una anàlisi dinàmica inversa de la marxa humana, s'acostumen a utilitzar com a dades d'entrada els paràmetres antropomètrics (geomètrics i inercials) dels segments, les dades cinemàtiques i les mesures de les plaques de força. En contraposició al que fan la majoria d'autors, en aquesta tesi, les mesures de les plaques de força no són utilitzades directament en l'anàlisi sinó que només s'usen per solucionar el problema del repartiment del torsor resultant de les forces de contacte durant la fase de doble suport. En aquesta fase, els dos peus es recolzen sobre el terra i les mesures cinemàtiques són insuficients per determinar el torsor en cada peu. El nou mètode de repartiment que es proposa (anomenat *contact force plate sharing*, CFP) és una de les aportacions de la tesi i destaca pel fet que permet determinar un conjunt de forces i moments dinàmicament consistents amb el model biomecànic, sense haver de modificar-ne les coordenades cinemàtiques ni afegir forces o moments residuals en algun dels segments.

Encara dins l'àmbit de l'estudi dinàmic invers, s'ha analitzat la sensitivitat dels parells articulars a errors comesos en estimar els paràmetres antropomètrics, a errors que poden contenir les mesures de les plaques de força i a errors que es poden cometre en el processament cinemàtic de les mesures. L'estudi permet concloure que els resultats són molt sensibles als errors cinemàtics i a les forces mesurades per les plaques, sent els errors en els paràmetres antropomètrics menys influents.

La tesi també presenta un nou model tridimensional de contacte peu-terra basat en el contacte esfera-pla i els seus paràmetres s'estimen mitjançant dos enfocaments diferents basats en tècniques d'optimització. El model s'utilitza com un mètode alternatiu per solucionar el problema del repartiment durant la fase de doble suport en dinàmica inversa, i també s'utilitza en simulacions de dinàmica directa per estimar les forces de contacte entre el model biomecànic i el seu entorn. En l'anàlisi dinàmica directa és

necessària la implementació d'un controlador que està basat, en aquest cas, en el filtre de Kalman estès.

Les contribucions més importants de la tesi, en el cas de l'anàlisi dinàmica inversa, es centren en el mètode CFP i en l'ús del model de contacte per solucionar el repartiment de forces de contacte en la fase de doble suport. Referent a l'anàlisi de la influència dels errors en les dades d'entrada del problema dinàmic invers, la modelització estadística dels errors conjuntament amb la pertorbació conjunta de més d'un paràmetre antropomètric a la vegada (mantenint constant l'alçada i el pes de la persona) és també una novetat.

Per altra banda, el model de contacte presentat és també una contribució original. En l'estat de l'art actual no es troben models que usin dades reals capturades al laboratori i que a la vegada s'utilitzin per solucionar el problema de repartiment en el doble suport i per simular el contacte peu-terra en una anàlisi dinàmica directa.

Finalment, el fet de desenvolupar un model que s'utilitzi tant per a l'anàlisi dinàmica directa com inversa és també una de les aportacions d'aquesta tesi. Tot i que les dues anàlisis, per separat, són temes de recerca comuns en l'àmbit de la Biomecànica, es troben a faltar estudis que comprovin la validesa dels resultats que se n'obtenen. En aquesta tesi, els resultats de la dinàmica inversa s'han utilitzat com a dades d'entrada de l'anàlisi dinàmica directa, el resultat de la qual (el moviment) ha pogut ser comparat amb el que s'obté de la captura del laboratori (entrada de la dinàmica inversa). D'aquesta manera, el cercle es tanca i es pot verificar la validesa tant dels models com dels resultats obtinguts.

List of Tables

List of Figures

List of Symbols

$\mathbf{a} = \{a_1, a_2, a_3\}^T$	cartesian coordinates of a point expressed in the local base
$b_i(u)$	Bernstein polynomial
b_j	Bézier coefficients
$\mathbf{b}$	generic vector
$\mathbf{b}_j$	control points in Bézier formulation
c_r	coefficient of restitution
c_{stick}	damping coefficient of the sticktion model
$\mathbf{e}(t)$	error signal in the PID control scheme
$f(t)$	shape functions used in the STA method
f_{stick}^m	function force that represents the behaviour of the bristles
$\mathbf{f}$	system dynamics function
$\mathbf{f_z}$	Jacobian matrix of the system dynamics function
g	number of degrees of freedom
$\mathbf{g}$	nonlinear function to be solved using Newton-Raphson scheme in Kalman Formulation
$\mathbf{h}$	function defining the relationship between the state of the dynamic system and the measurements in Kalman formulation (Appendix D) or weight vector in Chapter 6
h	incremental time-step
i, j, k	generic definition of rigid body points
k	index used to indicate the time step
k_{stick}	stiffness coefficient of the sticktion model
m	number of kinematic constraint equations
m_i	mass of the segment i

n	number of dependent coordinates used in multibody formulation (Chapter 3) or order of the Bézier curves in Appendix C
nr	number of rheonomic kinematic constraint equations
ns	number of scleronomic kinematic constraint equations
$\mathbf{n}$	normal vector at the tangent contact plane
$\mathbf{q} = \{q_1,...,q_n\}^T$	vector of generalized coordinates
$\dot{\mathbf{q}}$	vector of generalized velocities
$\ddot{\mathbf{q}}$	vector of generalized accelerations
$\dot{\mathbf{q}}^*$	vector of virtual generalized velocities
$\tilde{\mathbf{q}}$	natural coordinates in vector $\mathbf{q}$
$\mathbf{q}^{\text{filt}}$	filtered vector of natural coordinates
$\mathbf{q}^{\text{3D}}$	vector of inconsistent natural coordinates extracted from the 3D model
$\mathbf{q}_{\text{e}}$	vector of coordinates associated with the element e
r_i	radius of the sphere
$\mathbf{r}(t)$	reference signal at PID scheme
$\mathbf{r}_{\text{P}}$	position of point P expressed in the global coordinate system
$\dot{\mathbf{r}}_{\text{P}}$	velocity point P
$\mathbf{r}'_{\text{P}}$	position of point P expressed in the segment local coordinate system
$\mathbf{r}_{\text{cont}}$	position of the central point of the contact region
$\dot{\mathbf{r}}_{\text{cont}}$	time derivative of $\mathbf{r}_{\text{cont}}$
s	deformation of the bristles
t	time variable
t_i	ith time instant (i=1,...,N)
t_{h1}	heel strike time instant
t_{t0}	toe off time instant

t_{P}	peak force time instant
u	unit domain variable of Bézier curves
$\mathbf{u}(t)$	output of the controller and input to the process
$\mathbf{u}_{\mathbf{F}}$	vector of the unit lever-arm associated with moment $\boldsymbol{\Gamma}$
$\{\mathbf{u},\mathbf{v},\mathbf{w}\}_S$	unit vectors used to define the local basis of segment S
$\bar{x}$	arithmetic mean of a sample
$\mathbf{x}(t)$	sensor measurement in the PID control scheme in Chapter 4 or state vector in the Kalman filter in Chapter 6 and Appendix D
$\dot{\mathbf{x}}(t)$	time derivative of the state vector
$\mathbf{y}(t)$	control variable in the PID control scheme in Chapter 4 or measurement vector in the Kalman filter in Chapter 6 and Appendix D
$\hat{\mathbf{y}}$	predicted measurements
$\mathbf{z}$	vector of independent coordinats
$\dot{\mathbf{z}}$	vector of independent velocities
$\ddot{\mathbf{z}}$	vector of independent accelerations
$\dot{\mathbf{z}}^*$	vector of virtual independent velocities
z_i^{bez}	analytical expression of the ith independent coordinate of vector $\mathbf{z}$ through Bézier curves.
$z_i^{\exp}$	analytical function for the ith independent coordinate of vector $\mathbf{z}$
A_i	anthropometric measurements of the subject (i=1,...,20)
$\mathbf{A}$	coordinate transformation matrix
$\mathrm{B}_j^n(u)$	Bernstein basis polynomials
$\mathbf{B}$	matrix that relate independent and dependent coordinates
$\mathbf{C}$	damping matrix
E^*	effective Young's modulus

E_s	Young's modulus of the sphere material
E_p	Young's modulus of the of the plane material
$\mathbf{F}$	generic vector force in Chapter 3, 4 and 5 or matrix of a continuous linear differential equation defining a dynamic systemlinearization of **f** in Appendix D.
F_n	normal component of a contact force
$\mathbf{F}_t$	tangential components of a contact force
$\mathbf{F}_{\text{stick}}$	Sticktion force
$\mathbf{F}_{\text{slide}}$	Sliding force
G	centre of mass of a segment
$\mathbf{G}$	coupling matrix between the process noise and the state of a linear dynamic system
$\tilde{\mathbf{G}}$	external contact wrench acting on the lumbar joint
$\tilde{\mathbf{G}}^{\text{gr}}$	$\tilde{\mathbf{G}}$ translated to the projection of the lumbar joint onto the ground
$\mathbf{G}_{\text{FP}i}$	force plate measurements (where i indicates the index of the force plate, $i = 1, 2$)
$\mathbf{G}_{\text{FP}i}^{\text{gr}}$	$\mathbf{G}_{\text{FP}i}$ translated to the projection of the lumbar joint onto the ground
$\mathbf{G}_{\text{CM}}$	Contact wrench obtained through the foot-ground contact model
$\mathbf{G}_{\text{CM}}^{\text{gr}}$	$\mathbf{G}_{\text{CM}}$ translated to the projection of the lumbar joint onto the ground
$\mathbf{G}_{\text{FPL}}^{\text{ankle}}$	$\mathbf{G}_{\text{FP}i}$ translated to the ankle joint
$\mathbf{G}_{\text{CM}}^{\text{ankle}}$	$\mathbf{G}_{\text{CM}}$ translated to the ankle joint
$\mathbf{G}_1$, $\mathbf{G}_2$	Contact wrenches at the trailing and leading foot, respectively
$\mathbf{H}$	measurement sensitivity matrix
$\mathbf{I}_i$	identity matrix ($i \times i$)
I'_{ij}	components of the tensor of inertia about the centre of mass $\mathbf{\Pi}_G$ expressed in the segment local basis

I_{P}	in the 2D model, moment of inertia about point P (origin point of the local coordinate system)
$\mathbf{J}$	matrix with information regarding the inertia tensor of a rigid body
J_i	joint i (i=1,...17)
K	stiffness coefficient between contacting surfaces
K_d	derivative coefficient for PD and PID controllers
K_p	proporcional coefficient for PD and PID controllers
K_p^i	proportional gain associated with segment i
$\mathbf{K}$	stiffness matrix
$\bar{\mathbf{K}}$	Kalman gain matrix
L_i, L_{u}	length of the segment i, length of the vector $\mathbf{u}$
M_i	marker i (i=1,...,37)
$\mathrm{M}_i^{\max}$, $\mathrm{M}_i^{\min}$	maximum and the minimum value of M_i^{NP}
$\mathbf{M}$	global system mass matrix
$\mathbf{M}_{\mathrm{e}}$	mass matrix of the element e
M_i	in the planar model, internal moment at joint i (i=1,…,17)
M_i^{NP}	internal moment at joint i using non-perturbed parameters
N	number of recorded frames in a motion capture
O	origin of the global coordinate system which is defined using the axes $\{\mathrm{X}, \mathrm{Y}, \mathrm{Z}\}$
O′	origin of the local coordinate system of each segment S wich is defined using the local axes $\{\mathrm{X}', \mathrm{Y}', \mathrm{Z}'\}_S$
P	generic point
$\mathbf{P}$	covariance matrix of state estimation uncertainty
$\mathscr{P}^*$	virtual power
$\mathbf{Q}$	generalized force vector

$\mathbf{Q}_m$	generalized force vector associated to the independent coordinates
$\mathcal{Q}$	covariance matrix of the process noise
$\mathbf{R}$	matrix defining a basis of the nullspace of the constraint Jacobian matrix
$\mathcal{R}$	covariance matrix of the measurement uncertainty
$\mathbf{S}_S$	rotation matrix associated to the local basis attached to the segment S
T	kinetic energy
T_{hds}	half the double support duration
$\mathbf{T}$	coordinate transformation matrix
$\mathbf{T}_m$	actual internal joint torques
$\tilde{\mathbf{T}}_m$	internal joint torques obtained when the external contact wrench is applied at the lumbar joint.
V	error optimization criteria
$\mathbf{W}$	weighting diagonal matrix
$\{\mathrm{X},\mathrm{Y},\mathrm{Z}\}$	axis of the absolute basis
$\{\mathrm{X}',\mathrm{Y}',\mathrm{Z}'\}_S$	axis of the local basis associated to segment S
$\mathbf{X}'$	matrix representing a generic three-dimensional basis of vector
$\mathbf{Z}$	Matrix obtained from a transformation (rotation) of matrix $\mathbf{J}$
α_i	in the 2D model, relative orientation between two segments
$(\alpha,\beta,\gamma)_S$	orientation angles of the segment S
β	penalty factor used in kinematic data consistency procedure
δ_n	normal indentation between bodies
$\dot{\delta}_n$	time derivative of δ_n
$\dot{\delta}_0$	relative normal velocity between the colliding bodies when the contact is detected

$\boldsymbol{\delta}$	process noise
ε	specified error tolerance
$\boldsymbol{\varepsilon}$	measurement noise
κ	smooth function of the tangential velocity
$\boldsymbol{\lambda}$	vector of Lagrange multipliers
μ	friction coefficient between contacting surfaces
ν_s	Poisson's ratio of the sphere material
ν_p	Poisson's ratio of the the plane material
v_{stick}	parameter accounting for the velocity of the stick-slip transition
φ_i	generic absolute angular coordinate
$\varphi_i(t)$	analytical expression for angle φ_i
σ	Standard deviation of a sample
χ	hysteresis damping factor
$\boldsymbol{\Gamma}$	generic torque
$\boldsymbol{\Gamma}_i$	in the three-dimensional model, internal moment at joint *i*
$\boldsymbol{\Gamma}_S$	applied torques to segment *S*
$\boldsymbol{\Pi}_G$	tensor of inertia with respect to the centre of mass
$\boldsymbol{\Phi}$	vector of kinematic constraints
$\boldsymbol{\Phi}_\mathbf{q}$	Jacobian matrix of the kinematic constraints
$\dot{\boldsymbol{\Phi}}_\mathbf{q}$	time derivative of the Jacobian matrix
$\boldsymbol{\Phi}_t$	vector containing the partial derivatives of the constraints with respect to time
$\dot{\boldsymbol{\Phi}}_t$	time derivative of $\boldsymbol{\Phi}_t$
$\boldsymbol{\Omega}_S$	angular velocity vector of the segment *S* with respect to the global reference frame

In this thesis, the following typesetting rules have been adopted:

- vectors and matrices are in bold types (**a, A**)
- scalars are in italic font types (a, α)

Regarding to the over script

- $\dot{\mathbf{a}}$ first time derivative
- $\ddot{\mathbf{a}}$ second time derivative

Regarding to the superscript:

- $\mathbf{a}^T$, $\mathbf{A}^T$ transpose of a vector or matrix
- $\mathbf{A}^{-1}$ inverse matrix
- $\mathbf{A}^{-T}$ transpose of an inverse matrix
- $\mathbf{a}'$ **a** expressed in the local coordinate system

Acronyms

ASIS	anterior superior iliac spine
BSP	body segment parameter
CFP	corrected force plate
CM	contact model
CMA-ES	covariance matrix adaptation evolution strategy
COM	centre of mass
DAE	differential algebraic equation
DOF	degree of freedom
EKF	extended kalman filter
EMG	electromyography
FDA	forward dynamic analysis
FPL	force plate
FSO	full scale output
FVA	foot velocity algorithm
H	head
HAT	heat, arms and trunk
IDA	inverse dynamic analysis
KF	kalman filter
LA	left arm
LFA	left forearm
LFF	left forefoot
LH	left hand
LHF	left hindfoot
LS	left shank
LT	left thigh
MBS	multibody system
N	neck
NRMSE	normalized root mean square error
ODE	ordinary differential equation
P	pelvis
PD	proportional derivative
PID	proportional integral derivative

RA	right arm
REF	Reference signal
RFA	right forearm
RFF	right forefoot
RH	right hand
RHF	right hindfoot
RMSE	root mean square error
RS	right shank
RT	right thigh
SSA	singular spectrum analysis
STA	smooth transition assumption
T	torso

Chapter 1

Introduction

1.1 Motivation

Effective health care requires the work of multidisciplinary teams in which medical staff and engineers need to cooperate. Following this trend, biomechanics is becoming one of the most attractive fields to the mechanical engineering research community.

In this thesis, "Application of Multibody Dynamics Techniques to the Analysis of Human Gait", a 3D biomechanical model of human body is developed in order to study the dynamics of the human gait in healthy subjects. This work is part of a national research project entitled "Application of multibody dynamics techniques to active orthosis design for gait assistance", which is developed in the context of a new research line on Biomechanics in the Department of Mechanical Engineering at the School of Industrial Engineering of Barcelona (ETSEIB) and the Biomedical Engineering Research Centre (CREB) of the UPC (Universitat Politècnica de Catalunya).

This is a coordinated project that involves researchers from the Department of Mechanical Engineering at UPC, the Laboratory of Mechanical Engineering at UDC (Universidad de A Coruña) and the Department of Mechanical, Energetic and Materials Engineering at UEX (Universidad de Extremadura). Moreover, the medical staff of the Spinal Cord Injuries Unit at Complejo Hospitalario Universitario de A Coruña (CHUAC) is involved in the project.

The main objective of the project is to develope a computer application that enables to virtually test different types and designs of active orthoses for gait assistance on the computational model of a disabled subject. The challenge of the project is that the mentioned computer application should be able to combine the model of a real patient (whose data, motion and myographic signals will have been acquired), with the model of an orthosis, and to simulate the resulting motion of the patient wearing the orthosis, so that the obtained behaviour can be extrapolated to reality. For this purpose, the development of a human multibody model is a prerequisite to the simulation of the orthosis-assisted gait of subjects with incomplete spinal cord injuries. Before that, it is

necessary to develop, test and validate a tool that simulates the dynamics of human motion.

Several existing commercial packages deal with this application: Human Figure Modeller, SIMM (software for interactive musculoskeletal modelling), Kwon3D, AnyBody and OpenSim, for exemple. The results of these programs are acceptable in the case of normal gait simulation, but their utility is reduced when studying the function of impaired muscle models, when simulating active orthoses that assist gait, or when analysing the human-orthosis interaction. Therefore, in the context of the mentioned research project, it is necessary to create our own tool to simulate the dynamics of the human body motion. Given the ultimate goal of the project, firstly we need to obtain a realistic biomechanical model of a healthy subject and, secondly, this tool will be adapted to simulate and analyse the gait of spinal cord-injured subjects. Special emphasis will be given to the validation of the developed model by checking the correlation of experimental tests and simulations.

In addition, the opportunity to apply mechanics knowledge to the improvement of patient care provides a remarkable satisfaction, when considering that the basic objective is to improve the daily life of patients and/or society in general. Moreover, the interaction between the three groups involved in the project has given the opportunity of sharing experiences in the development of a common project in the field of biomechanics, which has been very motivating. The necessary convergence required by the three engineering groups, particularly, with the medical participants in the UDC group, has been an enriching experience that will hopefully lead to further projects and results in the future.

1.2 Gait Analysis

The interest in understanding animal locomotion dates back to the Greek civilization. However, in ancient times, the analyses were only based on observation. Although Aristotle in "De Motu Animalium" describes the action of muscles and the locomotion process, the first scientific biomechanical analysis method appears in 1680 with the same name "De Motu Animalium" by Borelli (Figure 1.1).

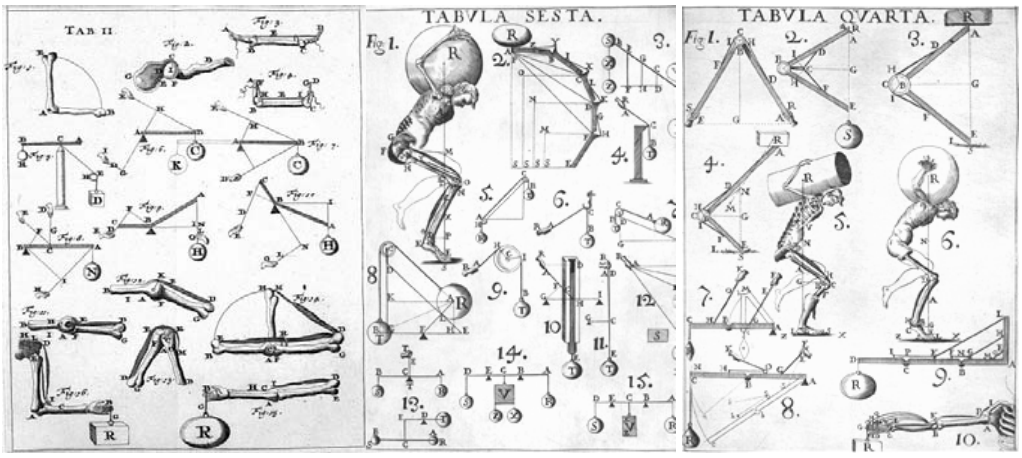

Figure 1.1 Ilustrations from "De Motu Animalium" by Borelli.

Borelli applied the lever principle to study both animal and human motion and to describe the relationship between the muscular and the skeletal system. He related the length and volume variations that muscles experience during the motion, not only in humans but also in mammals, fish, birds, and insects.

In 1836 the Weber brothers performed the first mechanical analysis of the human step. In their book "Mechanics of the Human Walking Apparatus", they described the phases of human walking, the motion of the centre of mass and analysed some gait disorders.

With the invention of photography some details of the motion were revealed. Muybridge (1887) in "Animal Locomotion" described the sequential photography techniques applied to the human gait analysis (Figure 1.2).

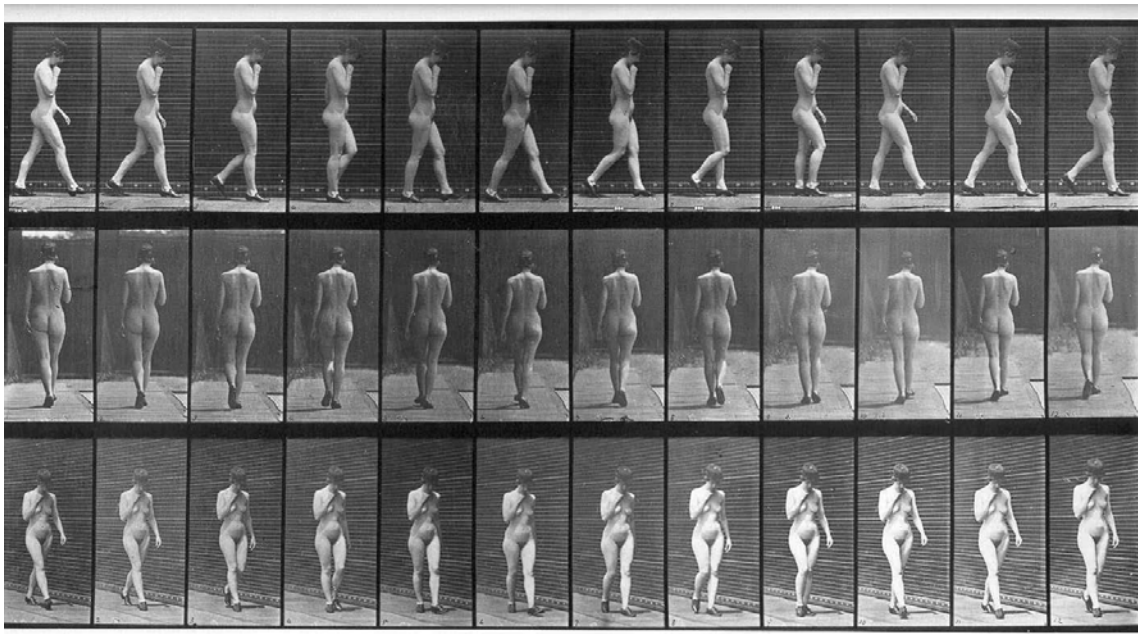

Figure 1.2 Animal Locomotion Slide EM1023 'female, nude, walking' [Muybridge, 1887].

During the last century, techniques of gait analysis have experienced a breakthrough due to the use of more precise measuring equipment and the introduction of the computer simulation. Nowadays, the motion capture systems include conventional video, infrared cameras and laser or acoustic emission systems. Usually, laboratories are also equipped with piezoelectric force plates, which are used to measure the foot-ground contact wrench. Moreover, new applications of sensor technologies (more accurate and reliable) are finding their way to biomechanics: EMG sensors to measure muscle activation, gyroscopes to measure angular velocity of body segments, goniometers to measure angular displacement of articulations, sensors to measure patient tracking, monitoring, etc. All these technologies provide a great deal of information that can be used to improve the dynamic analyses.

These sensors are used to estimate dynamic variables that, by definition, are non-observable, such as the vertical foot-ground contact force, the trajectory of the segments' centre of mass or the electrical activity produced by a muscle. The results of the biomechanical studies are highly dependent on the reliability of the data provided by them. Unfortunately, they are corrupted by numerous sources of error. Hazte describes

this phenomenon as the fundamental problem of myoskeletal inverse dynamics [Hazte 2002].

The biomechanical human model usually employed consists of an open kinematic chain composed by a number of rigid bodies connected by kinematic joints that represent a common human anatomical structure. Each rigid body represents a portion of the human body, called anatomical segment, and it is used to model the physical characteristics of each segment (mass, length, tensor of inertia about the centre of mass, and position of the centre of mass in a local coordinate system).

The muscular system is tipically modelled as a set of actuators which are responsible for the motion. They are defined by differential equations describing muscle activation and muscletendon contraction dynamics. [Ackermann and Schiehlen 2006, Rodrigo *et al.* 2008, Tsirakos *et al.* 1997]. Since several muscles serve each joint of the skeletal system, a redundant actuator problem appears in biomechanics. In order to solve this problem, optimization procedures are used [Ackermann and Schiehlen 2006, Anderson and Pandy 2001a, 2001b, Ralston 1976, Rodrigo *et al* 2008]. The approach to carry out the optimization should be carefully considered because the resolution computational cost can grow exponentially (making the process unfeasible) and the convergence of the algorithm can be seriously hindered depending on the chosen optimization method.

There are several procedures for obtaining the dynamic equations. The conventional methods involve the iterative formulation of the Newton-Euler equations of motion for each anatomical segment. In this thesis, analytical techniques based on multibody methodologies are used. These techniques have been used since the early 80's to study human walking [Ambrósio and Kecskeméthy 2007, Hardt and Mann 1980, Ramakrishnan *et al.* 1987, 1991, Tsirakos *et al.* 1997].

Depending on the purpose of the study, inverse or forward dynamic analyses are carried out. **Inverse dynamics techniques** are used to calculate the net joint reaction forces and driver torques that the musculoskeletal system produces during human locomotion from acquired kinematic data, foot-ground contact force and estimated body segment parameters (BSP). The results are suitable for recognizing normal and pathological gait patterns, determining muscle forces and/or studying how the central nervous system controls the motion. As said before, from the driver torques the muscle forces can be calculated via optimization techniques [Ambrósio and Kecskeméthy 2007]. **Forward dynamics techniques** are used to predict the body motion from known muscle forces (or resultant joint torques), based on ideas from neural or optimal control. This approach can help to investigate aspects of muscle function and energetic cost, simulate gait disorders or predict the motion of real subjects under virtual conditions.

Human motion analysis has applications in many research and development activities. It has become a diagnostics and research tool to optimize athletic performance [Herzog 2009, Milne and Davis 1992, de Wit *et al.* 2000], to detect gait patterns and gait disorders [Cooney *et al.* 2006, Crosbie and Nicol 1990, Wang *et al.* 2003], to animate computer characters [Faloustos *et al.* 2001, Thalmann 1999], to develop Virtual Reality applications [Goldberg 1997, Mirelman *et al.* 2010] and ergonomic studies [Lee *et al.* 2001, Tayyari and Smith 1997], to improve the design of orthosis and prosthesis [Font-Llagunes *et al.* 2011, Hansen *et al.* 2004, Glaister *et al.* 2009, Williams *et al.* 2009], etc.

Usually, the human gait analysis starts in a lab with the capture of the subject's motion by means of an optical system and the measurement of the foot-ground contact reactions through force plates. However, in some practical applications forces cannot be directly measured and need to be inferred. For instance, pressure platforms only provide the normal contact force (consequently tangential forces need to be estimated using a foot-ground contact model). In some sports applications (such as jumps), it is possible to situate cameras properly but it is not easy to put the force plate equipments in the exact best observation point. In these cases, a suitable foot-ground contact model would be necessary to perform the analysis as well.

1.3 Scope and Objectives

This thesis studies the human motion dynamics. The main objective of this work is to develop a dynamic model for the study of human gait in healthy subjects by properly using kinematic and dynamic information. The double support phase of the human gait will be solved with and without using force plates. An implicit goal is to develop a foot-ground contact model to reproduce the foot-ground contact during the gait.

The proposed methodology uses a general multibody formulation in mixed coordinates (natural plus angular) to describe the position of the anatomical segments and the topological structure of the human body. As a result, the analysis provides quantitative information on the external forces acting on the skeletal structure and the resultant joint torques that the involved muscles produce along the gait cycle.

The main goal is accomplished by means of the following specific objectives:

- Developing a three-dimensional biomechanical parametric human body model based on multibody dynamics techniques.

- Implementing an inverse dynamic analysis module to obtain the resultant joint efforts and the foot-ground contact wrenches produced by an able-bodied subject during the gait cycle.

- Developing a realistic contact model for the foot-ground interaction that allows to solve the IDA both during the single and double support phases.

- Implementing a forward dynamic analysis using as input data the joint torques and modelling the interaction between the subject and the enviroment by means of the mentioned foot-ground contact model.

The methodology needed to accomplish these goals consists of:

- **Development of a parametric biomechanical human body model** based on multibody techniques. The model characteristics are studied according to the purpose of the project –gait analysis of able-bodied and disabled subjects– and the balance between quality and simplicity of the different proposed models. The model needs to be three-dimensional, since the gait of disabled subjects cannot be considered to be planar. The program is developed using the specific libraries developed by the UDC group for multibody dynamics. The

mathematical part is coded in Fortran language and C++ is used for the graphical part.

- Set-up of the **experimental equipment** that comprises an optical system for motion capture and two force plates for the measurement of foot-ground contact wrenches. The experimental tests provide the positions of the markers attached on the subject's body during the gait cycle and the foot-ground contact wrenches during a complete gait cycle.

- **Signal processing**. Experimental measurements need to be processed in order to obtain a suitable data set for the inverse dynamic analysis. To this end, techniques for filtering marker positions, for differentiating independent coordinates and for ensuring kinematic consistency are applied.

- Implementation of an **inverse dynamic analysis** module to calculate the joint efforts during the human gait cycle using the previous processed data as inputs. Multibody techniques are used to obtain the motor efforts and the external forces applied to the multibody system.

- **Comparison between calculated and measured contact torques**. The external forces applied to the multibody system calculated in the previous step correspond to the foot-ground reaction wrenches that can also be measured using the force plate equipments. The calculated and measured values are compared to validate the model.

- Development of a suitable **foot-ground contact model.** For solving the indeterminacy of the foot-ground wrench during the double support phase and also as a necessary goal to compute forward dynamic analyses, a realistic model for the foot-ground interaction is required. Compliant contact models are studied and a novel foot-ground contact model is proposed. The corresponding parameters are estimated using optimization techniques until.

- Implementation of a **forward dynamic analysis** module to simulate the human motion having as input data the joint efforts calculated in the IDA. The multibody formulation combined with mathematical integrators are used to obtain the human movement and the external contact forces through the foot-ground contact model. To accomplish this goal, a controller needs to be emplemented. In this thesis, the extended Kalman filter is used for this purpose.

- **Comparison between simulated and measured human motion and between calculated and measured contact wrench.** The comparison of both the motion and the ground reactions obtained in FDA with those measured in the laboratory allows us assessing the correctness of the foot ground-contact model and the forward dynamics module.

1.4 Thesis contents

This section offers a brief summary of each chapter of the thesis and lists the congress presentations and journal papers related to them.

Chapter 2: State of the art

In this chapter, a literature review of the biomechanical models of the human body is presented. Many models characterized by number of segments, types of joints and number of actuators have been developed depending on the nature of the research and the objectives of the analysis. Focusing on gait analysis, the most important works in forward and inverse dynamic analysis are cited and compared. Furthermore, the signal processing techniques used to filter the marker trajectories, to ensure kinematic consistency and to differentiate coordinates are exposed. Finally, the main characteristics of published foot-ground contact models are presented.

Chapter 3: Dynamic modelling of the human body

This chapter contains a complete description of the two biomechanical models (2D and 3D) employed in the thesis. Although the 3D model is necessary to accomplish the final objective of the research project mentioned before, the 2D model is a useful tool for understanding the mechanism of gait, reducing the complexity of the problem and decreasing the computational time.

The chapter includes the topology of the models, its anthropometric body segment parameters and the motion reconstruction process used to define the position and the orientation of each anatomical segment. The multibody formulation applied to solve the kinematic and the dynamic problems is also accurately described including the definition of each constraint equation.

Chapter 4: Inverse dynamic analysis of human gait

This chapter focuses on the inverse dynamic analysis of human gait. In particular, it describes the method used to reduce the noise inherent to the kinematic capture process (based on the singular spectrum analysis algorithm), the processing to obtain a kinematically consistent data set at position level (computed following an augmented Lagrangian minimization process), and the differentiation procedure to obtain velocities and accelerations. All these techniques are applied in the case of gait analysis using laboratory data.

The IDA carried out in this thesis computes the net joint torques and the total contact wrench applied to the multibody system using as input data the measured 3D skeletal motion and the BSP (without using directly the force plate measurements). A new dynamically consistent method for solving the inverse dynamics problem (using the force plate measurmenets) during the double support is presented in this chapter. Moreover, the IDA results are used as input data to compute a FDA and a PID controller is implemented in order to stabilize the multibody system.

The results of this chapter have been published in two congress proceedings and a paper has been sent to an international journal:

Lugris U., Carlin J., **Pàmies-Vilà R.**, Font-Llagunes J.M., Cuadrado J., Inverse–dynamics based estimation of motor torques during the double–support phase of human gait. *Multibody System Dynamics* (under review).

Lugris U., Carlin J., **Pàmies-Vilà R.**, Cuadrado J., (2011). Comparison of methods to determine ground reactions during the double support phase of gait. Proceedings of the *4th International Symposium on Multibody Systems and Mechatronics* (MuSMe 2011), 129–142, València, Spain.

Cuadrado J., **Pàmies-Vilà R.**, Lugris U., Alonso F.J., (2011). A force-based approach for joint efforts estimation during the double support phase of Gait. *IUTAM Symposium on Human Body Dynamics: From Multibody Systems to Biomechanics,* Procedia IUTAM, Vol. 2, 26–34. Waterloo, Canada.

Chapter 5: Analysis of different uncertainties in the IDA

This chapter analyses the effect of some uncertainties in input data on the results of a human gait IDA, focusing on the flexion/extension lower limb torques in a 2D model. In order to quantify the errors inherent to the use of anthropometric tables to estimate body segment parameters (BSP), a statistical error analysis is performed assuming that errors in BSP estimation follow a normal distribution. In a second analysis, three sets of kinematic data are used to emulate different solutions that may be provided by the kinematic consistency algorithm and the effect on the IDA results is discussed. Finally, the foot-ground contact forces and torques are perturbed –according to data sheet specifications of commercial force plates– to emulate the maximum error committed when these data are used as inputs of the IDA.

These results have been presented in two congresses and a journal paper has been published:

Pàmies-Vilà R., Font-Llagunes J.M., Cuadrado J., Alonso F.J., (2012). Analysis of different uncertainties in the inverse dynamic analysis of human gait. *Mechanism and Machine Theory*, Vol. 58, 153–164.

Pàmies-Vilà R., Font-Llagunes J.M., Cuadrado J., Alonso F.J., (2010). Efectos del error en las mediciones de la fuerza de contacto pie-suelo en el análisis dinámico inverso de la marcha humana. Proceedings of the *XVIII National Conference on Mechanical Engineering,* 1–10, Ciudad Real, Spain.

Pàmies-Vilà R., Font-Llagunes J.M., Cuadrado J., Alonso F.J., (2010). Influence of input data errors on the inverse dynamics analysis of human locomotion. Proceedings of the *1st Joint International Conference on Multibody System Dynamics*, 1–9, Lappeenranta, Finland.

Chapter 6: Foot-ground contact model

The chapter presents a novel foot-ground contact model base on sphere-plane contact elements. Its contact parameters and the geometrical properties of the contact elements are estimated using an optimization procedure. The foot-ground contact model is used to solve the contact force sharing problem during the double support phase in the IDA, and it is also used to obtain the resulting motion and the foot-ground contact forces when a FDA is performed.

Related to the results of this chapter, one paper has been presented in an international congress and another one has been presented in the National Conference on Mechanical Engineering.

Pàmies-Vilà R., Font-Llagunes J.M., Lugris U., Cuadrado J., (2012). Estimación de los parámetros del modelo de contacto pie-suelo en la marcha humana. Proceedings of the *XIX National Conference on Mechanical Engineering*, 1-8, Castelló de la Plana, Spain.

Pàmies-Vilà R., Font-Llagunes J.M., Lugris U., Cuadrado J., (2012). Two Approaches to Estimate Foot-Ground Contact Model Parameters Using Optimizaton Techniques. *2nd Joint Int. Conference on Multibody System Dynamics* (IMSD 2012), Book of abstracts, 90–91, Stuttgart, Germany.

Chapter 7

In this chapter, the thesis conclusions are drawn and some extensions and future lines of research are proposed.

Appendix A

This appendix contains the analytical expressions used to calculate the joint positions and the segment unit vectors of the three-dimensional model from the captured marker positions. This formulation is used in Chapter 4.

Appendix B

This appendix includes the methodology used to obtain analytical expression from a discretw position signala. It contains the Bézier xurves formulation to define the mathematical expression of the independent coordinates used in the two-dimensional model. These equations are used, as explained in Chapter 5, to drive the motion in the statistical study of the influence of input data uncertainities on the results of a human gait IDA.

Appendix C

The equations of the extended Kalman filter (EKF) in its continuous-time form are reminded. This appendix also contains the expressions of the EKF using the matrix-R multibody formulation. The EKF is used in Chapter 6 as a controller for the forward dynamic analysis.

Finally, there are some publications and congress presentations made during the course of the thesis that are not directly related to one chapter but are in line with the work done:

Font-Llagunes J.M., Kövecses J., **Pàmies-Vilà R.**, Barjau A., (2012). Dynamic analysis of impact in swing-through crutch gait using impulsive and continuous contact models. *Multibody System Dynamics*, Vol. 28 (3), 257–282.

Alonso J., Romero F., **Pàmies-Vilà R.**, Lugris U., Font-Llagunes J.M., (2012). A simple approach to estimate muscle forces and orthosis actuation in powered assisted walking of spinal cord-injured subjects. *Multibody System Dynamics*, Vol. 28 (1–2), 109–124.

Pàmies-Vilà R., Font-Llagunes J.M., Lugris U., Cuadrado J., On the use of multibody dynamics techniques for the inverse and forward dynamic analysis of human gait. *Congress on Numerical Methods in Engineering 2013*, Bilbao, Spain (submitted)

Font-Llagunes J.M., Romero F., Lugrís U., **Pàmies-Vilà R.**, Alonso F. J., Cuadrado J., Gait analysis of incomplete spinal cord injured subjects walking with an active orthosis and crutches. *Congress on Numerical Methods in Engineering 2013*, Bilbao, Spain (submitted)

Romero F., **Pàmies-Vilà R**., Lugrís U., Alonso F. J., Font-Llagunes J.M., Cuadrado J. (2012). Design of an innovative gait-assistive active orthosis for incomplete spinal cord injured subjects based on human motion analysis. *II Reunión del Capítulo Nacional Español de la Sociedad Europea de Biomecánica,* Book of abstracts, 1, Sevilla, Spain

Font-Llagunes J.M., **Pàmies-Vilà R.**, Alonso F.J., Cuadrado J., (2012). Dynamic analysis of walking with a powered stance-control knee-ankle-foot orthosis. Proceedings of the *18th Congress of the European Society of Biomechanics* (ESB 2012), Lisbon, Portugal.

Pàmies-Vilà R., Romero F., Lugrís U., Font-Llagunes J.M., Alonso F. J., Cuadrado J. (2011). Application of multibody dynamics techniques to active orthosis design for gait assistance, *I Reunión del Capítulo Nacional Español de la Sociedad Europea de Biomecánica*, Book of abstracts, 40, Zaragoza, Spain.

Font-Llagunes J.M., **Pàmies-Vilà R.**, Alonso F.J., Lugrís U., (2011). Simulation and design of an active orthosis for an incomplete spinal cord injured subject. *IUTAM Symposium on Human Body Dynamics: From Multibody Systems to Biomechanics,* Procedia IUTAM, Vol. 2, 68–81. Waterloo, Canada.

Alonso J., Romero F., **Pàmies-Vilà R**., Lugrís U., Font-Llagunes J.M., (2011). A simple approach to estimate muscle forces and orthosis actuation in powered assisted walking of spinal cord-injured subjects. Proceedings of the *Euromech Colloquium 511,* 1–16, Ponta Delgada, Portugal.

Alonso F.J., Galán-Marín G., Salgado D.R., **Pàmies-Vilà R.**, Font-Llagunes J.M., (2010). Cálculo de esfuerzos musculares en la marcha humana mediante optimización estática-fisiológica. Proceedings of the *XVIII* National Conference on Mechanical Engineering*,* 1–9, Ciudad Real, Espanya.

Font-Llagunes J.M., Barjau A., **Pàmies-Vilà R**., Kövecses J., (2010). Two approaches for the dynamic analysis of impact in biomechanical systems. Proceedings of the *Symposium on Brain, Body and Machine,* Springer, ISBN 978-3-642-16258-9, 1–4, Montreal, Canada.

Font-Llagunes J.M., Kövecses J., **Pàmies-Vilà R.**, Barjau A., (2010). Comparison of impulsive and compliant contact models for impact analysis in biomechanical multibody systems. Proceedings of the *1st Joint International Conference on Multibody System Dynamics,* 1–10, Lappeenranta, Finland.

Chapter 2

State of the Art

Kinematic and dynamic studies of human locomotion have been used in many fields with a wide variety of objectives. The three most important areas are robotics, computer animation and biomechanics. The goal of robotics research is related to control techniques. The human gait is an unstable motion and the dynamic balance is a challenging issue in the field of humanoid robotics. In the area of computer animation, the purpose has usually been to simulate aesthetically motion for a human-like figure. In this area, usually, kinematic studies rather than dynamic simulations have been carried out. The aims addressed in the biomechanics field are varied: obtain human gait patterns, study gait disorders, evaluate the neural control of gait, look for non measurable variables, develop better lower limb prosthesis, improve sport performance, etc.

The purpose of this chapter is to provide an overview of the studies concerned with the biomechanics field and specifically with dynamic simulation of human gait based on multibody dynamics techniques. To cover the methodological tools that need to be applied in this PhD thesis, this section is divided into five subsections: biomechanical models, inverse dynamic analysis, forward dynamic analysis, motion reconstruction, and foot-ground contact force models.

Multibody systems (MBS) can be defined as interconnected systems of bodies. These connections are modelled by joints that constrain the relative motion of the bodies or via force transmission elements, such as dampers or springs and actuators. Moreover, the forces applied to the system can include contact forces, friction forces, impact forces, joint constraint forces and gravitational forces [García de Jalón and Bayo 1994].

The human body consists of a set of bones linked by joints forming the skeleton and a set of soft tissues (flesh, organs and muscles). If the bones are considered as rigid segments, it is possible to assume that the body is divided into segments and the motion between bones can be described by kinematic restrictions. With this assumption, the classical mechanical concepts provide us with the possibility of estimating the dynamic variables of the motion.

One of the aims of the human motion dynamic analysis is to know the forces and moments that the musculoskeletal system produces during a motion. Multibody dynamics techniques can provide quantitative results for a three dimensional motion using non-invasive devices and with minimal interference with the subject's motion.

Depending on the purpose of the study, multibody dynamics techniques and a musculoskeletal computational model can be employed in two different ways: inverse and forward dynamics [Ambrósio and Kecskeméthy 2007].

Inverse dynamics techniques are used to calculate the net joint reaction forces and driver torques that the musculoskeletal system produces during human locomotion using acquired kinematic and kinetic data and estimated body segment parameters (BSP). Using this analysis, the resultant joint wrench can be obtained. However, because of the existence of redundant muscles, there is no way to uniquely define the individual contribution of each muscle. This indeterminacy is called the myoskeletal indeterminacy problem [Hazte 2002, Anderson and Pandy 2003, Pandy 2003]. The musculoskeletal system is redundantly actuated and the forces exerted by the different muscles are currently calculated, from the net joint torques, using optimization techniques [Ambrósio and Kecskeméthy 2007]. Usually the objective function is associated with physiological criteria and is related to the strategy that the central nervous system follows to activate the muscles. The optimization problem is solved at each time step of the motion and in the literature is usually referred to as *static optimization* [Anderson and Pandy 2001b, Silva and Ambrósio 2002b]. The inverse dynamic studies are suitable for recognizing normal and pathological gait patterns, for determining muscle forces and/or studying how the central nervous system controls the movement.

Forward dynamics techniques are used to predict the body movement from known muscle forces (or resultant joint torques) using principles of neural or optimal control. This approach can be adequate for investigating aspects of muscle function and energetic cost, for simulating gait disorders or predicting the combined actuation of the musculoskeletal system and assistive devices, such as exoskeletons or orthoses. This approach needs a control strategy that manages the actuators and the resulting motion is computed through integration of the equations of motion. In recent years, new methods for efficient control of the musculoskeletal system with optimal control methods have been presented [Ackermann and Van den Bogert 2010, Chung *et* al 2007, Ren *et al.* 2007, Thelen and Anderson 2006, Van den Bogert *et al.* 2011, Xiang *et al* 2009, Yang *et al.* 2004]. A growing interest in motion prediction has appeared during the last years, e.g., to anticipate the result of surgery, to help in the design of prosthetic/orthotic devices, or to study human motion dynamics performing various tasks [Fregly *et al.* 2007, Kim *et al.* 2006, Monnier 2006]. To this end, the motion parameters can be considered as design variables of an optimization problem. In this context, the determination of the joint efforts for a given motion (inverse dynamic analysis) is a required step for the subsequent evaluation of cost functions and constraints.

2.1 Biomechanical Models for Gait Analysis

The characterization of the human body depends on the intended use of the model. The number of segments, the type of joints, the number of muscles, etc., are decisions that researchers have to make according to the purpose of their study.

The simplest model used to study human gait is the inverted pendulum [Buczek *et al.* 2006, Hemami and Golliday 1977, Kagawa and Uno, 2010, Kajita *et al.* 2003], which is a useful first approach to study the efficient transfer of kinetic and potential energy that takes place when a subject walks (Figure 2.1 (a)). Another simple model is the passive walker, a mechanism vaguely resembling human lower body, that can walk stably down a slight slope without external energy input or control (Figure 2.1 (b) and (c)). The pioneering passive dynamic walking work is published by McGeer (1990). Other models based on the same principle mechanisms are used to study highly efficient gaits in bipedal walking exploring the natural dynamics of two-legged machines [Collins et al. 2001, Font-Llagunes and Kövecses 2009, Garcia *et al.* 1998, Kuo 1999, Tedrake *et al.* 2004]. Both two-dimensional motion and three-dimensional motion studies are present in the literature. However, these simple models do not provide a realistic representation of the human anatomy.

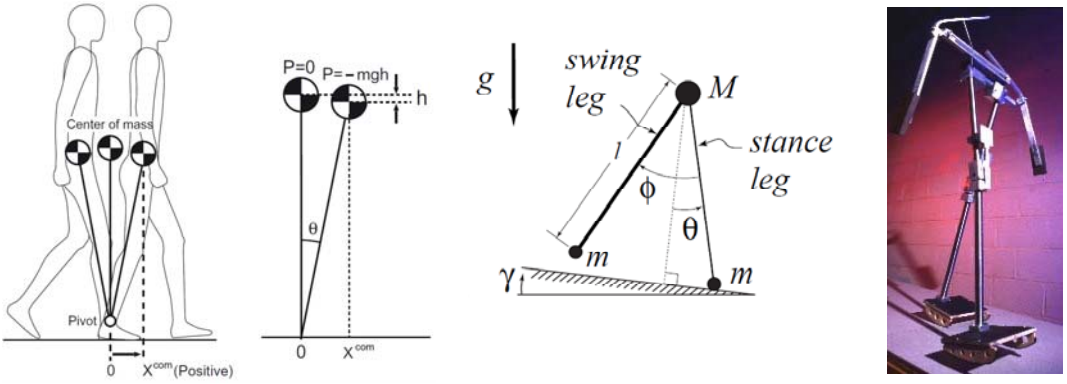

(a) **(b)** **(c)**

Figure 2.1 Simple models of human gait. (a) Inverted pendulum model [Kagawa and Uno, 2010]. (b) 2D passive walking [Garcia et al., 1998]. (c) Cornell 3D passive biped with arms [Collins, 2001].

Focusing on the models that realistically represent the body anatomy, two groups can be distinguished: the partial models [Gilchrist and Winter 1996, Maurel and Thalmann 1999, Pandy and Berme 1988a, Shelburne and Pandy 1997, Tumer and Engin 1993] and the whole-body models [Hatze 1984, Laananen *et al.* 1983, Pandy and Berme 1988c, Reich *et al.* 1999, Silva and Ambrósio 2002b]. The former describe anatomical joints with precise geometry and consider their physiological function. They usually use finite element methods [Dinis *et al.* 1999, Miller and Chinzei 1997, Prasad 1984, Saha *et al.* 1993, Wismans *et al.* 1994]. Conversely, the aim of whole-body models is to describe the global anatomy and the general motion characteristics.

Multibody dynamics techniques are used in these studies to analyse macroscopic motions, their interactions with the environment and kinematic relations among the elements [Amirouche *et al.* 1990, Anderson and Pandy 2001b, Hatze 1984, Morecki *et al.* 1984, Rasmussen *et al.* 2002, Reich *et al.* 1999, Silva and Ambrósio 2002a, Wismans 1996]. Some studies take advantage of the two levels and use a combination of both to obtain a more detailed analysis, although the computational cost of simulation

is obviously increased [Eberhard *et al.* 1999, Maurel and Thalmann 1999, Piazza and Delp 2001, Ribeiro *et al.* 2012]. An example of the combination of these two levels is the work presented by Ribeiro *et al.* (2012) where in order to represent the complexity of the knee joint, an accurate modelling of the condyle contact is used (Figure 2.2) and is included in a full model of the human gait using multibody methodologies.

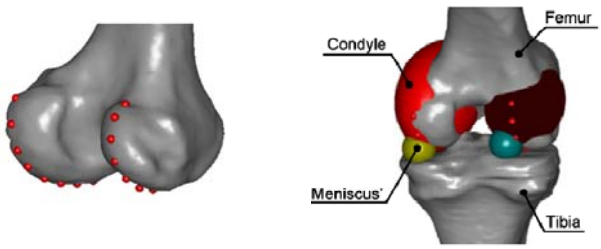

(a) **(b)**

Figure 2.2 Articular condyle model [Ribeiro *et al.* 2012]. (a) Points located used to define the femur condyle ellipses (b) knee model with two contact points defined on the tibial plateau.

The biomechanical model used in this thesis corresponds to the second group, it is a whole-body model aimed at describing the gait motion. Therefore, this literature review is focused on the models that represent the human body as a multibody system in which the anatomical segments are the bodies of the chain, the human articulations are modelled as mechanical joints and the muscles are the actuators that cause the motion. In all these studies, it is usual to assume that the bones are infinitely rigid, and the articulations are assumed to be ideal joints.

The level of detail of the models used when multibody techniques are applied also depends on the nature of the investigation and its goals [Eng and Winter 1994]. Models may include only the skeletal system [Fregly *et al.* 2007, Silva and Ambrósio 2004, Srinivasan *et al.* 2008] while other studies add the musculotendon actuation to this skeletal base [Ambrósio and Kecskeméthy 2007, Rodrigo *et al.* 2008, Van den Bogert *et al.* 2011]. In more detailed models, the muscular excitation-contraction coupling is included in the simulation, and even the behaviour of the motor neurons can be modelled [Kaplan 2000, Lee and Terzopoulos 2006, Nakamura *et al.* 2006, Seth *et al.* 2011, Winters 1995, Yamaguchi 2001, Zajac 1989].

Whole-body models used to analyse the human motion can be classified into those that consider the upper body as a single segment and those that include the upper limbs and head. The former assemble the head, arms and trunk (HAT) in a single body. This is the case of the model presented by Delp *et al*. (1990), a three-dimensional model with 43 muscles used to study musculoskeletal disorders and to analyse the effect of muscle strength in the wear of the joints. Hicks *et al*. (2007) use the same skeletal model (same joints and same degrees of freedom, DOF) but actuated by 92 muscles. This more detailed musculoskeletal model is used to simulate tibial torsion deformities and to determine the effect of these deformities on the capacity of lower limb muscles to extend the hip and the knee.

A similar HAT model is presented by Anderson and Pandy (1999) (Figure 2.3). A 23-DOF model formed by 10 anatomical segments and 54 muscles is used in several

studies to analyze different human motions [Anderson and Pandy 2001a, Arnold *et al*. 2005]. The same musculoskeletal model is also used by Reinbolt *et al*. (2008) to study a particular "disease" the *stiff knee gait*, characterized by a decreased knee flexion and a delay of the leg during the swing phase. Ackermann and Schiehlen (2006) propose a 27-DOF HAT model defining all the joints as spherical joints to study human gait disorders and how these disorders modify the metabolical cost estimation.

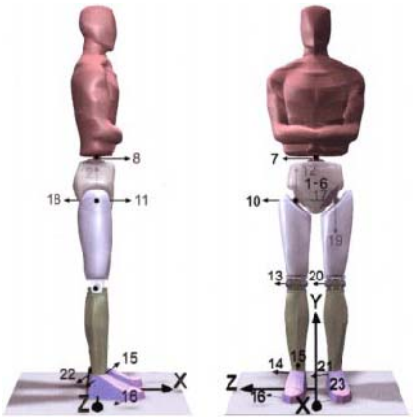

Figure 2.3 HAT human model [Anderson and Pandy, 1999].

Silva and Ambrósio's group has developed several models since 1996 considering as individual segments the head, trunk and arms (without using the HAT simplification). They often use natural coordinates and Lagrange equations to obtain the equations of motion. In [Silva *et al.* 1997], a model with 12 anatomical segments and 29 DOF is used. In this study, the feet modelling is not needed since authors consider that feet are not relevant to study the passive motion of the occupants during a vehicle crash. In a later work, Silva and Ambrósio (2004) extend the model to 33 rigid bodies which define 16 anatomical segments and 44 DOF. It should be noted that in this model the main human members are modelled with two coincident segments. This is to represent the rotation of the member with respect to its axis, or what is the same, it is done with the aim of approaching the rigid body rotation along a segment instead of about an articulate point (Figure 2.4).

The same model is used by Ambrósio and Kecskeméthy (2007) to analyse the problem of muscle activation using optimization techniques. The same group has presented a 16-segment model with 43 DOF [Rodrigo *et al.* 2007]. It is used to study muscle activity by means of optimization tools. The aim of the study is to identify cost functions describing the neural behaviour during human locomotion.

Besides the number of body segments and the type of joints, a set of anthropometric parameters (or body segment parameters, BSP) is needed to define the model. The first studies use corpses to determine the physical characteristics of the segments [de Leva 1993, 1996]. This explains why the median age of the subjects is higher and the study samples are few (no more than 13). This fact can produce some errors in the estimation of the anthropometry of the real subjects because some of the BSP change with age [Jensen 1986, 1993, Jensen and Fletcher 1994]. The median age on Dempster's study [Dempster 1955] is 68,5 years old, and in Clauser's work [Clauser *et al.* 1969] 49,3 years old. Further studies use gamma rays to estimate these parameters in living people

[Zatsiorsky 1990a, Zatsiorsky *et al.* 1990b, Zatsiorsky and Seluyanov 1985] and the error is highly reduced.

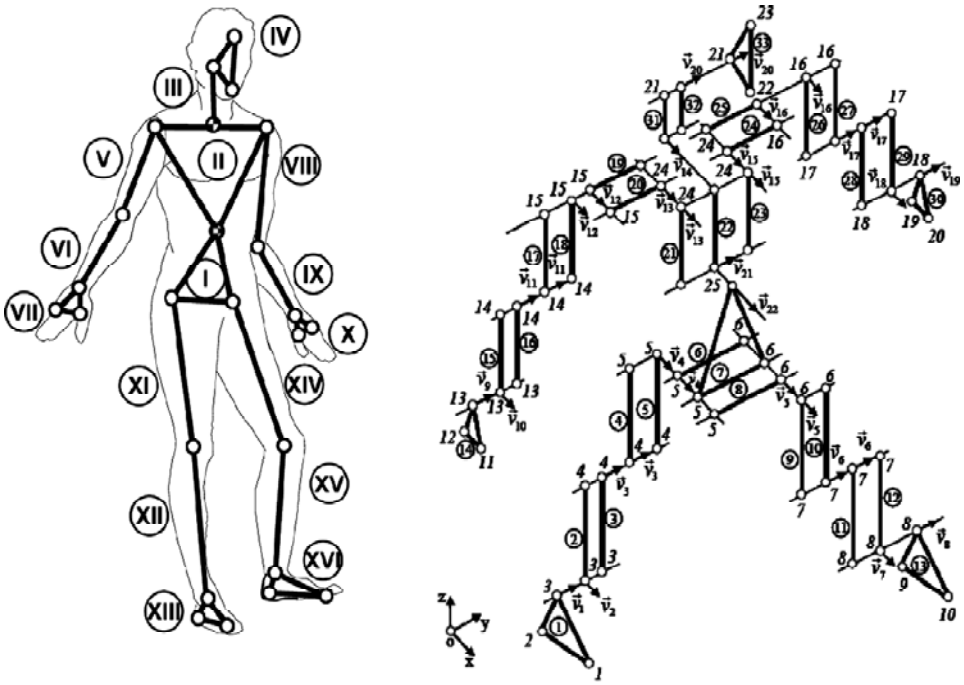

Figure 2.4 Human model [Silva and Ambrósio 2004].

Using the recorded data and statistical techniques, some anthropometric tables are provided in the literature. Zatsiorsky studies the use of bony landmarks as reference points for locating the centre of mass of the segments. Some of these landmarks are noticeably distant from the joint centres currently used by most researchers as reference points. Therefore, de Leva creates a new collection of parameters adapting and adjusting the Zatsiorsky's parameters defined as a function of the anatomical joints [de Leva 1996]. Similarly, Dumas *et al.* (2007b) readjusted McConville *et al.* (1980) and Young *et al.* (1983) parameters obtaining scale factors for men and women. In his popular book, Winter (1990) also presents anthropometric tables commonly used by researchers.

There are also particular cases (children, athletes, etc.) that require the use of digital images to estimate the segments' volume and their centroids [Davidson *et al.* 2008]. Similarly, Lee *et al.* (2009) describe an *in vivo* method that measures the parameters of the segments of the body via magnetic resonance imaging.

One of the studies with more samples is [Nikolova 2007]. It presents the anthropometric data of 5290 Bulgarian people from 30 to 40 years-old. This work determines the mass, the centre of mass and the inertia tensor about the centre of mass of 16 anatomic segments for male and female.

2.2 Inverse Dynamic Analysis

The objectives of the IDA are the calculation of the joint reaction forces, muscle forces and/or their resultant torque about the joints, that correspond to a measured human body motion. The pioneers of the estimation of forces and torques at lower limb joints are

Bernstein (1935), Elftman (1938, 1939), Bresler and Frankel (1950) and Blount (1956). All these studies determine forces and torques using the dynamic equations of each free body model and rudimentary techniques to obtain kinematic information (sequential photography techniques) and to measure ground reaction forces (e.g., a basograph or a device based on calibrated springs (Figure 2.5)).

In IDA a large set of input data is needed. These input data consist of the inertial properties of each segment, the kinematic information of the captured motion (trajectories of anatomical points) and the measurement of the applied external forces. All this information is measured experimentally or estimated via anthropometric tables and is prone to errors and uncertainties [de Leva 1996, Silva and Ambrósio 2004, Winter 1990].

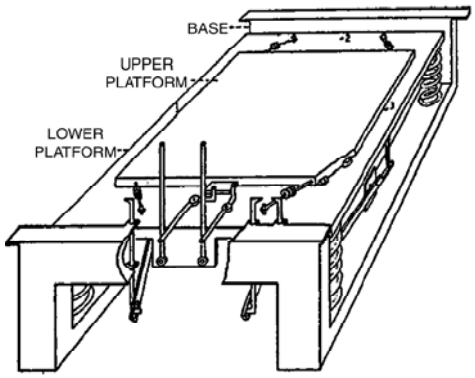

Figure 2.5 Illustration of a device capable of measuring the ground reaction in three directions [Elftman, 1938].

The results of the inverse dynamics problem are sensible to the uncertainties present in the input data. Different sources of errors in gait analysis are described in [Hazte, 2002]. Literature contains diverse studies that analyse the influence of BSP errors on the IDA results [Liu and Nigg 2000, Pearsall and Costigan 1999, Rao *et al.* 2006, Riemer *et al.* 2008, Davis *et al.* 1994, Silva and Ambrósio, 2004, Wu and Ladin 1993, Pearsall and Costigan 1999] and the effect of using different filter techniques to reduce the noise of the motion capture process [Winter *et al.* 1974, Gordon *et al.* 2003, Vaughan 1982, Cerveri *et al.* 2003, Senesch and Wolf 2009, Alonso *et al.* 2005, Cahouët *et al.* 2002]. There are different algorithms to obtain a new data set that guarantees kinematic consistency with the biomechanical model which can also introduce uncertainties in the analysis [Alonso *et al.* 2010, Celigüeta 1996, Silva and Ambrósio 2002a].

Some researchers have investigated the importance of having accurate kinematic measurements in gait analysis. Kadaba *et al.* (1989) compare the repeatability of gait analysis within the same day as well as in a day-to-day scenario. They have found that sagittal plane kinematics and kinetics are very consistent but, out of this plane, they are less repeatable for the day-to-day case and attribute this fact to errors in marker placement. In another study, Ramacrishnan *et al.* (1991) performed a sensitivity analysis of the joint centre position and its rotation axis orientation. Perturbing this position 10 or 20 mm, and the axis orientation ±15°, they found a variation up to a 114 % in magnitude of the ankle abduction moment.

Generally, in a gait analysis laboratory, foot-ground contact forces are also measured by means of force plates. If the kinematic information of the whole-body is known and the

results from two force plates are used as inputs of the IDA (employing one plate for each foot-ground contact), the biomechanical system is overdetermined because kinematic and force measurements outnumber the unknown torques [Cappozzo *et al.* 1975, Dumas *et al.* 2007a, Forner-Cordero *et al.* 2006, McCaw and DeVita 1995]. Some studies avoid this overdeterminacy by adding residual forces and torques or discarding the acceleration measurements of some segments and working with non-consistent data [Kuo 1998]. Other studies propose to use optimization techniques to minimize the residuals modifying the BSP [Vaughan *et al.* 1982], the joint trajectories [Chao and Rim 1973] or the joint accelerations [Cahouët *et al.* 2002, Remy and Thelen 2009]. All these studies assume that the residual torques are small, and this assumption highly depends on the accuracy of the force plate data.

2.3 Forward Dynamic Analysis

Forward dynamic analysis (FDA), in contrast with inverse dynamics, determines how a mechanical system will move due to the effect of external and internal forces without the need of experimentation, i.e., it is a predictive method. Using as input data dynamic information (BSP, forces, torques, etc.) the simulation predicts the motion of the body. In a FDA, the differential equations of motion are integrated in time in order to predict how a human would move. This technique is used to investigate the causal relationship between muscle forces and the motion generated during locomotion.

Most works on human gait analysis have focused on inverse dynamics studies. However, in the last years, the biomechanics community is attempting to go one step further: the prediction of the gait motion of real subjects under virtual conditions [Ackermann and Schiehlen 2006, Anderson and Pandy 2001b, Millard *et al.* 2008]. The most challenging aspect of FDA is the characterization and implementation of the control rules used to drive the model. An appropriate control to generate a forward dynamic simulation consistent with the locomotor task has not been clarified yet.

Usually, the FDA takes into account the muscle forces responsible of the motion. The methods most frequently used to predict the human gait are the dynamic optimization and the optimal control approach. In the *dynamic optimization* methodologies, the muscle force histories can be expressed in terms of parameters that are used as design variables of the optimization algorithm [Anderson and Pandy 2001a]. The main trouble of the dynamic optimizations is that the computational cost increases considerably due to the integration of the equations of human motion. Anderson and Pandy (2001a), reported more than 10000 hours of calculation in a computer with 32 processors to achieve a solution using a three-dimensional model. The *optimal control* approach uses controllers to preserve the stability of the walker model via closed-loop control algorithm which follows, for example, a gait pattern [Wojtyra 2003] or with a balance controller to dynamically maintain the stability of the model [Peasgood *et al.* 2007].

Usually, FDA works only simulate a single step, keeping the foot fixed to the ground, (avoiding modelling the foot motion) and without the control approach to guarantee stability. Moreover, the few multi-step forward-dynamic studies present in the literature use a relatively fixed gait pattern [Peasgood *et al.* 2007, Taga 1995]. Some researchers have used this technique in gait analysis employing constraint equations to restrict the motion and using a trial and error process to obtain the necessary torques to guide the

motion [Amirouche *et al.* 1990, Pandy and Berme 1989, Yamaguchi *et al.* 1992]. Other studies use the inverse dynamics results obtained in the laboratory to guide the motion [Bandera *et al.* 1990, Onyshko and Winter 1980, Ren *et al.* 2007].

One of the first studies of human locomotion where FDA is used is presented by Chow and Jacobson (1971, 1972). The 2D model used is composed of 7 segments and its mobility is constrained to 2 DOF. Despite the simplifications, the results are in agreement with the ground reaction forces obtained experimentally by other authors.

Hazte (1977) uses the Hill muscle model [Hill 1938] to define five muscular groups and determines, by means of optimization techniques, the optimal muscle coordination strategies for moving the leg to hit a specified target. In later studies, this author spreads the model throughout the body. Hatze (1980) analyzes the dynamic behaviour of all segments and then optimizes the muscle control through the stimulation of motor units. The same approach is used to study long jumps [Hazte 1981]. Similar works are presented by Hemami and Stokes (1983) using very simple models for gait simulation [Hurmuzlu and Moskowitz 1987a, 1987b].

Meglan (1991) presents a global approach to the FDA of human motion including a foot-ground contact model which is integrated in a full body 3D model composed by 13 segments with 34 DOF. Passive elements are placed at the joints to stabilize the motion and the model is actuated by dynamic data obtained via IDA.

Recently, Millard (2011) has presented a stance limb controller that uses a planar asymmetric spring loaded inverted pendulum (ASLIP) to compute a reference trajectory for a planar anthropomorphic multibody model (Figure 2.6). This work shows that the model reproduces the centre-of-mass kinematics and the ground reaction force profiles as in real human walking. According to this study, the quality of the FDA solution is closely related to the reliability of the model, to the control system used and to the definition that is used to measure how human-like a particular gait is. All this issues are active areas of research and still have many questions to solve.

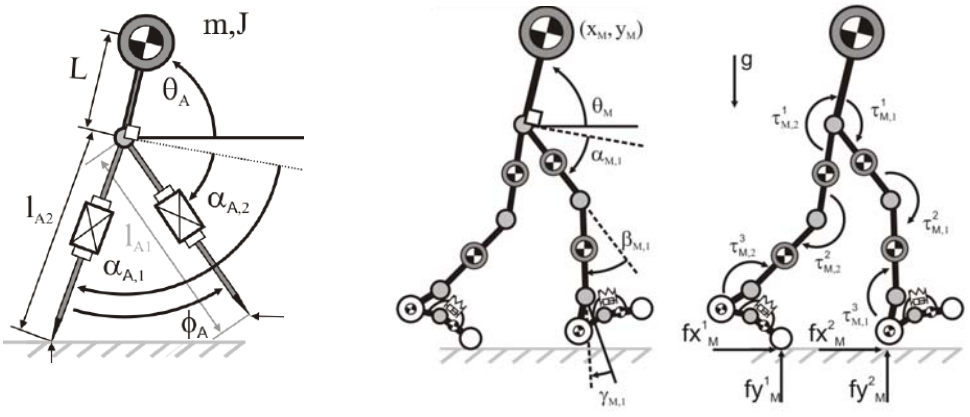

(a) **(b)**

Figure 2.6 Planar anthropomorphic model [Millard, 2011] (a) ASLIP model (b) Multibody model.

Humans have a remarkable ability to control their motions, which involve the cooperation of the nervous and the musculoskeletal systems. In biomechanics, and explicitly in FDA, one of the most important problems is to emulate how the brain works in order to control the body motion. Physically, the central nervous system sends

an electrical signal that stimulates the muscle, which at the same time produces the force that actuates the skeleton. Meanwhile, the brain collects and processes information from the senses allowing the central nervous system to adapt for the next muscle stimulation. How exactly this process works is an unknown and one of the biggest challenges in FDA is finding the optimal control strategy. The main problem is that the motor actions are the result of the neuro-muscular actuation and, hence, they are unknown.

Two different approaches are presented in order to predict how a human will move: to replicate the neuro-muscular system via an intelligent algorithm [Murai *et al.* 2008], and to state an optimization problem (so as to find the most likely motion) according to some objective functions such as minimizing weighted normalized torques, minimum metabolic energy cost, weighted joint accelerations, minimum muscle activation or minimum energy consumption [Ackermann and Schiehlen 2006, Anderson and Pandy 2001a, Ayoub *et al.* 1998, Fang and Pollard 2003, Kim *et al.* 2006, Marshall *et al.* 1989, Millard *et al.* 2009, Peasgood 2002, Rostami and Bossonnet 2001]. Nevertheless, not always a human-like solution is found. Up to now, the multibody community has chosen the second approach, surely as it is closer to their experience in mechanical fields. In this thesis, this is the approach that will be used.

The results present in the literature show that they are subjected to the optimization cost functions used, the convergence of the method, the accuracy of the initial guess, etc. If simple optimization approaches are used to predict the motion, the process can tend to local minima and then, the solution does not provide human-like motions [Ackerman and Schielen 2006, Anderson and Pandy 2001a, Bhushan and Shadmehr 1999]. If a control system is used to balance the biped, the control system can manipulate the behaviour of the system and can introduce relevant changes in the gait [Millard *et al.* 2008]. Moreover, in all optimization processes, the solutions found are strongly influenced by the definition used to measure how human-like a particular gait is.

2.4 Motion Reconstruction and Data Filtering

Input data used in the IDA are obtained from opto-electronic systems which capture the position of a set of markers attached to the body of the subject. These data contain errors introduced by the system itself, due to the marker's motion with respect to the skeletal system and also due to the movement of the soft tissue.

The capture system introduces errors in data as high frequency low amplitude noise. This noise is amplified when the raw displacement signals are differentiated (to obtain velocity and acceleration data) reaching unacceptable limits. Moreover, since the markers are placed on the skin of the subject, they move with respect to the underlying bones that they are intended to represent. There is a relative motion between the marker and the skeleton. This movement produces a kinematic inconsistence between the measurements and the actual motion of the skeleton and is one of the most critical sources of error in the analysis of human motion [Silva and Ambrósio 2002a]. This error cannot be removed using traditional filtering techniques, as its frequency content is close to the frequency of skeletal movement [Lu et al. 1999]. Finally, the effect of the soft tissue masses has to be considered. The human anatomical segments are formed by high rigidity elements (bones) and by soft tissues (muscles, ligaments, organs, adipose

tissue, skin and viscera). Usually, in biomechanical studies, these segments are represented as rigid bodies. This assumption can lead to errors, especially when impacts occur, due to the relative motion of the soft tissue mass over the skeleton [Gruber 1991, Andrews and Dowling 1993, Lafortune 1996, Neptune et al. 2000].

Filtering of high frequency error

The problem of differentiation of raw kinematic data has been extensively studied [Alonso 2005]. The high frequency noise in the position signal introduced by the motion capture system is highly amplified when obtaining velocity and acceleration data. Digital filters such as Butterworth filters, splines, polynomial function adjustments and spectral analysis filters are some of the techniques used to solve these problems.

Some studies show that the methods based on splines are more robust to different signal-noise combinations [Fazel-Rezi and Shedyck 1998, Walker 1998]. However, these methods may not be suitable for non-stationary signals such as those that exist in the impact phase of the heel to the ground during running [Giakas *et al.* 2000, Georgiakis *et al.* 2002a]. More effective filters for this purpose include the discrete wavelet transform [Adham and Shibab 1999] and the Wigner function [Giakas *et al.* 2000, Georgiakis e*t al.* 2002a, 2002b]. However, automating these methods is more complex than using the traditional ones.

In addition, Alonso (2005) has proved that the use of the singular spectrum analysis (SSA) presents better results and has proposed some methodologies to automate the process. This technique decomposes the original signal into the sum of a small number of independent and interpretable components that are used to reconstruct the signal (losing the least information possible). This is the method used in this thesis.

Correction of the skin motion

In a biomechanical laboratory, usually, markers are attached to the skin of the subjects and, therefore, they can move with respect to the skeleton. Consequently, the position signal contains a noise that has a similar frequency response as the motion itself. This type of error has been widely studied [Chèze 2000, Alexander and Andriacchi 2001, Manal *et al.* 2002, Silva and Ambrósio 2002a].

Techniques used to minimize the effects of this error can be divided into three groups: Some techniques model and simulate the viscoelastic behaviour of skin and model its relative motion with respect to the skeletal system. Other methods correct the position signals in order to impose that each segment satisfies kinematic constraints [Chèze *et al.* 1995]. Finally, invasive techniques place subcutaneous markers and techniques based on X-rays directly acquire the position of a set of skeletal points [Leardini *et al.* 2005]. It must be said, however, that this last technique has not yet provided a reliable estimation of the kinematics of the body segments [Leardini *et al.* 2005].

Soft tissue artifact effect

Being aware that the human body is not a mechanical system of rigid bodies, several authors have proposed different models of soft tissue artifacts. Soft tissue masses are

represented as punctual masses or rigid bodies linked to the multibody system by viscoelastic elements. These studies are still at an early stage of development and have some limitations [Hatze 2002]. The motion obtained for the masses is not very realistic, some studies do not always take into account the filtering errors and sometimes there are problems of kinematic inconsistency in the acquired data. In gait analysis, since the speed of movements made during human walking is low, the effect of soft tissue masses is small, and thus it can be neglected [Alonso 2005].

To conclude this section, note that literature reveals the importance of using some filters in order to compute properly the inverse dynamic analysis. In this thesis, the algorithm used to reduce high frequency noise contained in the measurements capture system is the SSA filter [Alonso 2005]. An automatic algorithm based on this filter is available and it is much simpler than other automatic filters, having only two parameters to be chosen: the size of the window and the set of components that will carry out the reconstruction. Furthermore, the data collected in the laboratory at 100 Hz cannot be enough in some cases (as will see in Chapter 6) and, consequently, a smoother interpolation is required, in this thesis smoothing spline techniques are used. We also use a method to ensure the consistency of kinematics measurements [Alonso *et al.* 2010]. However, since the study is focused on human walking motion, which involves relatively low velocities and accelerations, the effects of soft-tissue masses are not taken into account, as is justified in the literature.

2.5 Foot-Ground Contact Models

The interest for a correct model of the foot-ground interaction has increased during the last two decades. Initial studies in biomechanics do not use a realistic model of the foot; they keep it as a rigid body regardless of its actual multi-segment structure [Gull *et al.* 1998]. This assumption may be valid in an inverse dynamic analysis but cannot be applied in a forward dynamic study where an accurate modelization of the foot-ground interaction is necessary in order to obtain a realistic simulation of the motion.

The first biomechanical models assume that the ankle joint is fixed to the ground, neglecting the foot segment [Amirouche *et al.* 1990, Mochon and McMahon 1980, Siegler *et al.* 1982, Towsend and Seireg 1972]. Other studies consider that the foot segment is fixed to the ground during the support phase [Chou *et al.* 1995, Hemami *et al.* 1982, Onyshko and Winter 1980, Pandy and Berme 1988b, Yamaguchi and Zajac 1990]. The first model where second order curves are used to model the foot is presented by Ju and Mansour (1988) in a 2D simulation.

The first to use an explicit formulation for the foot-ground contact forces without imposing kinematic restrictions into the motion is Meglan (1991). His work contains three passive spheres and the contact is formulated using a visco-elastic model. The mechanical properties of these passive elements are taken from a previous experimental study [Valiant 1984].

Visco-elastic elements are also used by Gilchrist and Winter (1996). Their model consists of two segments (using revolute joints between phalanges and metatarsial segments). The values of stiffness and damping parameters are determined by trial and

error testing. The dynamics simulations using this model reproduce adequately the kinematics and dynamics of the movement, but the results are very sensitive to the values assumed as stiffness and damping. Similarly, Güller and Berme (1998) also use a visco-elastic sphere to represent the sole of the foot and Barbosa *et al.* (2005) use ellipsoids and an explicit force model to calculate the foot-ground force (which depends on the penetration of the ellipsoid and the stiffness and damping parameters of the materials in contact).

Cylinder elements are used in [Kecskeméthy 2011]. The model involves a two-segment representation of the foot with two cylinder-plane contact elements for the forefoot and the heel contact respectively (Figure 2.7 (a)). This model has the advantage of being capable of predicting the foot contact forces and a stable one-foot stance with only few contact elements and obtaining a good agreement with measurements. However, there are few tests published in the literature using this model, more experimental trials are needed to corroborate the model.

Another approach is presented by McPhee's group (Figure 2.7 (b)). They have developed a 9-DOF model consisting of seven rigid segments linked by revolute joints [Peasgood *et al.* 2007]. It is a two dimensional model and it is used in both inverse and forward dynamic analysis. The foot is modeled as a single segment with one contact point and when the model detects heel collision, it simulates a vertical force using a nonlinear spring-damper. The horizontal force is modelled using the Coulomb's dry friction model.

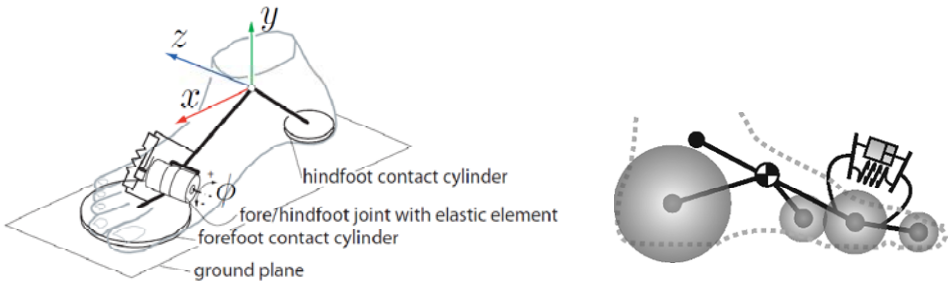

(a) **(b)**

Figure 2.7 Foot-ground contact models. (a) Cylinder-plane foot contact model [Kecskeméthy 2011]. (b) Planar foot contact model [Millard, 2011].

The same research group introduces another foot-ground contact model in the multibody biomechanical system, developed by Peasgood and Kubica (2007). In this case, the foot-ground contact force is calculated using two contact points, a point located at the heel and another placed at the metatarsal joint. The normal forces are represented using the Hunt-Crossley model [Hunt and Crossley 1975] and the tangential force is modelled using Coulomb's law of friction. However, the obtained foot-ground contact forces are taken from the published literature for a normal gait. Although the proposed model is computationally efficient, it does not reproduce the motion of a healthy person. So, they have proposed a modification of this model using 2, 3 or 4 spheres. The results using 4 spheres are similar to the experimental ones

Silva's research group has proposed a model where the foot is divided in two segments (plantar surface and toes) with a joint between the metatarsals and phalanges [Moreira

et al. 2009]. The interaction between the foot and the ground is modelled with 9 spheres (6 under the plantar surface and 3 under the toes), located along the midline of the foot. The model evaluates the position of the centre of pressure of the contact force, and calculates the contact force according to this position, the geometry properties, and the materials of the bodies in contact. The normal force is modelled using the Hunt-Crossley model [Hunt and Crossly 1975] and the friction force is modelled using the Coulomb's force model and a viscous component proportional to the horizontal tangential velocity of the contact point. Although the trend of the contact force is close to the published experimental results, there is not a comparison between the results found with this model and experimental data using force plates.

Recently, Flores *et al.* (2011) have presented a new continuous contact force model for soft materials that can be used for contact problems involving materials with low or moderate values of coefficient of restitution and, therefore, accommodating a high amount of energy dissipation. Although there are no foot-ground models using this contact formulation, it is expected that it can be of great importance for studying the foot-ground interaction in the biomechanics field.

From this literature review, it can be concluded that the published foot-ground contact models are still at an early stage. The forward dynamic problem and the interaction between the subject's body and the environment are not well resolved yet. Most studies use planar foot-ground contact models and rarely validate the results using real captures. Therefore, the use of 3D models together with real data can contribute to obtain more realistic simulations.

Chapter 3

Dynamic Modelling of the Human Body

In order to analyse human gait, a simplified model of the human body is needed. Biomechanical models are mechanical systems that resemble the physical structure of the human body and are suitable to study the dynamics of motion In this thesis, the anatomical segments are modelled as rigid bodies and the human joints correspond to kinematic pairs that connect the segments.

Moreover, to model the human body, a set of parameters that contain geometrical and inertial information of each segment is required. The inertial parameters define the mass and the inertia tensor of each segment and the geometric parameters contain the information necessary to describe the shape and volume used to represent the segment (length, width, height and radius).

Finally, to describe the multibody system, a set of coordinates is required to define the system configuration (position and orientation at each instant of time). In this thesis, the multibody system configuration is defined using mixed (natural plus angular) coordinates.

3.1 Biomechanical Models

The human body is modelled as a multibody system formed by rigid bodies, an approach which has been widely used to analyse human gait [Ackermann and Schiehlen 2006, Ambrósio and Kecskeméthy 2007, Ambrósio and Silva 1999, Dumas *et al.* 2007a]. The modelling of the human body by means of rigid bodies is a reasonable assumption if the motion involves big movements without strong impacts as in human locomotion [Ackermann and Schiehlen 2006]. The influence of soft tissue mass in the dynamics is only significant in situations with high jerk [Alonso 2005] that do not occur in gait.

To study the spatial human motion, a three-dimensional model of the human body is needed. However, many studies of human gait use a planar model to analyse both normal and pathological gait, taking advantage of the simplicity of computing a two-dimensional model. In this thesis, both 3D and 2D models are used. Although the 3D

model is necessary to accomplish the final objective of the research project mentioned in the introduction, the 2D model is a useful tool for understanding the mechanism of gait, reducing the complexity of the problem and decreasing the computational time. These two models are described below. The biomechanical model definition includes the topology used to represent the human body, the values of the anthropometric parameters and the process used to obtain the kinematic information related to the joints motion and the orientation of the anatomical segments.

3.1.1 Three-Dimensional Model

Topology of the Model

The 3D model consists of eighteen anatomical segments (Figure 3.1 and Table 3.1): two hindfeet, two forefeet, two shanks, two thighs, pelvis, torso, neck, head, two arms, two forearms and two hands. The segments are linked by ideal spherical joints defining a 57 degree of freedom (DOF) model.

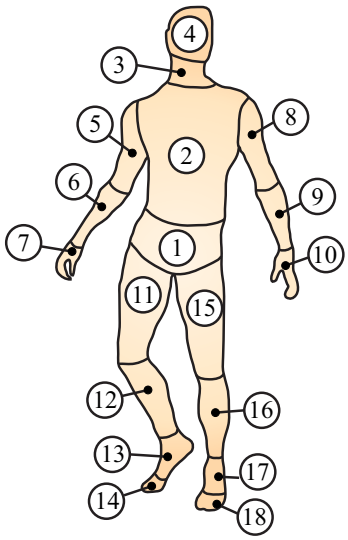

Figure 3.1 3D biomechanical model of the human body.

In contrast with the 3D models proposed by other authors [Ackermann and Schiehlen 2006, Anderson and Pandy 1999, 2001a, Arnold *et al.* 2005, 2007a, 2007b, Delp *et al.* 1990, Hicks *et al.* 2007, Reinbolt *et al.* 2008], who use the HAT simplification, the model used in this work cannot neglect head, arms and trunk motions. The main reason is that the upper body is expected to play a significant role in the gait of subjects with incomplete spinal cord injuries, who are the final target of the project.

The contact surfaces of a real human joint cannot be easily described. They have complex shapes and, moreover, the contact point between adjacent segments may change along motion. This implies the appearance of slight relative translations between segments. However, for large motions, like the ones present during gait, the body joints can be modelled as ideal joints that avoid relative translations and feature a fixed centre of rotation [Ackermann and Schiehlen 2006]. In this work, all the joints are modelled as spherical joints, that is, between two adjacent segments three rotations are allowed and translations are constrained (therefore, each joint restricts 3 DOF).

Nbr.	Name	Acronym	Description
1	Pelvis	P	From the first lumbar vertebra to the pelvic bone
2	Torso	T	From the first to the twelfth thoracic vertebra
3	Neck	N	From the first to the seventh cervical vertebra
4	Head	H	Cranium, upper and lower jaws
5	Right arm	RA	From right shoulder to right elbow
6	Right forearm	RFA	From right elbow to right wrist
7	Right hand	RH	From right wrist to right finger tips
8	Left arm	LA	From left shoulder to left elbow
9	Left forearm	LFA	From left elbow to left wrist
10	Left hand	LH	From left wrist to left finger tips
11	Right thigh	RT	From right hip to right knee
12	Right shank	RS	From right knee to right ankle
13	Right hindfoot	RHF	From right ankle to right metatarsals
14	Right forefoot	RFF	From right metatarsals to right toe
15	Left thigh	LT	From left hip to left knee
16	Left shank	LS	From left knee to left ankle
17	Left hindfoot	LHF	From left ankle to left metatarsals
18	Left forefoot	LFF	From left metatarsals to left toe

Table 3.1 Description of the model anatomical segments.

Anthropometric Measurements

In order to estimate the joint positions and the body segment parameters, some anthropometric measurements have to be taken. The inertial properties of the segments are extracted, for lower limbs, from a reduced set of measurements taken on the subject and by scaling published data according to his or her mass and height [Vaughan 1992]. For the upper body, Silva and Ambrósio (2002a) recommendations are followed using anthropometric parameters from [Laananen *et al.* 1983, Winter 1990].

The subject selected to perform the experiments is a healthy adult male, 34 years old, mass 85 kg and height 1,82 m. Since this subject possesses a similar stature and total body weight to the ones of the population considered in [Silva and Ambrósio 2002a] and [Vaughan 1992], the errors in the estimation of body segment parameters are expected to be low.

There are 20 measurements of the subject's lower extremities that need to be taken [Vaughan 1982]. They are illustrated in Figure 3.2. Finally, Table 3.2 shows the data for the selected subject.

The biomechanical model is a parametric model since its geometric and inertial properties depend on some measurements taken on the subject (the 20 measurements shown in Table 3.2 plus the total height of the analysed subject). The scaling factors to obtain the segments' anthropometric data are implemented on the general multibody program according to the equations presented in [Laananen *et al.* 1983, Winter 1990].

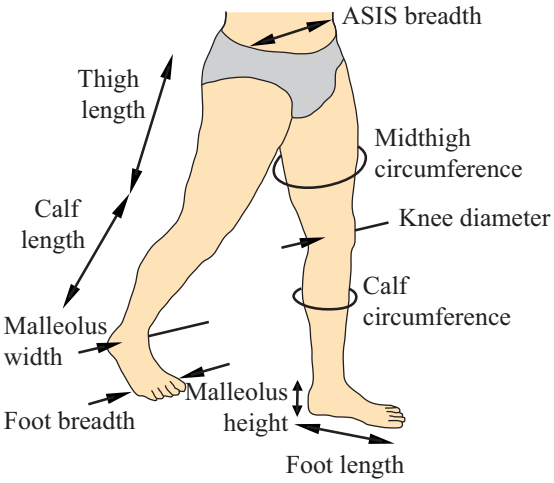

Figure 3.2 Anthropometric measurements of the lower extremities. Adapted from Vaughan [1992].

Symbol	Anthropometric Measurement	Value
A_1	Total body mass	85,00 kg
A_2	Anterior superior iliac spine (ASIS) breadth	0,290 m
A_3	Right thigh length	0,405 m
A_4	Left thigh length	0,405 m
A_5	Right mid-thigh circumference	0,490 m
A_6	Left mid-thigh circumference	0,490 m
A_7	Right calf length	0,410 m
A_8	Left calf length	0,410 m
A_9	Right calf circumference	0,375 m
A_{10}	Left calf circumference	0,375 m
A_{11}	Right knee diameter	0,099 m
A_{12}	Left knee diameter	0,099 m
A_{13}	Right foot length	0,275 m
A_{14}	Left foot length	0,275 m
A_{15}	Right malleolus height	0,087 m
A_{16}	Left malleolus height	0,087 m
A_{17}	Right malleolus diameter	0,073 m
A_{18}	Left malleolus diameter	0,073 m
A_{19}	Right foot breadth	0,091 m
A_{20}	Left foot breadth	0,091 m

Table 3.2 Anthropometric measurements of the subject.

3.1.2 Two-Dimensional Model

Topology of the Model

The second model used in this thesis is a simplified two-dimensional biomechanical model with 16 DOF. It consists of fourteen rigid bodies (Figure 3.3) linked with revolute joints, and it is constrained to move in the sagittal plane. Each foot is defined by means of two segments (as in the 3D model). In this second model, the pelvis and the torso are considered a single segment. The neck and head and the forearm and hand are also modelled as single bodies. The anthropometric information for this 2D model is extracted from the original three-dimensional model as will be seen in Section 3.3.

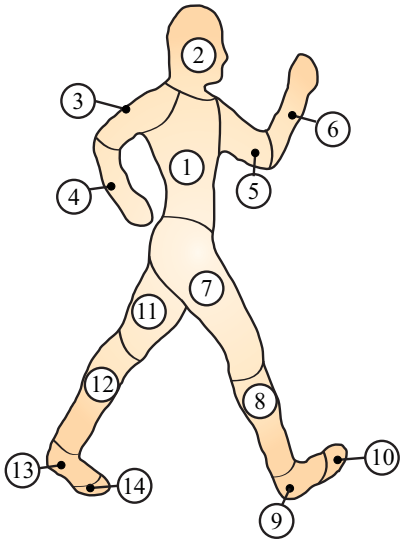

Figure 3.3 2D biomechanical model of the human body.

3.2 Motion Reconstruction

The kinematic information of the motion is obtained from the trajectories of a set of 37 markers attached to the human body. The position of each marker on the human body follows the marker set definition proposed by Vaughan (1992) for the lower limbs, and is based on Nigg and Herzog's (1995) configuration for the upper body (Figure 3.4 and Table 3.3).

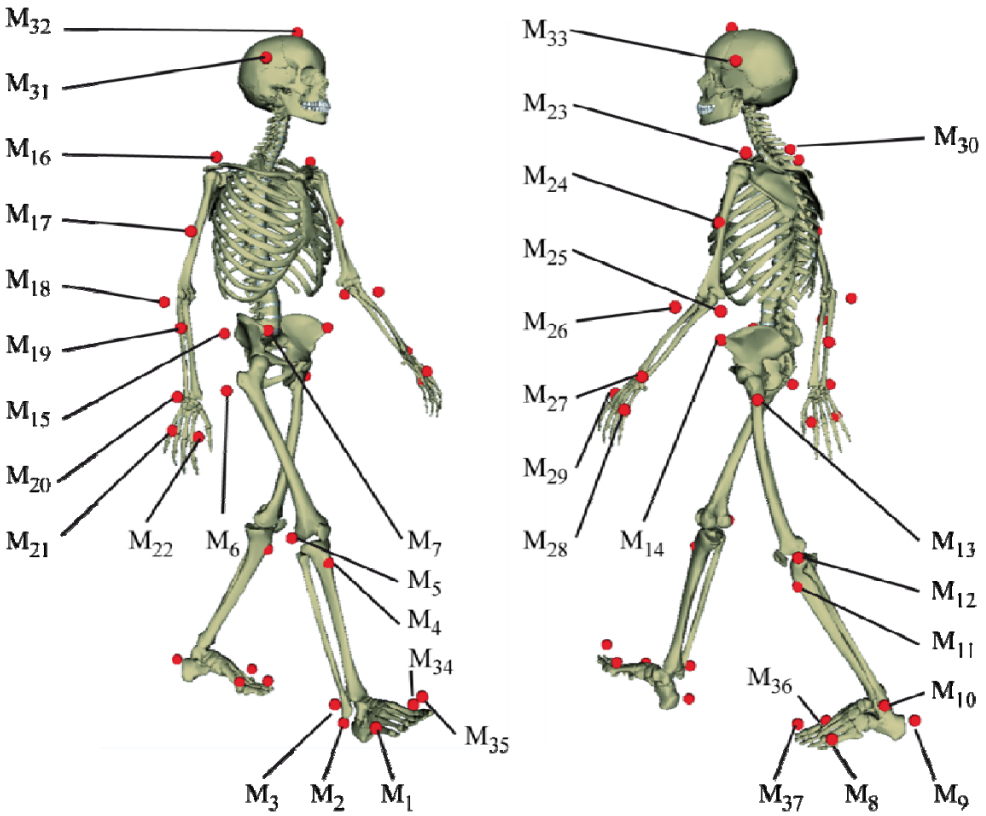

Figure 3.4 3D view of the human skeleton with the set of 37 markers used.

The markers positions are used to determine the orientation of each rigid body and to define the position of the 17 anatomical joints (Figure 3.5 (b)). The horizontal global axis X points to the direction of motion, the Z axis is perpendicular to the floor and pointing upwards, and the Y axis is defined so that $\{X, Y, Z\}$ is a positive defined orthonormal basis.

The configuration of a body segment is defined through the position of one of its points and its orientation with respect to the ground frame. For all segments, the chosen point will be the proximal joint. In order to compute the orientation, local bases $\{X', Y', Z'\}_S$ will be defined for all segments (Figure 3.5 (c)). Unit vectors $\mathbf{u}_S, \mathbf{v}_S, \mathbf{w}_S$ are used to define the axes of the local bases. Note that in the reference posture, the orientation of each local basis matches the one of the absolute basis $\{X, Y, Z\}$ (Figure 3.5 (d)).

Symbol	Placement	Symbol	Placement
M_1	Right metatarsal head V	M_8	Left metatarsal head V
M_2	Right calcaneus	M_9	Left calcaneus
M_3	Right lateral malleolus	M_{10}	Left lateral malleolus
M_4	Right tibial tuberosity	M_{11}	Left tibial tuberosity
M_5	Right lateral femoral epicondyle	M_{12}	Left lateral femoral epicondyle
M_6	Right femoral greater trochanter	M_{13}	Left femoral greater trochanter
M_7	Right ASIS	M_{14}	Left ASIS
M_{15}	Sacrum		
M_{16}	Right acromion in the shoulder girdle	M_{23}	Left acromion in the shoulder girdle
M_{17}	Right deltoid tuberosity	M_{24}	Left deltoid tuberosity
M_{18}	Right lateral humeral epicondyle	M_{25}	Left lateral humeral epicondyle
M_{19}	Middle of right forearm	M_{26}	Middle of left forearm
M_{20}	Right radial styloid in the wrist	M_{27}	Left radial styloid in the wrist
M_{21}	Right metacarpal head V	M_{28}	Left metacarpal head V
M_{22}	Right metacarpal head II	M_{29}	Left metacarpal head II
M_{30}	1st vertebra of the thoracic spine		
M_{31}	Right side of the head	M_{33}	Left side of the head
M_{32}	Top of the head		
M_{34}	Right metatarsal head I	M_{36}	Left metatarsal head I
M_{35}	Right distal phalange of the great toe	M_{37}	Left distal phalange of the great toe

Table 3.3 Placement of the set of markers used.

In Appendix A, Table A.1 shows the equations to determine the position of the 17 joints, $\mathbf{r}_{Ji}$, and the local unit vectors $\mathbf{u}_S, \mathbf{v}_S, \mathbf{w}_S$, as a function of the position of markers, $\mathbf{r}_{Mi}$.

The 3D model of the subject, shown in Figure 3.5, has been developed in mixed (natural plus angular) coordinates. (see Figure A.1 and A.2 in Appendix A for more details). It consists of 18 bodies and has 57 degrees of freedom, and it is modelled using 228 dependent coordinates: 22 points (which correspond to the positions of all the spherical

joints, along with the centres of mass of the five extreme segments: head, hands and forefeet) plus two orthogonal unit vectors for each rigid body (so, 36 vectors). Both, points and vectors are expressed using three Cartesian coordinates, thus making a total of 174 variables. The remaining 54 variables are the 18 sets of 3 angles that define the orientation of each segment with respect to the absolute frame.

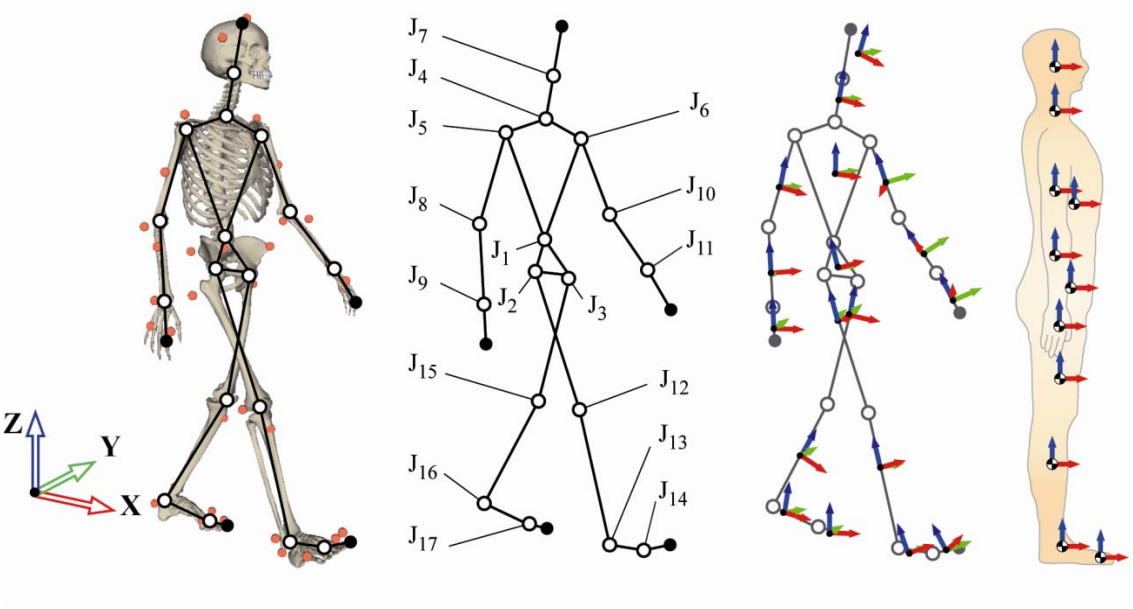

Figure 3.5 Biomechanical model used (a) 3D model of the human body, (b) Numeration of the seventeen joints, (c) Points and unit vectors defining the model in a general posture, (d) Sagittal view of the model at the reference posture.

The markers information is used to calculate the histories of the coordinates defining the motion. These data are processed to minimize the errors and differentiated to yield the histories of the coordinates at velocity and acceleration levels (see Section 3.4).

The kinematic information for the planar model is obtained from that of the 3D model, i.e., using the sagittal components of the position of joints J_2, J_4, J_8, J_{10}, J_{12}, J_{13}, J_{14}, J_{15}, J_{16}, J_{17}, and the sagittal components of the extreme points of the head, hands and forefeet (see Figure 3.5(b)). The history of these 2D coordinates is not kinematically consistent with the rigid body assumption and a new set of data is calculated by imposing this consistency at position level through the optimization algorithm explained in Chapter 5.

This second model (Figure 3.6) is defined by means of 15 points, representing the 10 revolute joints along with the centres of mass of the 5 extreme segments. Each point is expressed using two Cartesian coordinates (thus, 30 variables). Moreover, 14 angular variables (α_i) are used: 13 relative coordinates and one absolute angle used to orientate the leading hindfoot with respect to the ground. Therefore, the generalized coordinates vector $\mathbf{q}$ is composed of 44 variables.

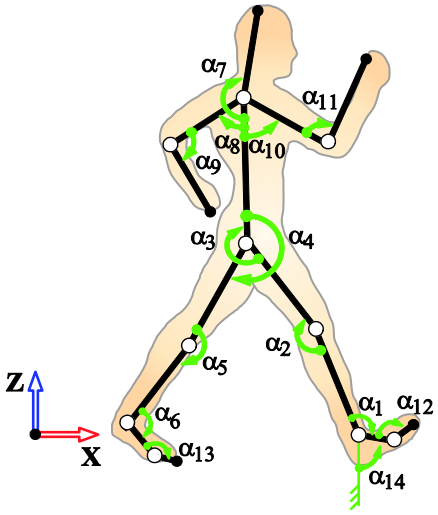

Figure 3.6 Points and angles used to define the configuration of the the planar model.

3.3 Body Segment Parameters

At this point, all the information to obtain the body segment parameters (BSP) is known. Due to errors in the motion capture, the distance between joints does not remain constant. Therefore, the length values contained in Table 3.4 are the mean segment lengths obtained during the captured motion

For the segments defined using two basic points, their lengths correspond to the straight-line distance between adjacent joint centres. For the trunk and the pelvis, more information is needed since they contain four and three joints, respectively. The mean distances between these joints are given in Figure 3.7.

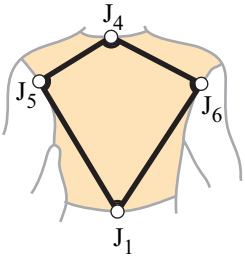

$L_{J1\text{-}J5}$=0,327 m $L_{J4\text{-}J5}$=0,212 m
$L_{J1\text{-}J4}$=0,253 m $L_{J4\text{-}J6}$=0,216 m
$L_{J1\text{-}J6}$=0,333 m $L_{J5\text{-}J6}$=0,424 m

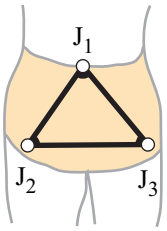

$L_{J1\text{-}J2}$=0,250 m
$L_{J1\text{-}J3}$=0,249 m
$L_{J2\text{-}J3}$=0,200 m

Figure 3.7 Representation of the major dimensions of the torso (left) and pelvis (right).

The position of the centre of mass (COM) of each segment $\mathbf{r}'_G = \{x'_G, y'_G, z'_G\}^T_S$ is expressed using the local coordinate system (with the origin at the proximal joint and local axes $\{X', Y', Z'\}_S$). These positions are presented in Table 3.4.

It should be noted that the moments of inertia of the segments are calculated with respect to the local basis attached to its COM. It is assumed that axes $\{X', Y', Z'\}_S$ are principal directions of inertia and I'_X, I'_Y, I'_Z are the principal moments of inertia about the COM (Table 3.4). Table 3.4 is properly adapted to obtain the corresponding BSP for the 2D model (Table 3.5).

No.	Name	Length	COM Location			Mass	Principal Moments of Inertia		
		L_i [m]	x'_G [m]	y'_G [m]	z'_G [m]	m_i [kg]	I'_X [10^{-2}kg·m^2]	I'_Y [10^{-2}kg·m^2]	I'_Z [10^{-2}kg·m^2]
1	Pelvis	*[1]	--	--	–0,193	12,895	26,220	13,450	26,220
2	Torso	*[1]	--	--	0,093	22,657	24,640	37,190	19,210
3	Neck	0,142	--	--	0,056	0,963	0,268	0,215	0,215
4	Head	0,103	0,047	--	0,018	3,851	2,453	2,249	2,034
5	Right arm	0,324	--	--	–0,140	1,808	1,492	1,356	0,249
6	Right forearm	0,229	--	--	–0,113	1,718	0,298	0,964	0,124
7	Right hand	0,179	--	--	–0,085	0,444	0,148	0,146	0,067
8	Left arm	0,305	--	--	–0,140	1,808	1,492	1,356	0,249
9	Left forearm	0,257	--	--	–0,113	1,718	0,298	0,964	0,124
10	Left hand	0,179	--	--	–0,085	0,444	0,148	0,146	0,067
11	Right thigh	0,406	--	--	–0,145	8,684	10,978	11,431	2,988
12	Right shank	0,432	--	0,005	–0,166	3,340	5,258	5,102	0,439
13	Right hindfoot	0,170	0,016	-0,009	–0,045	0,823	0,157	0,460	0,471
14	Right forefoot	0,092	0,023	-0,027	0,029	0,206	0,057	0,426	0,433
15	Left thigh	0,389	--	--	–0,139	8,446	10,978	11,431	2,988
16	Left shank	0,463	--	-0,005	–0,195	3,172	5,258	5,102	0,439
17	Left hindfoot	0,162	0,022	0,012	–0,040	0,818	0,157	0,460	0,471
18	Left forefoot	0,088	0,033	0,022	0,018	0,204	0,061	0,409	0,429

Table 3.4 Anthropometric data for the 3D model with eighteen segments.

No.	Name	Length	COM Location		Mass	Principal Moment of Inertia
		L_i [m]	x'_G [m]	z'_G [m]	m_i [kg]	I'_Y [10^{-2}kg·m^2]
1	Trunk	0,568	--	0,260	35,552	51,312
2	Head	0,245	0,038	0,133	4,814	2,472
3	Right arm	0,324	--	–0,140	1,808	1,356
4	Right forearm	0,408	--	–0,154	2,162	1,124
5	Left arm	0,305	--	–0,140	1,808	1,356
6	Left forearm	0,436	--	–0,154	2,162	1,124
7	Right thigh	0,398	--	–0,145	8,565	11,431
8	Right shank	0,448	--	–0,166	3,256	5,102
9	Right hindfoot	0,166	–0,016	–0,009	0,821	0,460
10	Right forefoot	0,090	0,023	0,029	0,206	0,426
11	Left thigh	0,398	--	–0,145	8,565	11,431
12	Left shank	0,448	--	–0,166	3,256	5,102
13	Left hindfoot	0,166	–0,016	–0,009	0,821	0,460
14	Left forefoot	0,090	0,023	0,029	0,206	0,426

Table 3.5 Anthropometric data for the 2D model with fourteen segments.

[1] For pelvis and torso, see Figure 3.7.

Note that the anthropometric parameters depend on the analyzed subject. The results presented in Tables 3.4 and 3.5 are obtained for the selected individual. Since BSP are used as input data in both, inverse and forward dynamic analyses, these values can be modified to compute sensitivity analyses. For example, in Chapter 5 a sensitivity analysis on the influence of BSP errors on the inverse dynamics results is presented.

3.4 Multibody Formulation. Kinematic Analysis

The simulated multibody system consists of a collection of rigid bodies. These bodies are constrained with respect to each other using a set of restrictions. Mathematically, these kinematic pairs (or joints) can be modelled by constraint equations that introduce kinematic relations between the coordinates describing the mechanical system.

The study of kinematics gives information about the motion of a system independently of the forces acting on it. The motion of the system depends on the geometry and configuration of its elements.

To understand the kinematics of human motion, it is necessary to study the general motion of a multibody system, with emphasis on the restrictions introduced by the kinematic pairs (corresponding to the anatomical joints of the human body). Therefore, in this section, the tools used to determine position, velocity and acceleration of the system are presented.

In this thesis, the anatomical segments are modelled as rigid bodies. Moreover, the multibody methodology is implemented using mixed coordinates (natural and relative). Therefore, the generalized coordinates describing the system are dependent and several algebraic equations need to be introduced to relate them. Those equations, called kinematic constraint equations, are used in this thesis to guarantee the characteristics of each segment (rigid body constraints) and also to guide the system motion using rheonomic constraints (driver constraints). They can be written as:

$$\mathbf{\Phi}(\mathbf{q},t)=\begin{Bmatrix}\Phi_1(\mathbf{q})\\ \vdots\\ \Phi_{ns}(\mathbf{q})\\ \Phi_{ns+1}(\mathbf{q},t)\\ \vdots\\ \Phi_{ns+nr}(\mathbf{q},t)\end{Bmatrix}=\mathbf{0} \tag{3.1}$$

where $\mathbf{q}=\{q_1,...,q_n\}^T$ is the n vector of generalized coordinates and $\mathbf{\Phi}$ represents the m kinematic constraints ($m = ns + nr$). The first ns restrictions are scleronomic constraints –which do not explicitly depend on time– and the rest (nr equations) are the rheonomic ones –equations with an explicit dependency on time–.

Usually, these equations are not linear. In order to solve the system, the Newton-Raphson method is used. This iterative method achieves quadratic convergence near the solution and it involves the linearization of Eq. (3.1). Using the first two terms of its expansion in a Taylor series and an approximate initial position $\mathbf{q}_j$, this equation can be written as:

$$\mathbf{\Phi}(\mathbf{q},t) \cong \mathbf{\Phi}(\mathbf{q}_j,t) + \mathbf{\Phi}_\mathbf{q}(\mathbf{q}_j)(\mathbf{q}-\mathbf{q}_j) = \mathbf{0} \tag{3.2}$$

which represents a system of linear equations, where $\mathbf{\Phi}_\mathbf{q}(\mathbf{q}_j)$ is the Jacobian matrix of the constraints evaluated at the approximate solution $\mathbf{q}_j$. This Jacobian matrix contains the partial derivatives of each kinematic restriction with respect to the generalized coordinates. It is expressed as:

$$\mathbf{\Phi}_\mathbf{q}(\mathbf{q}) \equiv \left[\frac{\partial \Phi_m}{\partial q_n}\right] = \begin{bmatrix} \frac{\partial \Phi_1}{\partial q_1} & \frac{\partial \Phi_1}{\partial q_2} & \cdots & \frac{\partial \Phi_1}{\partial q_n} \\ \frac{\partial \Phi_2}{\partial q_1} & \ddots & & \vdots \\ \vdots & & \ddots & \vdots \\ \frac{\partial \Phi_m}{\partial q_1} & \cdots & \cdots & \frac{\partial \Phi_m}{\partial q_n} \end{bmatrix} \tag{3.3}$$

The solution of Eq. (3.2) does not meet the constraints since the values of the vector $\mathbf{q}_j$ are an approximation of the solution. Therefore, the equation can be written as:

$$\mathbf{\Phi}_\mathbf{q}(\mathbf{q}_j)(\mathbf{q}-\mathbf{q}_j) = -\mathbf{\Phi}(\mathbf{q}_j) \tag{3.4}$$

It must be noted that vector $\mathbf{\Phi}(\mathbf{q},t)$ could contain redundant constraints. Mathematically, these redundant constraints contribute with linearly dependent rows of the Jacobian matrix, making this matrix rank-deficient. In this thesis, the least-square formulation is applied using the following iterative scheme [García de Jalon and Bayo 1994]:

$$\mathbf{\Phi}_\mathbf{q}^T(\mathbf{q}_j)\mathbf{\Phi}_\mathbf{q}(\mathbf{q}_j)(\mathbf{q}-\mathbf{q}_j) = -\mathbf{\Phi}_\mathbf{q}^T\mathbf{\Phi}(\mathbf{q}_j) \tag{3.5}$$

which is a system of linear equations obtained from the pre-multiplication of Eq. (3.4) by the transpose of the Jacobian matrix. The resultant matrix in Eq. (3.5) is no longer rank-deficient and the algorithm converges to a solution that satisfies all the constraint equations. Eq. (3.5) represents an iterative process that can be used until the norm of the residual $\Delta\mathbf{q}_j = (\mathbf{q}-\mathbf{q}_j)$ is less than a specified tolerance (in our case 10^{-9}).

The vector of generalized velocities $\dot{\mathbf{q}}$ can be calculated using the velocity constraints obtained differentiating Eq. (3.1) with respect to time:

$$\dot{\mathbf{\Phi}}(\mathbf{q},\dot{\mathbf{q}},t) \equiv \frac{d\mathbf{\Phi}(\mathbf{q},t)}{dt} = \mathbf{\Phi}_\mathbf{q}\dot{\mathbf{q}} + \mathbf{\Phi}_t = \mathbf{0} \tag{3.6}$$

where $\mathbf{\Phi}_t$ is the vector containing the partial derivatives of the constraints with respect to time. Note that the Jacobian matrix $\mathbf{\Phi}_\mathbf{q}$ is already known and $\mathbf{\Phi}_t$ can also be determined if the motion is known. Therefore, the vector $\dot{\mathbf{q}}$ can be calculated.

Similarly, the vector of generalized accelerations $\ddot{\mathbf{q}}$ can be determined from the time derivative of Eq. (3.6):

$$\ddot{\mathbf{\Phi}}\left(\mathbf{q},\dot{\mathbf{q}},\ddot{\mathbf{q}},t\right) \equiv \frac{d\dot{\mathbf{\Phi}}\left(\mathbf{q},\dot{\mathbf{q}},t\right)}{dt} = \dot{\mathbf{\Phi}}_{\mathbf{q}}\dot{\mathbf{q}} + \mathbf{\Phi}_{\mathbf{q}}\ddot{\mathbf{q}} + \dot{\mathbf{\Phi}}_{t} = \mathbf{0} \tag{3.7}$$

where $\dot{\mathbf{\Phi}}_{\mathbf{q}}$ is the time derivative of the Jacobian matrix, $\dot{\mathbf{\Phi}}_{\mathbf{q}}\dot{\mathbf{q}}$ depends on the velocities calculated through Eq. (3.6), and $\dot{\mathbf{\Phi}}_{t}$ is the time derivative of $\mathbf{\Phi}_{t}$.

In the presence of redundant constraint equations, the procedure described in Eq. (3.4) and (3.5) is also applied to velocity analysis.

3.4.1 Constraint Equations

As said before, mixed coordinates are used to define the system configuration. That is, the Cartesian coordinates of points and unit vectors are complemented with angles in order to easily drive the motion. It is simple to simulate, in this way, the motion of a multibody system driven by actuators located at the joints (which are directly related to the degrees of freedom) [García de Jalón and Bayo 1994]. Since the model is defined using dependent coordinates, a set of kinematic constraints between these variables has to be imposed.

The kinematic constraint related to the spherical joints used to link the segments can be described implicitly by sharing points between the two adjacent rigid bodies –decreasing the number of variables– [García de Jalón and Bayo 1994]. Therefore, no explicit equations are present in the constraints vector to define these pairs.

However, two types of kinematic constraints need to be imposed: the ones which guarantee the rigid body characteristics of each segment (rigid body constraints), and the ones which prescribe the motion of the system (driver constraints).

Rigid Body Constraints

Each rigid body is characterized by a set of points and unit vectors. There are several combinations of points and vectors that can be used when the rigid body is defined. In the presented human biomechanical model, the number of segment points coincides with the number of joints that the element shares with the rest of the chain. Furthermore, two local unit vectors are attached to each segment and will be used to determine its absolute orientation.

The total number of constraints directly depends on the combination of points and vectors that characterize each segment. For a given segment, the number of rigid body constraints is equal to the difference between the total number of coordinates related to the segment and the number of DOF of a general unconstrained rigid body (i.e., six DOF). These constraints are associated, for example, with the preservation of constant distances between any two points of the element and the preservation of constant angles between any two vectors.

Despite having different physical meaning, all of these kinematic restrictions can mathematically be defined using the scalar product of two generic vectors **u** and **v**:

$$\Phi(\mathbf{q},t) = \mathbf{v}^{T}\mathbf{u} - L_{\mathrm{u}}L_{\mathrm{v}}\cos\left(\left\langle \mathbf{v},\mathbf{u}\right\rangle(t)\right) = 0 \tag{3.8}$$

where L_u and L_v are the lengths of vectors **u** and **v** and $\langle \mathbf{v},\mathbf{u} \rangle(t)$ is the angle between them at time *t*. The rigid body constraints used in this thesis are exposed in Table 3.6.

Type	Constraint Description	v	u	L_v	L_u	$\langle \mathbf{v},\mathbf{u} \rangle$	Graphical representation
C01	Constant distance between points *i* and *j*	$(\mathbf{r}_j - \mathbf{r}_i)$	$(\mathbf{r}_j - \mathbf{r}_i)$	L_{ij}	L_{ij}	0	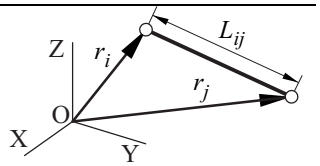
C02	Constant angle between segments $\mathbf{r}_{ij}$ and $\mathbf{r}_{ik}$	$(\mathbf{r}_j - \mathbf{r}_i)$	$(\mathbf{r}_k - \mathbf{r}_i)$	L_{ij}	L_{ik}	α	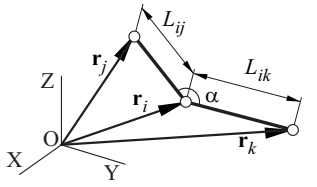
C03	Constant angle between segment $\mathbf{r}_{ij}$ and a unit vector **a**	$(\mathbf{r}_j - \mathbf{r}_i)$	**a**	L_{ij}	1	β	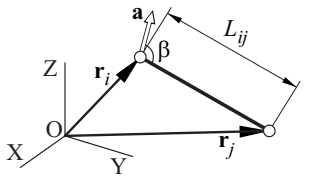
C04	Constant angle between 2 unit vectors	**a**	**b**	1	1	γ	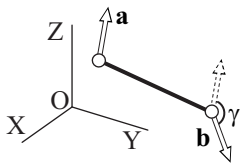
C05	Unit vector	**a**	**a**	1	1	0	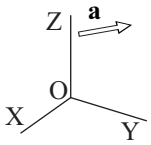

Table 3.6 Rigid body constraints using the scalar product equation.

Moreover, the linear dependency between the generalized coordinates associated with the rigid body can also be expressed using constraints C06 and C07. In its generic form, C06 expresses one vector **b** as a linear combination of a vectorial basis. The base can be defined using a vector (**a**) and two segments between body points ($\overline{ij}$ and $\overline{ik}$). In this case, the following constraint equation can be applied:

C06 $$\mathbf{\Phi}(\mathbf{q},t) = \mathbf{b} - a\left(\mathbf{r}_j - \mathbf{r}_i\right) - b\left(\mathbf{r}_k - \mathbf{r}_i\right) - c\mathbf{a} = \mathbf{0} \tag{3.9}$$

where *a*, *b*, *c* are the coefficients of the linear combination.

Similarly, if it is necessary, the local position of an extra point (point *n*) can also be expressed as a linear combination of the previous vectorial basis:

C07 $$\mathbf{\Phi}(\mathbf{q},t) = \left(\mathbf{r}_n - \mathbf{r}_i\right) - d\left(\mathbf{r}_j - \mathbf{r}_i\right) - e\left(\mathbf{r}_k - \mathbf{r}_i\right) - f\mathbf{a} = \mathbf{0} \tag{3.10}$$

where d, e, f are the coordinates of vector $\mathbf{r}_n - \mathbf{r}_i$ in the vectorial basis (this constraint is used in the torso definition). Note that Eqs. (3.9) and (3.10) represent three algebraic equations each, with a linear dependency on the generalized coordinates.

As an example, the constraints related to the pelvis segments (which is defined using the points and vectors shown in Figure 3.8) are explicitly described below.

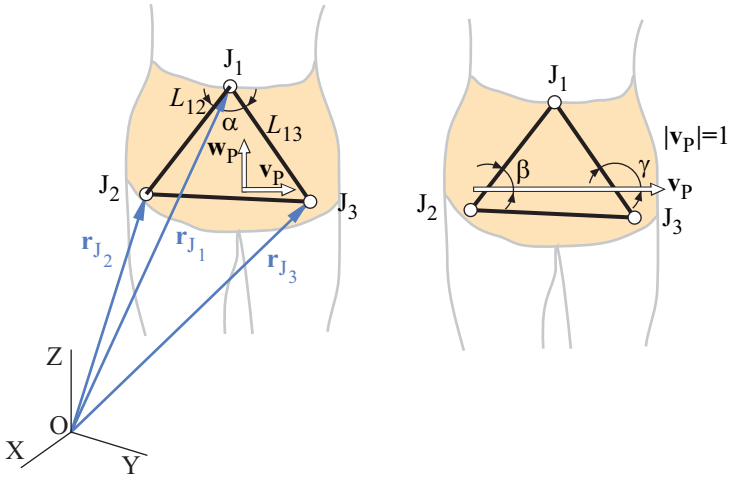

Figure 3.8 Pelvis segment defined using three points (J_1, J_2, J_3) and two vectors $\mathbf{v}_P, \mathbf{w}_P$.

Three points J_1, J_2, J_3 and two vectors $\mathbf{v}_P, \mathbf{w}_P$ are used for the pelvis segment in the 3D model. That makes a total of 15 variables related to the configuration of this segment. Therefore, 9 constraint restrictions are needed $(15-6=9)$. Two of them are the ones that guarantee a constant distance between joints J_1 and J_2 (L_{12}) and between joints J_1 and J_3 (L_{13}) –type C01 in Table 3.6–; another one guarantees the constant angle (α) between vectors $\mathbf{r}_{J2} - \mathbf{r}_{J1}$ and $\mathbf{r}_{J3} - \mathbf{r}_{J1}$ –type C02–; two more ensure a constant angle between vector $\mathbf{v}_P$ and the segment $\overline{J_1J_2}$ (β) and between vector $\mathbf{v}_p$ and the segment $\overline{J_1J_3}$ (γ) –type C03–; and the last one ensures that $\mathbf{v}_P$ is a unit vector –type C05–. That is:

C01 $$\left(\mathbf{r}_{J2} - \mathbf{r}_{J1}\right)^T \left(\mathbf{r}_{J2} - \mathbf{r}_{J1}\right) - L_{12}^2 = 0 \tag{3.11}$$

C01 $$\left(\mathbf{r}_{J3} - \mathbf{r}_{J1}\right)^T \left(\mathbf{r}_{J3} - \mathbf{r}_{J1}\right) - L_{13}^2 = 0 \tag{3.12}$$

C02 $$\left(\mathbf{r}_{J2} - \mathbf{r}_{J1}\right)^T \left(\mathbf{r}_{J3} - \mathbf{r}_{J1}\right) - L_{12}L_{13}\cos\alpha = 0 \tag{3.13}$$

C03 $$\left(\mathbf{r}_{J2} - \mathbf{r}_{J1}\right)^T \mathbf{v}_P - L_{12}\cos\beta = 0 \tag{3.14}$$

C03 $$\left(\mathbf{r}_{J3} - \mathbf{r}_{J1}\right)^T \mathbf{v}_P - L_{13}\cos\gamma = 0 \tag{3.15}$$

C05 $$\mathbf{v}_P{}^T \mathbf{v}_P - 1^2 = 0 \tag{3.16}$$

Consequently, six constraints are determined using the ones in Table 3.6. However, three more rigid body constraints are needed to express the linear dependency between the generalized coordinates; vector $\mathbf{w}_P$ can be expressed as a combination of the three joint points J_1, J_2, J_3 and vector $\mathbf{v}_P$. Therefore:

$$\mathbf{w}_P - a(\mathbf{r}_{J2} - \mathbf{r}_{J1}) - b(\mathbf{r}_{J3} - \mathbf{r}_{J1}) - c\mathbf{v}_P = \mathbf{0} \tag{3.17}$$

To conclude this part, Table 3.7 shows the types of restrictions that have been used to define the rigid body constraints among the coordinates associated to each anatomical segment of the three-dimensional model.

Segment	No. points	No. vectors	No. equations	Type of constraint
Pelvis (P)	3	2	2	C01
			1	C02
			2	C03
			1	C05
			1(x3)	C06
Torso (T)	4	2	2	C01
			1	C02
			2	C03
			1	C05
			1(x3)	C06
			1(x3)	C07
Rest of segments (N, H, RA, RFA, RH, LA, LFA, LH, RT, S, RHF, RFF, LT, LS, LHF, LFF)	2	2	1	C01
			2	C03
			1	C04
			2	C05

Table 3.7 Number of points and vectors that define each rigid body and type of constraint used to describe relationships among the body coordinates.

Driver constraints

In the inverse dynamic analysis, the motion is completely known, and the joint positions and the segment unit vectors are calculated from the captured marker positions. Angular variables have been introduced to easily drive the motion and to obtain the joint motor torques, or what is the same, the resultant moment of the muscle forces about the center of the joint.

The orientation of each rigid body is imposed by means of three fixed basic rotations about orthogonal axes. As it is known, its rotation matrix $\mathbf{S}_i$ can be expressed as:

$$\mathbf{S}_i = \mathbf{S}_\gamma \mathbf{S}_\beta \mathbf{S}_\alpha \tag{3.18}$$

where

$$\mathbf{S}_\alpha = \begin{bmatrix} 1 & 0 & 0 \\ 0 & \cos\alpha & -\sin\alpha \\ 0 & \sin\alpha & \cos\alpha \end{bmatrix}; \mathbf{S}_\beta = \begin{bmatrix} \cos\beta & 0 & \sin\beta \\ 0 & 1 & 0 \\ -\sin\beta & 0 & \cos\beta \end{bmatrix}; \mathbf{S}_\gamma = \begin{bmatrix} \cos\gamma & -\sin\gamma & 0 \\ \sin\gamma & \cos\gamma & 0 \\ 0 & 0 & 1 \end{bmatrix} \quad (3.19)$$

Therefore, a vector **b** belonging to one rigid segment is expressed as a vector **a** belonging to the global reference transformed following the rotation matrix $\mathbf{S}_i$:

$$\mathbf{b} = \mathbf{S}_i \mathbf{a}; \quad (3.20)$$

$$\mathbf{b} - \mathbf{S}_\gamma \mathbf{S}_\beta \mathbf{S}_\alpha \mathbf{a} = \mathbf{0} \quad (3.21)$$

In order to obtain these three absolute angles (α, β, γ), two unit vectors of the segment local basis are expressed as a function of the corresponding unit vectors of the global basis using Eq. (3.21). Then, a Newton-Raphson procedure as the one describe in Eqs. (3.2) – (3.4) is used to solve for the angles. As an example, for the the pelvis segment, α_P, β_P and γ_P can be obtained solving:

$$\mathbf{u}_\mathrm{P} - \mathbf{S}_{\gamma\mathrm{P}} \mathbf{S}_{\beta\mathrm{P}} \mathbf{S}_{\alpha\mathrm{P}} \mathbf{u}_\mathrm{X} = \mathbf{0} \quad (3.22)$$

$$\mathbf{w}_\mathrm{P} - \mathbf{S}_{\gamma\mathrm{P}} \mathbf{S}_{\beta\mathrm{P}} \mathbf{S}_{\alpha\mathrm{P}} \mathbf{w}_\mathrm{Z} = \mathbf{0} \quad (3.23)$$

where $\mathbf{u}_\mathrm{P}$ and $\mathbf{w}_\mathrm{P}$ are the pelvis unit vectors (which are function of the markers) and $\mathbf{u}_\mathrm{X}$ and $\mathbf{w}_\mathrm{Z}$ are the unit vectors of the global reference frame.

This procedure is implemented for all the segments obtaining the absolute angles between the segments and the ground. As said before, these angles represent sequential absolute rotations around the fixed axes $\{\mathrm{X}, \mathrm{Y}, \mathrm{Z}\}$.

The degrees of freedom chosen to represent the multibody system mobility are the position of the proximal pelvis joint (J_1) and the absolute angles α_i, β_i, γ_i of each segment. In order to explicitly impose the motion of these DOF, in the inverse dynamic approach, the following driver constraints are used:

C08 $$\varphi_i - \varphi_i(t) = 0 \quad (3.24)$$

C09 $$\mathbf{r}_{\mathrm{J1}} - \mathbf{r}_{\mathrm{J1}}(t) = 0 \quad (3.25)$$

where φ_i represents each absolute angular coordinate α, β or γ, and $\varphi_i(t)$ is its corresponding analytical expression (obtained using B-splines). Similarly, $\mathbf{r}_{\mathrm{J1}}$ is the absolute position of the joint J_1 and $\mathbf{r}_{\mathrm{J1}}(t)$ is its analytical expression.

Table 3.7 summarizes 117 rigid body constraints between natural coordinates (9 constraints for the pelvis segment, 12 for the torso and 6 for the other 16 segments).

Eq. (3.22) is the general form of a constraint between one angular variable and one unit vector (it represents three algebraic equations). Since this equation is implemented for each segment, it represents $18 \times 3 = 54$ restrictions. Note that Eqs. (3.22) and (3.23) are

redundant equations; both are computed and the least-square method explained previously is applied.

As known, $g = n - m$, being g the number of degrees of freedom, m the number of independent constraintss and n the number of dependent coordinates (in the proposed model, n = 228).The number of constraints m in the IDA and in the FDA is not the same. In the FDA, there are 57 free independent motions, therefore 171 constraints need to be implemented $\left(m = n - g = 228 - 57 = 171\right)$. These constraints correspond to the rigid body restrictions (117 constraints summarized in Table 3.7) plus the angular variable restriction presented in Eq. (3.22) (54 constraints)

In an inverse dynamic analysis, since the whole system is determined at kinematics level, there are no free motions, therefore $n = m$ = 228. Hence, a set of additional constraint equations is defined (equal in number to the DOF of the multibody system). These 57 additional constraints correspond to the absolute angles between each rigid body and the ground, Eq. (3.24) ($18 \times 3 = 54$ rheonomic constraints), and the position of the lumbar joint, Eq. (3.25) (3 more rheonomic constraints).

The kinematic restrictions used to define the planar model are a particular case of the previous general constraint equations. Each link of the planar model is defined using only its extreme points, i.e., two points for each rigid body. Moreover, similarly as in the 3D case, the kinematic restriction that constrains the motion between two adjacent bodies (allowing only for rotation) is imposed implicitly by sharing points between the two rigid bodies.

The number of independent algebraic constraint equations needed to represent the biomechanical model is equal to the difference between the number of coordinates (44) and the number of degrees of freedom of the system (16). That implies 28 constraint equations. The first 14 restrictions are related to rigid body constraints. They ensure a constant distance between two segment points i and j. Therefore, for each segment it is imposed that:

$$(\mathbf{r}_j - \mathbf{r}_i)^T (\mathbf{r}_j - \mathbf{r}_i) - L_{ij}^2 = 0 \tag{3.26}$$

where $\mathbf{r}_i = \{x_i, z_i\}^T$ and $\mathbf{r}_j = \{x_j, z_j\}^T$ are the absolute position vectors of points i and j, and L_{ij} is the distance between these points. Note that Eq. (3.26) is the analog two-dimensional expression of C01 in Table 3.6.

The remaining 14 constraints are those that relate the angular coordinates with the point positions. For a general case, they can be illustrated as Figure 3.9:

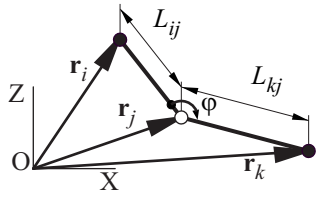

Figure 3.9 Angular variable between two segments linked by a revolute joint.

This condition can be imposed by means of either the scalar or the cross product (more specifically, the *y* component of the cross product) of vectors $(\mathbf{r}_i - \mathbf{r}_j)$ and $(\mathbf{r}_k - \mathbf{r}_j)$:

$$\left(x_i - x_j\right)\left(x_k - x_j\right) + \left(z_i - z_j\right)\left(z_k - z_j\right) - L_{ij}L_{jk}\cos\varphi = 0 \tag{3.27}$$

$$\left(x_i - x_j\right)\left(z_k - z_j\right) + \left(z_i - z_j\right)\left(x_k - x_j\right) - L_{ij}L_{jk}\sin\varphi = 0 \tag{3.28}$$

These two equations cannot be used interchangeably. When the angle φ is close to 0º or 180º, the scalar product is not valid for imposing the angle condition, and the cross product of vectors must be used. In turn, the cross product is not valid when φhas a value close to $\pm 90º$ [García de Jalón and Bayo 1994].

As it can be seen in Figure 3.6, the angular variables are defined so that in a normal gait their range of motion includes the values of 0º or 180º, but not ±90º. Therefore, the cross product equation, Eq. (3.28), is used to impose the mentioned angular restrictions.

Finally, to drive the motion in inverse dynamic analysis, the rheonomic constraints have to be imposed. In the planar model, the driver constraints are the position of the right ankle and the relative angles between segments. The type of restrictions used is the same as in Eqs. (3.24) and (3.25). However, in this case φ_i represents the relative angle between two adjacent segments, $\varphi_i(t)$ its analytical expressions as function of time, and $\mathbf{r}_{J1}$ and $\mathbf{r}_{J1}(t)$ the coordinates of the ankle joint position and its analytical expression.

3.5 Multibody Formulation. Dynamic Analysis

There are several procedures to obtain the dynamic equations of motion. In this thesis, the analysis is formulated using a multibody dynamics methodology. These equations can be expressed using dependent coordinates as:

$$\frac{d}{dt}\left(\frac{\partial T}{\partial \dot{\mathbf{q}}}\right) - \frac{\partial T}{\partial \mathbf{q}} + \boldsymbol{\Phi}_{\mathbf{q}}^T\boldsymbol{\lambda} = \mathbf{Q} \tag{3.29}$$

where T is the kinetic energy of the multibody system, $\mathbf{Q}$ is the vector of generalized forces and $-\boldsymbol{\Phi}_{\mathbf{q}}^T\boldsymbol{\lambda}$ are the generalized forces associated to the Lagrange multipliers $\boldsymbol{\lambda}$.

The kinetic energy can be written as:

$$T = \frac{1}{2}\dot{\mathbf{q}}^T\mathbf{M}\dot{\mathbf{q}} \tag{3.30}$$

where $\mathbf{M}$ is the mass matrix of the system. Therefore, Eq. (3.29) can be written as:

$$\mathbf{M}\ddot{\mathbf{q}} + \boldsymbol{\Phi}_{\mathbf{q}}^T\boldsymbol{\lambda} = \bar{\mathbf{Q}} \tag{3.31}$$

If the mass matrix is not constant, vector $\bar{\mathbf{Q}}$ of Eq. (3.31) includes the generalized forces plus all the velocity-dependent inertia terms –as a result of the derivatives of the kinetic energy–. Consequently, if the mass matrix is constant, then $\bar{\mathbf{Q}} = \mathbf{Q}$.

The system of equations in Eq. (3.31) contains *n* equations, where *n* is the total number of coordinates. The number of unknown values is $n+m$, where *m* is the number of constraints which coincides in turn with the *m* Lagrange multipliers. Therefore, the system can be written as:

$$\begin{cases} \mathbf{M}\,\ddot{\mathbf{q}} + \boldsymbol{\Phi}_{\mathbf{q}}^{T}\boldsymbol{\lambda} = \bar{\mathbf{Q}} \\ \boldsymbol{\Phi}\left(\mathbf{q},t\right) = \mathbf{0} \end{cases} \tag{3.32}$$

This system is a differential algebraic equation (DAE) system with *n* differential equations and *m* algebraic equations. In what follows, it is explained how to obtain the mass matrix of one element, and the generalized force vector for a generic rigid body.

3.5.1 Mass Matrices

As it can be seen in Table 3.7, the rigid bodies of the three-dimensional model are defined using at least two unit vectors and the Cartesian coordinates of two points. Accordingly to this rigid body modelling, the expressions of the mass matrix and the generalized force vector are explained. Note that for the pelvis and torso segments, defined with 3 and 4 points respectively, it is necessary to choose any two points, and the same methodology can be applied.

Figure 3.10 shows an element defined by two basic points *i* and *j* and two non-coplanar unit vectors **u** and **v**. $\{X,Y,Z\}$ are the axes of the global coordinate system (with origin at O) and $\{X',Y',Z'\}$ are the ones of the local coordinate system with its origin at point O' (which is not necessarily the element its centre of mass, G). Point P represents a generic point belonging to this rigid body.

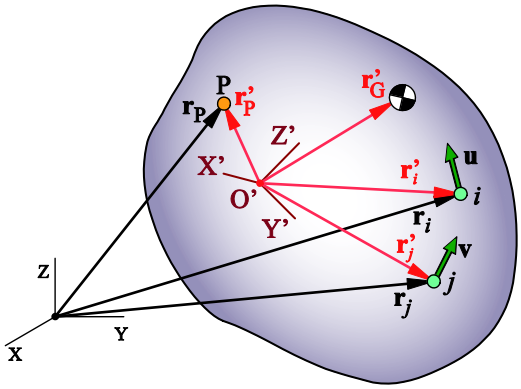

Figure 3.10 Representation of a generic rigid body using natural coordinates.

.

The position of any point P can be written as:

$$\mathbf{r}_P = \mathbf{r}_i + a_1\left(\mathbf{r}_j - \mathbf{r}_i\right) + a_2\mathbf{u} + a_3\mathbf{v} \tag{3.33}$$

where a_1, a_2, a_3 are the components of vector $(\mathbf{r}_\mathrm{P} - \mathbf{r}_i)$ in the basis formed by vectors $\left(\mathbf{r}_j - \mathbf{r}_i\right)$, **u** and **v**. Eq. (3.33) can be written as:

$$\mathbf{r}_\mathrm{P} = \begin{Bmatrix} x \\ y \\ z \end{Bmatrix} = \begin{bmatrix} (1-a_1)\mathbf{I}_3 & a_1\mathbf{I}_3 & a_2\mathbf{I}_3 & a_3\mathbf{I}_3 \end{bmatrix} \begin{Bmatrix} \mathbf{r}_i \\ \mathbf{r}_j \\ \mathbf{u} \\ \mathbf{v} \end{Bmatrix} \equiv \mathbf{A}\mathbf{q}_\mathrm{e} \tag{3.34}$$

where $\mathbf{I}_3$ is the 3×3 identity matrix and $\mathbf{q}_\mathrm{e}$ is the vector of coordinates associated with the element. Note that matrix $\mathbf{A}$ is independent of the system's motion and remains constant with time.

In the local coordinate system, the position of point P can be written as:

$$\mathbf{r}'_\mathrm{P} = \begin{Bmatrix} x' \\ y' \\ z' \end{Bmatrix} = \mathbf{r}'_i + a_1\left(\mathbf{r}'_j - \mathbf{r}'_i\right) + a_2\mathbf{u}' + a_3\mathbf{v}' \tag{3.35}$$

and, in matrix form:

$$\mathbf{r}'_\mathrm{P} - \mathbf{r}'_i = \begin{bmatrix} \mathbf{r}'_j - \mathbf{r}'_i & \mathbf{u}' & \mathbf{v}' \end{bmatrix} \begin{Bmatrix} a_1 \\ a_2 \\ a_3 \end{Bmatrix} \equiv \mathbf{X}'\mathbf{a} \tag{3.36}$$

with $\mathbf{a} = \{a_1, a_2, a_3\}^T$ and $\mathbf{X}'$ containing as columns the components of the vectors $\mathbf{r}'_\mathrm{P} - \mathbf{r}'$, $\mathbf{u}'$ and $\mathbf{v}'$. As these three vectors are non-coplanar, matrix $\mathbf{X}'$ can always be inverted. Therefore, **a** can be calculated from Eq. (3.36) as:

$$\mathbf{a} = \mathbf{X}'^{-1}\left(\mathbf{r}'_\mathrm{P} - \mathbf{r}'_i\right) \tag{3.37}$$

and matrix **A** can be determined using Eq. (3.34). Since **A** is constant, the velocity of the generic point P can be written as:

$$\dot{\mathbf{r}}_\mathrm{P} = \mathbf{A}\dot{\mathbf{q}}_\mathrm{e} \tag{3.38}$$

and the kinetic energy is:

$$T = \frac{1}{2}\int \dot{\mathbf{r}}_\mathrm{P}{}^T \dot{\mathbf{r}}_\mathrm{P}\, dm = \frac{1}{2}\dot{\mathbf{q}}_\mathrm{e}^T\left(\int \mathbf{A}^T\mathbf{A}\, dm\right)\dot{\mathbf{q}}_\mathrm{e} \equiv \frac{1}{2}\dot{\mathbf{q}}_\mathrm{e}^T\mathbf{M}_\mathrm{e}\dot{\mathbf{q}}_\mathrm{e} \tag{3.39}$$

Thus, the mass matrix of a rigid body defined with 2 points and 2 vectors is a 12×12 matrix that can be expressed as:

$$\begin{aligned}\mathbf{M}_{\mathrm{e}} &= \int \begin{bmatrix} (1-a_1)^2\mathbf{I}_3 & (1-a_1)a_1\mathbf{I}_3 & (1-a_1)a_2\mathbf{I}_3 & (1-a_1)a_3\mathbf{I}_3 \\ (1-a_1)a_1\mathbf{I}_3 & a_1^2\mathbf{I}_3 & a_1a_2\mathbf{I}_3 & a_1a_3\mathbf{I}_3 \\ (1-a_1)a_2\mathbf{I}_3 & a_1a_2\mathbf{I}_3 & a_2^2\mathbf{I}_3 & a_2a_3\mathbf{I}_3 \\ (1-a_1)a_3\mathbf{I}_3 & a_1a_3\mathbf{I}_3 & a_2a_3\mathbf{I}_3 & a_3^2\mathbf{I}_3 \end{bmatrix} \mathrm{d}m \\ &= \int \begin{bmatrix} (1-2a_1+a_1^2)\mathbf{I}_3 & (a_1-a_1^2)\mathbf{I}_3 & (a_2-a_1a_2)\mathbf{I}_3 & (a_3-a_1a_3)\mathbf{I}_3 \\ & a_1^2\mathbf{I}_3 & a_1a_2\mathbf{I}_3 & a_1a_3\mathbf{I}_3 \\ & & a_2^2\mathbf{I}_3 & a_2a_3\mathbf{I}_3 \\ \text{symmetric} & & & a_3^2\mathbf{I}_3 \end{bmatrix} \mathrm{d}m \end{aligned} \tag{3.40}$$

Eq. (3.40) involves the following integrals:

$$\int dm = m \tag{3.41}$$

$$\int \mathbf{a}\, dm = \int \mathbf{X}'^{-1}\left(\mathbf{r}'_{\mathrm{P}} - \mathbf{r}'_i\right) dm = \mathbf{X}'^{-1}\int \left(\mathbf{r}'_{\mathrm{P}} - \mathbf{r}'_i\right) dm = m\mathbf{X}'^{-1}\left(\mathbf{r}'_{\mathrm{G}} - \mathbf{r}'_i\right) \equiv m\mathbf{d}_i \tag{3.42}$$

$$\begin{aligned}\int \mathbf{a}\mathbf{a}^T dm &= \int \mathbf{X}'^{-1}\left(\mathbf{r}'_{\mathrm{P}} - \mathbf{r}'_i\right)\left(\mathbf{r}'_{\mathrm{P}} - \mathbf{r}'_i\right)^T \mathbf{X}'^{-T} dm \\ &= \mathbf{X}'^{-1}\left(\int \left(\mathbf{r}'_{\mathrm{P}} - \mathbf{r}'_i\right)\left(\mathbf{r}'_{\mathrm{P}} - \mathbf{r}'_i\right)^T dm\right)\mathbf{X}'^{-T} \\ &= \mathbf{X}'^{-1}\mathbf{J}_i\,\mathbf{X}'^{-T} \equiv \mathbf{Z}\end{aligned} \tag{3.43}$$

where $\mathbf{r}'_{\mathrm{G}}$ is the position vector of the centre of mass of the element in the local coordinate system and $\mathbf{d}_i = \{d_1, d_2, d_3\}^T$. In Eq. (3.42), it is used that $\int \mathbf{r}'_{\mathrm{P}} dm = \mathbf{r}'_{\mathrm{G}} \int dm$. In Eq. (3.43), $\mathbf{J}_i$ contains the information regarding the moments and products of inertia of the rigid body about point *i* and using the local axes $\{\mathrm{X}', \mathrm{Y}', \mathrm{Z}'\}$:

$$\begin{aligned}\mathbf{J}_i &= \int \left(\mathbf{r}'_{\mathrm{P}} - \mathbf{r}'_i\right)\left(\mathbf{r}'_{\mathrm{P}} - \mathbf{r}'_i\right)^T dm = \int \left(\mathbf{r}'_{\mathrm{P}} - \mathbf{r}'_{\mathrm{G}} + \mathbf{b}'\right)\left(\mathbf{r}'_{\mathrm{P}} - \mathbf{r}'_{\mathrm{G}} + \mathbf{b}'\right)^T dm = \\ &= \int \left(\mathbf{r}'_{\mathrm{P}} - \mathbf{r}'_{\mathrm{G}}\right)\left(\mathbf{r}'_{\mathrm{P}} - \mathbf{r}'_{\mathrm{G}}\right)^T dm + \int \mathbf{b}'\mathbf{b}'^T dm + \int \left(\mathbf{r}'_{\mathrm{P}} - \mathbf{r}'_{\mathrm{G}}\right)\mathbf{b}'^T dm + \int \mathbf{b}'\left(\mathbf{r}'_{\mathrm{P}} - \mathbf{r}'_{\mathrm{G}}\right)^T dm\end{aligned} \tag{3.44}$$

where $\mathbf{b}' \equiv \mathbf{r}'_{\mathrm{G}} - \mathbf{r}'_i$. The first term of the right hand side of Eq. (3.44) is related to the tensor of inertia about the centre of mass using local axes [García de Jalón and Bayo 1994]

$$\begin{aligned}\mathbf{\Pi}_{\mathrm{G}} &\equiv \int \left(\mathbf{r}'_{\mathrm{P}} - \mathbf{r}'_{\mathrm{G}}\right)\left(\mathbf{r}'_{\mathrm{P}} - \mathbf{r}'_{\mathrm{G}}\right)^T \mathrm{d}m = \\ &= \begin{bmatrix} \frac{1}{2}\left(-I'_{xx} + I'_{yy} + I'_{zz}\right) & I'_{xy} & I'_{xz} \\ I'_{xy} & \frac{1}{2}\left(I'_{xx} - I'_{yy} + I'_{zz}\right) & I'_{yz} \\ I'_{xz} & I'_{yz} & \frac{1}{2}\left(I'_{xx} + I'_{yy} - I'_{zz}\right) \end{bmatrix}\end{aligned} \tag{3.45}$$

where I'_{ij} are components of the tensor of inertia about the centre of mass $\mathbf{\Pi}_{\mathrm{G}}$, which is usually known beforehand (obtained for one anathomical segment, usually, scaling table data according to the mass and height of the subject).

The second term of the right hand side of Eq. (3.44) is:

$$\int \mathbf{b}'\mathbf{b}'^{T} \mathrm{d}m = m\mathbf{b}'\mathbf{b}'^{T} = m\left(\mathbf{r}'_{\mathrm{G}} - \mathbf{r}'_{i}\right)\left(\mathbf{r}'_{\mathrm{G}} - \mathbf{r}'_{i}\right)^{T} \tag{3.46}$$

and the third and fourth terms are null, because they represent the static moment of first order with respect to the COM [García de Jalón and Bayo 1994]. Therefore, Eq. (3.44) can be rewritten as:

$$\mathbf{J}_{i} = \int \left(\mathbf{r}'_{\mathrm{P}} - \mathbf{r}'_{i}\right)\left(\mathbf{r}'_{\mathrm{P}} - \mathbf{r}'_{i}\right)^{T} dm = \mathbf{\Pi}_{\mathrm{G}} + m\left(\mathbf{r}'_{\mathrm{G}} - \mathbf{r}'_{i}\right)\left(\mathbf{r}'_{\mathrm{G}} - \mathbf{r}'_{i}\right)^{T} \tag{3.47}$$

and the matrix $\mathbf{Z}$ defined in Eq. (3.43) can then be calculated. Using this, the mass matrix of the element can be written as [García de Jalón and Bayo 1994]:

$$\mathbf{M}_{\mathrm{e}} = \begin{bmatrix} \left(m - 2ma_1 + z_{11}\right)\mathbf{I}_3 & \left(ma_1 - z_{11}\right)\mathbf{I}_3 & \left(ma_2 - z_{12}\right)\mathbf{I}_3 & \left(ma_3 - z_{13}\right)\mathbf{I}_3 \\ & z_{11}\mathbf{I}_3 & z_{12}\mathbf{I}_3 & z_{13}\mathbf{I}_3 \\ & & z_{22}\mathbf{I}_3 & z_{23}\mathbf{I}_3 \\ \text{symmetric} & & z_{32}\mathbf{I}_3 & z_{33}\mathbf{I}_3 \end{bmatrix} \tag{3.48}$$

where z_{ii} are the components of matrix $\mathbf{Z}$.

Note $\mathbf{M}_{\mathrm{e}}$ is constant in time and, for that reason, needs to be evaluated and assembled in the global mass matrix only once at the beginning of the analysis. This is one advantage of working with natural coordinates. Moreover, it only depends on ten different values: the total mass of the rigid body, the coordinates of its COM in the local coordinate system and the six elements of the local inertia tensor about the COM.

When the planar model is used, the segments are defined using two basic points i and j (ends of the links). Using the vector of generalized coordinates $\mathbf{q}_{\mathrm{e}} = \left\{\mathbf{r}_i, \mathbf{r}_j\right\}^T$, the general expression in Eq. (3.48) can be written as:

$$\mathbf{M}_{\mathrm{e}} = \begin{bmatrix} m - 2m\dfrac{x'_{\mathrm{G}}}{L_{ij}} + \dfrac{I_i}{L_{ij}^2} & 0 & m\dfrac{x'_{\mathrm{G}}}{L_{ij}} - \dfrac{I_i}{L_{ij}^2} & -m\dfrac{y'_{\mathrm{G}}}{L_{ij}} \\ & m - 2m\dfrac{x'_{\mathrm{G}}}{L_{ij}} + \dfrac{I_i}{L_{ij}^2} & m\dfrac{y'_{\mathrm{G}}}{L_{ij}} & m\dfrac{x'_{\mathrm{G}}}{L_{ij}} - \dfrac{I_i}{L_{ij}^2} \\ & & \dfrac{I_i}{L_{ij}^2} & 0 \\ \text{symmetric} & & 0 & \dfrac{I_i}{L_{ij}^2} \end{bmatrix} \tag{3.49}$$

where m is the total mass of the element, x'_{G} and y'_{G} are the local coordinates of the centre of mass, I_i is the moment of inertia about point i (origin point of the local

coordinate system) and L_{ij} is the distance between points *i* and *j*, that is, the length of the segment.

The system global mass matrix **M** is obtained assembling all the element mass matrices $\mathbf{M}_e$. For example, if the mass matrix of one three-dimensional element is obtained using the coordinates $q_5, q_6, ..., q_{16}$ the elements of this matrix $\mathbf{M}_e$ will be added to the previous values in the global mass matrix **M** in the adequate positions, as it is represented in Figure 3.11.

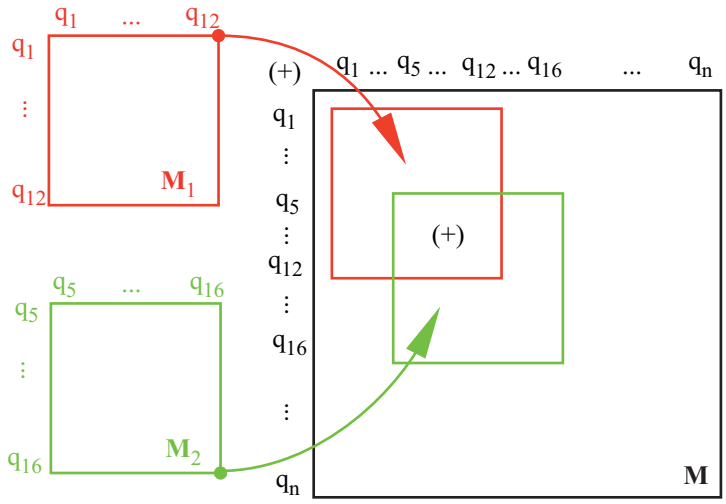

Figure 3.11 Assembly of the element mass matrices into the global mass matrix.

3.5.2 Generalized Force Vectors

The formulation of a force and a moment applied to a generic rigid body is explained below. As in the previous section, the methodology is explained assuming that the rigid body is defined using two points *i* and *j* and two non-coplanar vectors **u** and **v**. Figure 3.12 illustrates this generic element with a force **F** applied on point P.

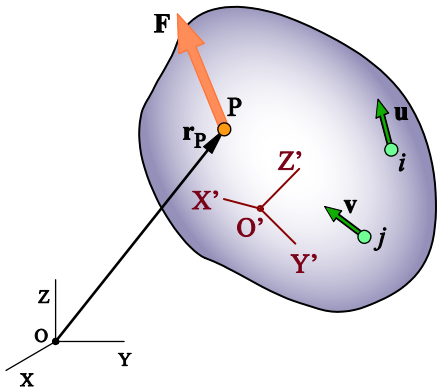

Figure 3.12 Generic force applied on point P.

Using Eq. (3.38), the velocity of a generic point P can be written as:

$$\dot{\mathbf{r}}_P = \mathbf{A}\dot{\mathbf{q}}_e \tag{3.50}$$

The virtual power of this force $\mathbf{F}$ can be expressed as:

$$\mathscr{P}^* = \mathbf{F}^T \dot{\mathbf{r}}_P^* = \mathbf{F}^T \mathbf{A} \dot{\mathbf{q}}_e^* \equiv \mathbf{Q}^T \dot{\mathbf{q}}_e^* \tag{3.51}$$

where $\dot{\mathbf{q}}_e^*$ is the vector of virtual velocities. Thus, the generalized force vector $\mathbf{Q}$ is obtained as:

$$\mathbf{Q} = \mathbf{A}^T \mathbf{F} \tag{3.52}$$

This last equation shows the transformation of a generic force $\mathbf{F}$ into an equivalent generalized force vector and it is valid for 3D and 2D elements. If a torque needs to be introduced, it will be decomposed into two equivalent forces and the previous process will be applied. The torque $\boldsymbol{\Gamma}$ can be transformed into an equivalent pair of forces $\mathbf{F}$ and $-\mathbf{F}$ of equal magnitudes, opposite directions and separated by a unit vector $\mathbf{u}_F$, which acts on a plane perpendicular to the direction of $\boldsymbol{\Gamma}$ (Figure 3.13).

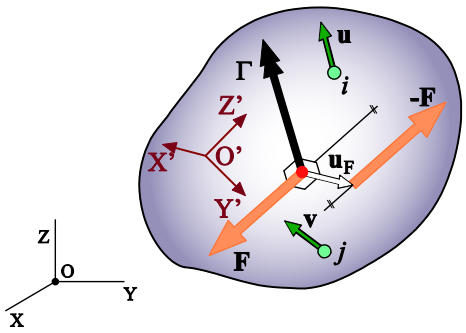

Figure 3.13 Generic moment applied on a rigid body.

The torque $\boldsymbol{\Gamma}$ can be expressed as a function of $\mathbf{F}$ as:

$$\boldsymbol{\Gamma} = \mathbf{F} \times \mathbf{u}_F \tag{3.53}$$

where $\mathbf{u}_F$ represents a unit vector that needs to be properly selected.

3.5.3 Solution of the Equations of Motion

The applied formulation uses dependent coordinates along with a set of algebraic constraints. The use of Lagrange equations with multipliers yields:

$$\begin{cases} \mathbf{M}\ddot{\mathbf{q}} + \boldsymbol{\Phi}_{\mathbf{q}}^T \boldsymbol{\lambda} = \mathbf{Q} \\ \boldsymbol{\Phi}(\mathbf{q}, t) = \mathbf{0} \end{cases} \tag{3.54}$$

which is a system of differential algebraic equations (DAE) with n second order ordinary differential equations and with m algebraic constraints. $\ddot{\mathbf{q}}$ is the n vector of generalized acceleration and $\boldsymbol{\Phi}$ is the m vector of constraints.

The strategy to solve these DAE system is based on turning it into an ordinary differential equation (ODE) system, since there are many well-known methods for their integration. In this thesis, to solve the motion equations a velocity projection method proposed by García de Jalón and Bayo (1994) is used. The equations are reduced to their state-space form, i.e., their independent coordinates $\dot{\mathbf{z}}$. In both models (2D and 3D), the chosen independent coordinates are the angular variables together with the position of one joint.

As seen in Section 3.4:

$$\dot{\mathbf{\Phi}}\left(\mathbf{q},\dot{\mathbf{q}},t\right)=\mathbf{\Phi}_{\mathbf{q}}\dot{\mathbf{q}}+\mathbf{\Phi}_{t}=0;\quad \mathbf{\Phi}_{t}\equiv-\mathbf{b} \tag{3.55}$$

The independent velocities $\dot{\mathbf{z}}$ are chosen from the dependent ones $\dot{\mathbf{q}}$ and a matrix $\mathbf{B}$ can be defined, such that:

$$\dot{\mathbf{z}}=\mathbf{B}\dot{\mathbf{q}} \tag{3.56}$$

Using Eqs. (3.55) and (3.56), it is obtained that:

$$\begin{bmatrix}\mathbf{\Phi}_{\mathbf{q}}\\ \mathbf{B}\end{bmatrix}\dot{\mathbf{q}}=\begin{bmatrix}\mathbf{\Phi}_{\mathbf{q}}^{\mathrm{d}} & \mathbf{\Phi}_{\mathbf{q}}^{\mathrm{i}}\\ \mathbf{0}_{gxm} & \mathbf{I}_{g}\end{bmatrix}\begin{Bmatrix}\dot{\mathbf{q}}^{\mathrm{d}}\\ \dot{\mathbf{q}}^{\mathrm{i}}\end{Bmatrix}\equiv\begin{Bmatrix}\mathbf{b}\\ \dot{\mathbf{z}}\end{Bmatrix} \tag{3.57}$$

where superscripts “d” and “i” indicate dependent and independent coordinates respectively, $g=n-m$ are the number of degrees of freedom and $\mathbf{I}_{g}$ is the g identity matrix. From Eq. (3.57), it can be deduced that the rows of matrices $\mathbf{\Phi}_{\mathbf{q}}$ and $\mathbf{B}$ are linearly independent. Therefore, vector $\dot{\mathbf{q}}$ can be calculated inverting the matrix of the $n\times n$ linear system:

$$\dot{\mathbf{q}}=\begin{bmatrix}\mathbf{\Phi}_{\mathbf{q}}\\ \mathbf{B}\end{bmatrix}^{-1}\begin{Bmatrix}\mathbf{b}\\ \dot{\mathbf{z}}\end{Bmatrix}\equiv\mathbf{S}\mathbf{b}+\mathbf{R}\dot{\mathbf{z}} \tag{3.58}$$

$$\begin{bmatrix}\mathbf{\Phi}_{\mathbf{q}}\\ \mathbf{B}\end{bmatrix}\begin{bmatrix}\mathbf{\Phi}_{\mathbf{q}}\\ \mathbf{B}\end{bmatrix}^{-1}=\begin{bmatrix}\mathbf{\Phi}_{\mathbf{q}}\\ \mathbf{B}\end{bmatrix}\begin{bmatrix}\mathbf{S} & \mathbf{R}\end{bmatrix}=\begin{bmatrix}\mathbf{\Phi}_{\mathbf{q}}^{\mathrm{d}} & \mathbf{\Phi}_{\mathbf{q}}^{\mathrm{i}}\\ \mathbf{0}_{gxm} & \mathbf{I}_{g}\end{bmatrix}\begin{bmatrix}\mathbf{S}^{\mathrm{d}} & \mathbf{R}^{\mathrm{d}}\\ \mathbf{S}^{\mathrm{i}} & \mathbf{R}^{\mathrm{i}}\end{bmatrix}=\begin{bmatrix}\mathbf{I}_{m} & \mathbf{0}_{mxg}\\ \mathbf{0}_{gxm} & \mathbf{I}_{g}\end{bmatrix} \tag{3.59}$$

and identifying terms:

$$\mathbf{S}=\begin{bmatrix}\mathbf{S}^{\mathrm{d}}\\ \mathbf{S}^{\mathrm{i}}\end{bmatrix}=\begin{bmatrix}\left[\mathbf{\Phi}_{\mathbf{q}}^{\mathrm{d}}\right]^{-1}\\ \mathbf{0}_{gxm}\end{bmatrix} \tag{3.60}$$

$$\mathbf{R}=\begin{bmatrix}\mathbf{R}^{\mathrm{d}}\\ \mathbf{R}^{\mathrm{i}}\end{bmatrix}=\begin{bmatrix}-\left[\mathbf{\Phi}_{\mathbf{q}}^{\mathrm{d}}\right]^{-1}\mathbf{\Phi}_{\mathbf{q}}^{\mathrm{i}}\\ \mathbf{I}_{g}\end{bmatrix} \tag{3.61}$$

The acceleration equation can be similarly determined. As seen in Section 3.4:

$$\ddot{\mathbf{\Phi}}\left(\mathbf{q},\dot{\mathbf{q}},\ddot{\mathbf{q}},t\right)=\mathbf{\Phi}_{\mathbf{q}}\ddot{\mathbf{q}}+\dot{\mathbf{\Phi}}_{\mathbf{q}}\dot{\mathbf{q}}+\dot{\mathbf{\Phi}}_{t}=\mathbf{0};\quad \mathbf{\Phi}_{\mathbf{q}}\ddot{\mathbf{q}}=-\dot{\mathbf{\Phi}}_{t}-\dot{\mathbf{\Phi}}_{\mathbf{q}}\dot{\mathbf{q}}\equiv\mathbf{c} \tag{3.62}$$

Therefore, since **B** is constant:

$$\begin{bmatrix} \boldsymbol{\Phi}_{\mathbf{q}} \\ \mathbf{B} \end{bmatrix} \ddot{\mathbf{q}} \equiv \begin{Bmatrix} \mathbf{c} \\ \ddot{\mathbf{z}} \end{Bmatrix} \tag{3.63}$$

$$\ddot{\mathbf{q}} = \begin{bmatrix} \boldsymbol{\Phi}_{\mathbf{q}} \\ \mathbf{B} \end{bmatrix}^{-1} \begin{Bmatrix} \mathbf{c} \\ \ddot{\mathbf{z}} \end{Bmatrix} = \mathbf{S}\mathbf{c} + \mathbf{R}\ddot{\mathbf{z}} \tag{3.64}$$

If an inverse dynamic analysis is performed using this formulation, the only unknown variable in Eq. (3.54) is the vector of Lagrange multipliers $\boldsymbol{\lambda}$, which can be perfectly determined at each time instant.

In forward dynamic analysis, motion is not known and Eq. (3.54) presents fewer equations than unknowns, it is an underdetermined system. The number of unknown dependent variables is greater than the total number of independent geometric and driver constraint equations. As a result, to determine the motion it is necessary to establish the dynamic equilibrium condition that leads to a second order differential system.

To solve the equations of motion, a method based in the explained projection matrix R is also used. As seen before:

$$\dot{\mathbf{q}} = \mathbf{R}\dot{\mathbf{z}} + \mathbf{S}\mathbf{b} \tag{3.65}$$

and then, differentiating this equation with respect to time, we obtain:

$$\ddot{\mathbf{q}} = \mathbf{R}\ddot{\mathbf{z}} + \dot{\mathbf{R}}\dot{\mathbf{z}} + \mathbf{S}\dot{\mathbf{b}} + \dot{\mathbf{S}}\mathbf{b} \tag{3.66}$$

The principle of virtual power establishes that the sum of the virtual powers produced by the forces acting on a multibody system must be zero at any time instant [García de Jalón and Bayo 1994]:

$$\dot{\mathbf{q}}^{*T}\left(\mathbf{M}\ddot{\mathbf{q}} - \mathbf{Q}\right) = 0 \tag{3.67}$$

The virtual dependent velocities can be expressed as a function of the virtual independent velocities (degrees of freedom):

$$\dot{\mathbf{q}}^{*} = \mathbf{R}\dot{\mathbf{z}}^{*} \tag{3.68}$$

Then, using Eqs. (3.65) and (3.67):

$$\dot{\mathbf{z}}^{*T}\mathbf{R}^{T}\left(\mathbf{M}\ddot{\mathbf{q}} - \mathbf{Q}\right) = 0 \tag{3.69}$$

Since Eq. (3.69) must be verified for any vector of independent virtual velocities, it must also be satisfied that:

$$\mathbf{R}^{T}\mathbf{M}\ddot{\mathbf{q}} = \mathbf{R}^{T}\mathbf{Q} \tag{3.70}$$

Using Eq. (3.66), Eq. (3.70) can be rewritten as:

$$\mathbf{R}^T\mathbf{M}\mathbf{R}\ddot{\mathbf{z}} = \mathbf{R}^T\left(\mathbf{Q} - \mathbf{M}\left(\dot{\mathbf{R}}\dot{\mathbf{z}} + \mathbf{S}\dot{\mathbf{b}} + \dot{\mathbf{S}}\mathbf{b}\right)\right) \tag{3.71}$$

which represents the equations of motion in terms of the independent coordinates. Then, using (3.64) and (3.66):

$$\mathbf{S}\mathbf{c} = \dot{\mathbf{R}}\dot{\mathbf{z}} + \mathbf{S}\dot{\mathbf{b}} + \dot{\mathbf{S}}\mathbf{b} \tag{3.72}$$

and, therefore:

$$\mathbf{R}^T\mathbf{M}\mathbf{R}\ddot{\mathbf{z}} = \mathbf{R}^T\left(\mathbf{Q} - \mathbf{M}\mathbf{S}\mathbf{c}\right) \tag{3.73}$$

This can be expressed in a compact form as:

$$\tilde{\mathbf{M}}\ddot{\mathbf{z}} = \tilde{\mathbf{Q}} \tag{3.74}$$

where

$$\tilde{\mathbf{M}} = \mathbf{R}^T\mathbf{M}\mathbf{R} \tag{3.75}$$

$$\tilde{\mathbf{Q}} = \mathbf{R}^T\left(\mathbf{Q} - \mathbf{M}\mathbf{S}\mathbf{c}\right) \tag{3.76}$$

Eq. (3.74) is a system of $g = n - m$ equations with g unknowns which can be easily solved for the independent accelerations $\ddot{\mathbf{z}}$. Vectors $\mathbf{z}$ and $\dot{\mathbf{z}}$ are obtained by numerical integration and, using Eqs. (3.65) and (3.66), the dependent variables $\mathbf{q}$, $\dot{\mathbf{q}}$ and $\ddot{\mathbf{q}}$ are calculated. Finally, the Lagrange multipliers (which are related to the joint wrench, see Section 3.5.5) can be obtained from Eq (3.54).

3.5.4 Integration of the Equations of Motion

There are several numerical algorithms in the literature to integrate the equations of motion when they have been transformed into a second order ODE system [García de Jalón and Bayo 1994]. In this thesis, the well-known trapezoidal rule is used. The position and velocity vectors at time-step $n+1$ are calculated as:

$$\begin{aligned} \mathbf{z}_{n+1} &= \mathbf{z}_n + \frac{h}{2}\left(\dot{\mathbf{z}}_n + \dot{\mathbf{z}}_{n+1}\right) \\ \dot{\mathbf{z}}_{n+1} &= \dot{\mathbf{z}}_n + \frac{h}{2}\left(\ddot{\mathbf{z}}_n + \ddot{\mathbf{z}}_{n+1}\right) \end{aligned} \tag{3.77}$$

where h is the time step. If the positions are used as primary variables, Eq. (3.77) can be rewritten as:

$$\begin{aligned}\dot{\mathbf{z}}_{n+1} &= \frac{2}{h}\mathbf{z}_{n+1} + \hat{\dot{\mathbf{z}}}_n; \quad \hat{\dot{\mathbf{z}}}_n = -\left(\frac{2}{h}\mathbf{z}_n + \dot{\mathbf{z}}_n\right) \\ \ddot{\mathbf{z}}_{n+1} &= \frac{4}{h^2}\mathbf{z}_{n+1} + \hat{\ddot{\mathbf{z}}}_n; \quad \hat{\ddot{\mathbf{z}}}_n = -\left(\frac{4}{h^2}\mathbf{z}_n + \frac{4}{h}\dot{\mathbf{z}}_n + \ddot{\mathbf{z}}_n\right)\end{aligned} \tag{3.78}$$

Combining Eq. (3.78) with the equations of motion, Eq. (3.74):

$$\mathbf{f}(\mathbf{z}) \equiv \tilde{\mathbf{M}}_{n+1}\mathbf{z}_{n+1} - \frac{h^2}{4}\tilde{\mathbf{Q}}_{n+1} + \frac{h^2}{4}\tilde{\mathbf{M}}_{n+1}\hat{\ddot{\mathbf{z}}}_n = 0 \tag{3.79}$$

This equation can be resolved using a Newton-Raphson iteration process:

$$\left[\frac{\partial \mathbf{f}(\mathbf{z})}{\partial \mathbf{z}}\right]_j \Delta\mathbf{z}_n^{j+1} = -\left[\mathbf{f}(\mathbf{z})\right]_j \tag{3.80}$$

$$\mathbf{z}_n^{j+1} = \mathbf{z}_n^j + \Delta\mathbf{z}_n^{j+1} \tag{3.81}$$

where j is the iteration index. An approximated tangent matrix is used [Dopico 2004]:

$$\mathbf{f}_z \equiv \left[\frac{\partial \mathbf{f}(\mathbf{z})}{\partial \mathbf{z}}\right] \simeq \mathbf{R}^T\mathbf{M}\mathbf{R} + \frac{h^2}{4}\mathbf{R}^T\mathbf{K}\mathbf{R} + \frac{h}{2}\mathbf{R}^T\left(\mathbf{C}\mathbf{R} + \mathbf{M}\dot{\mathbf{R}}\right) \tag{3.82}$$

being $\mathbf{K} = -\dfrac{\partial \tilde{\mathbf{Q}}}{\partial \mathbf{z}}; \quad \mathbf{C} = -\dfrac{\partial \tilde{\mathbf{Q}}}{\partial \dot{\mathbf{z}}}$

The residual is obtained evaluating Eq. (3.79) or, what is the same, evaluating the motion equations at time $n + 1$:

$$\mathbf{f}(\mathbf{z}) = \left(\tilde{\mathbf{M}}\ddot{\mathbf{z}} - \tilde{\mathbf{Q}}\right)_{n+1} \tag{3.83}$$

The iterative procedure for obtaining the position at step $n + 1$ starts by calculating an initial guess:

$$\mathbf{z}_{n+1}^0 = \mathbf{z}_n + h\dot{\mathbf{z}}_n + \frac{h^2}{2}\ddot{\mathbf{z}}_n \tag{3.84}$$

and obtaining the corresponding velocity and acceleration at $n + 1$ using the integrator's equations, Eq. (3.78). Then, the Newton-Raphson iteration is computed by calculating the terms of the tangent matrix and the residual. After that, the system is solved using Eq. (3.80) and the new positions are calculated through Eq. (3.81). Using the trapezoidal rule, the new velocities and accelerations are calculated until the convergence error $\|\Delta\mathbf{z}\|$ goes under a specified tolerance (Figure 3.14).

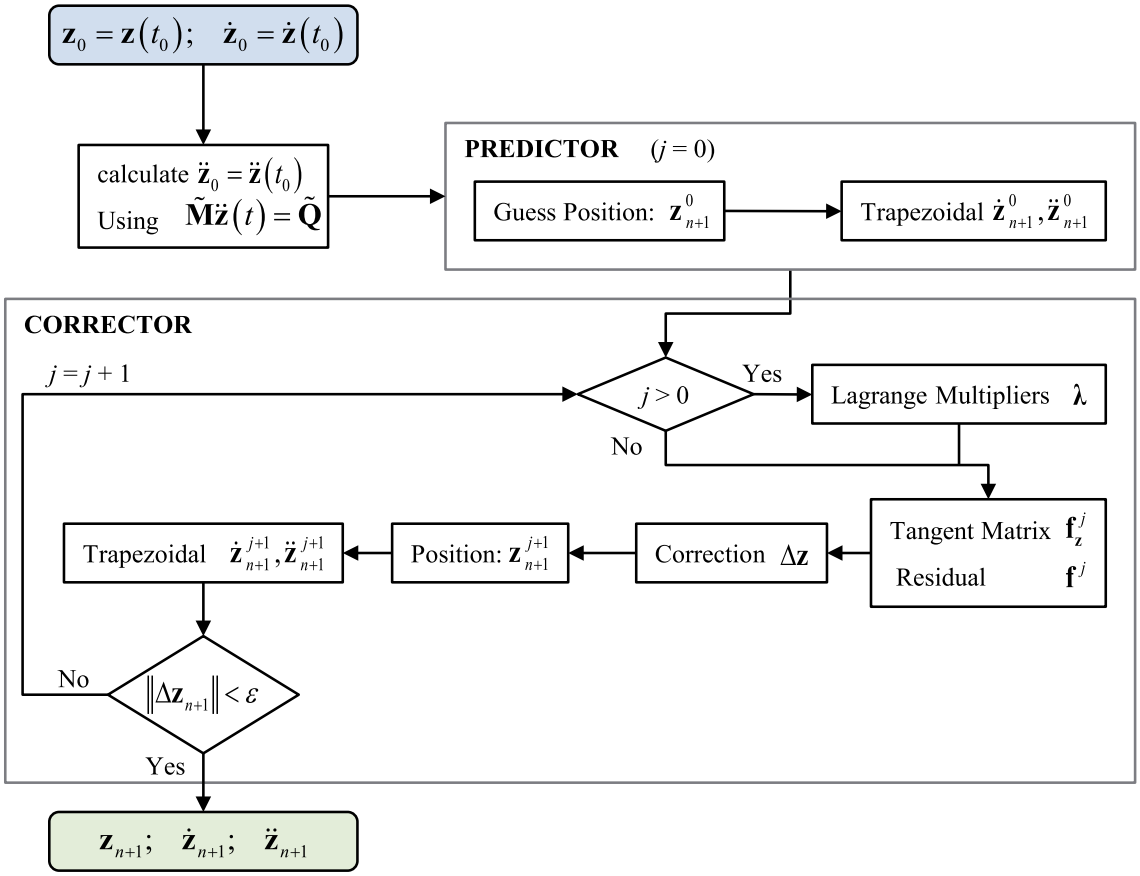

Figure 3.14 Scheme of the iterative procedure to integrate the equations of motion.

3.5.5 From Lagrange Multipliers to Contact Forces and Torques

As explained in Section 3.4.1, the applied multibody methodology associates one actuator to each degree of freedom of the system. That is, for the three-dimensional model, three linear actuators between the ground and the proximal joint of the pelvis (J_1), and three angular actuators between the ground and each segment. These actuators are introduced in the multibody equations as driver kinematic constraints (using Eqs. (3.24) and (3.25)). The Lagrange multipliers associated with these rheonomic constraints (when performing the inverse dynamic analysis) have physical meaning, since they are the motor efforts applied to the DOF coordinates. For a linear driver constraint, the related Lagrange multiplier is associated with a force and, for the rotational driver it is associated with a net torque. The procedure to obtain the actual external forces on the feet and the joint motor torques depends on the coordinates used to define the model and, therefore, on the kinematic constraints used.

The linear actuators drive the proximal pelvis joint $\mathbf{r}_{\mathrm{J1}}$ with respect to the ground. That is:

$$\boldsymbol{\Phi}(\mathbf{q}_{\mathrm{J1}}) = \begin{Bmatrix} x_{\mathrm{J1}} - x_{\mathrm{J1}}(t) \\ y_{\mathrm{J1}} - y_{\mathrm{J1}}(t) \\ z_{\mathrm{J1}} - z_{\mathrm{J1}}(t) \end{Bmatrix} = \mathbf{0} \tag{3.85}$$

where $\mathbf{q}_{J1} \equiv \mathbf{r}_{J1} = \{x_{J1}, y_{J1}, z_{J1}\}^T$ are the absolute Cartesian coordinates of point J_1 and $x_{J1}(t), y_{J1}(t)$ and $z_{J1}(t)$, their analytical expressions with respect to time (which are known in an inverse dynamic analysis using B-splines). The Jacobian matrix of Eq. (3.85) is:

$$\mathbf{\Phi}_{\mathbf{q}_{J1}}(\mathbf{q}_{J1}) = \begin{bmatrix} 1 & 0 & 0 \\ 0 & 1 & 0 \\ 0 & 0 & 1 \end{bmatrix} \tag{3.86}$$

Associating a set of independent virtual velocities $\dot{\mathbf{q}}^*_{J1} = \{\dot{x}^*_{J1}, \dot{y}^*_{J1}, \dot{z}^*_{J1}\}^T$, the principle of virtual power can be formulated as [García de Jalón and Bayo 1994]:

$$\mathscr{P}^* = \dot{\mathbf{q}}^{*T}_{J1} \left(\mathbf{\Phi}_{\mathbf{q}_{J1}} \boldsymbol{\lambda} \right) = \dot{\mathbf{q}}^{*T}_{J1} \boldsymbol{\lambda} \tag{3.87}$$

Moreover, since the joint position is expressed as three translations in the global reference frame, the virtual power can also be expressed as:

$$\mathscr{P}^* = \dot{\mathbf{q}}^{*\,T}_{J1} \mathbf{F}_e \tag{3.88}$$

where $\mathbf{F}_e$ is the vector of all the forces that produce virtual power, including the interia ones. From Eqs. (3.87) and (3.88) it can be deduced that:

$$\mathbf{F}_e = \boldsymbol{\lambda} \tag{3.89}$$

The physical meaning of the Lagrange multipliers associated with the constraints in Eq. (3.85) is the global body-ground contact force acting on the lumbar joint (which represents the total ground reaction since no feet-ground interaction is considered at this point). In a next step, a procedure to translate the force from the lumbar joint to the feet is needed. Moreover, during the double support, this requires an estimation of how the total force is shared between both feet. This problem is addressed in Chapter 4.

The main advantage of driving the lumbar joint is that it allows us to use the same dynamic model along the complete gait cycle. In contrast, if the feet were driven, this would imply the use of two models depending on which foot is in contact with the ground.

As seen in Section 4.3.1, the orientation of each rigid body is imposed by means of three fixed basic rotations about global orthogonal axes. As it is known, its rotation matrix $\mathbf{S}_i$ is:

$$\mathbf{S}_i = \mathbf{S}_\gamma \cdot \mathbf{S}_\beta \cdot \mathbf{S}_\alpha \tag{3.90}$$

where

$$\mathbf{S}_\alpha = \begin{bmatrix} 1 & 0 & 0 \\ 0 & \cos\alpha & -\sin\alpha \\ 0 & \sin\alpha & \cos\alpha \end{bmatrix}; \quad \mathbf{S}_\beta = \begin{bmatrix} \cos\beta & 0 & \sin\beta \\ 0 & 1 & 0 \\ -\sin\beta & 0 & \cos\beta \end{bmatrix}; \quad \mathbf{S}_\gamma = \begin{bmatrix} \cos\gamma & -\sin\gamma & 0 \\ \sin\gamma & \cos\gamma & 0 \\ 0 & 0 & 1 \end{bmatrix} \tag{3.91}$$

The angular velocity vector $\mathbf{\Omega}_i$ of the rigid body *i* with respect to the global reference frame is associated with $\mathbf{S}_i$ and can be deduced from [Agulló 2002]:

$$\mathbf{S}_i^T \dot{\mathbf{S}}_i = \begin{bmatrix} 0 & -\Omega_3 & \Omega_2 \\ \Omega_3 & 0 & -\Omega_1 \\ -\Omega_2 & \Omega_1 & 0 \end{bmatrix} \Rightarrow \mathbf{\Omega}_i = \begin{Bmatrix} \Omega_1 \\ \Omega_2 \\ \Omega_3 \end{Bmatrix} = \begin{Bmatrix} \dot{\alpha}\cos\beta\cos\gamma - \dot{\beta}\sin\gamma \\ \dot{\beta}\cos\gamma + \dot{\alpha}\cos\beta\sin\gamma \\ \dot{\gamma} - \dot{\alpha}\sin\beta \end{Bmatrix} \tag{3.92}$$

and in a matrix form:

$$\mathbf{\Omega}_i = \begin{bmatrix} \cos\beta\cdot\cos\gamma & -\sin\gamma & 0 \\ \cos\beta\sin\gamma & \cos\gamma & 0 \\ -\sin\beta & 0 & 1 \end{bmatrix} \begin{Bmatrix} \dot{\alpha} \\ \dot{\beta} \\ \dot{\gamma} \end{Bmatrix} \equiv \mathbf{T}\dot{\mathbf{q}}_i \tag{3.93}$$

The rheonomic constraint equations for the rotational driver described in (3.24) can be written as:

$$\mathbf{\Phi}(\mathbf{q}_i) = \begin{Bmatrix} \alpha - \alpha(t) \\ \beta - \beta(t) \\ \gamma - \gamma(t) \end{Bmatrix} = \mathbf{0} \tag{3.94}$$

where $\mathbf{q}_i = \{\alpha, \beta, \gamma\}^T$ is the vector containing the three finite global successive rotations, and $\alpha(t)$, $\beta(t)$ and $\gamma(t)$ their analytical expressions obtained from the motion capture and using B-spline. Also, in this case, the Jacobian of Eq. (3.94) is the identity matrix:

$$\mathbf{\Phi}_{\mathbf{q}_i}(\mathbf{q}_i) = \begin{bmatrix} 1 & 0 & 0 \\ 0 & 1 & 0 \\ 0 & 0 & 1 \end{bmatrix} \tag{3.95}$$

With a new set of independent virtual velocities $\dot{\mathbf{q}}_i^* = \{\dot{\alpha}^*, \dot{\beta}^*, \dot{\gamma}^*\}^T$, the principle of virtual power can be formulated and the Eq. (3.87) is also valid.

The orientation of the segment is expressed as rotations with respect to the global frame. Therefore, P

$$\mathcal{P}^* = \mathbf{\Omega}_i^{*T} \mathbf{\Gamma}_i \tag{3.96}$$

where $\mathbf{\Gamma}_i$ is the net external torque applied to the segment. Similarly to Eq. (3.87):

$$\mathcal{P}^* = \dot{\mathbf{q}}_i^{*T} \left(\mathbf{\Phi}_{\mathbf{q}_i} \boldsymbol{\lambda} \right) = \dot{\mathbf{q}}_i^{*T} \boldsymbol{\lambda} \tag{3.97}$$

Therefore,

$$\boldsymbol{\Omega}_i^{*T}\boldsymbol{\Gamma}_i = \dot{\mathbf{q}}_i^{*T}\boldsymbol{\lambda} \tag{3.98}$$

and using Eq. (3.93):

$$\dot{\mathbf{q}}_i^{*T}\mathbf{T}^T\boldsymbol{\Gamma}_i = \dot{\mathbf{q}}_i^{*T}\boldsymbol{\lambda} \tag{3.99}$$

$$\boldsymbol{\Gamma}_i = \mathbf{T}^{-T}\boldsymbol{\lambda} \tag{3.100}$$

which allows us to determine the external torque applied to the segment. Using these data and by means of a simple linear transformation, the joint relative torques can be determined as explained in Chapter 4.

For the particular case of the 2D model, two linear actuators drive the ankle joint of the leading foot with respect to the ground and fourteen rotational actuators express relative rotations between adjacent segments. It can be deduced that the Lagrange multipliers associated to the linear actuators represent the foot-ground contact forces (applied to the ankle joint), and the information obtained via the Lagrange multipliers associated to the rotational actuators can be transformed, using the previous general procedure, to the joint torques.

Chapter 4

Inverse Dynamic Analysis of Human Gait

Inverse dynamics techniques are used to calculate the net joint forces and torques that the musculoskeletal system produces during human locomotion using acquired kinematic data and estimated body segment parameters (BSP). These results are suitable for recognizing normal and pathological gait patterns [Perry 1992, Sauders *et al.* 1952, Winter 1991], for determining muscle forces or for studying how the central nervous system controls the motion. The musculoskeletal system is redundantly actuated and the forces exerted by the different muscles can be calculated using optimization techniques [Ambrósio and Kecskeméthy 2007].

4.1 Problem Statement

The study of human gait and the calculation of the net joint forces and torques that the musculoskeletal system produces during human locomotion are of major importance in many areas of research such as biomedical engineering. The results of the inverse dynamics problem are known to be very sensible to the uncertainties present in input data [Hazte 2002].

Kinematic errors are intrinsic to the motion capture process. The markers motion, the skin motion, and the optical system resolution are the most important sources of error. Different methods are used to reduce the noise present in the data, e.g., digital filters, splines, or singular spectrum analysis techniques [Alonso 2005]. In this thesis, as it will be explained in Section 4.3, a SSA algorithm is used to reduce the noise.

Furthermore, the result of the previous signal processing does not guarantee kinematic consistency with the multibody system. The process of transforming this kinematic information into a convenient kinematic data set for an inverse dynamic analysis (IDA) is not straightforward and can introduce some errors in the analysis. Different reconstruction methods are present in the literature [Alonso *et al.* 2010, Silva and Ambrósio 2002a] and all of them produce small variations of joint positions which can highly influence the results. As it will also be seen in Section 4.3, the consistency at position level is guaranteed using an optimization approach. The differentiation method applied to obtain velocities and accelerations can also introduce numerical uncertainties

in the IDA [Ackermann and Schiehlen 2006, Silva and Ambrósio 2002a]. To reduce this effect, the independent coordinates **z** are expressed using smooth spline functions, and the velocity and acceleration coordinates can be calculated analytically using spline differentiation techniques.

The IDA carried out in this thesis computes the net joint torques and the total contact wrench applied to the multibody system using as input data the measured 3D skeleton motion (without using directly the force plate measurements). This differs from the conventional implementation of IDA, where the force plate data are used as inputs of the analysis.

Using the kinematic information of the whole-body and combining the equations of motion of all the segments, the total contact forces acting on the system and the torques between the ground and each segment can be calculated by means of the procedure presented in Section 3.5. Since, during walking, the only unknown external forces and torques acting on the human body are the foot-ground contact forces, the global external wrench can be determined. This total wrench corresponds to the foot-ground contact wrench during the single support phase. However, during the double support phase, how this wrench is distributed between the two feet cannot be known only from kinematic information.

Generally, this indeterminacy is overcome by the measurement of the individual foot-ground contact wrenches by means of force plates [Cappozzo *et al.* 1975, Dumas *et al.* 2007a, Forner-Cordero *et al.* 2006, McCaw and DeVita 1995a]. However, if two force plate measurements are used together with all the kinematic segment information (traditional approach), the inverse dynamic problem becomes overdetermined.

In order to obtain a single unique solution, some studies add a set of force and torque components (known as residual wrench) to a segment (usually pelvis or trunk) obtaining a new determinate system (same number of equations and unknowns). The residual wrench does not have physical meaning and, in an ideal case, this wrench should be null. However, due to the errors in the data, it is not zero in general [Kuo 1998]. Thus, it is not possible to use inverse dynamics results as inputs of forward simulation without including these nonphysical residual wrenches.

Some studies propose to use optimization techniques to minimize the residual wrench modifying the BSP [Vaughan 1982], the joint trajectories [Chao and Rim 1973] or the joint accelerations [Cahouët *et al.* 2002]. All these studies assume that the residual wrench value must be small, and this assumption highly depends on the accuracy of the force plate data. The main problem of using force plate data as inputs of the IDA is that there are several sources of error in this type of devices [Barlett 2007, Psycharakis and Miller 2006]. The hysteresis of the sensors, the linearity errors, the signal interference, the electrical inductance, etc., affect the measurements and, therefore, the IDA results.

Another method to solve the double support indeterminacy is to perform a least-squares inverse dynamics approach [Kuo 1998]. The constraints formed by imperfect measurements are relaxed and a static optimization problem is used to adjust the angular acceleration of the segments and the foot-ground contact forces to obtain the solution that is simultaneously most consistent with measured accelerations and contact forces.

However, the estimates of the torques are not dynamically consistent over time and thus, the resulting accelerations, when integrated in a forward dynamic analysis, will not reproduce the original motion. To solve this indeterminacy using only kinematic information, different approaches have been published in the literature: the simple ground reaction transfer assumptions [Koopman *et al.* 1995], the centre of pressure based methods [Davis and Cavanagh 1993], and the "smooth transition assumption" (STA) which is based on simple functions [Ren *et al*., 2008] are some of them.

With the aim of using inverse dynamics results as inputs of a forward dynamic analysis, a new dynamically consistent method, for solving the inverse dynamics problem during the double support period in human gait, is presented in this Chapter.

4.2 Experimental Set-up

4.2.1 Gait Analysis Laboratory

The biomechanical model presented in Chapter 3 is used together with the measurements from the biomechanics laboratory placed in the Department of Mechanical Engineering of the School of Industrial Engineering of Barcelona (ETSEIB) as illustrated in Figure 4.1.

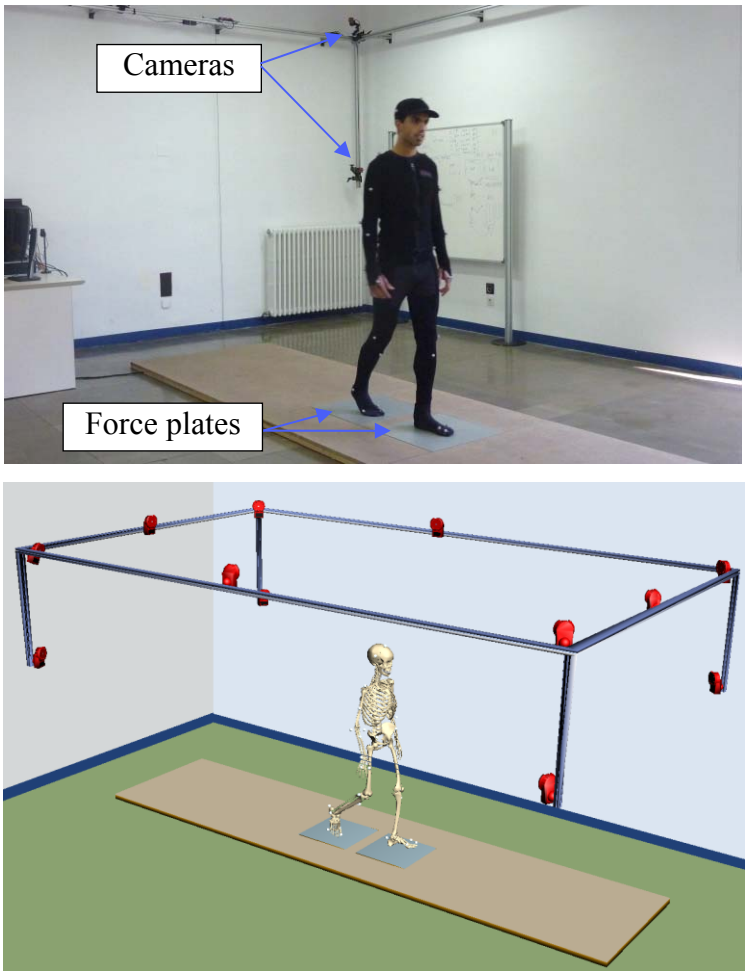

Figure 4.1 Biomechanics laboratory configuration.

This laboratory includes an optoelectronic system in order to capture the motion and two force plates for measuring the foot-ground contact wrench (Figure 4.1). The motion data is collected using twelve 100 Hz Opti-track FLEX:V100R2 cameras and the software which provides the 3D trajectories of the thirty-seven passive markers attached to the human body.

The foot-ground contact wrench is measured using two AMTI AccuGait force plates located on a walkway where the subject walks. Each force plate measures the ground reactions on one foot during the gait cycle.

All these data are exported to Matlab and to Microsoft Visual Studio, where the signal processing and the dynamic analysis are performed.

4.3 Signal Processing

4.3.1 Filtering

The motion capture process provides the 3D position of each marker at each time during the gait cycle. These signals usually present low-level noise which is amplified when numerical differentiation is used to calculate their corresponding velocities and accelerations. Figure 4.2 shows the vertical displacement z^{exp}_{M15} of marker M_{15}, (see Figure 3.4) and the acceleration $\ddot{z}^{exp}_{M15}$ calculated using the finite difference method. It is clear that signal processing is absolutely necessary in order to reduce noise and obtain meaningful acceleration signals.

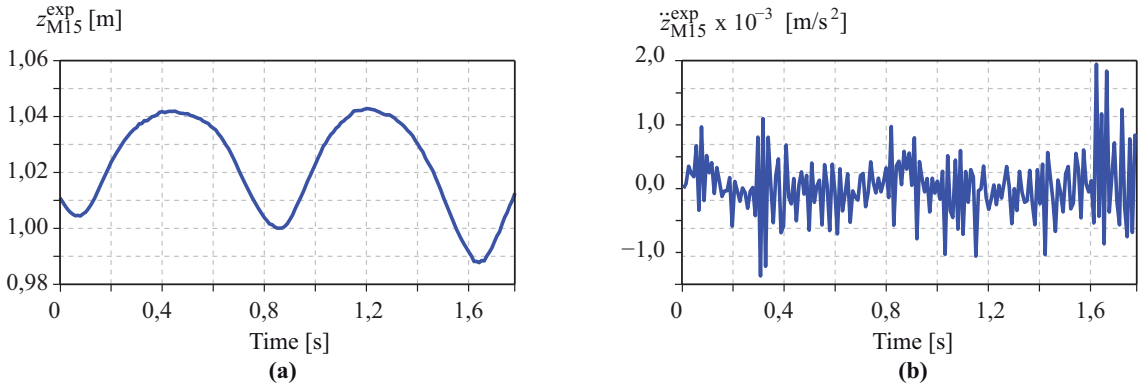

Figure 4.2 (a) Noisy vertical displacement of marker M_{15}.
(b) Acceleration calculated from the noisy vertical displacement of marker M_{15}.

In this thesis, a filter based on singular spectrum analysis (SSA) is applied to the marker position histories. The algorithm decomposes the original signal into independent additive components with decreasing weight. This processing facilitates extracting the signal latent trend from the inherent random noise in the motion capture process [Alonso 2005].

Moreover, the algorithm only requires the selection of two parameters, namely, the window length (L) and the number of components to use for reconstruction (r). A way to overcome the uncertainty in the choice of L is to apply sequentially the SSA filter, as explained in [Alonso *et al.* 2005]. When this sequential procedure is applied, the results are not very sensitive to the window length. In this thesis, the SSA filter is applied three

consecutive times, the window length is fixed as $L = 10$ and the two main components of the decomposition are used in the signal reconstruction. Using this procedure, r takes into account at least the 99,9 % of the sum of the eigenvalues at each iteration.

Figure 4.3 shows the singular spectrum evolution of the vertical position of marker M_{15} (z^{exp}_{M15}). Each branch of the singular spectrum corresponds to an iteration of the sequential SSA procedure, plotted in logarithmic scale. It can be observed that the first few components of the SSA decomposition contain practically all the information needed to reconstruct the original signal.

The original and the reconstructed signals for the same raw displacement are plotted in Figure 4.4 (a). Figure 4.4 (b) shows their difference $\Delta z_{M15} = z^{exp}_{M15} - z^{filt}_{M15}$ where z^{exp}_{M15} is the original evolution of the z position of marker M_{15} and z^{filt}_{M15} is the reconstructed one.

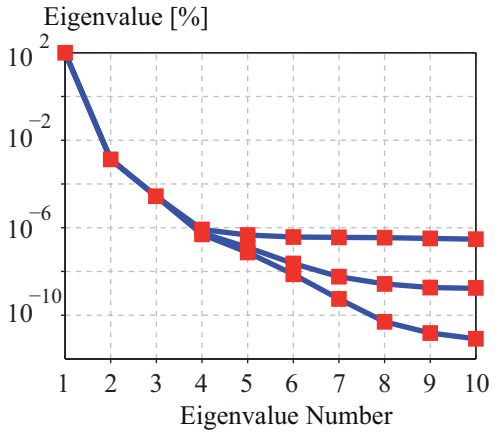

Figure 4.3 Singular spectrum of the vertical displacement signal z^{exp}_{M15}.

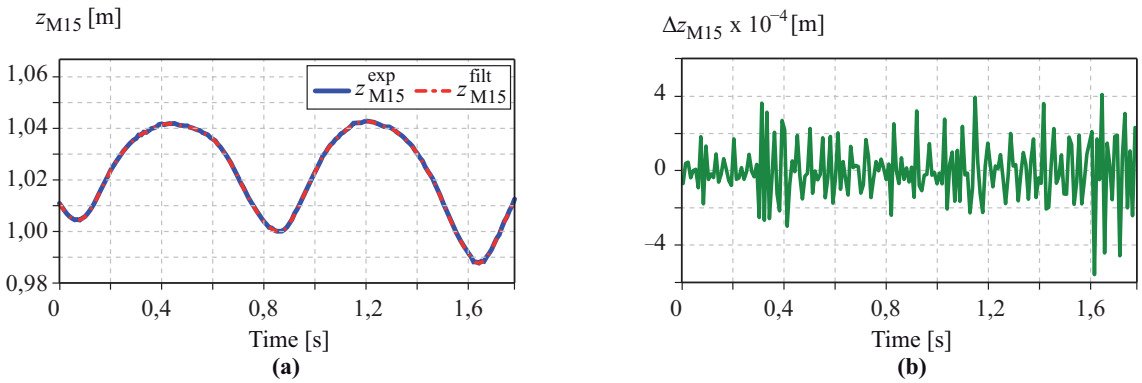

Figure 4.4 Signal processing of the z position of the marker M_{15}. (a) Original and reconstructed signals (z^{exp}_{M15} and z^{filt}_{M15}, respectively). (b) Difference between the two previous signals.

The result of applying twice the finite difference method to the reconstructed signal z^{filt}_{M15} is shown in Figure 4.5 ($\ddot{z}^{filt}_{M15}$) together with the previously calculated $\ddot{z}^{exp}_{M15}$

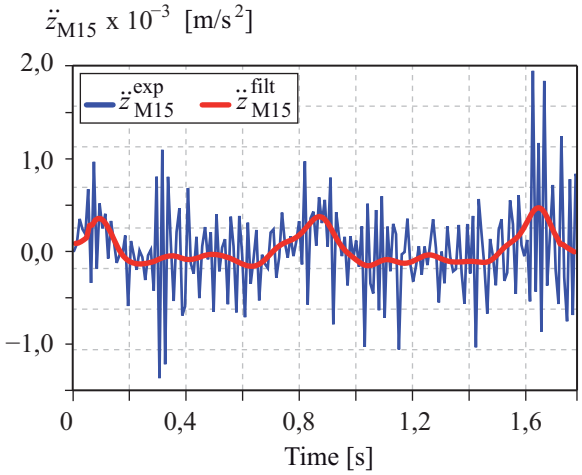

Figure 4.5 Acceleration calculated from the original signal $\mathbf{z}^{exp}_{M15}$ and from the reconstructed signal $\mathbf{z}^{filt}_{M15}$.

This procedure is applied to all the components of the markers position vector. Then, they are used to calculate the histories of the natural coordinates $\mathbf{q}^{filt}$ of the model by means of simple algebraic relations between the markers positions (see Chapter 3).

During gait, skin motion and muscle deformations cause the motion of the markers with respect to the skeleton. This motion affects, obviously, the estimation of the joints position, and leads to violations of the kinematic constraints. It is regarded as one of the most critical sources of error in human movement analysis [Ackermann and Schiehlen 2006, Silva and Ambrósio 2002a]. As an example, it can be observed that the segments length varies significantly during the simulation if vector $\mathbf{q}^{filt}$ is directly used to define the human body motion. Figure 4.6 shows the length of right shank and thigh segments if $\mathbf{q}^{filt}$ is directly used.

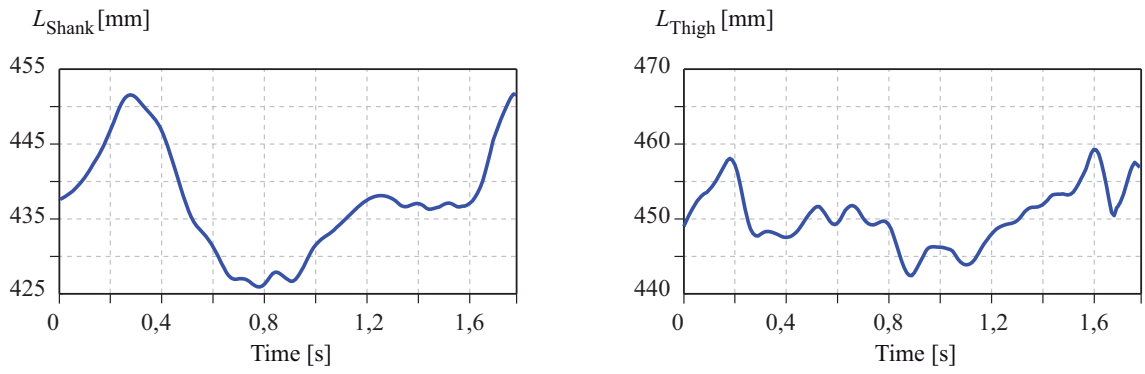

Figure 4.6 Segment's length calculated from $\mathbf{q}^{filt}$ along the captured motion. (a) Right shank length (b) Right thigh length.

In order to avoid this problem, a new set of coordinates $\tilde{\mathbf{q}}$ is calculated by imposing the kinematic consistency at position level through a minimization problem:

$$\min_{\mathbf{q}} V = \frac{1}{2}\left(\tilde{\mathbf{q}} - \mathbf{q}^{filt}\right)^T \mathbf{W}\left(\tilde{\mathbf{q}} - \mathbf{q}^{filt}\right) \quad \text{s.t.} \quad \boldsymbol{\Phi}\left(\tilde{\mathbf{q}}\right) = \mathbf{0} \tag{4.1}$$

where $\mathbf{W}$ is a weighting diagonal matrix that allows assigning different weights to the coordinates. Higher weighting factors are associated to those coordinates with lower expected error. The minimization is only subjected to scleronomic constraints $\mathbf{\Phi}(\tilde{\mathbf{q}}) = \mathbf{0}$, and $\tilde{\mathbf{q}}$ includes only the natural coordinates of the generic vector $\mathbf{q}$ (the three Cartesian coordinates of the 22 points and the three Cartesian components of the 36 unit vectors).

The process used to guarantee kinematic data consistency at position level is explicitly described in [Alonso *et al.* 2010]. Following an augmented Lagrangian minimization process [Bayo and Ledesma 1996], an iterative scheme to obtain the consistent positions $\tilde{\mathbf{q}}$ is used:

$$\begin{aligned} &\left(\mathbf{W} + \mathbf{\Phi}_{\tilde{\mathbf{q}}}^T \beta \mathbf{\Phi}_{\tilde{\mathbf{q}}}\right) \Delta\tilde{\mathbf{q}}_{j+1} = -\mathbf{W}\left(\tilde{\mathbf{q}} - \mathbf{q}^{\text{filt}}\right) - \mathbf{\Phi}_{\tilde{\mathbf{q}}}^T \left(\beta \mathbf{\Phi} + \tilde{\boldsymbol{\lambda}}_j\right) \\ &\tilde{\boldsymbol{\lambda}}_{j+1} = \tilde{\boldsymbol{\lambda}}_j + \beta \mathbf{\Phi} \end{aligned} \tag{4.2}$$

where $\mathbf{q}^{\text{filt}}$ is the vector of the natural coordinates vector filtered using the SSA (nonconsistent natural coordinates) , $\Delta\tilde{\mathbf{q}}_{j+1} = \tilde{\mathbf{q}}_{j+1} - \tilde{\mathbf{q}}_j$, $\mathbf{\Phi}_{\tilde{\mathbf{q}}}$ is the Jacobian matrix of the constraint equations $\mathbf{\Phi}$ with respect to the natural coordinates $\tilde{\mathbf{q}}$, $\tilde{\boldsymbol{\lambda}}_j$ is the vector of Lagrange multipliers, β is the penalty factor and the subscripts *j* indicates the iteration number.

In this study, matrix $\mathbf{W}$ allows little changes in the positions of the upper body joints, their associated weighting factors are defined as the unit. In contrast, the weighting factors of the lower body joints have a value of one hundred.

Equation (4.2) is solved iteratively until $\|\Delta\tilde{\mathbf{q}}\| < \varepsilon$, where ε is a specified tolerance (in this case, $\varepsilon = 10^{-8}$). According to Bayo and Ledesma (1996), the value of the penalty factor only affects the convergence rate. In this work, it is fixed at $\beta = 10^9$. All this processing allows obtaining a convenient 3D kinematic data set of the human gait that can be used as input of the inverse dynamic analysis.

4.3.2 Differentiation using Spline Functions

From the kinematically consistent data set obtained above, a set of independent coordinates **z** is calculated: the three Cartesian coordinates of the proximal pelvis joint, and the three angles of each segment with respect to the global frame, defining a total of 57 degrees of freedom (DOF).

Prior to differentiating these configuration histories, the SSA filter is applied to them (using the same parameters explained in Section 4.3.1) in order to reduce the noise introduced by the kinematic consistency processing. As the chosen independent coordinates define the position of one point and the orientation of each segment, these new histories are also kinematically consistent.

As it will be seen at the end of this chapter, the data collected in the laboratory at 100 Hz will not be enough to compute forward dynamics, thus, a smoother interpolation is required. In this case, the Reinsch approach is used [Reinsch 1967]. For each coordinate of the independent coordinate vector $\mathbf{z}$, and for a given tolerance, a B-spline form of the temporal function is calculated. The MATLAB function “spaps” with a tolerance of

10^{-9}, which guarantees that the RMSE between the original data and the new values is less than 0,001 %, is used. Since the "spaps" function returns the B-form function of the input data, the velocities $\dot{\mathbf{z}}$ and the accelerations $\ddot{\mathbf{z}}$ can be obtained using analytical spline differentiation techniques. Consequently, the kinematic data set required to perform the IDA is completely known $\left(\mathbf{z},\dot{\mathbf{z}},\ddot{\mathbf{z}}\right)$, and it is consistent with the rigid body assumption of the multibody system at position, velocity and acceleration levels.

4.4 Wrench of Contact Forces

As seen in the previous Chapter, the equations of motion are expressed as:

$$\begin{cases} \mathbf{M}\ddot{\mathbf{q}} + \boldsymbol{\Phi}_{\mathbf{q}}^{\mathrm{T}}\boldsymbol{\lambda} = \mathbf{Q} \\ \boldsymbol{\Phi}\left(\mathbf{q},t\right) = \mathbf{0} \end{cases} \tag{4.3}$$

Once the histories of the independent coordinates $\mathbf{z}$, and their time derivatives, $\dot{\mathbf{z}}$ and $\ddot{\mathbf{z}}$, have been obtained, the inverse dynamics problem is solved by means of the velocity transformation formulation known as matrix–R [García de Jalón and Bayo 1994] , which provides the required actuation in the form of generalized forces associated to the independent coordinates $\mathbf{z}$. As seen in Eq. (3.73):

$$\mathbf{R}^T\mathbf{M}\mathbf{R}\ddot{\mathbf{z}} = \mathbf{R}^T\left(\mathbf{Q} - \mathbf{M}\mathbf{S}\mathbf{c}\right) \tag{4.4}$$

which can be rewritten as:

$$\mathbf{R}^T\mathbf{M}\mathbf{R}\ddot{\mathbf{z}} = \mathbf{R}^T\left(\hat{\mathbf{Q}} - \mathbf{M}\mathbf{S}\mathbf{c}\right) + \mathbf{Q}_m \tag{4.5}$$

being $\mathbf{R}^T\mathbf{Q} = \mathbf{R}^T\hat{\mathbf{Q}} + \mathbf{Q}_m$, where $\hat{\mathbf{Q}}$ are the known generalized forces associated to constant forces or forces that only depend on the system mechanical state (such as the gravitatory forces), and $\mathbf{Q}_m$ are the generalized forces associated to the independent coordinates, i.e., the unknowns of the inverse dynamics problem:

$$\mathbf{Q}_m = \mathbf{R}^T\mathbf{M}\mathbf{R}\ddot{\mathbf{z}} - \mathbf{R}^T\left(\hat{\mathbf{Q}} - \mathbf{M}\mathbf{S}\mathbf{c}\right) \tag{4.6}$$

Nevertheless, since the independent coordinates $\mathbf{z}$ are the position of the lumbar joint and the absolute angles of all the bodies, the generalized forces $\mathbf{Q}_m$ calculated via IDA do not correspond to the actual contact forces and the joint motor torques. The procedure to obtain the actual forces and torques involves different steps as it is explained in Appendix B.

As a previous state, and in order to validate the inverse dynamics processing, another set of forces are calculated. The previous generalized forces $\mathbf{Q}_m$ are transformed into an equivalent set of internal torques $\tilde{\mathbf{T}}_m$ (joint torques) and a contact wrench $\tilde{\mathbf{G}}$ acting on the pelvis segment (Appendix B). The tilde denotes that the wrench does not correspond to the contact wrench acting at their actual location, i.e., the contacting foot/feet.

Since at the laboratory two force plates measure the foot-ground contact wrenches $\mathbf{G}_{\mathrm{FP}i}$ (where i indicates the index of the force plate, $i = 1, 2$), these measurements can be compared with the inverse dynamic results $\tilde{\mathbf{G}}$, since the latter is actually the resultant of those contact wrench.

The AMTI force plate provides the three orthogonal components of the foot-ground contact force and moment acting at the plate centre, whereas the inverse dynamics wrench $\tilde{\mathbf{G}}$ is expressed at the lumbar joint. In order to make them comparable, they have been properly translated to a common point, namely the projection of the lumbar joint onto the ground (that is, $\tilde{\mathbf{G}}^{\mathrm{gr}}$ and $\mathbf{G}^{\mathrm{gr}}_{\mathrm{FP}i}$, respectively).

The instants when these wrenches are comparable start at the toe off of one foot, include one double support, and finish at the heel strike of the other foot (Figure 4.7). That is, from $t_{t0} = 0,22$ s to $t_{h1} = 1,58$ s. The instants before t_{t0} and after t_{h1} are not taken into account because during these periods one foot contacts the walkway and the other one the force plate device and thus, the global contact wrench cannot be measured. As a result, only one double support phase is analysed.

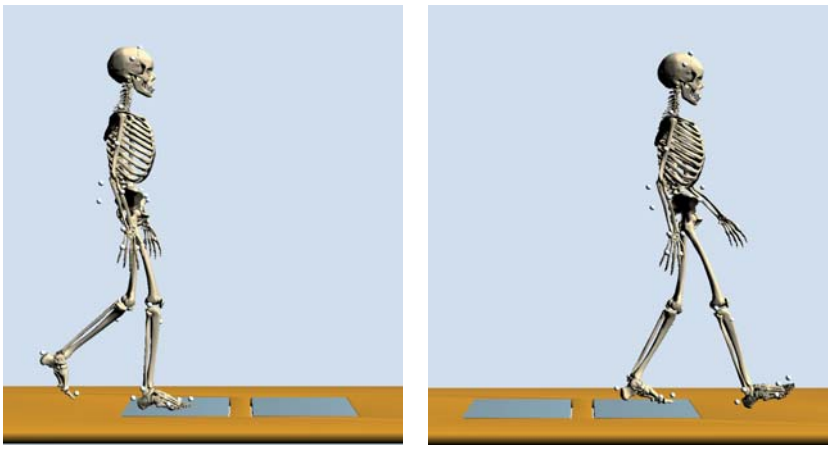

Initial frame $t_{t0} = 0,22$ s Final frame $t_{h1} = 1,58$ s

Figure 4.7 Initial and final frames of the analysed motion.

Figure 4.8 shows the comparison of the total contact wrenches obtained from inverse dynamics $\left(\tilde{\mathbf{G}}^{\mathrm{gr}}\right)$ and from the force plate data $\left(\mathbf{G}^{\mathrm{gr}}_{\mathrm{FP}i}\right)$. The two vertical lines delimitate the double support phase, during which the inverse dynamics provides the resultant force and moment components due to both foot-ground contacts. The plot shows a good agreement between the two curves. As an error indicator, the root mean square error (RMSE) is used:

$$\mathrm{RMSE} = \sqrt{\frac{1}{N}\sum_{n=1}^{N}\left(Q^{\mathrm{REF}}(k) - Q(k)\right)^2} \tag{4.7}$$

where Q refers to the dynamic variable (force or moment component) that will be compared, $Q^{REF}(k)$ is the reference force or moment component at instant k (in this case, the values measured by the force plate), and N is the number of time steps of the studied period

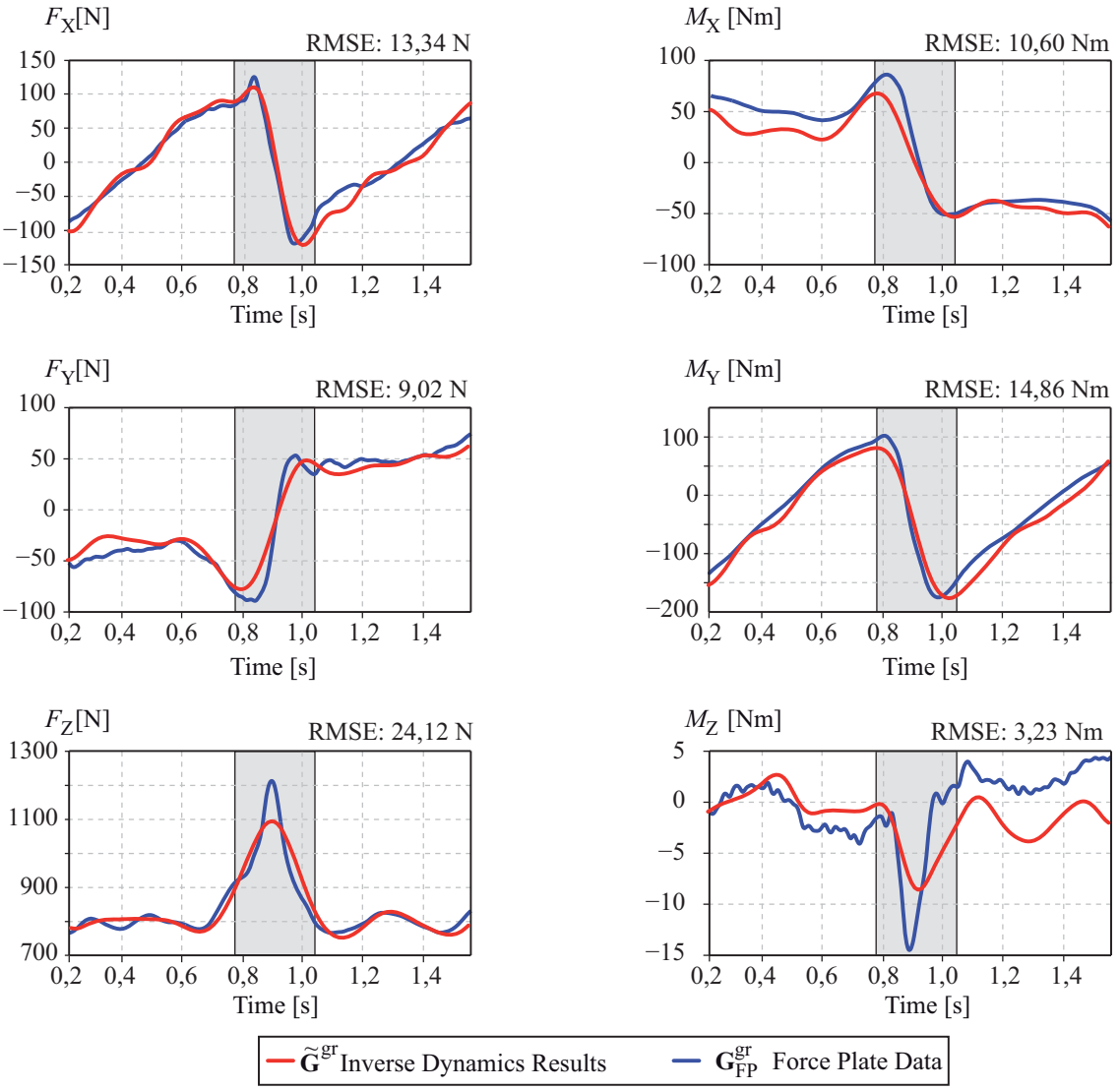

Figure 4.8 Comparison of the total contact wrenches obtained from inverse dynamics and from the force plate data.

The most important absolute errors (RMSE) are detected in F_Z and M_Y with 24,12 N and 14,86 Nm, respectively. However, in relative terms (the instantaneous absolute value divided by the range of the actual component) these errors are small. This can be seen in Figure 4.8, the IDA results tend to be very close to the ones measured in the laboratory.

In contrast most significant differences can be appreciate in M_Z plot, however they only represent an absolute RMSE of 3,23 Nm. From the analysis of the results, it can be concluded that a very good correlation can be found between the global contact wrench

calculated using IDA and the one provided by the force plates. The force plate devices have been used to validate the model and the implemented multibody methodology.

In order to obtain the actual internal joint torques $\mathbf{T}_m$, the double support indeterminacy problem needs to be solved. The procedure used to solve this indeterminacy is explained in the next section.

4.5 Solution of the double support contact force sharing problem

The computed inverse dynamic analysis only provided a contact wrench formed by one force (three components) and one moment (also three components) acting on the pelvis segment. However, these actions are fictitious, since no contact force or moment acts on the pelvis. Therefore, in order to obtain the joint motor torques, the contact wrench must be expressed at its actual location, i.e., the contacting foot/feet.

During the single support phase, the problem is determined, so that, the resultant reaction can be translated to the contacting foot, and the actual joint torques can be recalculated properly equating their corresponding generalized forces to those obtained when the contact wrench acts on the pelvis (see Appendix B). However, during the double support phase, how this wrench is shared between the two foot-ground contacts is unknown and a sharing criterion has to be used for estimating the amount of the total wrench assigned to each foot.

In this section, two different methods to solve this indeterminacy are compared: the first one uses the foot-ground contact wrenches measured by force plates, and the second one is the "smooth transition assumption" presented in [Ren *et al*. 2008].

4.5.1 Method that uses force plate measurements

Usually, in a biomechanics laboratory, the contact interaction between the foot and the ground is measured by means of force plates. These devices provide the individual foot-ground contact wrench along the gait. However, due to errors accumulated in the estimation of the body segment parameters and the motion capture process, and also to the measurement error of the force plates themselves, these measurements do not exactly coincide with the global contact wrench estimated via IDA (translated to the same point). These differences can be seen in Figure 4.8 and, because of them, the inverse dynamics results are inconsistent with the force plate measurements.

As explained at the beginning of the chapter, there are several methods that combine the results from inverse dynamics with the measured reactions [Cahouët *et al.* 2002, Chao and Rim 1973, Kuo 1998, Vaughan 1982]. However, all these methods modify the motion to solve the problem. In order to preserve the kinematics, this thesis proposes a simpler alternative method, which we denote corrected force plate sharing (CFP).

The contact wrench calculated from inverse dynamics, $\tilde{\mathbf{G}}$, must be shared between both feet along the double support phase, i.e., between the heel strike of the leading foot, time instant t_h, and the toe off of the trailing foot, time instant t_t. Thus, the residual between the calculated and measured reactions, $\boldsymbol{\varepsilon} = \tilde{\mathbf{G}}^{\mathrm{gr}} - \mathbf{G}^{\mathrm{gr}}_{\mathrm{FP1}} - \mathbf{G}^{\mathrm{gr}}_{\mathrm{FP2}}$, can be split and added to each of the force plate values to make their resultant consistent with the

inverse dynamics. $\tilde{\mathbf{G}}^{\mathrm{gr}}$, $\mathbf{G}^{\mathrm{gr}}_{\mathrm{FP1}}$ and $\mathbf{G}^{\mathrm{gr}}_{\mathrm{FP2}}$ are, respectively, the IDA wrench $\tilde{\mathbf{G}}$ and the force plate wrenches $\mathbf{G}_{\mathrm{FP1}}$ and $\mathbf{G}_{\mathrm{FP2}}$ (see Figure 4.9) translated to the projection of the lumbar joint onto the ground. This residual is a 6-row vector that contains the differences between the two curves of each plot in Figure 4.8. (only during double support).

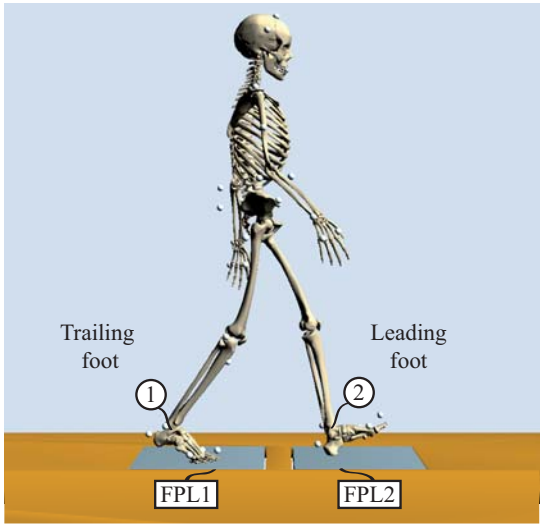

Figure 4.9 An instant of the double support phase.

This process assumes that the errors come from the force plate measurements, or what is the same, the motion is considered as the actual movement and the rest of the measurements are adapted to compute a consistent dynamic analysis. In order to avoid discontinuities between single and double support, the correction is split between both force plates by using a linearly varying function:

$$\begin{aligned}\mathbf{G}^{\mathrm{gr}}_{1}(t) &= \mathbf{G}^{\mathrm{gr}}_{\mathrm{FP1}}(t) + \frac{t_t - t}{t_t - t_h}\boldsymbol{\varepsilon}(t) \qquad t_h \le t \le t_t \\ \mathbf{G}^{\mathrm{gr}}_{2}(t) &= \mathbf{G}^{\mathrm{gr}}_{\mathrm{FP2}}(t) + \frac{t - t_h}{t_t - t_h}\boldsymbol{\varepsilon}(t) \qquad t_h \le t \le t_t\end{aligned} \tag{4.8}$$

where $\mathbf{G}^{\mathrm{gr}}_{1}$ and $\mathbf{G}^{\mathrm{gr}}_{2}$ are the wrenches at the trailing and leading foot respectively, and $\mathbf{G}^{\mathrm{gr}}_{\mathrm{FP1}}$ and $\mathbf{G}^{\mathrm{gr}}_{\mathrm{FP2}}$ are their force plate counterparts. After this sharing process, the wrenches $\mathbf{G}^{\mathrm{gr}}_{1}$ and $\mathbf{G}^{\mathrm{gr}}_{2}$ are properly translated to the corresponding ankle joints obtaining the actual wrenches $\mathbf{G}_1$ and $\mathbf{G}_2$.

This leads to a wrench at each foot that is close to the force plate measurements, but keeps the consistency with inverse dynamics. Therefore, the force plate information is used only for approximating the transition of the reactions, instead of as an input to the whole inverse dynamics problem.

It could be also necessary to compute the sharing problem when one foot contacts the walkway and the other a force plate. That is, for exemple, during the first double support phase of the captured gait cycle, from the heel strike of the leading foot with the first force plate (t_{h0}) to the end of this initial double support phase (t_{t0}) (Figure 4.10).

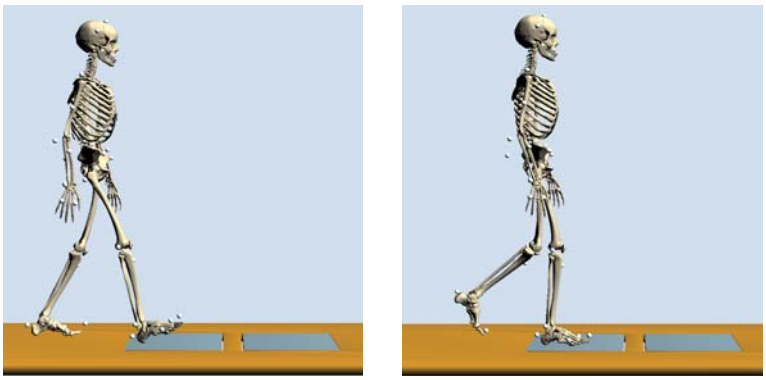

First heel strike t_{h0} = 0,00 s

First toe off t_{t0} = 0,22 s
Single Support inital frame

Figure 4.10 Initial and final frame of the double support phase when only one foot is in contact with the force plate at double support.

Firstly, the difference between the total contact wrench calculated via an IDA and the force plate data at toe off instant (t_{t0}) needs to be calculated. This instant corresponds to the beginning of the single support phase, thus, the contact wrench applied to the system calculated via IDA and that calculated using the force plate should be equal. However, due to errors inherent to the capture, the following difference $\boldsymbol{\varepsilon}(t_{t0})$ is not zero.

$$\boldsymbol{\varepsilon}(t_{t0}) = \tilde{\mathbf{G}}^{\mathrm{gr}}(t_{t0}) - \mathbf{G}^{\mathrm{gr}}_{\mathrm{FP1}}(t_{t0}) \tag{4.9}$$

As a result, the measurements of the force plate device cannot be directly used as the wrench of the foot-ground contact, they need to be adjusted to compute the dynamically consistent wrench $\mathbf{G}^{\mathrm{gr}}_{1}(t)$. Also, in this case, the correction is split during the double support phase (from the heel strike of one foot t_{h0} to the toe off of the other foot t_{t0}) using the following linear function:

$$\mathbf{G}^{\mathrm{gr}}_{1}(t) = \mathbf{G}^{\mathrm{gr}}_{\mathrm{FP1}}(t) + \frac{t_{t0} - t}{t_{t0} - t_{h0}}\boldsymbol{\varepsilon}(t_{h0}) \qquad t_{h0} \le t \le t_{t0} \tag{4.10}$$

Note that $\mathbf{G}^{\mathrm{gr}}_{1}(t)$ ensures continuity with the inverse dynamics results, that is $\mathbf{G}^{\mathrm{gr}}_{1}(t_{t0}) = \mathbf{G}^{\mathrm{gr}}(t_{t0})$. Moreover, the information of the force plate is used for approximating the wrench of the foot in contact with it. After that, and in order to obtain dynamically consistent results, the difference between the inverse dynamics wrench $\tilde{\mathbf{G}}^{\mathrm{gr}}(t)$ and $\mathbf{G}^{\mathrm{gr}}_{1}$ needs to be applied to the other foot. Therefore:

$$\mathbf{G}^{\mathrm{gr}}_{2}(t) = \tilde{\mathbf{G}}^{\mathrm{gr}}(t) - \mathbf{G}^{\mathrm{gr}}_{1}(t) \qquad t_{h0} \le t \le t_{t0} \tag{4.11}$$

As previously noted, the generalized wrenches $\mathbf{G}^{\mathrm{gr}}_{1}(t)$ and $\mathbf{G}^{\mathrm{gr}}_{2}(t)$ can be translated to the ankle joints and the actual joint torques can also be calculated as explained in Section 4.4.

4.5.2 The Smooth Transition Assumption

Another way to calculate the double support force sharing without perturbing the motion data was proposed by Ren *et al*. (2008). The authors propose using a reasonable transition criteria called smooth transition assumption (STA) to estimate the foot-ground contact wrench without using force plate data.

The algorithm is based on the assumption that the foot-ground contact wrench at the trailing foot decays according to a certain law along the double support phase. In their work, two shape functions $f(t)$ are proposed. The first one is used for the anteroposterior reaction force and the second one for the remaining five components of the contact wrench:

$$f_j(t)=\begin{cases} e^{-(t/T_{hds})^3}; & j=1 \qquad t_h \le t \le t_t \\ k_1 e^{-\left[(t-t_P)/T_{hds}\right]^2} - k_2 \dfrac{t}{T_{hds}}; & j=2,...,6 \end{cases} \tag{4.12}$$

where j is the index that coincides with the subscript of each component of the reaction wrench $\left(\mathbf{G}(t)=\left\{F_x,\ F_y,\ F_z,\ M_x,\ M_y,\ M_z\right\}^T\right)$, T_{hds} is half the double support duration, $t_P = 2T_{hds}/3$ is the peak force time, and the two constants are determined imposing that the transition function is equal to 1 at the heel strike of the leading foot, and to 0 at the toe off of the trailing foot. As a result, $k_1 = e^{4/9}$ and $k_2 = 0,5k_1 e^{-16/9}$.

Thus, the reaction component j $\left(j=1,...,6\right)$ is obtained as:

$$G_{1,j}(t)=f_j(t)G_{1,j}(t_h) \qquad t_h \le t \le t_t \tag{4.13}$$

Where $G_{1,j}(t_h)$ is the value of the j component of the reaction wreanch acting on the trailing foot at the beginning of the double support phase $\left(t=t_h\right)$.

For the smoothing function to correctly mimic the decay of the reaction moments, the reaction forces must be considered as applied at the respective centres of mass of each foot, which are not fixed to the foot if it is modelled with two segments. Once the reactions along the double–support phase are estimated for the trailing foot, their counterparts at the leading foot are the result of forcing the resultant wrench to be equivalent to the one obtained by inverse dynamics.

4.6 Results and Discussion

The previous two methods have been implemented and they are compared in the following plots. The recorded motion contains more than one cycle. It covers all instants with force plate information available. It starts at the heel strike of the right foot (0 % of gait cycle), includes also the next heel strike of the same foot (100 %) and finishes at the toe off of the left foot belonging to the next cycle (~116 %). The initial and final frames of this motion are illustrated inFigure 4.11.

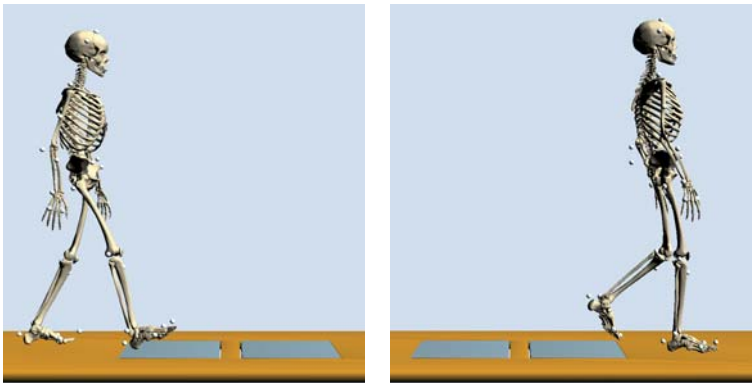

Initial frame Final frame

Figure 4.11 Initial and final frames of the studied motion.

Five phases can be distinguished (Figure 4.12): three double support phases and two single support phases. These phases are delimited using vertical lines in Figures 4.13 and 4.14.

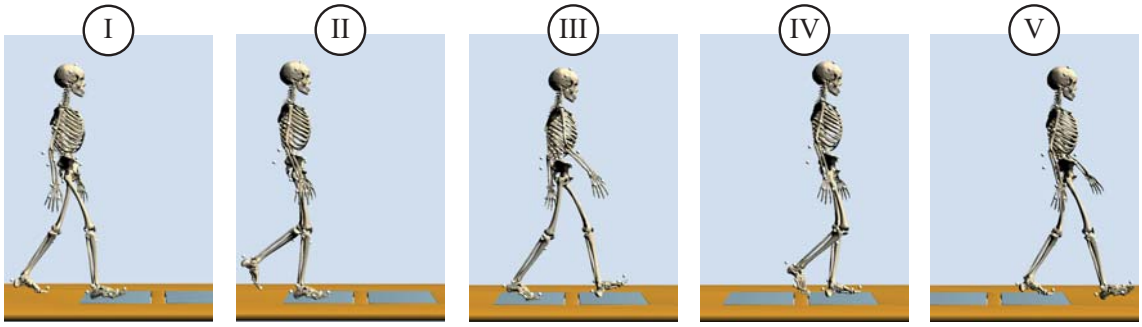

Double support 1 Single support 1 Double support 2 Single support 2 Double support 3

Figure 4.12 Phases of the captured gait motion.

The results obtained from applying the different reaction sharing strategies (Figures 4.13 and 4.14), namely, corrected force plates sharing (CFP, in red) and the smooth transition assumption (STA, in green), are compared to their reference values, i.e., the actual force plate measurements (in black).

Moreover, during the single support phases, the results of the inverse dynamic analysis (plotted in blue) can directly be compared to the force plate data. The X, Y and Z axes correspond to the anteroposterior, mediolateral and vertical absolute directions, respectively. It must be noted that the foot-ground contact moments at each foot are now calculated with respect to their corresponding ankle joint.

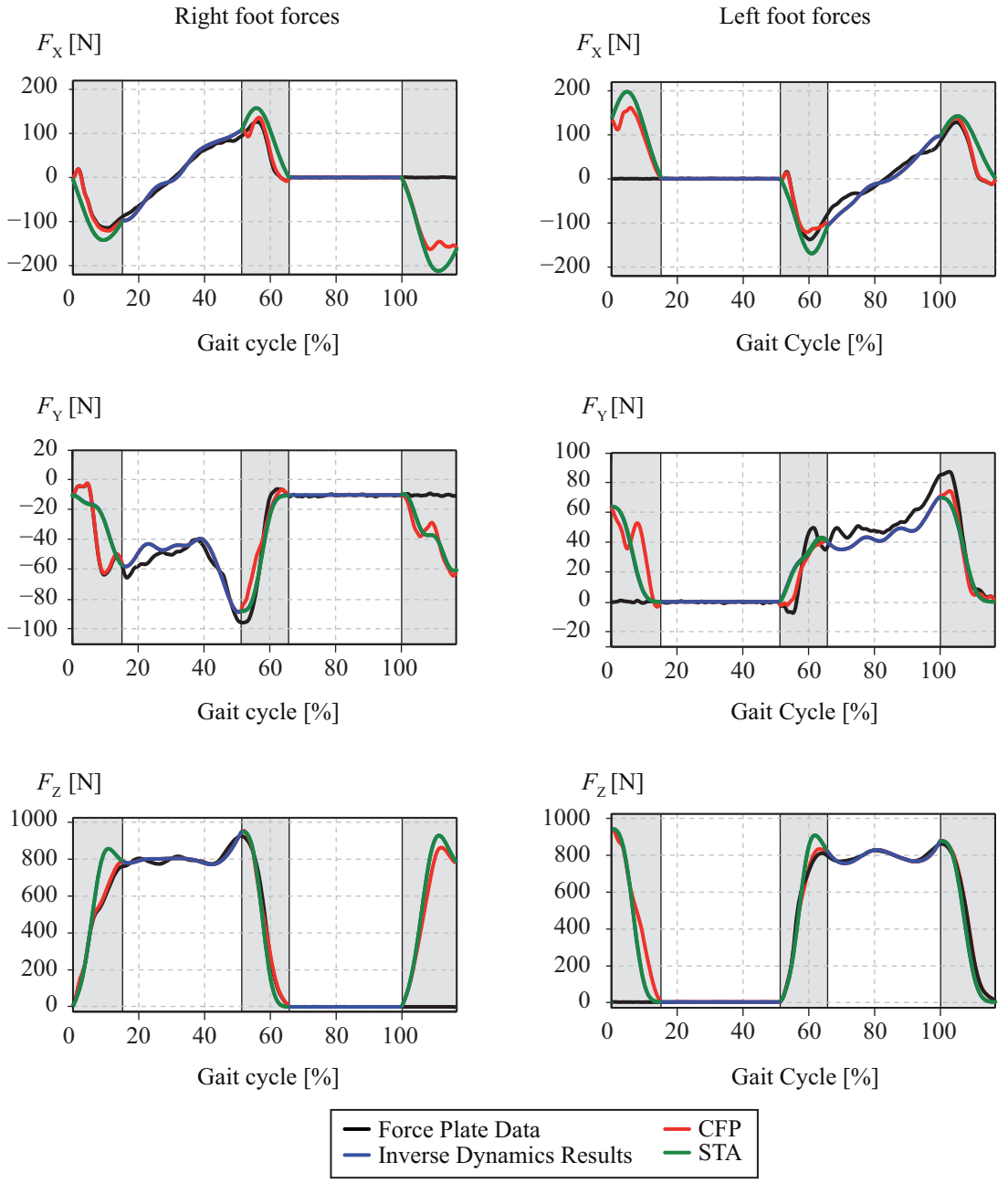

Figure 4.13 Foot-ground contact forces during the studied motion using two different sharing methods, corrected force plate (CFP) and smooth transition assumption (STA).

Figure 4.13 shows good correlation between the foot-ground forces obtained from inverse dynamics (in blue) and the force plate measurements (in black). For the foot-ground moments, the differences are significantly more important but a common trend can be observed. That is something expected because Figure 4.8 (comparison of the total contact wrenches obtained from inverse dynamics and from the force plate data) also shows better correlations for forces signals than for moment ones. As previously, the RMSE is used all over this section as an error indicator. Table 4.1 shows the error for the six components of the foot contact wrench.

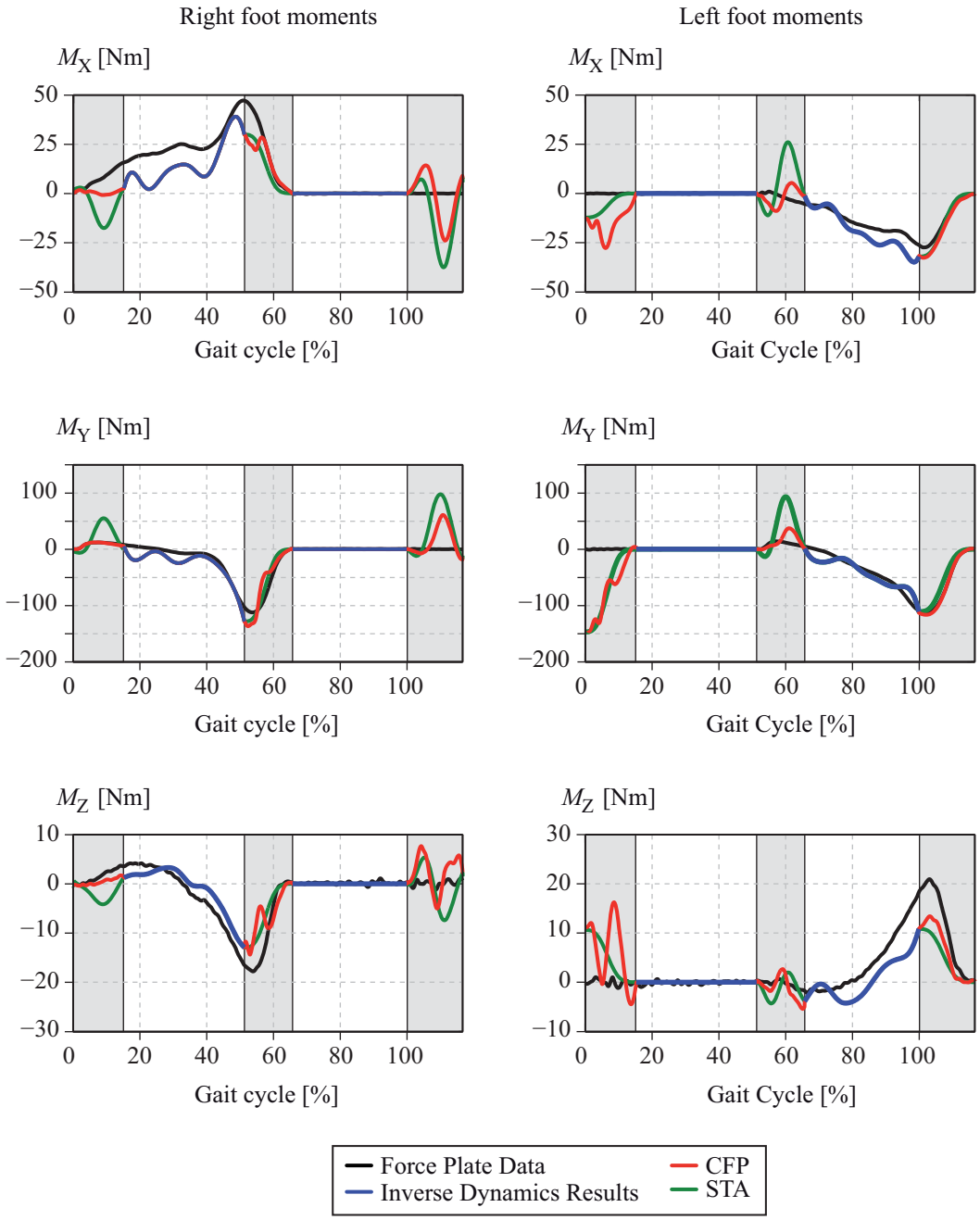

Figure 4.14 Foot-ground contact moments (at ankle joints) during the studied motion using two different sharing methods, corrected force plate (CFP) and smooth transition assumption (STA).

	F_X[N]	F_Y[N]	F_Z[N]	M_X[Nm]	M_Y[Nm]	M_Z[Nm]
RMSE Right Foot (phase II)	8,023	5,766	15,188	11,379	12,367	2,294
RMSE Left foot (phase IV)	16,788	8,899	9,208	5,583	11,771	4,420

Table 4.1 RMSE between force plate data and inverse dynamics results during single support phases (phases II and IV).

Double support phases need to be analysed separately, because during the first and the last double support phases (phases I and V at Figure 4.12) only information of one force

plate is available. In contrast, during the second double support phase (phase III) the data of the two force plate devices are used. This difference is important when the CFP sharing strategy is used.

At phase I, the three components of the foot-ground contact force present similar values for STA and CFP (Figure 4.13) Moreover, for the CFP sharing method, the tendency matches with the force plate data.

The results for the left foot cannot be compared with the reference because the force plate is not available. However, again the two sharing strategies lead to similar results, although STA presents a smoothest tendency. In contrast, when the foot-ground contact moments are compared important differences are detected between both methods (Figure 4.14).

STA differs considerably from the reference signal and CFP presents significant differences at M_X. This trend is also observable at phase V, where the leading and trailing foot are now the right and the left foot, respectively (in this phase, the left foot wrench is the one that can be compared with the force plate data).

The RMSE is used again as an indicator of these differences. Table 4.2 shows the RMSE when the STA and CFP are used. It is calculated using the force plate data as the reference signal, therefore the values of the right foot are calculated at phase 1 and the RMSE corresponding to the left foot belongs to phase V.

		F_X[N]	F_Y[N]	F_Z[N]	M_X[Nm]	M_Y[Nm]	M_Z[Nm]
RMSE STA	Right Foot (phase I)	34,600	18,218	126,547	14,591	24,405	8,494
	Left Foot (phase V)	37,024	11,488	61,517	2,665	12,532	7,058
RMSE CFP	Right Foot (phase I)	5,017	0,891	16,631	8,193	0,917	1,283
	Left Foot (phase V)	7,129	8,657	10,894	3,244	2,852	5,163

Table 4.2 RMSE between force plate data and each sharing method (STA and CFP) during double support phases (phases I and V).

At phase III, as expected, CFP and STA give the better results. In fact, the error of CFP is, almost always, lower than that of STA (Table 4.3). These results should be understood as the best approximation possible without modifying neither the model parameters nor the motion. It can be observed that STA approximates, mostly, the reactions of the right foot better than those at the left foot, which is something expected due to the nature of the method.

Note that STA algorithm is based on the assumption that the reaction forces and moments at the trailing foot (right foot) decay according to a certain law along the double support phase and, therefore, the leading foot forces and moments include all the differences between the global wrench and the wrench assigned to the trailing foot (thus, the leading foot is adapted to compute a consistent dynamic analysis). The moments at the leading foot are especially highly overestimated.

As expected, significant differences can be observed between Table 4.2 and Table 4.3 when the CFP method is used. If data from the two force plates data are available, the

CFP provides better results (especially in force magnitudes) than the ones obtained when only one force plate device is used.

		F_X[N]	F_Y[N]	F_Z[N]	M_X[Nm]	M_Y[Nm]	M_Z[Nm]
RMSE STA	Right Foot	39,383	7,166	71,764	9,908	13,465	4,011
	Left Foot	31,541	14,234	74,961	16,257	43,869	2,315
RMSE CFP	Right Foot	9,011	12,557	35,746	10,122	20,838	5,277
	Left Foot	10,467	8,148	27,432	6,014	12,963	1,879

Table 4.3 RMSE between force plate data and each sharing method (STA and CFP) during double support phase III.

At this point, the information necessary to compute all the joint torques is known. That is, the net muscle moments at each joint during all the time course of motion. The procedure is implemented and the results regarding the components of the ankle, knee and hip torques perpendicular to the sagittal plane are presented in Figure 4.15. They are compared with reference results of similar gait analyses (grey area) by Winter (1990). Figure 4.15 shows in blue the left leg joint torques calculated using the inverse dynamics results and the CFP as a sharing strategy during double support. Note that in this case, and in order to compare the torques with Winter's results, positive moment values indicate extension/plantarflexion.

Since Winter's methodology uses force plate data as input information to compute the IDA, and two force plate devices were available in the lab, the results provide information of only one double support of the gait cycle[2] (when both feet contact force plates). In contrast, as the CFP can be applied using only one force plate, Figure 4.15 shows ~116 % of a cycle (like in Figure 4.13) including three complete double support phases.

The results obtained for the inverse dynamic method proposed are in agreement with the literature results. Figure 4.15 shows a good correlation between our laboratory results and the Winter's one, the trend of all the moments are almost always between the boundered standard deviation obtained by Winter.

[2] Note that Winter provides the results of the 100 % of a gait cycle separately for each leg (therefore two double support phases). However only one double support is common for both legs.

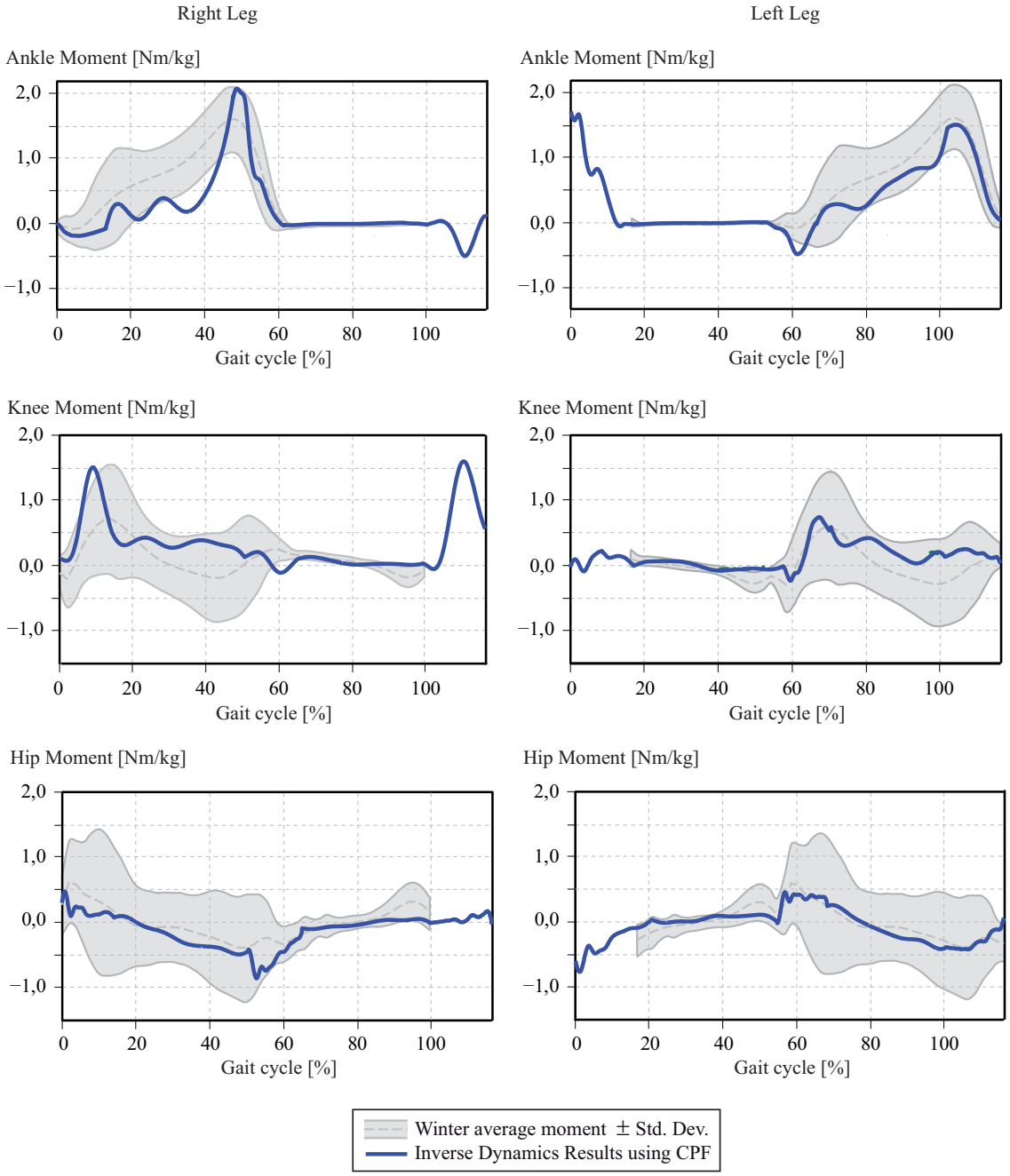

Figure 4.15 Lower limb joint torques calculated using CPF sharing methods and comparison with Winter's results [Winter 1990].

4.7 Application to Forward Dynamic Analysis

The use of the CFP provides a set of dynamically consistent joint torques and external contact forces. Therefore, this information can be used as input of a forward dynamic analysis (FDA) to predict the dynamic response of the human body to this particular set of applied forces and torques.

In this case, the principal objective of the analysis is to simulate the movement of the multibody system. In an ideal case, the motion obtained throughout FDA using the results of the IDA as inputs should be the original motion captured at the laboratory. However, in a real application, the simulated motion differs from the captured one due to errors in the integrator and stability and numerical problems.

The integration of the equations of motion plays a key role in the quality of the FDA results. Moreover, the computational cost increases considerably depending on the chosen integrator. As explained in Section 3.4.4, a multi-step method is used. The information of previous time steps is used to calculate the next step. The selected integration method is implicit, that is, the solution for the next iteration is approximated using a guess of its value, obtained by an explicit procedure known as predictive step.

The FDA is computed using a time step $\Delta t = 0{,}01$ s. However, using this interval, the multibody system becomes unstable and it is not possible to simulate the entire motion. At this point, the IDA needs to be recalculated using a smaller time step. The use of spline functions to define the motion allows obtaining kinematic information at any instant. Therefore, a time step $\Delta t = 0{,}001$ s is chosen and the IDA results are again calculated.

The external forces and moments (calculated at $\Delta t = 0{,}001$ s) are used as inputs of the FDA and the resultant motion is obtained. Figure 4.16 shows the joint flexion-extension angles (in red) and their actual values (in blue) for the ankle, knee and hip of both legs.

It can be observed that during about 80 % of the cycle both curves match; the two motions are really similar. However, at the end of the simulation, both curves begin to differ and the obtained motion does not correspond to normal human gait.

Note that using the proposed IDA method, the obtained dynamic results obtained do not contain residual torques. The FDA is computed using only external moments and forces, without any controller and, still, the results shown in Figure 4.16 are really accurate.

There are some methods to define joint angles. Figure 4.16 shows the joint angles as a rotation of the distal segment relative to the proximal segment. The flexion-extension takes place about the mediolateral axis (y axis) of the proximal segment.

In order to improve these results for the whole cycle, a proportional integral derivative (PID) controller is implemented. The control unit presents a typical structure of an elementary closed-loop system (**Figure 4.17**).

Besides the plant (the process that will be controlled), the system is composed of sensors, which evaluate the system state, actuators, which translate the controller output into meaningful data to the plant and the controller itself, which is responsible for guiding the system to follow a certain reference input.

Besides the plant (the process that will be controlled), the system is composed of sensors, which evaluate the system state, actuators, which translate the controller output into meaningful data to the plant and the controller itself, which is responsible for guiding the system to follow a certain reference input.

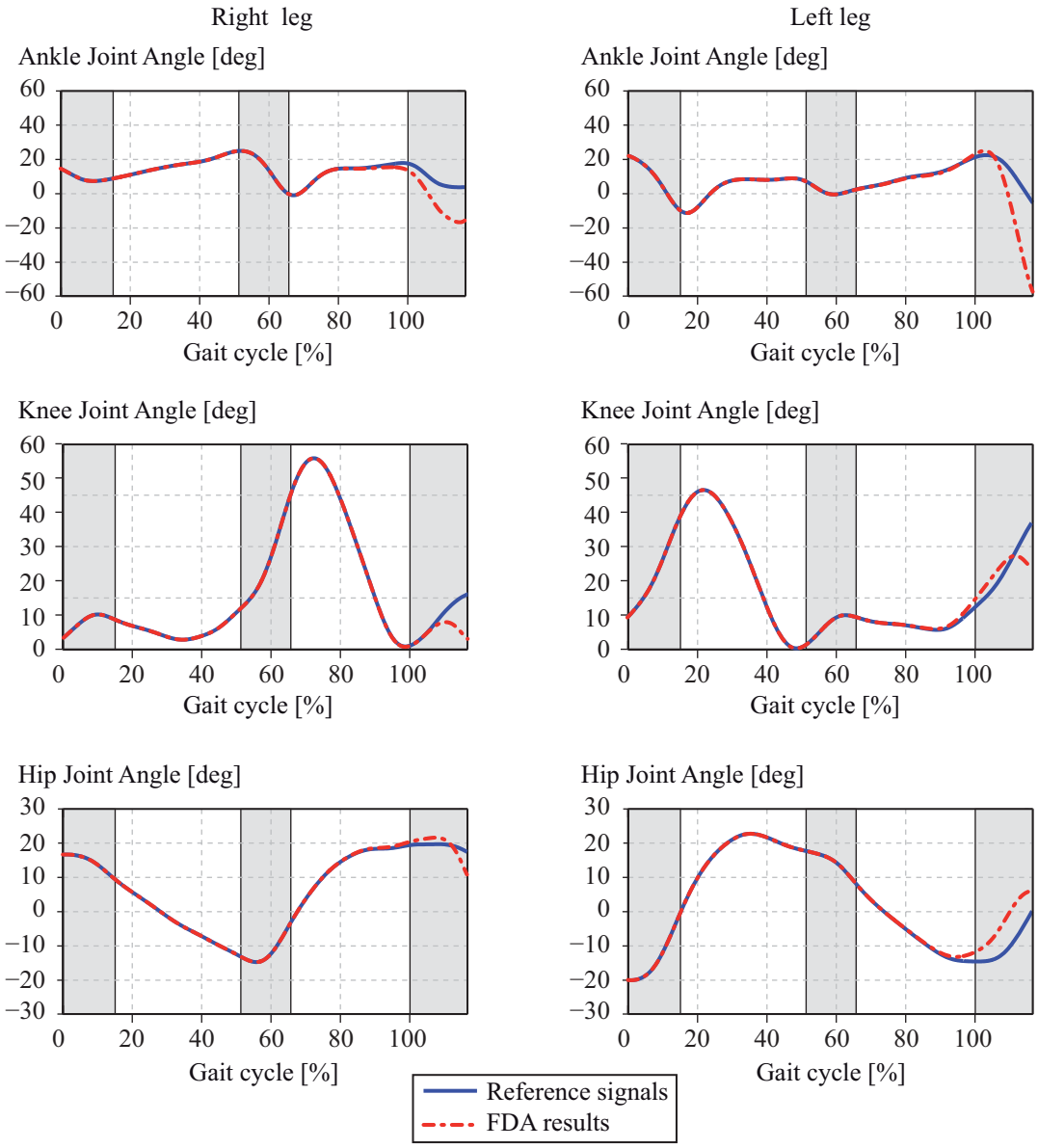

Figure 4.16 Ankle, knee and hip flexion angles.

The output of the system, called control variable, is represented by $\mathbf{y}(t)$, which is measured by the sensors which provide the signal $\mathbf{x}(t)$. The reference is represented by $\mathbf{r}(t)$, the error $\mathbf{e}(t)$ contains the difference between the reference and the sensor measurement. The output of the controller and input to the process is represented by $\mathbf{u}(t)$ (the process contains the actuators and the plant).

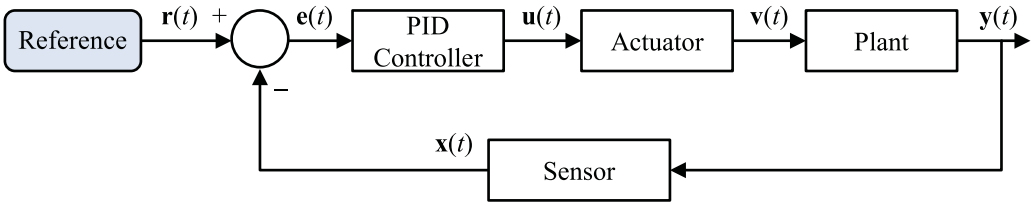

Figure 4.17 Block diagram of a generic closed-loop system.

The output of the system, called control variable, is represented by $\mathbf{y}(t)$, which is measured by the sensors which provide the signal $\mathbf{x}(t)$. The reference is represented by $\mathbf{r}(t)$, the error $\mathbf{e}(t)$ contains the difference between the reference and the sensor measurement. The output of the controller and input to the process is represented by $\mathbf{u}(t)$ (the process contains the actuators and the plant).

The PID controller family is the name given to the group of controllers PI, PD, P or I, in which only one or two control actions are present. In this thesis, a PD controller is used. The PD controller algorithm is schematically represented in Figure 4.18. It involves two contributions, the proportional and the derivative terms. The proportional term, K_p, also called proportional gain, determines the reaction to the current error; and the derivative gain K_d, $\left(K_d = K_p T_d\right)$ determines the response based on the rate at which the error has been changing [Botto 2008]. The process in Figure 4.18 refers to the whole multibody system.

The proportional term contributes to the output of the controller by multiplying the error (difference between the measurement and the corresponding reference) by the constant K_p. This means that larger values of the gain lead to faster response and to a controller more able to respond to potential system disturbances. However, if the gain is too high, the system might oscillate and become unstable.

Figure 4.18 Block diagram of a generic closed-loop system with a PD controller.

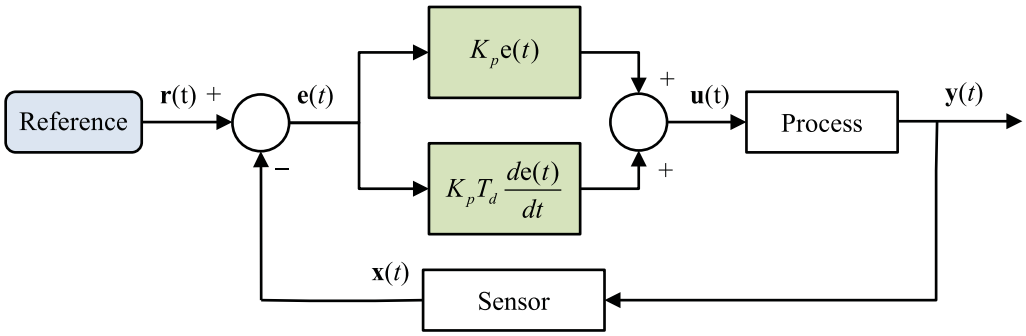

The contribution from the derivative term to the controller output is proportional (by the value of $K_p T_d$) to the slope of the error over time (i.e., its first derivative with respect to time). The derivative term has an anticipative corrective action, being quicker to respond to the disturbance of the system [Botto 2008]. The derivative control is used to reduce the magnitude of the overshoot produced by the integral component and to improve the combined controller process stability.

The integral term accelerates the progression of the process towards the reference and eliminates the residual steady-state error. However, it can cause the overshoot of the

process (the output of the process crosses over the reference) or even lead to instability, and it is not used in this study.

The controller is implemented in discrete time form, and the reference signals (the path that the system must follow) are the original time evolution of the degrees of freedom $\mathbf{z}^{ref}$, that is, the position of the lumbar joint and the three angles defining the absolute orientation of each segment. Therefore, the controller has the following form at each instant t_k ($k = 1,...,N$, where N is the number of time steps of the simulation):

$$\mathbf{e}(t_k) = \mathbf{z}^{ref}(t_k) - \mathbf{z}(t_k); \tag{4.14}$$

$$\frac{d\mathbf{e}(t_k)}{dt} = \frac{\mathbf{e}(t_k) - \mathbf{e}(t_{k-1})}{\Delta t}; \qquad \frac{d\mathbf{e}(t_0)}{dt} = 0 \tag{4.15}$$

Eqs. (4.14) and (4.15) 57 controllers and the respective actuators are adopted. The actuators have the function of converting the position and angular error differences into the corresponding generalized forces. There are 3 linear actuators and 54 angular ones. Therefore, the controller outputs are the external lumbar joint forces and the absolute segment torques that are needed to counteract the deviation of the controlled variable $\mathbf{z}$ from the prescribed reference $\mathbf{z}^{ref}$.

The proportional gain K_p^i associated with segment i is proportional to the mass of the segment m_i:

$$K_p^i = \tilde{K}_p \, m_i \tag{4.16}$$

where $\tilde{K}_p = 400$ ($[\mathrm{N/kg\ m}]$ or $[\mathrm{Nm/kg\ rad}]$ depending on whether the actuator is linear or rotative, respectively) and $T_d = 2{,}5 \cdot 10^{-5}$ ($[s]$), have been chosen in order to avoid oscillations and minimize overshoot. Note that these values are adjusted by trial-and-error work.

Once this procedure is implemented, it can be observed that the biomechanical model is able to follow the prescribed motion. During all the analysis, the controlled variables are concurrent with the reference variables.

Figure 4.19 (a) shows the differences between the actual position of the lumbar joint J_1 (captured motion) and the same variable calculated through forward dynamics. Similarly, Figure 4.19 (b) and (c) show these differences for the angle β (see driver constraints in Section 3.4.1) of the thigh, shank, hindfoot, and forefoot for both, right and left legs, respectively.

Figure 4.19 depicts a really small difference between the two signals ($< 8 \cdot 10^{-7}$ m in position and $< 5 \cdot 10^{-6}$ rad in angle). The biomechanical model followed the used reference, leading to the conclusion that this simple control scheme is enough to effectively control the biomechanical system during gait under a simulated condition.

The dynamic effect of the controller is a force acting on the lumbar joint (J_1) and a set of torques acting on each segment. Figure 4.20 shows each component of the controller force ($F_{X,J1}$, $F_{Y,J1}$, $F_{Z,J1}$) and the absolute Y component of the torques for the thighs, shanks, hindfeet and forefeet of both legs (M_{RT}, M_{RS}, M_{RHF}, M_{RFF}, M_{LT}, M_{LS}, M_{LHF}, M_{LFF}).

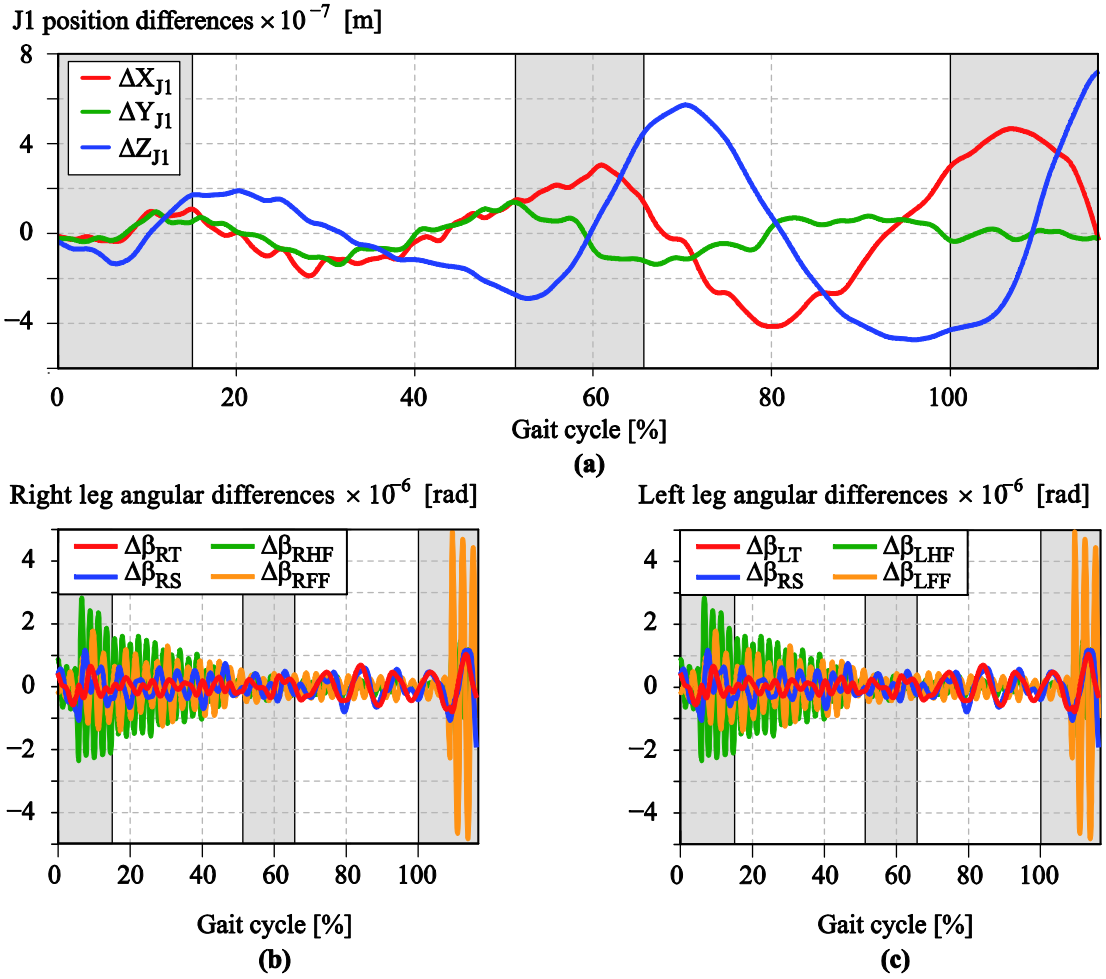

Figure 4.19 Differences between the reference signal and the signal obtained through FDA using the controller. (a) Position differences at lumbar joint. (b) and (c) Absolute angle β differences for the thigh, shank, hindfoot and forefoot segments at right and left leg, respectively.

As Figure 4.20 illustrates, the force and moment amplitude of the controllers is really small. The high frequency of the signals is associated to the instability of the multibody system and to the numeric errors of the integrator. It cannot be related to the actual musculoskeletal dynamics, the role of the PD controller is to balance the numerical integration errors. Moreover, it can be seen than the dynamic contribution of the PD controller is less than $5{\cdot}10^{-3}$ N and $4{\cdot}10^{-3}$ Nm. These magnitudes are much lower than the range of variation of the joint forces and torques for a normal gait, thus the dynamic contribution of the PD is negligible. It can be concluded, that the joint efforts calculated using forward dynamics and the ones calculated via an IDA are practically equivalent.

The PID is designed as a first step for a future work related to human motion prediction. It is not an optimal controller, however, it allows us to simulate a first forward dynamic analysis of human gait, which is a necessary step to complete the goal of the project in which this thesis is involved.

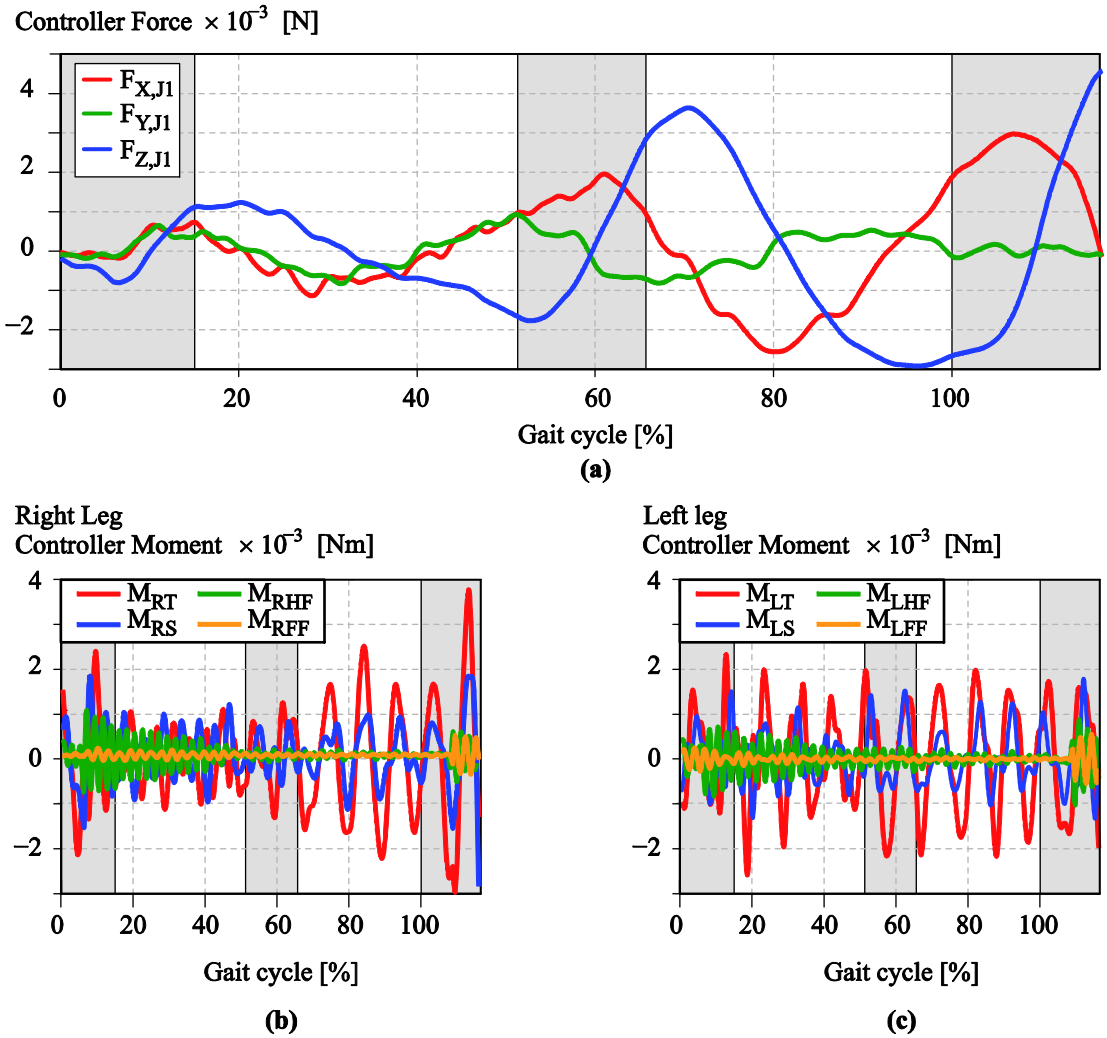

Figure 4.20 Dynamic contribution of the PD controller. (a) Components of the force acting on the lumbar joint. (b) and (c) Y component of the absolute torque acting on the right and left leg segments, respectively.

4.8 Discussion

The inverse dynamic analysis is a useful tool for estimating joint torques that the musculoskeletal system generates during human gait. However, in the case that the only available input data are the motion and the estimated body segment parameters, its use is limited to the single–support phase of gait. In order to obtain the motor efforts while both feet are in contact with the ground, the indeterminacy must be solved with the help of additional data, such as external reaction measurements provided by force plates.

In this chapter, a new method (called corrected force plate sharing) for solving the double support sharing problem in human gait is presented. It uses force plate measurements to obtain a set of joint torques and external forces acting on the feet

which are dynamically consistent with the captured motion. The new method has been compared with another method known as the smooth transition assumption [Ren *et al*. 2008] which neither requires the availability of force plate information. Finally, the resultant joint torque that the muscles generate during the gait cycle, and the contact wrench at each foot are obtained.

The inverse dynamics results obtained via the new method have been used as inputs of a forward dynamics problem, obtaining good results to simulate up to 80 % of the gait cycle. To improve the simulation for the whole gait cycle, a simple PD controller has been implemented. As the results show, the dynamic effect of the controller in the system is really low and provides a way to easily stabilize the biomechanical system during the simulated period. Therefore, this simple method has been implemented to get experience in the field of forward dynamic simulation and it is a a first step of a future work in human gait prediction.

Chapter 5

Analysis of Different Uncertainties in the IDA

As seen in the previous chapter, inverse dynamics techniques are used in gait analysis to calculate the net joint torques that the musculo-skeletal system produces during human locomotion. Errors present in the input data may affect significantly the results of the inverse dynamics problem, and knowing their effect on the gait results is important to determine what input data have to be more accurately known.

Different sources of errors in gait analysis have been described in [Hatze 2002]. This chapter is focused on three of them: uncertainties in body segment parameters (BSP) estimation, errors in force plate measurements and inaccuracies generated by kinematic data processing. These errors are unavoidable when analysing human gait and have been modelled in different ways depending on their nature.

The influence of BSP errors is a controversial question. While some studies suggest that BSP can introduce significant errors [Liu and Nigg 2000, Pearsall and Costigan 1999, Rao *et al.* 2006, Riemer *et al.* 2008] others have noted that BSP effects are not very important in kinetic gait results [Davis *et al.* 1994, Silva and Ambrósio 2004, Wu and Ladin 1993]. The main problem is that the actual value of most BSP cannot be directly measured and this is why the published values can differ by more than 40 % between each other [Pearsall and Costigan 1999].

There are several studies that analyse the influence of BSP errors on the IDA results. Silva and Ambrósio (2004) analyse how sensible the joint torques are to a BSP fixed perturbation. Other works, however, focus on a particular joint, that is, on how the errors affect, for instance, to the knee joint torque [McCaw and DeVita 1995]. There are also some studies that investigate how the IDA results change when different literature BSP estimations are used [Pearsall and Costigan 1999, Rao *et al.* 2006].

Kinematic errors are intrinsic to the motion capture process. Markers movement, skin motion and resolution of the optical system are the most important sources of error. Other uncertainties appear due to the difficulties in identifying broad anatomical points, where the markers are usually placed. With the aim of reducing the impact of marker

placement errors, Groena *et al.* (2012) study the effect of two different marker protocols on the accuracy of the calculated kinematic data (lower extremity joint angles).

Also related to kinematic errors, some methods are used to reduce the noise present in the data, namely, digital filters, splines or spectrum analysis techniques [Alonso *et al.* 2005]. Moreover, some algorithms to obtain a new data set that guarantees kinematic consistency with the biomechanical model appear in the literature [Alonso *et al.* 2010, Silva and Ambrósio]. The differentiation method applied to obtain velocities and accelerations can also introduce numerical uncertainties in the analysis: in this case, kinematic consistency must also be ensured at velocity and acceleration levels. According to [Alonso 2005], and in order to reduce the influence of kinematic errors on the IDA results, it is necessary to apply smoothing and kinematic consistency to kinematic signals.

Generally, in a gait analysis laboratory, force plates are used to measure the foot-ground contact wrench. There are several sources of error in this type of devices [Barlett 2007, Psycharakis and Miller 2006]: the hysteresis of the sensors, the linearity errors, the signal interference, the electrical inductance, etc., affect the measurements and, therefore, will affect the results computed using data from these devices.

The joint torques calculated using IDA are the result of the moments developed by all muscles spanning a joint. Biomechanical simulations of human gait generally use Hill muscle models to estimate muscle forces [Hill 1938]. There are also studies that investigate the sensitivity of Hill's parameters to the dynamic results [De Groote *et al.* 2010, Scovil and Ronsky 2006].

The objective of this chapter is to investigate the effects of some uncertainties in input data on the results of a human gait IDA focusing on the flexion/extension lower limb torques. Three different cases are studied. Firstly, to quantify the errors inherent to the use of anthropometric tables, a statistical error analysis is performed assuming that errors in BSP estimations follow a normal distribution. The perturbed BSP are the mass and length of the body segments, the distance from the centre of mass (COM) to the proximal joint, and the moment of inertia about the COM. Secondly, different sets of kinematic data are used to emulate different solutions that may be provided by the algorithm ensuring kinematic consistency. Then, it is analysed how these differences affect the IDA results. Finally, the foot-ground contact forces and torques are perturbed –according to data sheet specifications of commercial force plates– to emulate the maximum error committed when these data are used as inputs of the IDA.

5.1. Biomechanical Model

The experimental data for a normal human walking are collected in the laboratory as explained in Chapter 4. For this motion, the sagittal plane is where much of the movement takes places. Therefore, the present study is focused on the sensitivity of the flexion/extension moments and the bidimensional model has been used in order to minimize the number of variables and the simulation computer time.

The information of the original 3D model is used to compute a 16 degree-of-freedom (DOF) biomechanical model (see Section 3.1.2). The BSP are exposed at Table 3.5. The

generalized coordinate vector $\mathbf{q}$ is composed of forty-four variables: thirty are position variables, which are related to the endpoints of each segment ($\tilde{\mathbf{q}}$); the other fourteen variables are angular coordinates α_i that define the orientation of the segments $\mathbf{q} = \left[\tilde{\mathbf{q}}^{\mathrm{T}}, \alpha_1, ..., \alpha_{14}\right]^{\mathrm{T}}$.

The 2D kinematic information is obtained from the 3D joint position using the two sagittal components. However, the history of the 2D natural coordinates is not kinematically consistent with the rigid body model. Therefore, a new set of data is calculated by imposing this consistency at position level through the same minimization algorithm explained in Chapter 4:

$$\min_{\mathbf{q}} V = \frac{1}{2}\left(\tilde{\mathbf{q}} - \mathbf{q}^{3\mathrm{D}}\right)^T \mathbf{W}\left(\tilde{\mathbf{q}} - \mathbf{q}^{3\mathrm{D}}\right) \quad \text{s.t.} \quad \boldsymbol{\Phi}\left(\tilde{\mathbf{q}}\right) = \mathbf{0} \tag{5.1}$$

where $\mathbf{q}^{3\mathrm{D}}$ contains the inconsistent natural coordinates subtracted from the 3D model. $\tilde{\boldsymbol{\Phi}}(\tilde{\mathbf{q}}, t) = \mathbf{0}$ includes the physical constraints between the generalized vector $\tilde{\mathbf{q}}$.

As previously seen, $\mathbf{W}$ is a weighting diagonal matrix that allows assigning different weights to the coordinates. Higher weighting factors are associated to those coordinates with lower expected error. In this study, the weighting factors associated to the positions of the upper body joints are defined as the unit. In contrast, the weighting factors of the hip and ankle joints are ten times higher and the ones related to the knee joints have a value of five.

Using this process (see Eq. (4.2)), a consistent set of natural coordinates is created and used to calculate the fourteen angular variables (Figure 5.1). Those angular variables together with the ankle position define the set of sixteen independent coordinates of the multibody system.

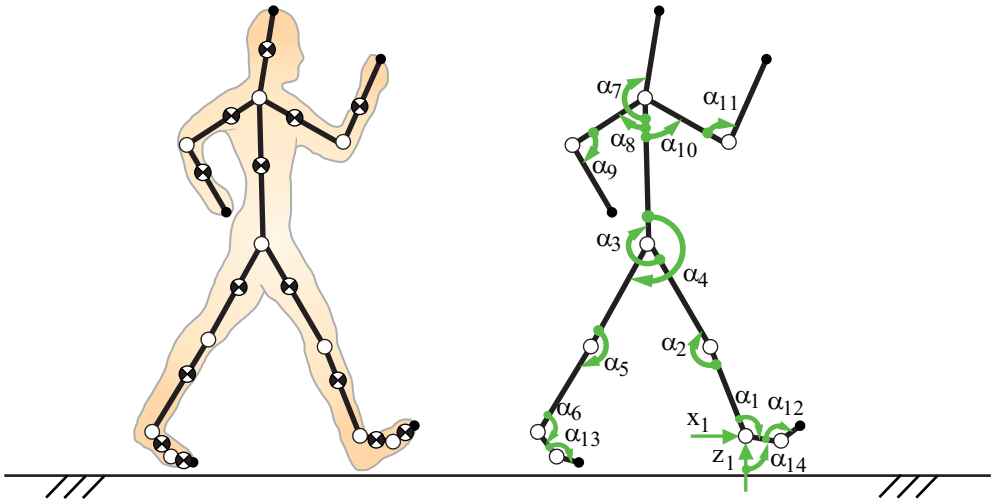

Figure 5.1 Planar biomechanical model of the human body.

With the purpose of defining a completely known motion, which guarantees kinematic consistency at velocity and acceleration levels, analytical expressions of the time evolution of these independent coordinates are calculated. These analytical expressions are defined by means of Bézier curves (see Appendix B). The order of these curves is

the minimum that guarantees that the RMSE between the actual measured curve and the analytical curve expression is lower than a chosen tolerance. By doing this, velocities and accelerations can be analytically known and the noise amplification during the differentiation process is avoided.

The biomechanical model described in this section is used along this chapter as a reference model. All the comparisons are done with respect to the results obtained when the above mentioned data are used.

This study is focused on the gait cycle period when only one foot is in contact with the ground (single support phase). During this phase, the influence of the input data errors on the IDA can be analysed separately for the stance and the swing leg. Moreover, during this period, the results of the IDA allow comparison of the force plate measurements with the calculated external loads. Note that during double support phase kinetic input data are needed to perform and IDA (as explained in the previous chapter).

5.2. Multibody Formulation

The IDA is formulated using the multibody dynamics methodology described previously. In this case, the constraint equations $\mathbf{\Phi}(\mathbf{q},t)=0$ include the physical constraints between variables (vector $\tilde{\mathbf{\Phi}}$ defined above) and the rheonomic constraints $\alpha_i(t), x_1(t), z_1(t)$ that drive the motion. The equations of motion can be written as:

$$\begin{cases} \mathbf{M}\ddot{\mathbf{q}} + \mathbf{\Phi}_{\mathbf{q}}^{\mathrm{T}}\boldsymbol{\lambda} = \mathbf{Q} \\ \mathbf{\Phi}(\mathbf{q},t) = \mathbf{0} \end{cases} \tag{5.2}$$

where $\mathbf{M}$ is the mass matrix, $\ddot{\mathbf{q}}$ is the acceleration vector, $\boldsymbol{\lambda}$ are the Lagrange multipliers, and $\mathbf{Q}$ is the generalised force vector. Due to all the degrees of freedom are controlled kinematically using analytical functions (all the input elements are known as a function of time), Eq. (5.2) constitutes a system of *m* algebraic equations with *m* unknowns (and with rank *m*). The solution of this system is perfectly determined. Therefore, the only unknown value in Eq. (5.2) is the vector of Lagrange multipliers $\boldsymbol{\lambda}$ that can be determined at each instant of time.

This formulation is used with non-perturbed data to obtain the actual non-perturbed joint torques and the ground contact force and torque on the stance foot. Those are the reference values used for comparison throughout the work.

Along the study, when BSP and kinematic information are perturbed, the same multibody formulation is used and the perturbed net joint torques are again calculated. However, when the foot-ground contact force is introduced as an input force acting on the stance leg, the equations of motions in Eq. (5.2) become overdetermined. In this work, to analyse separately the effect that errors in force plate can introduce in the IDA, the analysis is carried out by applying the recursive method based on the Newton-Euler equations of motion which is commonly applied when force plate measurements are used [Dumas *et al.* 2007]. Starting at the foot, where the distal force and torque are the ground reaction force and torque, the forces and torques in the stance lower limb joints are determined. If force plate data and captured movement were kinetically consistent, the actual hip torque and the torque calculated using this method would be the same.

However, due to experimental errors, these torques are not in agreement and the differences are studied in section 5.4.3.

5.3. Error Statistics Quantification

Two different error indicators are used: the root mean square error (RMSE) and the normalized root mean square error (NRMSE). The RMSE is calculated to estimate the global error magnitude in joint torques at each dynamic simulation. The NRMSE is obtained as the quotient between the RMSE and the range of the non-perturbed torque:

$$\mathrm{RMSE}_i = \sqrt{\frac{1}{N}\sum_{k=1}^{N}(M_i^{\mathrm{NP}}(k) - M_i^{\mathrm{P}}(k))^2} \tag{5.3}$$

$$\mathrm{NRMSE}_i = \frac{\mathrm{RMSE}_i}{\mathrm{M}_i^{\max} - \mathrm{M}_i^{\min}} \cdot 100 \tag{5.4}$$

where index i refers to the same index as the angles in Figure 5.1, $M_i^{\mathrm{NP}}[k]$ is the actual net joint torque at instant k using non-perturbed –actual– parameters, $M_i^{\mathrm{P}}[k]$ is the net joint torque at instant k when input parameters are perturbed and N is the number of time steps of the simulation. $\mathrm{M}_i^{\max}$ and $\mathrm{M}_i^{\min}$ are, respectively, the maximum and the minimum value of M_i^{NP}.

While the RMSE assesses the overall error in each simulation, the NRMSE evaluates the relative error with respect to the actual range of variation. For example, an RMSE of 1 Nm of a torque whose actual range of values is 1 Nm (NRMSE = 100 %) is much more relevant than the same RMSE of a torque with a range of values of 100 Nm (NRMSE = 1 %).

5.4. Modelling of the Uncertainties

The errors in in the body segment parameters estimation, in the kinematic data processing and in the ground reaction force measurement have been modelled differently depending on their nature. Each modelization is explained in the next subparts.

5.4.1 BSP Perturbation

Errors in BSP can be described as spread data around their actual value. The total error committed in BSP estimation may come from multiple sources. Thus, according to the central limit theorem, the distribution of the sum of these errors has (approximately) a normal distribution. In this work, normal (or Gaussian) distributions with zero mean and a certain variance σ^2 have been used. To obtain the variance of the Gaussian distribution, the maximum error, defined as a percentage of the actual value (for example, 10 %), is associated to 3σ. In that way, it is assumed that the 99,7 % of the values are within the error interval (for example, the actual value ±10 %). Hence, instead of adding fixed errors as in [Silva and Ambrósio 2004], a statistical analysis taking a sample of errors from a normal distribution is performed.

A sample size of 1000 random values drawn from a Gaussian distribution is generated for each parameter. Three different error variances have been considered, simulating

three different maximum errors: 5, 10 and 15 %. When a mass perturbation is performed, the mass of each segment is normalized so that the total body mass remains always constant. In the same way, when the length of each segment is perturbed, the height of the subject also remains constant. These seem to be reasonable assumptions, since the total mass and height are parameters that can be known with little error.

Using the 1000 values of each inertial parameter for a fixed maximum error, inverse dynamics simulations are carried out. The joint torques are calculated and compared with the actual non-perturbed ones. The RMSE and the NRMSE are used as indicators of the accuracy of the results for each simulation. In this study, the mass, the COM and the moment of inertia are varied independently (though being dependent) because most BSP tables provide their values separately.

This study differs from those in the literature because the emulated errors are a real approximation of the errors that researchers cannot avoid when performing an IDA of human locomotion. This work does not compare the effect of using one or another anthropometric BSP table as in [Rao *et al.* 2006, Riemer *et al.* 2008], and does not determine how an error in a single BSP can affect the IDA results as in [Silva and Ambrósio 2004] either. The error statistical modelling explained above allows us to simulate the real errors that can appear when anthropometric BSP are estimated. Inaccuracies are always present in the BSP estimation, and they appear in all segments at once.

5.4.2 Errors in Kinematic Data Processing

The process to transform kinematic information in a convenient kinematic data set for an IDA is not straightforward and can introduce some errors in the analysis. According to Eq. (4.2), different sets of consistent data can be obtained using different criteria to define the weighting factors in matrix **W**. These criteria are related to the expected position error in the markers used to define each joint.

Two different cases are studied to account for different degree of skin movement in the markers. The first one penalizes in the same way the errors in each natural coordinate (**W** is the identity diagonal matrix). The second one considers, according to [Pearsall and Costigan 1999], that the expected errors in stance leg markers are lower than in swing leg. In this case, weighting factors related to the natural coordinates of the stance leg are ten times higher than the rest of weighting factors.

5.4.3 Force Plate Data Measurement Errors

We study how net joint torques are modified when uncertain force plate data are used as inputs of the IDA. According to different datasheets of commercial force plates, the measurements error can be bounded between 0,2 and 2 % of their full scale output (FSO). Typical values of FSO in these devices are 500 N for F_X, 2500 N for F_Z and 500 Nm for M_Y. Although these error percentages are not constant along the simulation, the maximum error that might occur has been considered. Hence, two different quantities are added to the ground reaction force and torque according to data sheet specifications. That is, 1 and 10 N in the horizontal ground reaction force, 5 and 50 N in the vertical ground reaction force and 1 and 10 Nm for the mediolateral torque.

5.5. Results

According to the methodology explained above, uncertainties in input data are simulated. Then, a statistical study is carried out and the results are compared and discussed along this section.

5.5.1 Errors in Body Segment Parameters

In this study, perturbed inertial parameters are the mass and length of the body segments, the distance from the centre of mass to the proximal joint, and the moments of inertia about the centre of mass. These are modified following the procedure described in Section 5.4.1. Table 5.1 and Table 5.2 show the mean, the standard deviation and the maximum value of the RMSE and the NRMSE obtained in the different simulations, for the stance leg torques (M1, M2, M 3) and the swing leg torques (M 4, M 5, M 6), respectively. The errors have been obtained for variances associated with maximum errors of 5 %, 10 % and 15 %.

As expected, the RMSE and the NRMSE increase when the maximum BSP error grows. Along this section, the errors when the BSP are perturbed with maximum errors of ±10 % are discussed. The same behaviour is observed for maximum errors of ±5 % and ±15 %.

When the mass of each body segment is perturbed, the highest RMSE is found at the ankle torque of the stance leg (M_1) with a peak of 2,3 Nm. However, in relative terms, this error is lower than the 2 % of the range of variation of the actual torque values. The mean RMSE in the swing leg ankle (0,034 Nm) is lower than the same error value in M_1. But due to the little range of variation of this torque, the mean NRMSE exceeds the 2 % with a pick higher than 11 %.

The same behaviour is observed between the stance leg knee and the swing leg knee and also between the results of the swing leg hip and the stance leg hip. From the results obtained, it can be concluded that the absolute error (RMSE) is more important at the stance leg and the relative error (NRMSE) is higher at the swing leg.

RMSE and NRMSE are estimators of the average of the error at each simulation. However, it is also interesting to know the error magnitude at each instant. The maximum difference –in absolute value– between the perturbed and the actual torque of the 1000 simulations is presented in Figure 5.2. Figure 5.2 (a) represents the instantaneous absolute error, that is, $\Delta M_i(k) = \max\left(\left|M_i^{\mathrm{NP}}(k) - M_i^{\mathrm{P}}(k)\right|\right) \quad \forall k$. In the same way, Figure 5.2 (b) shows the error in relative terms, namely, the instantaneous absolute error divided by the range of each actual torque. As explained above, only the single support phase is computed, that is, from the toe off of one leg until the heel strike of the same leg.

Stance Leg	**Ankle Torque (M_1)**			**Knee Torque (M_2)**			**Hip Torque (M_3)**		
% Max. Error	**5 %**	**10 %**	**15 %**	**5 %**	**10 %**	**15 %**	**5 %**	**10 %**	**15 %**
Mass									
$\bar{x}$RMSE [Nm]	0,337	0,679	0,993	0,234	0,472	0,689	0,175	0,355	0,526
σ RMSE [Nm]	0,157	0,327	0,502	0,112	0,229	0,349	0,088	0,175	0,267
Max RMSE [Nm]	1,075	2,346	3,860	0,641	1,664	2,351	0,494	1,169	1,635
NRMSE [%]	0,285	0,573	0,838	0,319	0,643	0,939	0,915	1,854	2,747
σ NRMSE [%]	0,132	0,276	0,424	0,153	0,312	0,476	0,457	0,912	1,395
Max NRMSE [%]	0,908	1,982	3,260	0,873	2,269	3,205	2,578	6,101	8,533
Length									
$\bar{x}$RMSE [Nm]	0,370	0,552	0,772	0,251	0,376	0,516	0,369	0,423	0,517
σ RMSE [Nm]	0,126	0,235	0,332	0,085	0,169	0,246	0,088	0,162	0,226
Max RMSE [Nm]	0,918	1,633	2,146	0,627	1,122	1,606	0,643	0,986	1,363
$\bar{x}$ NRMSE [%]	0,313	0,467	0,652	0,343	0,513	0,703	1,926	2,208	2,700
σ NRMSE [%]	0,106	0,198	0,281	0,115	0,231	0,336	0,459	0,848	1,177
Max NRMSE [%]	0,775	1,379	1,812	0,854	1,530	2,190	3,358	5,146	7,117
COM Location x'_G									
$\bar{x}$RMSE [Nm]	0,285	0,555	0,826	0,194	0,379	0,557	0,136	0,270	0,394
σ RMSE [Nm]	0,131	0,268	0,385	0,096	0,195	0,285	0,086	0,167	0,249
Max RMSE [Nm]	0,810	1,588	2,444	0,641	1,288	1,926	0,521	1,068	1,448
$\bar{x}$ NRMSE [%]	0,241	0,469	0,698	0,265	0,516	0,760	0,711	1,408	2,058
σ NRMSE [%]	0,110	0,226	0,326	0,131	0,266	0,388	0,446	0,873	1,297
Max NRMSE [%]	0,684	1,341	2,064	0,874	1,756	2,625	2,720	5,573	7,558
COM Location z'_G									
$\bar{x}$ RMSE [Nm]	0,079	0,096	0,117	0,059	0,087	0,120	0,054	0,103	0,153
σ RMSE [Nm]	0,010	0,028	0,048	0,019	0,043	0,070	0,034	0,071	0,106
Max RMSE [Nm]	0,130	0,229	0,348	0,148	0,273	0,492	0,218	0,389	0,631
$\bar{x}$NRMSE [%]	0,067	0,081	0,099	0,080	0,119	0,163	0,284	0,537	0,799
σ NRMSE [%]	0,009	0,024	0,041	0,025	0,059	0,096	0,180	0,372	0,555
Max NRMSE [%]	0,110	0,193	0,294	0,202	0,372	0,671	1,140	2,028	3,295
Moment of Inertia									
$\bar{x}$ RMSE [Nm]	0,075	0,083	0,096	0,048	0,059	0,076	0,027	0,043	0,063
σ RMSE [Nm]	0,008	0,017	0,028	0,009	0,019	0,030	0,010	0,021	0,032
Max RMSE [Nm]	0,101	0,144	0,211	0,081	0,137	0,203	0,071	0,132	0,196
$\bar{x}$ NRMSE [%]	0,063	0,070	0,081	0,065	0,081	0,103	0,139	0,224	0,331
σ NRMSE [%]	0,007	0,014	0,024	0,012	0,025	0,041	0,054	0,108	0,166
Max NRMSE [%]	0,086	0,121	0,178	0,110	0,187	0,276	0,370	0,687	1,022

Table 5.1 Errors in the stance leg joint torques when BSP are perturbed with zero-mean Gaussian errors with variances associated with maximum error intervals of ±5, ±10 and ±15 % of their actual value.

Swing Leg	**Ankle Torque (M_6)**			**Knee Torque (M_5)**			**Hip Torque (M_4)**		
% Max. Error	**5 %**	**10 %**	**15 %**	**5 %**	**10 %**	**15 %**	**5 %**	**10 %**	**15 %**
Mass									
$\bar{x}$RMSE [Nm]	0,018	0,034	0,052	0,080	0,162	0,244	0,119	0,236	0,361
σ RMSE [Nm]	0,012	0,023	0,034	0,050	0,101	0,153	0,059	0,121	0,184
Max RMSE [Nm]	0,079	0,182	0,214	0,302	0,677	0,883	0,344	0,720	1,184
$\bar{x}$NRMSE [%]	1,095	2,126	3,253	1,942	3,905	5,888	1,181	2,338	3,577
σ NRMSE [%]	0,723	1,430	2,124	1,199	2,444	3,697	0,585	1,196	1,822
Max NRMSE [%]	4,900	11,263	13,277	7,280	16,355	21,304	3,405	7,129	11,727
Length									
$\bar{x}$RMSE [Nm]	0,039	0,043	0,052	0,057	0,106	0,153	0,325	0,343	0,395
σ RMSE [Nm]	0,012	0,022	0,027	0,031	0,066	0,099	0,068	0,131	0,165
Max RMSE [Nm]	0,080	0,129	0,153	0,184	0,420	0,578	0,574	0,760	0,991
$\bar{x}$ NRMSE [%]	2,409	2,659	3,222	1,375	2,549	3,684	3,221	3,400	3,912
σ NRMSE [%]	0,769	1,370	1,675	0,739	1,602	2,399	0,677	1,294	1,629
Max NRMSE [%]	4,960	7,977	9,507	4,450	10,148	13,949	5,687	7,524	9,809
COM Location x'_G									
$\bar{x}$ RMSE [Nm]	0,004	0,006	0,008	0,062	0,122	0,191	0,059	0,122	0,178
σ RMSE [Nm]	0,001	0,003	0,004	0,048	0,090	0,141	0,035	0,075	0,100
Max RMSE [Nm]	0,010	0,017	0,029	0,296	0,612	0,792	0,212	0,451	0,623
$\bar{x}$NRMSE [%]	0,226	0,374	0,516	1,499	2,949	4,608	0,589	1,211	1,759
σ NRMSE [%]	0,077	0,173	0,260	1,169	2,176	3,401	0,345	0,739	0,989
Max NRMSE [%]	0,641	1,040	1,771	7,145	14,767	19,116	2,103	4,469	6,172
COM Location z'_G									
$\bar{x}$ RMSE [Nm]	0,006	0,012	0,017	0,025	0,050	0,073	0,042	0,086	0,128
σ RMSE [Nm]	0,003	0,006	0,009	0,016	0,034	0,050	0,031	0,062	0,090
Max RMSE [Nm]	0,025	0,037	0,057	0,125	0,188	0,287	0,226	0,335	0,515
$\bar{x}$NRMSE [%]	0,375	0,717	1,034	0,612	1,205	1,771	0,420	0,853	1,265
σ NRMSE [%]	0,185	0,390	0,580	0,391	0,816	1,195	0,303	0,616	0,895
Max NRMSE [%]	1,529	2,310	3,526	3,028	4,546	6,939	2,241	3,318	5,105
Moment of Inertia									
$\bar{x}$RMSE [Nm]	0,005	0,010	0,013	0,018	0,031	0,048	0,020	0,037	0,057
σ RMSE [Nm]	0,003	0,006	0,009	0,010	0,021	0,032	0,011	0,022	0,033
Max RMSE [Nm]	0,020	0,038	0,049	0,060	0,124	0,191	0,068	0,137	0,202
$\bar{x}$NRMSE [%]	0,320	0,592	0,829	0,423	0,758	1,161	0,194	0,368	0,569
σ NRMSE [%]	0,171	0,367	0,553	0,247	0,503	0,783	0,113	0,215	0,329
Max NRMSE [%]	1,239	2,339	3,011	1,453	2,996	4,612	0,675	1,359	2,003

Table 5.2 Errors in the swing leg joint torques when the BSP are perturbed with zero-mean Gaussian errors with variances associated with maximum error intervals of ±5, ±10 and ±15 % of their actual value.

Figure 5.2 clearly illustrates the differences between the torques of the stance (red) and the swing (blue) leg. Absolute errors of the stance leg are higher than those of the swing leg ones, but in percentage –with respect to the range of the actual value–, the most sensible torques are the ones of the swing leg.

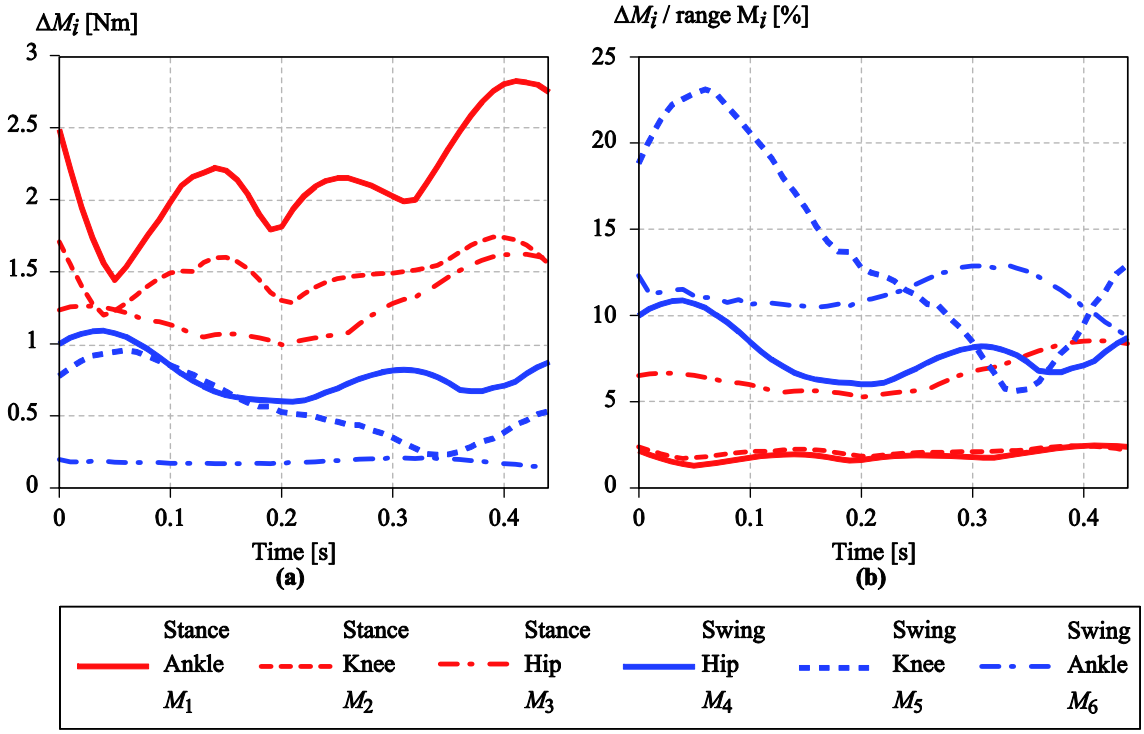

Figure 5.2 Errors in lower limb torques when the mass is perturbed with zero-mean Gaussian errors with variances associated with maximum error intervals of ±10 %. (a) Absolute errors. (b) Relative errors.

Inaccuracies in the lengths of the segments produce the highest mean NRMSE in M_4 (3,4 %). As before, the most important absolute errors (RMSE) are detected in the torques related to the joints that belong to the stance leg. A mean of 0,552 Nm with a peak of 1,633 Nm can be found in M_1. Nevertheless, uncertainties of 10 % in the length of a body segment are improbable because this parameter can be accurately measured compared to other BSP.

The position of the centre of mass is expressed in the local coordinates system of each segment $\left(x'_G, z'_G\right)$. The origin of the local system is placed at the proximal joint, the X' axis is defined from the proximal to the distal joint, and the Z' axis is obtained by rotating the X' axis 90 degrees counterclockwise. Errors in the centre of mass (COM) coordinates have different effects in the kinetic results. The RMSE analysis shows that the errors in z'_G are one order of magnitude lower than errors in coordinate x'_G.

Errors in z'_G slightly influence the final results of the stance leg (with RMSE of 0,15 Nm). Moreover, the low standard deviation associated to the stance leg z'_G indicates that the results tend to be very close to the mean.

Regarding the errors in the moments of inertia, the results show that the most affected torque is M_5 (swing leg knee), with a mean NRMSE of 0,7 % and a peak of 3 %. The RMSE values are similar to the errors found when z'_G is inaccurate, and are one order of magnitude lower than the errors found when any other BSP is perturbed. Thus, it can be concluded that uncertainties in the moments of inertia have little influence in the gait analysis results.

Table 5.1 and Table 5.2 indicate that the standard deviation of the errors depends on the perturbed BSP. While the NRMSE corresponding to perturbations in the moment of inertia and the *z* coordinate of the COM tends to be very close to the mean, the NRMSE due to perturbations in the mass, length and *x* coordinate of the COM spreads out over a large range of values.

In general, the results indicate differences between the errors in swing and stance leg torques. Regarding absolute errors, RMSE in M_1 (stance leg ankle) are always larger than those obtained in M_6 (swing leg ankle). The same behaviour can be also observed between M_2 (stance leg knee) and M_5 (swing leg knee); and between M_3 (swing leg hip) and M_4 (stance leg hip). The analysis of the RMSE is in agreement with [Silva and Ambrósio 2004], which concludes that the IDA results are more sensitive to errors in those kinematic chains that have external forces applied to them (foot-ground contact force).

In relative terms, the behaviour is just the opposite: the highest NRMSE are found in swing leg torques. The differences in this case are more significant due to the torque range of variation during the swing phase, which is much lower than the one during the stance phase.

The obtained results can also be compared with [Pearsall and Costigan 1999], where the authors use an analysis of variance (ANOVA) and compute the NRMSE to determine the differences in the IDA results when different anthropometric tables are used. The published results indicate that the maximum NRMSE of the stance leg is found in the hip (with a NRMSE of 7,94 %), which is comparable to the result obtained in this work (6,1 %). Similarly, they found a maximum NRMSE in the stance leg knee of 2,35 %, which is close to the value, shown in Table 5.1, of 2,27 % in the same torque.

5.5.2 Influence of the Weighting Matrix during the Reconstruction of Kinematic Data

As explained in Section 5.2, the technique applied to obtain a new set of kinematically consistent data requires the definition of a weighting matrix **W**. To analyse how this matrix can affect the results, two different weighting matrices are used. The first one ($\mathbf{W}_1$) considers that all the markers have the same expected errors ($\mathbf{W}_1$ is equal to the identity matrix). The second case considers that errors in stance leg are less probable, so the values of $\mathbf{W}_2$ associated to the stance leg coordinates are ten times higher than the

others. An IDA is computed for each value of **W** and the results are compared to the ones obtained using the actual **W** (defined at Section 2.1). Table 5.3 shows the NRMSE and RMSE results in the two cases considered.

If the identity matrix is used ($\mathbf{W}_1$), an absolute error greater than 15 Nm is detected in ankle and knee torques corresponding to the stance leg. Furthermore, a NRMSE close to 13 % can be found in the torque of the stance leg knee.

Comparing Table 5.3 with Tables 5.1 and 5.2, it can be concluded that the weighting matrix used during the kinematic data reconstruction has more influence in the kinetic results than errors in BSP. In this case, the RMSE are almost one order of magnitude above the mean RMSE obtained with BSP perturbations. In relative terms, the error produces a NRMSE in the swing leg hip of 17,92 %, while the maximum NRMSE in this torque was 6,1 % when BSP were perturbed. The results obtained using $\mathbf{W}_2$ also present high RMSE and NRMSE values (compared to those in Tables 1 and 2).

	Stance Leg			**Swing Leg**		
$\mathbf{W}_1$	**Ankle Torque (M_1)**	**Knee Torque (M_2)**	**Hip Torque (M_3)**	**Ankle Torque (M_6)**	**Knee Torque (M_5)**	**Hip Torque (M_4)**
RMSE [Nm]	15,181	9,674	3,433	0,796	0,352	0,055
NRMSE [%]	12,821	13,187	17,919	7,877	8,508	3,391
$\mathbf{W}_2$						
RMSE [Nm]	7,298	5,313	2,454	0,847	0,419	0,112
NRME [%]	6,164	7,243	12,811	8,384	10,122	6,932

Table 5.3 Errors in the swing leg joint torques when the BSP are perturbed with zero-mean Gaussian errors with variances associated with maximum error intervals of ±5, ±10 and ±15 % of their actual value.

This study reveals the importance of an adequate criterion to define the weighting matrix. Although the values obtained for RMSE and NRMSE depend on the original **W** matrix used, the study shows how sensible are the IDA results to different plausible weighting matrices. There are no studies in the literature describing how this matrix can exactly be defined and, as observed in the results, using a non appropriate criterion can affect significantly the results.

Similar to

Figure 5.2, Figure 5.3 clearly represents how errors in the kinematic reconstruction can affect the torque results along the time. In this case, the absolute instantaneous error is defined as $\Delta M_i(k) = \left| M_i^{\mathrm{NP}}(k) - M_i^{\mathbf{W}_j}(k) \right| \quad \forall k$ where $M_i^{\mathbf{W}_j}$ are the torques M_i calculated using the matrix $\mathbf{W}_j$ (with j=1,2), and the relative errors are obtained as a quotient between ΔM_i and the range of variation of each torque. Figure 5.3 (a) and (b)

shows, in absolute and in relative terms respectively, the errors when $\mathbf{W}_1$ is used and, similarly, Figure 5.3 (c) and (d) represents the errors when the matrix $\mathbf{W}_2$ is applied.

Significant differences can be observed between the torques of the stance and the swing leg. Figure 5.3 (a) and (c) clearly shows that stance leg torques have a higher absolute error. These results are in agreement with [Silva and Ambrósio 2004], which concludes that the quality of the IDA results depends on the precision of the kinematic reconstruction of the stance leg joints; and with [Riemer *et al.* 2008] which identifies the estimated segment angles as the main contributors of the uncertainties in torque estimates. However, the relative error in swing leg torques is not negligible. Therefore, improving the kinematic reconstruction of the swing leg is also important. Note that these results highlight the influence of little variations at joint positions in the IDA results. These variations are inherent in all kinematic data reconstruction methods published in the literature [Alonso *et al.* 2010, Silva and Ambrósio 2002a]. Therefore, all these processes need to be studied further in order to improve the results.

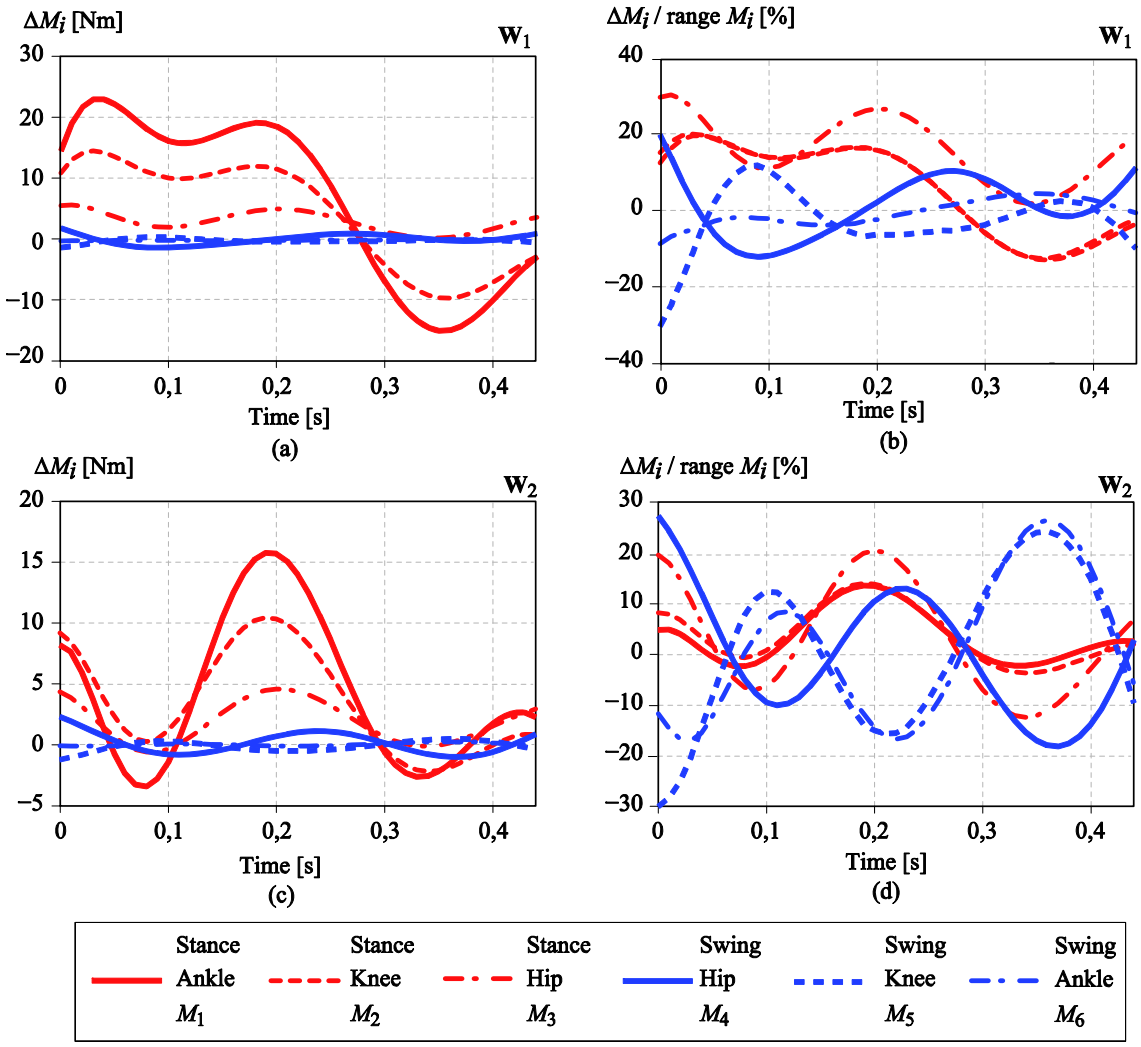

Figure 5.3 Errors in lower limb torques: (a) Absolute errors using $\mathbf{W}_1$; (b) Relative errors using $\mathbf{W}_1$; (c) Absolute errors using $\mathbf{W}_2$; (d) Relative errors using $\mathbf{W}_2$.

5.5.3 Errors in the Ground Reaction Force

In this section, the ground reaction force and torque are used as an input to the inverse dynamics problem. We add an error to these three dynamic components obtained using multibody techniques in order to emulate the errors that force plate measurements could contain.

Two cases are simulated –as explained in section 5.3–, adding fixed quantities to the ground reaction force (1 and 10 N for the horizontal component and 5 and 50 N for the vertical one) and to the ground reaction torque (5 and 50 Nm). The error analysis results are shown in Table 5.4.

As expected –according to the Newton-Euler laws–, the ankle torque (M_1) does not change when the errors are in the foot-ground contact force. This torque is only sensible to errors in the foot-ground contact torque.

The force plate errors are amplified along the stance leg due to the recursive method used (using Newton-Euler equations from the foot to the trunk). As a result, a 2 % FSO error in the horizontal ground reaction force causes a NRMSE of 5,85 % in the knee joint, which grows up to more than 43 % in the hip joint.

	Ankle Torque (M_1)		**Knee Torque (M_2)**		**Hip Torque (M_3)**	
Perturbed F_X [N]	**0,2 % FSO**	**2 % FSO**	**0,2 % FSO**	**2 % FSO**	**0,2 % FSO**	**2 % FSO**
RMSE [Nm]	0	0	0,427	4,292	0,826	8,300
NRMSE [%]	0	0	0,582	5,85	4,311	43,325
Perturbed F_Z [N]						
RMSE [Nm]	0	0	0,240	2,403	0,557	5,567
NRMSE [%]	0	0	0,328	3,275	2,906	29,061
Perturbed M_Y [Nm]						
RMSE [Nm]	0,999	9,998	0,998	9,998	0,995	9,995
NRMSE [%]	0,844	8,445	1,36	13,629	5,196	52,176

Table 5.4 Error values in stance leg torque when ground contact forces are perturbed adding a 0,2 % and 2 % of the full scale output (FSO).

The errors in each component of the ground reaction forces have different effects in the net joint torques. The main effect is produced by the horizontal component of the ground reaction force, both in terms of absolute and relative errors.

The error in the ground reaction torque highly affects the results. If the torque measurement contains errors and this information is used as input data, all the torques obtained as a result of an IDA will be extremely affected, up to a NRMSE of 52 % in the hip torque.

This analysis shows that having error in the ground reaction force produces higher RMSE and NRMSE than those obtained when BSP are inaccurate, but a similar error magnitude to the one that occurs if the kinematic processing is not adequate.

The obtained RMSE are in accordance with the results of [Silva and Ambrósio 2004], where a sensitivity greater than 0,8 Nm/N (approximately constant along the stance phase) is obtained in the hip torque with a perturbation in the horizontal component of the ground reaction force. This sensitivity can be compared with the RMSE of 0,826 Nm obtained in M_3 when the horizontal component of the force is perturbed 1 N. Similarly, Silva and Ambrósio (2004) obtain a sensitivity of approximately 0,4 Nm/N for the knee joint, a result closed to the 0,427 Nm obtained in our case with 1 N perturbation. The errors calculated when a perturbation is introduced in the vertical force are also similar to those obtained in their study.

In this work, the maximum RMSE is obtained when the ground reaction torque is perturbed. Although this result cannot be directly compared to [Silva and Ambrósio 2004], this ground reaction torque is directly related to the centre of pressure. Silva and Ambrósio conclude that the ankle, knee and hip joint torques are extremely sensitive to errors in the application point of the external force. Therefore, the results are also in agreement.

5.6. Discussion

Errors in the input data influence differently the stance and swing leg torques. The RMSE are higher in the results of the stance leg, however, the NRMSE are higher in the swing leg torques.

Errors in the moments of inertia have a little effect in the IDA results. Compared to the others cases analysed, these inaccuracies are almost negligible.

The process to obtain kinematic consistent data can introduce large errors in the IDA results. This process needs to be further studied to determine the best weight associated to each joint coordinate in order to improve the results of the analysis.

The net joint torques are more sensitive to errors in the force plate measurements than in BSP parameters. The use of force plate data as an input to the IDA can introduce important errors in the analysis. In this case, the obtained hip torque can be highly affected.

In conclusion, to enhance the gait analysis results, the efforts must focus on improving the accuracy of the kinematic data processing and the force plate measurements. The refinement of the anthropometric body segment parameters has little effect in gait analysis results.

Chapter 6

Foot-Ground Contact Model

The biomechanics research community has demonstrated, in the last two decades, an increasing interest to obtain an accurate forward dynamic analysis (FDA) of human locomotion. When the aim of the analysis is to simulate the gait motion (using FDA), a foot-ground contact model is needed to reproduce the interaction between the biomechanical system (the subject) and the environment (the ground). In an inverse dynamic analysis (IDA), a constitutive foot-ground contact model can also be useful to solve the double support sharing problem when force plate data are not available.

Since the objective of the research project explained in the introductory chapter is to simulate the resulting motion of patients wearing an orthosis, a realistic model for the foot-ground contact is required. Moreover, as explained in Chapter 4, in this thesis the IDA is computed using only kinematic information and anthropometric body segment parameters (BSP) as input data, therefore, an accurate foot-ground model is also useful to solve the contact wrench indeterminacy during the double support phase. Consequently, in this chapter, a foot-ground contact model will be applied to both methods, FDA and IDA.

Some foot-ground contact models have been presented in the literature. They are based on sphere-plane contact elements [Güller *et al.* 1998, Meglan 1991, Millard *et al.* 2008, Moreira *et al.* 2009], hipper-ellipsoid surfaces [Barbosa *et al.* 2005], cylinder-plane contact elements [Kecskeméthy 2011], or a set of springs and dampers [Gilchrist and Winter 1996]. However, there is neither an accepted way to model the foot-ground interaction nor an accepted way to validate the foot-ground contact model.

These models are used to reproduce the relationship between the developed contact forces (normal and tangential) and the relative foot-ground displacements and velocities. The main problem is how to determine all the parameters of the contact model (i.e., stiffness, damping and friction coefficients, and geometrical properties of the contact elements), and how to relate their values with the actual contact phenomenon.

This chapter presents a comparison of two approaches (based on optimization techniques) used to estimate the parameters of a compliant foot-ground contact model based on sphere-plane contact elements. The foot-ground contact model is used to solve the contact wrench sharing problem during the double support phase (in an IDA approach) and is also used to simulate the motion when a FDA is performed.

6.1 Modelling

A constitutive foot-ground contact model representing the forces as a function of the system state is presented. The foot sole surface is approximated using a set of spheres and a continuous contact force model. The foot geometry and the normal and tangential force models employed are described below.

In this model, two foot segments are considered: the hindfoot and the forefoot. The relative rotations between them are modelled through a spherical joint. The sole surface of the hindfoot is approximated with three spherical contact elements and another sphere is used for approximating the forefoot sole surface (Figure 6.1).

For each foot, the $\{X',Y',Z'\}_{HF}$ and $\{X',Y',Z'\}_{FF}$ coordinate systems are rigidly attached to the hindfoot and forefoot segments, respectively and are defined using the unit vectors defined in Table A.1 (therefore, obtaining $\{X',Y',Z'\}_{RHF}$, $\{X',Y',Z'\}_{RFF}$, $\{X',Y',Z'\}_{LHF}$, $\{X',Y',Z'\}_{LFF}$ for the right and left feet). For each sphere, four parameters need to be determined: x_i', y_i' and z_i', that is, the local position of the sphere centre, and the radius r_i.

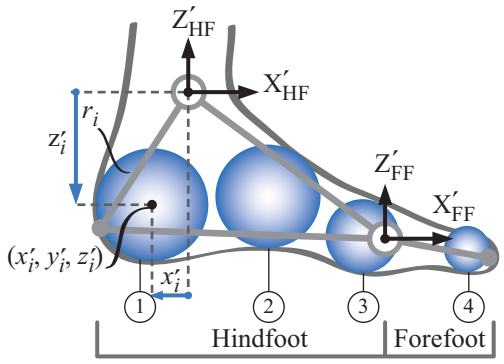

Figure 6.1 Side view of the 3D foot–ground contact model.

The normal force model is the one proposed by Lankarani and Nikravesh (1990) which defines the normal force F_n as:

$$F_n = K\left|\delta_n\right|^{3/2} + \chi\left|\delta_n\right|^{3/2}\dot{\delta}_n \tag{6.1}$$

where the stiffness parameter K parameter is dependent on the material properties and the shape of the surfaces, the exponent is fixed at 3/2 due to the fact that all contacts are considered as point contacts between spherical and planar surface bodies, $\dot{\delta}_n$ is the time

derivative of the normal indentation between bodies δ_n, and χ is the hysteresis damping factor given by:

$$\chi = \frac{3K\left(1-c_r^2\right)}{4\dot{\delta}_0} \tag{6.2}$$

where c_r is the coefficient of restitution and $\dot{\delta}_0$ is the relative normal velocity between the colliding bodies when contact is detected. For a sphere-plane contact, the generalized stiffness K can be calculated as:

$$K = \frac{4E^*\sqrt{R_S}}{3} \tag{6.3}$$

where R_S is the radius of the sphere and E^* is the effective Young's modulus, which in turn can be calculated through:

$$E^* = \left[\frac{1-\nu_s^2}{E_s} + \frac{1-\nu_p^2}{E_p}\right]^{-1} \tag{6.4}$$

In this last equation, E_s and E_p are the Young's modulus of the materials of the sphere and the plane respectively, and ν_s and ν_p are their Poisson's ratios. This model assumes that the energy loss during the contact is associated with the material damping of the bodies in contact.

Using Eqs. (6.1) and (6.2), the normal force can be expressed as:

$$F_n = K\left|\delta_n\right|^{3/2} + \frac{3\left(1-c_r^2\right)}{4\dot{\delta}_0} K\left|\delta_n\right|^{3/2}\dot{\delta}_n \tag{6.5}$$

The Coulomb friction law of sliding friction is the simplest model between dry contacting surfaces. When sliding takes place, this law states that the tangential friction force is proportional to the magnitude of the normal force at the contact point. This law does not take into account that friction forces can also depend on material properties, velocity of sliding, surfaces cleanliness, etc.

The tangential force $\mathbf{F}_t$ used in this thesis follows the bristle–type model proposed by Dopico *et al*. (2011). It is based on Coulomb's law including sticktion and a viscous friction component. Its general form is:

$$\mathbf{F}_t = \kappa\mathbf{F}_{\text{stick}} + \left(1-\kappa\right)\mathbf{F}_{\text{slide}} - \mu_{\text{visc}}\,\mathbf{v}_t \tag{6.6}$$

The first two terms of the right hand side of Eq. (6.6) are related to the dry friction and the third term takes into account the viscous friction. $\mathbf{F}_{\text{stick}}$ and $\mathbf{F}_{\text{slide}}$ are the components of the sticktion and sliding force, κ is a smooth function of the tangential velocity, μ_{visc} is the viscous damping coefficient, and $\mathbf{v}_t$ (the subscript *t* comes from tangential) is defined as:

$$\mathbf{v}_t = \dot{\mathbf{r}}_{\text{cont}} - \left(\mathbf{n}^T \dot{\mathbf{r}}_{\text{cont}}\right)\mathbf{n} \tag{6.7}$$

where $\mathbf{r}_{\text{cont}}$ and $\mathbf{r}_{\text{cont}}$ are the position and velocity of the central point of the contact region and $\mathbf{n}$ is the normal vector perpendicular to the tangent contact point (in the studied case the normal vector of the ground plane). The transition between sticking and sliding is accomplished using the smooth function κ, which matches the following conditions:

$$\kappa = \begin{Bmatrix} 0; & |\mathbf{v}_t| \gg v_{stick} \\ 1; & |\mathbf{v}_t| = 0 \end{Bmatrix} \tag{6.8}$$

where v_{stick} is a parameter of the model accounting for the velocity of the stick-slip transition. As Goldsmith (1960) proposed, the function κ is assumed as:

$$\kappa = e^{-\left(\mathbf{v}_t^T \mathbf{v}_t\right)/v_{stick}^2} \tag{6.9}$$

The sticktion forces are modelled by means of viscoelastic elements, called bristles, acting between the colliding bodies. The expressions of the sliding and sticktion forces are given by Cuadrado *et al*. (2001, 2004):

$$\mathbf{F}_{\text{slide}} = \begin{Bmatrix} 0; & |\mathbf{v}_t| = 0 \\ -\mu |\mathbf{F}_n| \dfrac{\mathbf{v}_t}{|\mathbf{v}_t|}; & |\mathbf{v}_t| > 0 \end{Bmatrix} \tag{6.10}$$

$$\mathbf{F}_{\text{stick}} = \begin{Bmatrix} 0; & s = 0 \\ \dfrac{f_{\text{stick}}^m}{s}\left(\mathbf{I}_3 - \mathbf{n}\mathbf{n}^T\right)\left(\mathbf{r}_{\text{cont}} - \mathbf{r}_{\text{stick}}\right); & s > 0 \end{Bmatrix} \tag{6.11}$$

where μ is the friction coefficient under dynamic conditions, $\mathbf{r}_{\text{stick}}$ is the sticktion point position, $s = |\mathbf{r}_{\text{cont}} - \mathbf{r}_{\text{stick}}|$ is the deformation of the bristles and $\mathbf{I}_3$ is the identity matrix of size 3×3. Note that at the instant at which the contact begins, $\mathbf{r}_{\text{stick}}$ equals to $\mathbf{r}_{\text{cont}}$. Finally, f_{stick}^m is the force representing the viscoelastic behaviour of the bristles:

$$f_{\text{stick}}^m = -k_{\text{stick}} s - c_{\text{stick}} \dot{s} \tag{6.12}$$

In this last equation, k_{stick} and c_{stick} are the stiffness and damping coefficients of the sticktion model. Figure 6.2 shows a representation of the geometric parameters used to define the sliding and sticktion forces. More details of the tangential model are given in [Dopico *et al.* 2011].

Note that, for each sphere, the design variables for the tangential model are the friction coefficient μ, the parameter v_{stick}, and the stiffness and damping coefficients k_{stick} and c_{stick}. In the studied case, the viscous damping coefficient μ_{visc} is fixed to 0.

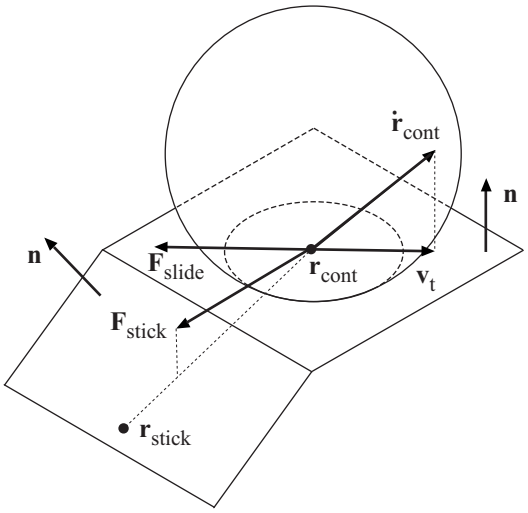

Figure 6.2 Scheme of the tangential contact between sphere and plane. Adapted from [Dopico *et al.* 2011].

6.2 Optimization Approaches for Parameter Identification

Two approaches to determine the contact model parameters are compared in this thesis in order to seek the parameters of the contact force model that provide the same reactions than those estimated through inverse dynamics in Chapter 4. The first one uses BSP and kinematic information as input data and identifies the model parameters that minimize the difference between the resultant contact wrenches obtained by IDA and through the contact model. The second one uses BSP and dynamic information (ankle and metatarsal joint wrenches) as input data, computes a FDA (using a controller to ensure the convergence of the kinematics) and obtains the contact model parameters that minimize the difference between the force plate data and the reactions obtained through the contact model.

Some optimization details are given in Table 6.1 where both methods are compared. Note that the multibody model used, the input data, the time step and the objective function are different in each approach.

For both approaches, the design variables of the compliant contact model are the following nine parameters for each sphere (see Figure 6.1): local position x', y' of the sphere centre for a given z' (in the corresponding coordinate system), the sphere radius r, the stiffness K and restitution coefficient c_r of the normal contact force model; for the tangential model, the friction coefficient μ, the parameter v_{stick} which accounts for

the velocity of the stick-slip transition, and the stiffness and damping coefficients (k_{stick} and c_{stick}) of the sticktion model.

Upper and lower boundaries are set for each design variable (remaining constant for both feet) as it can be seen in Table 6.2 The value of z' is fixed at –0,0525 m in the local coordinate system. Note that the spheres are numbered consecutively (see Figure 6.1) from heel (sphere 1) to toes (sphere 4).

Inverse Dynamics Approach	**Forward Dynamics Approach**
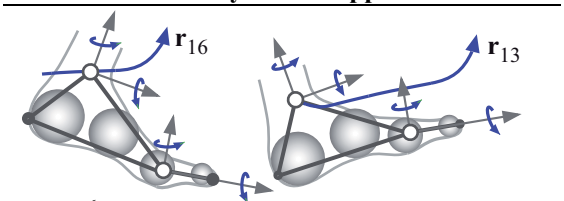 $\mathbf{q} = \{x_{13}, y_{13}, z_{13}, x_{16}, y_{16}, z_{16},$ $\alpha_{RHF}, \beta_{RHF}, \gamma_{RHF}, \alpha_{LHF}, \beta_{LHF}, \gamma_{LHF}$ $\alpha_{RFF}, \beta_{RFF}, \gamma_{RFF}, \alpha_{LFF}, \beta_{LFF}, \gamma_{LFF}\}^T$	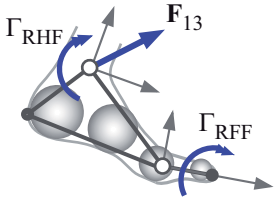
Two feet motion	One foot motion
Kinematic information as input data: ankles position, hindfeet and forefeet absolute angular variables	Dynamic information as input data: Force and torque at right ankle joint and torque at metatarsal joint
Time step: 10 ms	Time step: 1 ms
Objective Function: Minimize the difference between the global contact wrench obtained by IDA and through the contact model	Objective Function: Minimize the difference between the force plate data and the contact model wrench
	Extended Kalman filter as controller

Table 6.1 Details of the two optimization approaches used to estimate the foot-ground contact model parameters.

A null value of the normal and tangential force is imposed when the foot is not contacting the ground. The latter constraint requires the identification of the heel strike and toe off instants during the gait cycle. This identification has been done by using the information of force plate data if available. When this information was not accessible, the method based on kinematics called foot velocity algorithm (FVA) was used for this purpose [O'Connor *et al.* 2007].

Although the parameters of the contact model are considered as the design variables the procedure in both approaches (inverse and forward analysis), the optimization approach varies slightly. In the following subsections, the two methods are discussed separately.

Sphere 1	Min.	Max.
r [m]	0,015	0,04
x'[m]	–0,035	0
y' [m]	–0,010	0,01
$K \cdot 10^{-5}[\mathrm{Nm}^{-3/2}]$	0	0,6
c_r	0	1
μ	0	1
v_{stick} [m/s]	0	0,1
k_{stick} 10^5[N/m]	0	1
c_{stick} $\cdot 10^2$ [Ns/m]	0	1

Sphere 3	Min.	Max.
r [m]	0,03	0,05
x'[m]	0,118	0,138
y' [m]	–0,03	0,03
$K \cdot 10^{-5}[\mathrm{Nm}^{-3/2}]$	0	0,6
c_r	0	1
μ	0	1
v_{stick} [m/s]	0	0,1
k_{stick} 10^5[N/m]	0	1
c_{stick} $\cdot 10^2$ [Ns/m]	0	1

Sphere 2	Min.	Max.
r [m]	0,025	0,05
x'[m]	0,015	0,085
y' [m]	–0,030	0
$K \cdot 10^{-5}[\mathrm{Nm}^{-3/2}]$	0	0,6
c_r	0	1
μ	0	1
v_{stick} [m/s]	0	0,1
k_{stick} 10^5[N/m]	0	1
c_{stick} $\cdot 10^2$ [Ns/m]	0	1

Sphere 4	Min.	Max.
r [m]	0,03	0,05
x'[m]	0,04	0,075
y' [m]	–0,005	0,02
$K \cdot 10^{-5}[\mathrm{Nm}^{-3/2}]$	0	0,6
c_r	0	1
μ	0	1
v_{stick} [m/s]	0	0,100
k_{stick} 10^5[N/m]	0	1
c_{stick} $\cdot 10^2$ [Ns/m]	0	1

Table 6.2 Upper and lower boundaries for the design variables.

6.2.1 Inverse Dynamics Optimization Approach

As shown in Table 6.1, the inverse dynamics approach is computed using only the feet motion. The position and orientation of each foot segment are obtained from the whole human body model. The forces introduced by the contact model depend on feet kinematic information (indentation histories, that are known) and contact parameters. The latter are design variables of an optimization problem. The objective function to be minimized in this approach is defined as the difference between the global contact wrench obtained through inverse dynamics and the foot-ground wrench yielded by the contact model.

Note that, as exposed in Chapter 4, computing the inverse dynamic analysis using only kinematic information as input allows for the calculation of one external contact wrench (three force components and three moment components) during the whole gait cycle. This is the wrench used as a reference curve.

In order to make the wrenches comparable the contact wrench acting on the lumbar joint obtained by the IDA $\left(\tilde{\mathbf{G}}\right)$ and the contact wrenches obtained through the foot-ground contact model $\left(\mathbf{G}_{\text{CM1}}, \mathbf{G}_{\text{CM2}}\right)$ have been translated to a common point, namely the

projection of the lumbar joint onto the ground (as explained in Chapter 4), thus obtaining $\tilde{\mathbf{G}}^{\mathrm{gr}}$ and $\mathbf{G}_{\mathrm{CM}}^{\mathrm{gr}}$. Note that the two foot-ground contact wrenches are properly added to obtain $\mathbf{G}_{\mathrm{CM}}^{\mathrm{gr}}$. The error is defined as the NRMSE of each component (i.e., RMSE divided by signal range) in order to balance their different scales and use a dimensionless magnitude. The error optimization criterion to be minimized can be written as:

$$\min V = \mathbf{h}^T \mathrm{NRMSE}\left(\tilde{\mathbf{G}}^{\mathrm{gr}}, \mathbf{G}_{\mathrm{CM}}^{\mathrm{gr}}\right) \tag{6.13}$$

where $\mathbf{h}$ is a 6×1 weight vector and each component of the $\mathrm{NRMSE}\left(\tilde{\mathbf{G}}^{\mathrm{gr}}, \mathbf{G}_{\mathrm{CM}}^{\mathrm{gr}}\right)$ is obtained as:

$$\mathrm{NRMSE}\left(\tilde{G}^{\mathrm{gr}}, G_{\mathrm{CM}}^{\mathrm{gr}}\right) = \frac{1}{\mathrm{range}\left(\tilde{G}^{\mathrm{gr}}\right)} \sqrt{\frac{1}{N}\sum_{k=1}^{N}\left(\tilde{G}^{\mathrm{gr}}(k) - G_{\mathrm{CM}}^{\mathrm{gr}}(k)\right)^2} \tag{6.14}$$

where $\mathrm{range}\left(\tilde{G}^{\mathrm{gr}}\right)$ is calculated as the absolute difference between the maximum and the minimum value of component $\tilde{G}^{\mathrm{gr}}$ during the gait cycle. Note that $\mathrm{NRMSE}\left(\tilde{\mathbf{G}}^{\mathrm{gr}}, \mathbf{G}_{\mathrm{CM}}^{\mathrm{gr}}\right)$ is a 6×1 vector containing the six components calculated using Eq. (6.14).

The evolutive optimization method known as Covariance Matrix Adaptation Evolution Strategy (CMA–ES) has been applied [Hansen 2006]. The implementation of this algorithm in Matlab code is available on *http://www.lri.fr/~hansen/*. Each function evaluation is carried out by a Fortran code packed into a MEX–file that calculates the foot-ground contact forces according to the contact model and obtains the error with respect to the inverse dynamics results.

6.2.2 Forward Dynamics Optimization Approach

The dynamic information obtained performing an IDA, that is, the joint forces and joint torques along the gait cycle, is used as input data to compute a FDA. Unfortunately, the FDA of human gait requires a high computational time [Anderson and Pandy 2001a, Neptune *et al.* 2001]. The forward dynamic analysis developed in this thesis is a first step for a future work related to human gait prediction. Therefore, in order to assess the correctness, validate the methodology used, and perform the simulation with a reasonable computational time, a single foot model is employed for this study

As previously, a CMA-ES algorithm is used. To speed up the optimization process and since evolutive optimization does not require executing sequentially the function evaluations; the optimization process has been parallelized using the Matlab Parallel Computing Toolbox.

In this second approach, as exposed in Table 6.1, the optimization procedure minimizes the difference between the wrench obtained from force plate data $\left(\mathbf{G}_{\mathrm{FPL}}\right)$ and the one derived from the foot-ground contact model reactions $\left(\mathbf{G}_{\mathrm{CM}}\right)$. Since only one foot is

used, both wrenches are translated to the ankle joint to be compared. Therefore, in this case the error optimization criterion to be minimized is defined as:

$$\min V = \mathbf{h}^T \mathrm{NRMSE}\left(\mathbf{G}_{\mathrm{FPL}}^{\mathrm{ankle}}, \mathbf{G}_{\mathrm{CM}}^{\mathrm{ankle}}\right) \tag{6.15}$$

and, similarly to Eq. (6.14), for each component of the contact wrench:

$$\mathrm{NRMSE}\left(G_{\mathrm{FPL}}^{\mathrm{ankle}}, G_{\mathrm{CM}}^{\mathrm{ankle}}\right) = \frac{1}{\mathrm{range}\left(G_{\mathrm{FPL}}^{\mathrm{ankle}}\right)} \sqrt{\frac{1}{N}\sum_{k=1}^{N}\left(G_{\mathrm{FPL}}^{\mathrm{ankle}}(k) - G_{\mathrm{CM}}^{\mathrm{ankle}}(k)\right)^2} \tag{6.16}$$

Also, in this case, the error is defined as the NRMSE of each component and **h** is the vector that gives the possibility to associate different weights to each error component.

The foot-ground contact model introduces contact forces that are not exactly the same as the ones measured at the laboratory. Therefore, the use of the contact model in a FDA approach introduces uncertainties in the contact wrench that may unstabilise the system, which is extremely sensitive to inaccuracies.

There is no agreement in the way to obtain a realistic gait predictive simulation. However, some researchers have proposed the use of controllers to balance the system as a method to prevent the model from falling down [Millard *et al.* 2008, Peasgood *et al.* 2007]. In this thesis, a controller based on state observers through the extended Kalman filter (EKF) is used [Cuadrado *et al.* 2009].

The Kalman filter (KF) concerns the task of estimating the state of the biomechanical system having access to inaccurate measurements from the process. The KF is an optimal observer for linear systems. When nonlinear systems are considered (as in this thesis), the extended Kalman filter (EKF) is the most widely used algorithm [Grewal and Andrews, 2008]. The formulation of the EKF is outlined in Appendix D.

Based on the available information, the EKF estimates the state of the dynamic process so as to minimize the mean-squared estimation error [Grewal and Andrews 2008]. In this thesis, it is used as a controller using as a reference signal the motion captured in the laboratory. The use of this controller increases significantly the simulation time, this is why it was not used in Section 4.7, where the whole 3D body model is used to perform FDA. When the foot-ground contact model is used, it has not been possible to obtain a whole simulation using the PD controller described in Section 4.7 because the uncertainties introduced by the contact model destabilise the system.

The foot has been modelled (as the previous multibody models) using mixed coordinates. The motion of the actual foot is obtained via the kinematic analysis formulated in Chapter 4. The generalized coordinate vector contains the three Cartesian coordinates of the ankle joint position, the three Cartesian components of 4 unit vectors (two vectors for each segment) and the angular variables that orientate each segment with respect to the ground (three angles for each segment). Therefore, vector **q** contains all the n_d dependent variables and is a 21×1 vector.

The independent variables $\mathbf{z}$ for the matrix-R method are the ankle joint position and the absolute angular variables for the 2 segments (with a total of $n_i = 9$ independent variables). The mass matrix $\mathbf{M}$, the generalized force vector $\mathbf{Q}$ and the constraints of the multibody system $\mathbf{\Phi}$ are obtained according to the methodology presented in Chapter 3.

In order to apply the Kalman filter formulation, the dynamics of the multibody system needs to be expressed as:

$$\dot{\mathbf{x}}(t) = \mathbf{f}\left(\mathbf{x}(t), t\right) + \boldsymbol{\delta}(t) \quad \boldsymbol{\delta}(t) \sim \mathcal{N}\left(0, \mathcal{Q}(t)\right) \tag{6.17}$$

$$\mathbf{y}(t) = \mathbf{h}\left(\mathbf{x}(t), t\right) + \boldsymbol{\varepsilon}(t) \quad \boldsymbol{\varepsilon}(t) \sim \mathcal{N}\left(0, \mathcal{R}(t)\right) \tag{6.18}$$

where $\mathbf{x}$ is the state vector and $\dot{\mathbf{x}}$ its time derivative, $\mathbf{f}$ is the system dynamics function, $\mathbf{y}$ contains the measurements, $\mathbf{h}$ is the function defining the relationship between the state of the dynamic system and measurements, and $\boldsymbol{\delta}$ and $\boldsymbol{\varepsilon}$ are the process noise and the measurement noise, respectively. For the sake of simplicity, noises are modelled as zero-mean Guassian errors with covariances $\mathcal{Q}$ and $\mathcal{R}$, respectively.

The equations of the EKF can be written as:

$$\dot{\hat{\mathbf{x}}}(t) \simeq \mathbf{f}\left(\hat{\mathbf{x}}(t)\right) + \bar{\mathbf{K}}(t)\left[\mathbf{y}(t) - \hat{\mathbf{y}}(t)\right] \tag{6.19}$$

$$\hat{\mathbf{y}}(t) \simeq \mathbf{h}\left(\hat{\mathbf{x}}(t)\right) \tag{6.20}$$

$$\dot{\mathbf{P}}(t) \simeq \mathbf{F}(t)\mathbf{P}(t) + \mathbf{P}(t)\mathbf{F}^T(t) - \mathbf{P}(t)\mathbf{H}^T(t)\mathcal{R}^{-1}(t)\mathbf{H}(t)\mathbf{P}(t) + \mathcal{Q}(t) \tag{6.21}$$

$$\bar{\mathbf{K}}(t) = \mathbf{P}(t)\mathbf{H}^T(t)\mathcal{R}^{-1}(t) \tag{6.22}$$

where $\hat{\mathbf{x}}$ is the estimated state vector and $\dot{\hat{\mathbf{x}}}$ its time derivative, $\bar{\mathbf{K}}$ is the Kalman Gain, $\hat{\mathbf{y}}$ are the predicted measurements, $\mathbf{P}$ is the covariance matrix of the state estimation uncertainty (which is solved iteratively using fixed point iteration), $\mathbf{F}$ is the matrix of a continuous linear differential equation defining a dynamic system (obtained as the Jacobian of $\mathbf{f}$) and $\mathbf{H}$ is the measurement sensitivity matrix (defined as the Jacobian of $\mathbf{h}$). Note that the estate estimation (Eq. (6.19)) has a prediction correction structure, where the prediction is the system dynamics function $\mathbf{f}\left(\hat{\mathbf{x}}(t)\right)$ and the correction depends on the output error affected by the Kalman gain $\bar{\mathbf{K}}$. See Appendix D for more details.

In order to adopt the equations of the dynamics of a multibody system using matrix-R formulation, the state vector $\mathbf{x}$ is defined as:

$$\mathbf{x}^T = \left\{\mathbf{z}^T \quad \mathbf{w}^T\right\} \tag{6.23}$$

where $\mathbf{z}$ is the vector of independent coordinates and $\mathbf{w} = \dot{\mathbf{z}}$. The actual motion of the foot is acquired in the laboratory and processed as explained in Sections 4.2 and 4.3.

The histories of the ankle joint position coordinates and the three angles that orientate each segment with respect to the ground are the magnitudes of the virtual sensors of the plant.

Matrix $\mathbf{F}$ is described in Eq. (D.22), its expression depends on the multibody formulation used. Regarding matrix $\mathbf{H}$, it is defined as:

$$\mathbf{H}(t,\mathbf{x}) \equiv \frac{\partial \mathbf{h}(t,\mathbf{x})}{\partial \hat{\mathbf{x}}} = \left[\frac{\partial \mathbf{h}(t)}{\partial \hat{\mathbf{z}}} \quad \frac{\partial \mathbf{h}(t)}{\partial \hat{\mathbf{w}}} \right] = \left[\mathbf{H}^{\mathrm{Z}} \quad \mathbf{H}^{\mathrm{W}} \right] \tag{6.24}$$

Since the measurement vector contains directly the n_i coordinates of the state vector $\mathbf{x}$, $\mathbf{H}^{\mathrm{Z}}$ is defined as the $n_i \times n_i$ identity matrix and $\mathbf{H}^{\mathrm{W}}$ is a zero-matrix block.

The error covariance matrices $\mathcal{Q}$ and $\mathcal{R}$ need to be chosen (see Appendix D). To facilitate the tuning, both matrices are assumed to be diagonal, $\mathcal{Q} = \mathrm{diag}(\theta_{\mathrm{i}})$, $\mathcal{R} = \mathrm{diag}(\xi_{\mathrm{i}})$, or what is the same, errors are considered to be independent.

The $n_i \times n_i$ matrix $\mathcal{R}$ is the covariance of the zero mean noise $\boldsymbol{\varepsilon}$ in Eq. (6.18), which is related to the measurement errors. According to the expected error of the motion capture system, the covariance is fixed at $1\ \mathrm{mm}^2$ for the terms related to the position coordinates and is fixed at $1\ \mathrm{mrad}^2$ for the terms related to angular variables.

Concerning to the $2n_i \times 2n_i$ covariance matrix of the process noise $\boldsymbol{\delta}$:

$$\mathcal{Q} \equiv \begin{bmatrix} \mathcal{Q}^{\mathrm{Z}} & 0 \\ 0 & \mathcal{Q}^{\mathrm{W}} \end{bmatrix} \tag{6.25}$$

where $\mathcal{Q}^{\mathrm{Z}}$ is $n_i \times n_i$ and $\mathcal{Q}^{\mathrm{W}}$ is $n_i \times n_i$. The process noise $\boldsymbol{\delta}$ is not always easy to model and the components of $\mathcal{Q}$ are usually adjusted by trial and error [Cuadrado *et al.* 2009].

Finally, since the model and the sensors start from exactly the same initial condition, the initial uncertainty is zero at position and velocity levels, or what is the same, matrix $\mathbf{P}$ is initially zero $\left(\mathbf{P}(t=0) = \mathbf{0}\right)$. The state vector at initial time is also known $\left(\mathbf{x}(t_0)\right)$.

As said before, the EKF is used as a controller. The forward dynamic analysis uses wrenches, BSP and the foot-ground contact model as input information and, as a result, obtains the motion of the biomechanical system. However, both kinetic and kinematic information contain error and, moreover, the numerical procedures and the foot-ground contact model introduce uncertainties in the system. The Kalman filter provides a mean to infer the final motion from noisy measurements using the kinematics captured in the laboratory as a reference signal, ensuring that the resultant FDA kinematics is close to the one captured at the laboratory. The time step of the FDA is fixed at 1 ms (therefore, the sensors are available at each instant of time).

A simplified scheme of the procedure is shown in Figure 6.3. The real biomechanical model corresponds to the human model captured into the laboratory. The 'system dynamics' block represents the real-world model behaviour of the foot, being $\boldsymbol{\Gamma}$ the joint torques that actuate the musculo-skeletal system. This model can contain error that

is modelled through the process noise vector $\boldsymbol{\delta}$. As a result the motion of the biomechanical model is contained in the state vector $\mathbf{x}$. This information is captured through the 'sensor model' obtaining $\mathbf{y}$ (the kinematic values measured in the laboratory)

Regarding to the Kalman filter model, the 'state dynamics' contains a fairly faithful replication of the true system dynamics, in this case, a forward dynamic analysis of one foot. As a result $\hat{\mathbf{x}}(-)$ is obtained as the *a priori* estimate of $\mathbf{x}$ and the 'sensor model' allows us to virtually measure the kinematics obtained via the FDA, i.e., $\hat{\mathbf{y}}$. This vector can be compared with the laboratory measurements $\mathbf{y}$. The 'covariance dynamics' contains the Riccati equation (Eq. (6.21)), which lets us calculate the covariance matrix $\mathbf{P}$ and, using this information, the Kalman gain matrix $\bar{\mathbf{K}}$ can also be determined. Using all the available information (all the measurements and taking into account the Kalman correction) an *a posteriori* value of the 'estimated state' $\hat{\mathbf{x}}(+)$ is finally calculated.

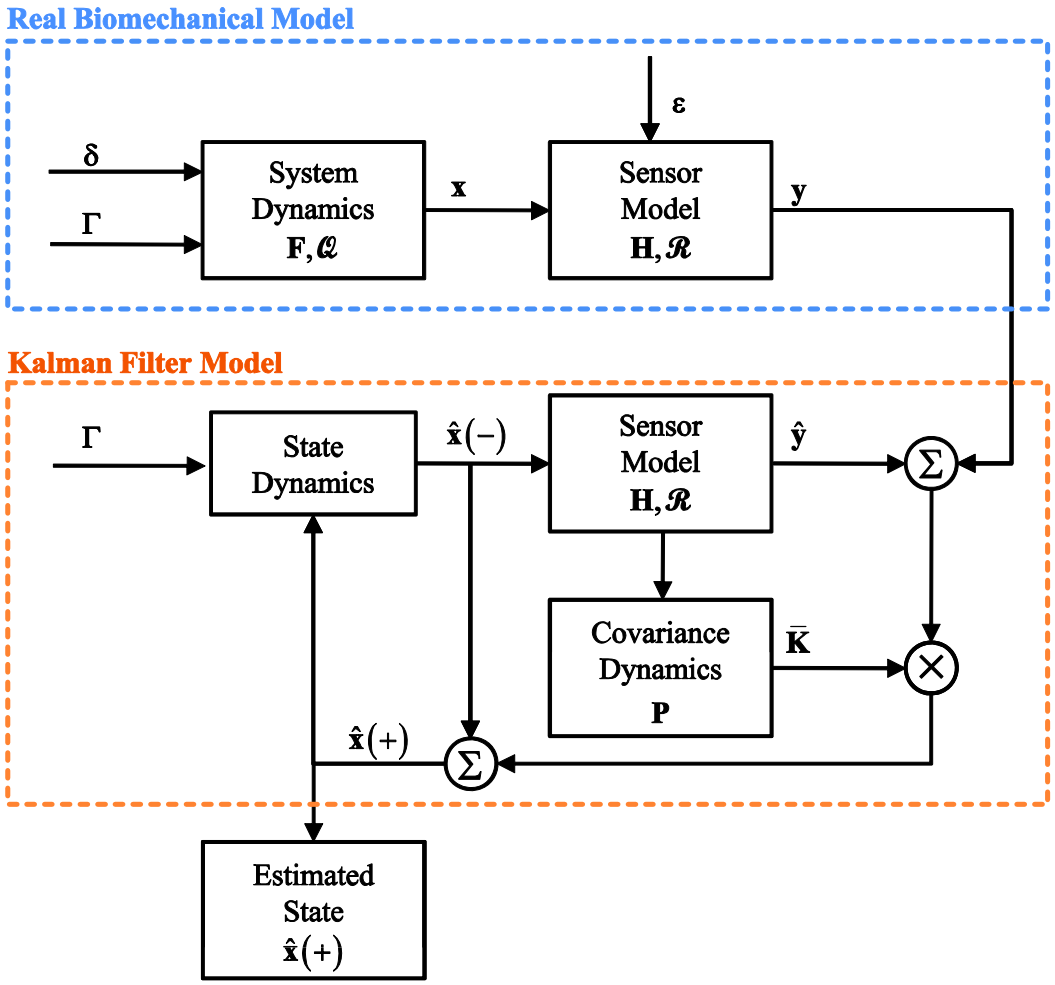

Figure 6.3 Schematic of Kalman filter implementation. Adapted from [Grewal and Andrews, 2008].

The Kalman filter, through matrices $\mathcal{Q}$ and $\mathcal{R}$, can be understood as a weigthing algorithm that compares the quality of the measurements against that of the current state estimate and then determines the correction that should be provided to the *a priori* state prediction.

6.3 Results

The foot model presented in Section 6.1 is the result of a compromise between the fidelity of the model and the cost of the simulation. To achieve the desired fidelity, four different models have been tested starting from the very simple one-sphere model. For each model, the inverse dynamics optimization approach is implemented in order to adjust the nine parameters of the sphere(s) to the force plate results. As a representation of these four models, the vertical foot-ground contact force has been plotted in Figure 6.4 and compared with the force plate data which are used as a reference signal to compute the RMSE and NRMSE.

Figure 6.4 shows that using a single sphere, a rough approximation of the vertical force can be obtained. Nevertheless, when the sphere contacts the floor it causes an abrupt change on the force (~800 N), which does not represent the force evolution during the actual contact. Moreover, using a sphere on the hindfoot segment has proved to be relevant in this study, since it leads to notably lower errors.

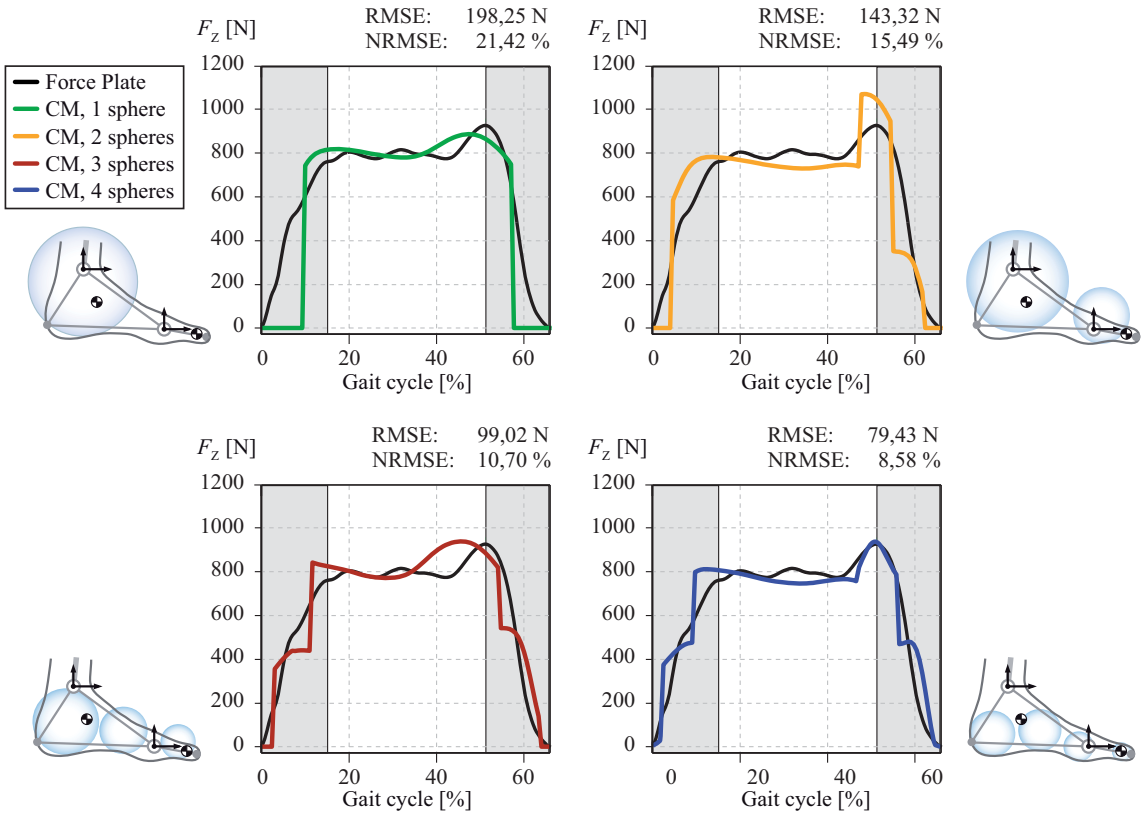

Figure 6.4 Comparison between foot-ground normal forces obtained from the force plate and from contact model optimization (CM).

As it can be seen in the plots, both the RMSE and NRMSE decrease when the number of spheres increases. However, the improvement between the model with three and four spheres is small. In fact, the two error indicators present similar values to the model with four spheres if more than four spheres are used. Therefore, the four-sphere model is used in the following sections.

6.3.1 Inverse Dynamic Approach Results

The optimization process is computed with a total of 72 design variables starting at the toe off of one foot, including one double support and finishing at the heel strike of the other foot (see Figure 4.7). Different weight vectors $\mathbf{h}$ are used to adjust each component of the external wrench applied to the multibody system. Figure 6.5 shows, for each component *j* of the wrench, the comparison between the foot-ground contact model ($\tilde{\mathbf{G}}^{\mathrm{gr}}_{\mathrm{CM}}$ in red) and the inverse dynamic results ($\tilde{\mathbf{G}}^{\mathrm{gr}}$ in blue), respectively when the weight vector used contains the unit at component *j* and is zero for the rest of the components $\mathbf{h} = \{h_{\mathrm{FX}},\ h_{\mathrm{FY}},\ h_{\mathrm{FZ}},\ h_{\mathrm{M}X},\ h_{\mathrm{M}Y},\ h_{\mathrm{MZ}}\}^T$. Note that the resultant force and moment are calculated at the projection of the lumbar joint onto the ground (see Chapter 4).

As error indicators, the RMSE and the NRMSE between the two wrench components are calculated. They are given at the top of each segment. The grey area corresponds to the double–support phase, in which the inverse dynamics can only provide the resultant force and moment due to both feet. In contrast, the contact model provides forces and moments for each foot.

Figure 6.5 shows several slope discontinuities, mainly due to the use of a discrete number of spheres instead of a continuous contact surface. The time step used by the motion capture system (10 ms), which is rather large for contact problems, further amplifies this problem, since every time a sphere enters or loses contact with the ground, a sudden force variation appears.

Moreover, the notable error present in the captured trajectories of the feet markers greatly affects the results, since, due to the nature of the contact model, small errors in the imposed feet trajectories might translate into large force variations.

Figure 6.5 shows that the tangential forces $(F_{\mathrm{X}}, F_{\mathrm{Y}})$ cannot be correctly modelled. It has not been possible to find a reasonably good set of tangential contact parameters. This problem is also present in Millard's work [Millard *et al.* 2008].

Note that if the use of the defined vector $\mathbf{h}$ (defined with the aim of optimizing each component separately) did not allow us to obtain a good agreement between each component individually, it is not expected that any vector $\mathbf{h}$ would give better results for the tangential components.

In order to identify the cause of the problem in the tangential forces, a new test is performed. The optimization procedure is computed for a single foot and using the force plate measurements as the reference signal. This new test eliminates the error introduced by the sharing method, and also the amount of error introduced by the whole-body inverse dynamic analysis. Moreover, only the force components (not the moments) have been included in the objective function. These results are presented in Figure 6.6.

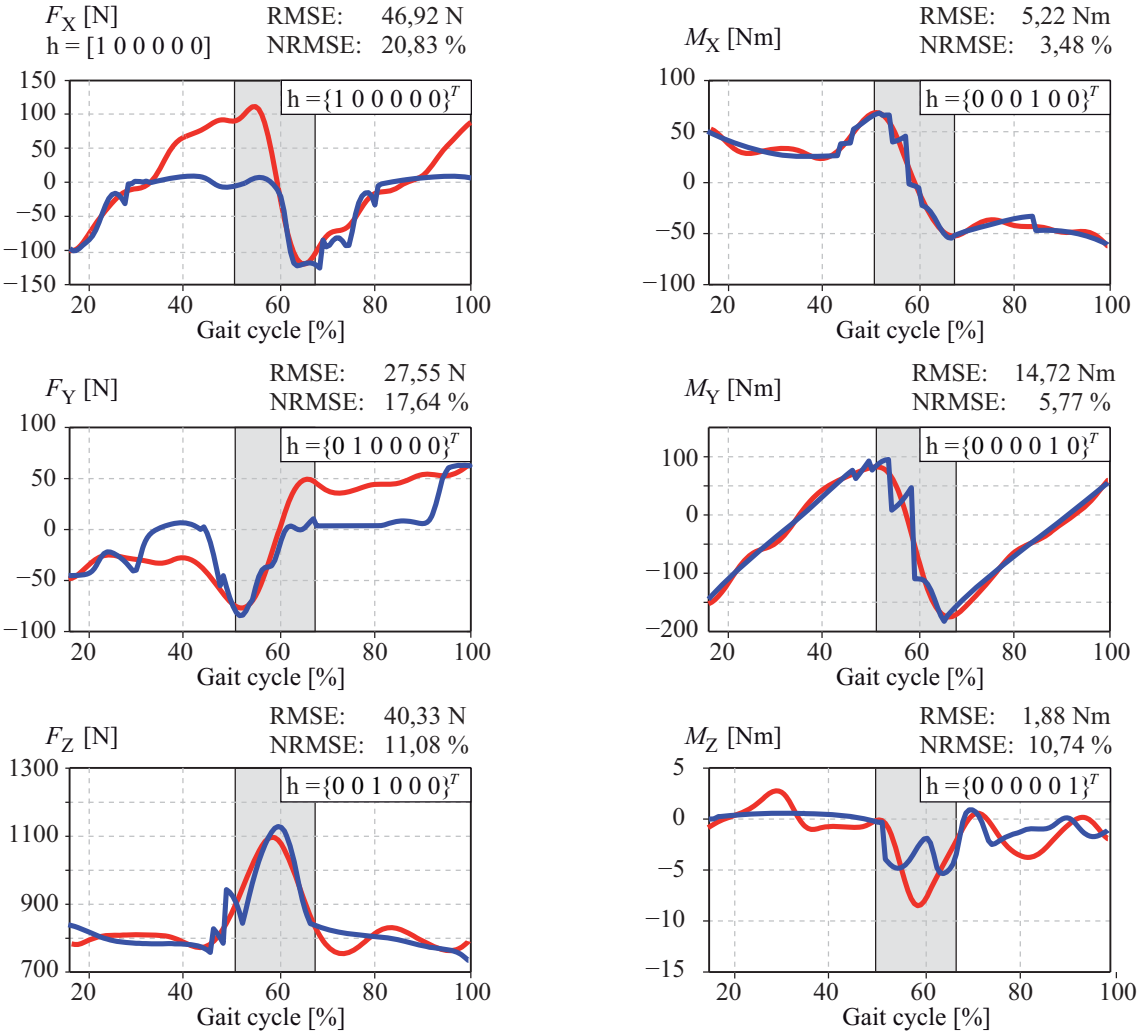

Figure 6.5 Comparison between foot-ground wrenches from inverse dynamics (ID) and contact model optimization (CM) for different weight vectors h.

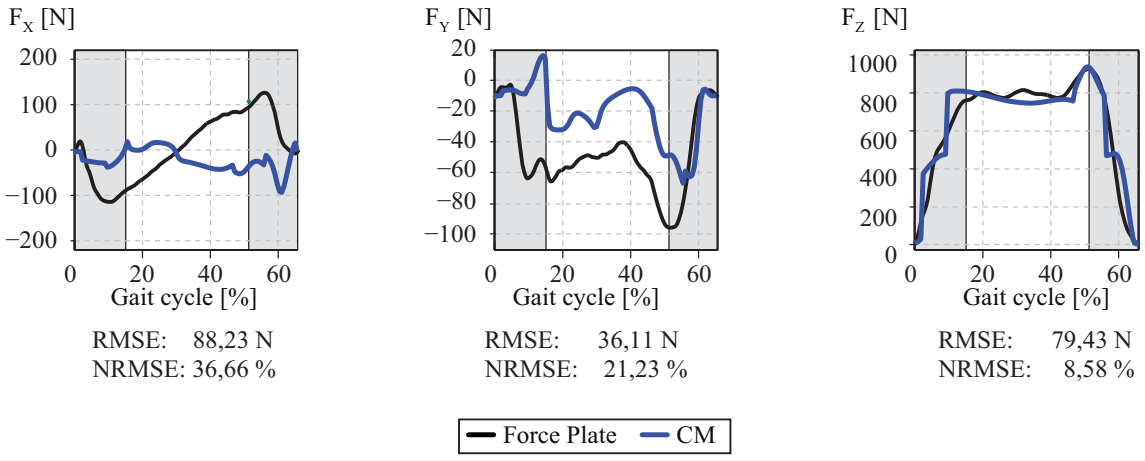

Figure 6.6 Comparison between foot-ground forces calculated via contact model optimization (CM) and force plate measurements (FPL).

Figure 6.6 shows that the solution obtained for the normal force F_Z significantly smaller normalized error than those obtained for the tangential directions, F_X, F_Y which do not represent the actual forces. However, these results may not be attributed to the model. The laboratory conditions and the equipment used do not guarantee an accurate measurement of the foot-ground interaction in the tangential direction. For example, in the studied motion the distance between two markers belonging to the same segment (forefoot and hindfoot) can vary more than 8 % in some cases (between 1,7 and 9,7 mm). The kinematic consistency procedure imposes a constant distance between joints, however, since the marker measurement have higher noise, the imposed history of the joint positions cannot be accurate enough and could invalidate the results of the inverse dynamic analysis, or what is the same, skin stretch can likely skew the data used to compute the analysis.

These results led to the conclusion that the motion capture system is not accurate enough for capturing feet deformation and that the tangential contact model is more sensible to skin motion errors than the normal one. Therefore, the results presented below are obtained using only the normal contact model.

Solving the Contact Force Sharing Problem during Double Support

A weight vector is chosen to take into account the normal force and the longitudinal and lateral torques $\mathbf{h} = \{0,\ 0,\ 1,\ 1,\ 1,\ 0\}^T$. The optimization process starts at the beginning of the single support of the right leg (~18 % of the gait cycle), shows the double support phase and finishes at the heel strike of the right foot (100 % of the gait cycle).

The simulation provides the values of the 40 design variables which best approximate the foot-ground contact wrenches to the inverse dynamics results. Note that since only the normal contact model is used in the optimization procedure, 5 design variables for each sphere are employed (instead of the initial 9 variables). The optimized parameters are summarized in Table 6.3.

Sphere 1	**Right Foot**	**Left Foot**	**Sphere 3**	**Right Foot**	**Left Foot**
r [m]	0,035	0,049	r [m]	0,050	0,070
x' [m]	–0,035	–0,017	x' [m]	0,138	0,138
y' [m]	0,010	–0,009	y' [m]	–0,020	0,028
$K \cdot 10^{-5}$ [Nm$^{-3/2}$]	0,283	0,465	$K \cdot 10^{-5}$ [Nm$^{-3/2}$]	0,181	0,177
c_r	0,005	0,174	c_r	1,000	0,948

Sphere 2	**Right Foot**	**Left Foot**	**Sphere 4**	**Right Foot**	**Left Foot**
r [m]	0,047	0,080	r [m]	0,032	0,040
x' [m]	0,074	0,027	x' [m]	0,043	0,052
y' [m]	–0,030	0,026	y' [m]	–0,005	0,005
$K \cdot 10^{-5}$ [Nm$^{-3/2}$]	0,245	0,263	$K \cdot 10^{-5}$ [Nm$^{-3/2}$]	0,382	0,298
c_r	1,000	0,328	c_r	1,000	0,819

Table 6.3 Optimized values for the design variables using the IDA approach.

Regarding efficiency, the optimization process that led to the presented results took a wall-clock time of around 14 seconds on an Intel Core i7 950 computer, and roughly required 12000 function evaluations, being these values representative of the general trend observed during the study.

Figure 6.7 shows the mentioned components of the resultant feet-ground wrench in blue. Torques are calculated, as previously, at the lumbar projection point (see Chapter 4). As a reference signal, the same components computed through inverse dynamics are plotted in red.

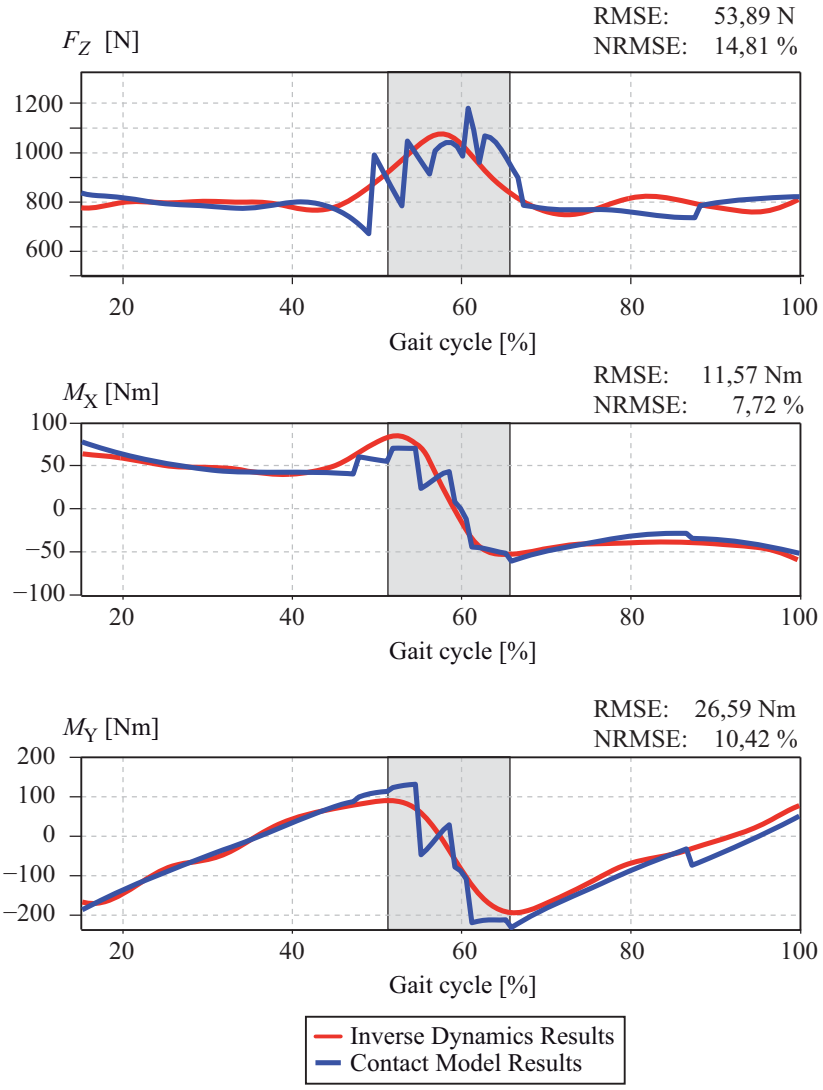

Figure 6.7 Foot-ground contact wrench: inverse dynamic results vs. contact model.

As expected, several slope discontinuities appear in the plots due to the use of spheres instead of a continuous contact surface. Moreover, during the double support phase, both feet contact the ground and more discontinuities appear during this phase. Even so, the foot-ground contact model provides a reasonably good dynamic response with a NRMSE less than 15 % with respect to the inverse dynamics results.

As explained in the beginning of this chapter, the proposed foot-ground contact model can be used to solve the sharing problem during the double support phase. Figures 6.8

and 6.9 show the results obtained from applying the three sharing strategies explained in this thesis, namely, corrected force plate (CFP), smooth transition assumption (STA) and contact model optimization (CM).

These results are compared to the force plate data (FPL), which are also plotted in these figures and are used as a reference to calculate the errors shown in Table 6.4. The torques at each foot are calculated with respect to their corresponding ankle joint. Note that, since the foot model only provides good results for the normal contact forces, only F_Z, M_X and M_Y results obtained via CM are plotted in these figures.

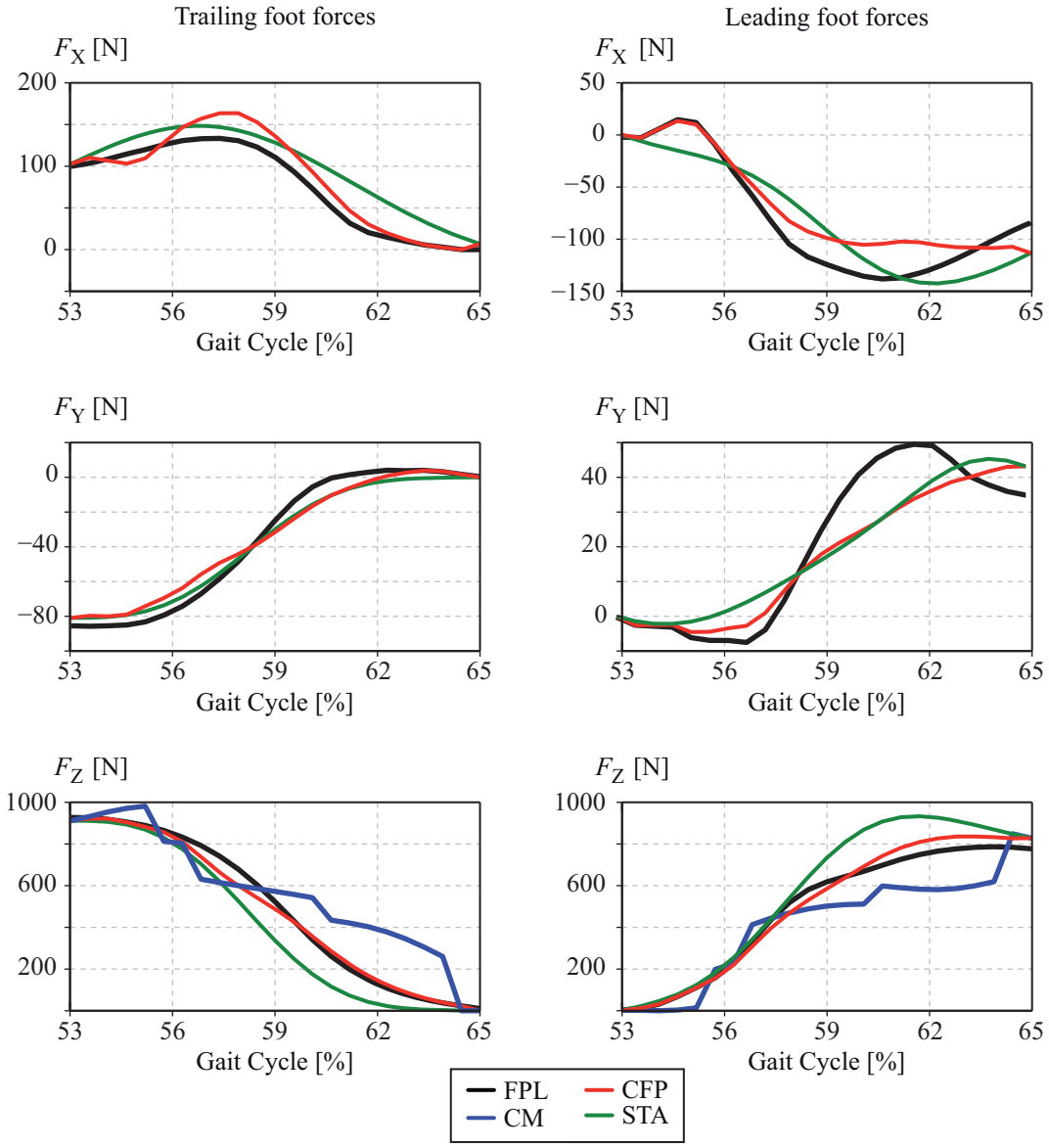

Figure 6.8 Foot-ground contact forces: reference (FPL, force plates) vs. sharing methods: Contact Force Plate (CFP), Contact Model (CM) and Smooth Transition Assumption (STA).

Figures 6.8 and 6.9 illustrate the second double support of the captured gait (from 53 % until 65 % of the gait cycle). They are a complement to Figures 4.13 and 4.14, where foot-ground contact forces for 116 % of a gait cycle were illustrated when CFP and

STA sharing methods were used, in order to show in detail the evolution of the forces and moments during this phase.

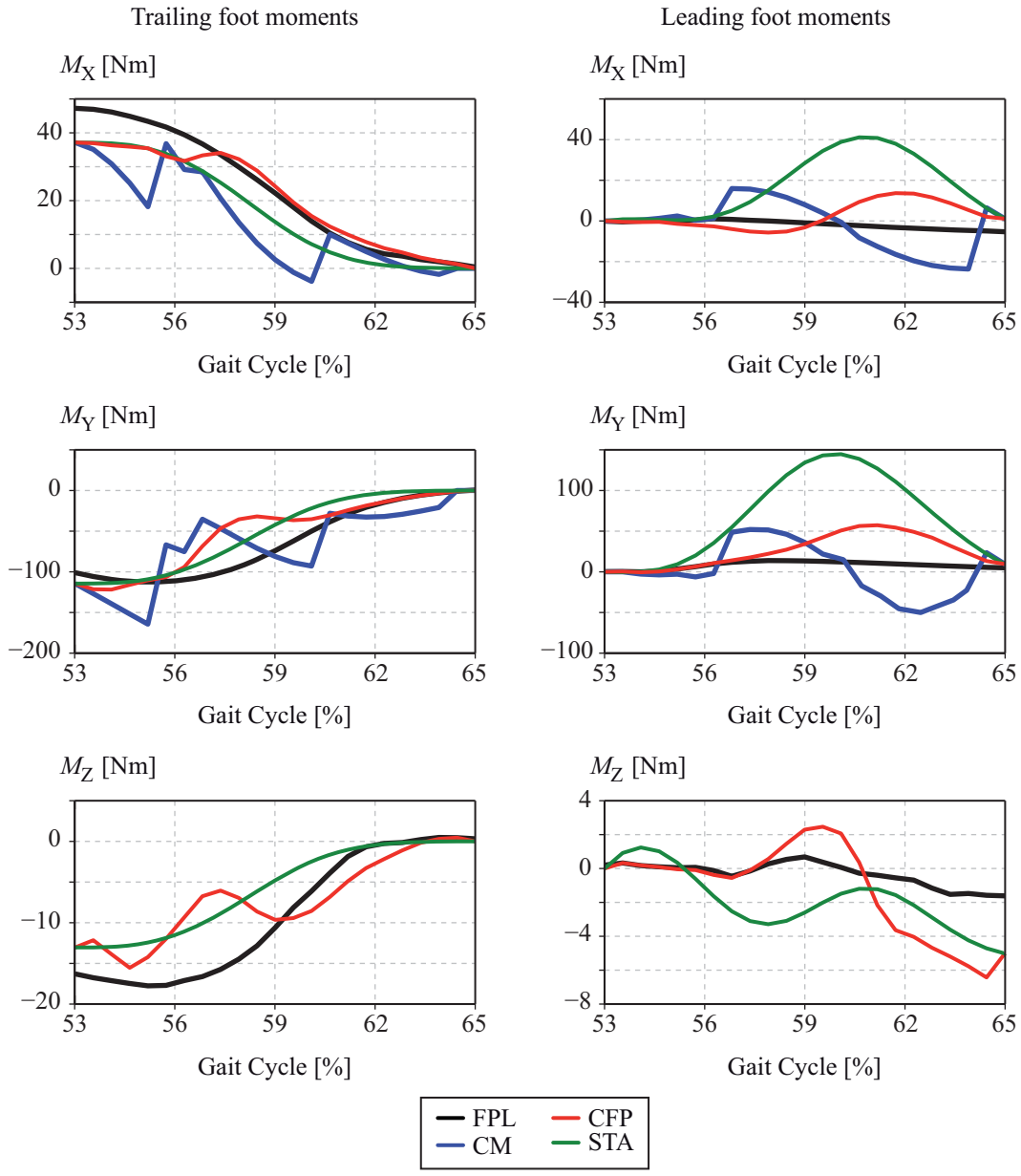

Figure 6.9 Foot-ground contact moments: reference FPL, force plates) vs. sharing methods: Contact Force Plate (CFP), Contact Model (CM) and Smooth Transition Assumption (STA).

Method	Foot	F_X [N]	F_Y [N]	F_Z [N]	M_X [Nm]	M_Y [Nm]	M_Z [Nm]
CFP	Trailing	9,011	12,557	35,746	10,122	20,838	5,277
	Leading	10,467	8,148	27,432	6,014	12,963	1,879
STA	Trailing	39,383	7,166	71,764	9,908	13,465	4,011
	Leading	31,541	14,234	74,961	16,257	43,869	2,315
CM	Trailing	--	--	158,018	12,893	32,770	--
	Leading	--	--	111,343	11,248	36,643	--

Table 6.4 RMSE during double stance for the different reaction sharing methods.

The results obtained using the CFP and STA have been already discussed in Chapter 4. Regarding the contact model optimization (CM), the errors in the normal force are slightly higher than those obtained by the STA, whereas the moments at the leading foot are, at least from the RMSE point of view, much better than those obtained by the STA.

Furthermore, using the foot-ground contact model, the inverse dynamic analysis can be calculated over a complete gait cycle using only kinematic measurements. It must be noted that, without the solution of the tangential problem, the CM method cannot calculate the tangential forces and the vertical moment, necessary for obtaining the motor torques. Moreover, the use of a set of spheres instead of a continuous contact model produces several slope discontinuities that do not represent the physical phenomenon of the contact.

6.3.2 Forward Dynamics Approach Results

The EKF has been implemented as a controller and a forward dynamic analysis has been performed using a foot model. Figure 6.10 shows the obtained motion (in blue) which can be compared with the actual one (in red). As representative coordinates of the biomechanical model, the right ankle position (numbered as joint 13 in Figure 3.5) (x_{13}, y_{13}, z_{13}) and the absolute angles of the hindfoot $(\alpha_{RHF}, \beta_{RHF}, \gamma_{RHF})$ are plotted in this figure. The graphs show the whole range in which a foot is in contact with the ground, from heel strike until toe off (approximately 60 % of the gait cycle). Note that, at the initial frame, the positions and the angular variables of the simulated motion perfectly match with the actual motion, since the simulated motion starts at the same initial conditions (position and velocity) of the actual captured movement.

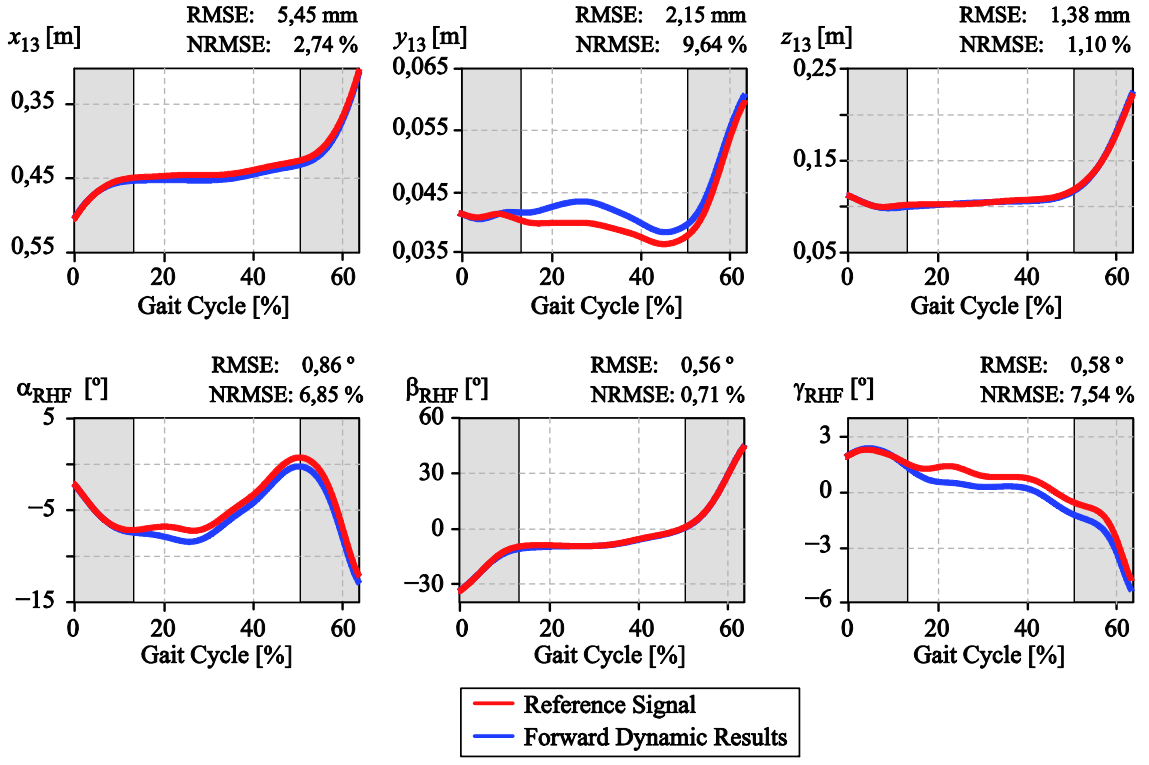

Figure 6.10 Comparision between the ankle position of the hindfoot angles. In red, the reference signal (motion capture) and, in blue, the results obtained via the FDA.

The results are obtained using the vector $\mathbf{h} = \{0,\ 0,\ 1,\ 1,\ 1,\ 0\}^T$ in Eq. (6.15). As in the inverse dynamics approach, the optimization is performed optimizing the normal component of the contact force F_Z and the horizontal torques M_X and M_Y.

Comparing the two curves in the plots of Figure 6.10, it can be observed a very good correlation, i.e., the results are very similar. We conclude, therefore, that the final movement obtained by forward dynamic simulation is very similar to the original. The largest normalized square error is obtained in the y_{13} component of the ankle position with a value of NRMSE=9,64 %. However, in absolute terms, this error only represents a RMSE = 2,15 mm. The maximum error (in RMSE) never exceeds 6 mm in position and in the case of the angles errors are less than 1º.

These results can be compared with [Millard *et al.* 2008], where each joint is actuated using a proportional-derivative controller. In this work, the ankle joint angle obtained through a FDA is quite different from the reference signal, with a peack of error near 30º.

In this approach, the simulation provides the values of the 20 design variables that best approximate the foot-ground contact wrench to the force plate measurements. They are summarized in Table 6.5.

As expected, these results differ from the ones obtained using the IDA (see Table 6.3). However, it must be noted that the values of the design variables have the same order of magnitude in both approaches.

Regarding the dynamic results, Figure 6.11 shows the results related to the normal contact force of the foot model that is the vertical component of the force (F_Z) and the horizontal components of the torque at the ankle joint $(M_X$ and $M_Y)$.

Sphere 1		**Sphere 3**	
r [m]	0,051	r [m]	0,030
x'[m]	–0,020	x'[m]	0,298
y' [m]	–0,005	y' [m]	–0,030
$K{\cdot}10^{-5}$[Nm$^{-3/2}$]	0,754	$K{\cdot}10^{-5}$[Nm$^{-3/2}$]	0,031
c_r	0,080	c_r	0,870
Sphere 2		**Sphere 4**	
r [m]	0,070	r [m]	0,012
x'[m]	0,032	x'[m]	0,035
y' [m]	0,046	y' [m]	–0,007
$K{\cdot}10^{-5}$[Nm$^{-3/2}$]	0,487	$K{\cdot}10^{-5}$[Nm$^{-3/2}$]	0,252
c_r	0,312	c_r	0,870

Table 6.5 Optimized values for the design variables of the foot-ground contact model.

Figure 6.11 shows that the trend of the foot-ground contact model results (in blue) is really similar to that of the force plate measurements (in read). However, in relative terms, the standard errors are between 12 and 20 %, and in absolute terms (RMSE)

more than 100 N is obtained for the vertical force, an error about 10 Nm for M_X and almost 24 Nm for M_Y. These error magnitudes are similar to the ones obtained using the inverse dynamics approach (see Figure 6.7). Nevertheless, the forward dynamic approach presents a smoother behaviour, and the slope discontinuities have been reduced.

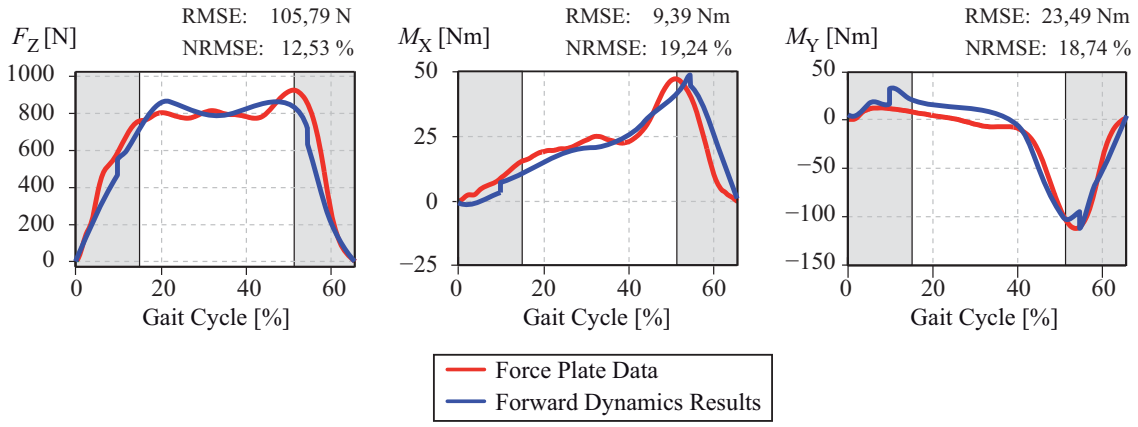

Figure 6.11 Wrench of the contact forces at the ankle joint. In red, the values of the force plate devices and, in blue, the results obtained via the FDA.

The calculated normal force can be compared with the results obtained by Millard et al. (2008) (Note that there are no studies in the literature showing the results for the horizontal moment components). This study uses the model proposed by Gonthier *et al.* (2004) to model the normal force. Although no error indicator is calculated in this work, the graphical representation of the normal contact force using a planar foot-ground contact model (obtained in a slow walk cadence) can be compared with Figure 6.11. From the visual examination of the plots, it can be concluded that the model proposed in this thesis matches better the experimental results than Millard's work.

6.4 Discussion

A novel foot-ground contact model based on spheres has been presented in this chapter. An optimization procedure has been implemented using two approaches: the inverse dynamics approach is computed in order to determine the parameters of a force contact model that produces the same foot-ground contact wrenches than those estimated from inverse dynamics and to solve the sharing problem during the double support phase. The forward dynamics approach is used to determine the contact model parameters that minimize the differences between the force plate data and the contact model reactions.

The normal and the tangential forces have been separately discussed. The contact surface and normal force parameters have been considered as design variables, being the normal foot-ground contact force and the horizontal components of the contact moment the magnitudes whose error has been minimized.

The agreement between the simulation and the actual values is validated through examining the quality of the match between the ground reaction forces developed at the simulated foot and the ones measured by means of the force plates or calculated via IDA, depending on the approach. The RMSE and the NRMSE have been used as error indicators.

The proposed model has shown a good correlation with measurements taken from force plates, and the computational times required have been kept moderated. Regarding efficiency, the inverse dynamic optimization process took a wall–clock time of around 14 seconds on an Intel Core i7 950 computer, and roughly required 12 000 function evaluations. In the second approach (forward dynamic) more than 2,5 hours have been required (using the same computer) and 10 000 function evaluations were needed.

The two approaches need to be discussed separately:

In the first case (inverse dynamics), the model is also used to solve the sharing problem during the double support phase in human gait. Thus, a method that does not require the availability of force plate measurements to solve this problem is presented. However, the bristle friction model used does not provide good results and the sharing problem is only solved for the vertical force and the moments in the horizontal plane. It remains unclear if the friction model is inadequate to represent the foot-ground contact or if the measurements of the feet markers position are inaccurate to capture the stick-slip phenomena (which are taken into account in the model).

The notable error present in the captured trajectories of the feet markers greatly affects the results, since small errors in the imposed trajectories might translate into large force variations. It should be noted that the method is not intended for identifying the physical parameters of the foot–ground contact, something that would require a much more precise motion capture system, suited to the smaller scale of the contact problem.

The normal contact model yields a force value that depends on the sphere indentation and its time derivative. In the tangential direction, when no sliding occurs –as in this case–, the bristle model is dominant, and it essentially consists of a linear spring–damper pair which depends on the bristle deformation. The main difference between the normal and tangential models is that the normal model can modify the indentation by adjusting the position and size of the contact spheres, whereas the bristle deformation of the tangential model is mostly imposed by the motion. Therefore, if the amount of error in the position of the underlying rigid body is too high, the tangential model cannot be properly adjusted.

Although the presented model allows the partial solution of the double support sharing problem, the characterization of a foot–ground contact model by means of inverse dynamics using the typical motion capture system does not seem to be the most appropriate path to follow, due to the high influence of skin motion in the quality of the results.

Regarding to the forward dynamics approach, the use of a single foot has been necessary in order not to spend large computational time. The same design variables have been adjusted and, moreover, the predicted motion provided by the forward dynamics optimization is very close to the captured motion. This second approach properly reproduces the foot-ground contact wrench for the normal force and the horizontal components of the torque. The concordance between the contact wrench obtained in the simulation and the experimental values measured using the force plate validates the presented model.

The good correlation of the results suggests that the proposed contact model could be use in a forward dynamic analysis (using the whole-body model) in order to address the prediction of human motion. The tangential force has a lower degree of agreement with experimental data. It is therefore proposed as future work to better adjust the modelling of this force.

Chapter 7

Conclusions and Future Work

All the multibody dynamics techniques presented in this thesis are aimed at achieving a 3D biomechanical model of the human body in order to study the dynamics of the human gait in healthy subjects.

It is important to remark that the thesis is developed in the context of a new research line on Biomechanics in the Department of Mechanical Engineering of the Technical University of Catalonia. Therefore, the laboratory setup, the process of learning how to use the new equipment, and the review of the state of the art have represented a great challenge to get experience in the biomechanics field.

7.1 Conclusions

In this thesis, a multibody methodology for the three-dimensional dynamic analysis of human gait has been implemented. The inverse dynamics problem is addressed with the aim of calculating the musculoskeletal forces developed at the anatomical joints of the human body while performing a prescribed movement. The forward dynamic analysis is aimed at predicting the response of the human body when subjected to the musculoskeletal forces calculated through the inverse dynamic analysis. In this case, a suitable foot-ground contact model is needed.

The main conclusions that can be extracted from this thesis are described below. They are structured in the following subsections:

Inverse and forward dynamic results

Kinematic information and body segment parameters (BSP) are used as input data to perform an inverse dynamic analysis of human gait using a general 3D model formed by 18 rigid bodies and with a total of 54 degrees of freedom. According to the procedure explained in Chapter 4, in a first stage the inverse dynamics yields the total external contact forces and moments acting on the pelvis of the subject during gait. However, this wrench is fictitious, since in reality no contact force or moment acts on the pelvis during gait. Therefore, in order to obtain the joint motor torques, the wrench must act on its actual location, i.e., the contacting foot/feet.

During the single support phase, the problem is determined, so that, the wrench can be translated to the contacting foot, and the motor torques are derived by equating the corresponding generalized forces to those obtained when the contact forces are characterised at the pelvis. However, during the double support phase, a reaction sharing criterion must be used for estimating the amount of the total wrench assigned to each foot (and afterwards the motor torques can be again calculated by equating the generalized forces). A new sharing criterion is presented in this thesis. It uses force plate

measurements to obtain a set of joint torques and external forces acting on the feet which are dynamically consistent with the captured motion. The method is named corrected force plates sharing (CFP).

In the laboratory, the external contact wrench is measured using force plate devices. However, the resultant contact wrench calculated via IDA and the one obtained through the force plates (translated to the same point) do not coincide. This means that the inverse dynamics results are inconsistent with the force plate measurements. However, these force plate measurements can still be used as an input for the solution of the double support problem, since their shapes contain information on how the total reaction is transferred from the trailing foot to the leading foot. The aim of the CFP sharing method proposed is to combine the inverse dynamics contact wrench with the measured foot-ground interaction in order to obtain each foot-ground contact reactions without modifying the captured motion. Therefore, in order to preserve the kinematics and obtaining a set of dynamically consistent data, a simpler alternative method is presented.

The CFP method is compared with another method which does not require the availability of force plate information, namely the smooth transition assumption (STA), and with the force plate data used as reference signals (when they are available). The results show that the error of CFP, in RMSE and NRMSE terms, is in most cases lower than that of STA.

In contrast to STA, the presented approach can be applied not only for a normal gait but also for pathological cases when the duration of the double support phase represents a relevant part of the full gait period or when the gait pattern is altered. The method can be understood, for a generic 3D gait motion, as the best approximation possible to compute an IDA without modifying neither the model parameters nor the motion.

Note that another advantage of the proposed methodology is that a set of wrenches dynamically consistent with the biomechanical model are obtained with no need neither to modify the motion nor to add residual wrenhces. After solving the sharing problem using the CFP method, all the joint torques are calculated. It has been swhon that the obtained results present a good correlation when compared with results published in the literature.

The IDA results obtained via the new method are used as inputs of a forward dynamic problem, obtaining good simulation results until 80 % of the gait cycle without using any type of controller. The instability of the system can be related to numerical errors and to errors in the integration of the motion equations. To improve the results until 100 % of the gait cycle, a simple PD controller has been implemented and its dynamic effect is shown to be really low, providing a way to easily control the biomechanical system during the forward dynamic simulations.

As a conclusion, the presented results confirm that the techniques described can be successfully applied to the inverse and forward dynamic analysis of the human body motion.

Uncertainties in the inverse dynamic analysis

The inverse dynamics analysis of the human motion is reviewed so as to identify the effect of different sources of error in the results. A sensitivity analysis is carried out using a 2D model formed by 14 segments (with 16 degrees of freedom) in order to asses the importance of the accuracy of the input data.

Three different errors in IDA input data are studied. Firstly, with the purpose of modelling the error present in body segment parameters estimation –due to inaccurate measurements or the use of standard parameters–, zero-mean Gaussian errors have been added to their actual values. Secondly, two different weighting matrices have been used to simulate different data sets obtained during the kinematic reconstruction process. Finally, to quantify the error when inaccurate force plate measurements are used, ground reaction forces are perturbed by adding an error proportional to its full scale output, which is the case in commercial force plates.

The results show that errors in input data influence differently the resultant joint moments in both the swing and stance legs. Significant differences are detected between RMSE and NRMSE in the results of each leg: RMSE values are higher in the results of the stance leg and NRMSE values are higher in the swing leg torques.

The study of uncertainties in BSP differs from those in the literature because this work does not compare the effect of using one or another anthropometric BSP table, and does not determine how an error in a single BSP can affect the IDA results. The error statistical modelling allows us to simulate the real inaccuracies that can appear when anthropometric BSP are estimated. Inaccuracies are always present in the BSP estimation, and they appear in all segments at the same time. Moreover, in the study the BSP are perturbed taking into account that the total body mass and height of the subject remain always constant, an assumption that is used in the experimental procedure in most laboratories. Therefore, the tables presented in Chapter 5 summarize the expected errors that cannot be avoided in an experimental procedure of gait analysis.

The study of errors in BSP allows us to conclude that errors in the moments of inertia have little effect in the IDA results, and compared to the other cases analyzed, these inaccuracies are almost negligible. The most affected torque is the swing leg knee, where a mean NRMSE of 0,7 % (with a peak of 3 %) is obtained when the moments of inertia are perturbed with maximum errors of ±10 % . These error magnitudes lead to the conclusion that uncertainties in the moments of inertia have little influence in the gait analysis results.

In contrast, the process to obtain kinematic consistent data can introduce large errors in the IDA results. There exist different methods to ensure the kinematic consistency; however, all these methods change the initial estimated joint positions in order to ensure the rigid body assumption. The technique applied in this thesis to obtain a new set of kinematically consistent data requires the definition of a weighting matrix **W**, which accounts for different accuracies in the measurement of marker position (due to soft tissue artifacts). The study shows that the IDA results are highly sensitive to the weighting matrix used. The RMSE values obtained using different (and plausible) weighting matrices are almost one order of magnitude above the mean RMSE obtained

with BSP perturbations. The NRMSE in the swing leg hip moment can be close to 20 %, an amount that is non-acceptable for a gait analysis. Moreover, there are no studies in the literature describing how this matrix can be exactly defined; therefore it is difficult to estimate the weight factors. A new work in this way can be a key to improve the IDA results.

Note that these results highlight the influence of little variations at joint positions in the IDA results (which are related to the marker protocol used and how the anatomical joints have been identified). These variations are inherent in all kinematic data reconstruction methods published in the literature. This leads to the conclusion that all the kinematic procedures (from marker position, including filtering, identification of joints position and kinematic consistency processing) need to be studied further in order to improve the results.

Finally, the results presented in Chapter 5 show that the net joint torques are highly sensitive to errors in the force plate measurements, which are amplified along the stance leg (if they are used as input data applying the conventional scheme that involves the iterative solution of the Newton-Euler equations of motion for each body segment starting from the foot up to the trunk). The errors in each component of the ground reaction forces have different effects in the net joint torques. The main effect is produced by the horizontal component of the ground reaction force (both in terms of absolute and relative errors): a 2 % FSO error in this component causes a NRMSE of 5,85 % in the knee joint, which grows up to more than 43 % in the hip joint torque.

The study shows that BSP errors produce smaller RMSE and NRMSE than those which occur if the kinematic processing is not adequate and when errors are presented in the foot-ground wrench. In conclusion, in order to improve the quality of the IDA results the kinematic data processing needs to be studied further and effort must be focused on obtaining more accurate force plate data.

Foot-ground contact model

A novel 3D continuous foot-ground contact model is used to describe the contact between the foot and the ground in a normal human gait. The foot is divided into two segments, hindfoot and forefoot, and the relative rotations between them are modelled through a spherical joint. The sole surface is approximated using a set of spheres. The total contact force is divided into the normal and tangential components. The normal component follows the model proposed by Lankarani and Nikravesh (1990) and the tangential component of the contact forces follows the bristle–type model proposed by Dopico *et al*. (2011).

Note that, unlike most models found in the literature, the presented model is a three-dimensional model that allows us to calculate the whole components of the foot-ground contact wrench (three force components and three moment components) as a function of the system state. Moreover, it must be said that modelling the foot as two segments proved to be relevant: a single segment foot model was also tested but it led to notably higher errors in all the analyses.

The characterization of the mechanical properties and geometry of contacting surfaces has been implemented using two optimization approaches based on inverse and forward dynamic analysis respectively, being the normal foot-ground contact force and the horizontal components of the contact moment the magnitudes whose error has been minimized.

Using the values of the design variables obtained through the inverse dynamic optimization approach, the foot-ground contact model is used to solve the sharing problem during the double support phase in human gait. As expected, several slope discontinuities in the results are obtained due to the use of spheres instead of a continuous contact surface. Nevertheless, the foot-ground contact model can provide a dynamic response with a NRMSE lower than 15 % (in the normal force component) with respect to the inverse dynamic results.

Regarding the tangential model, the bristle-friction model parameters cannot be adequately adjusted to reproduce the actual tangential foot-ground contact force. The comparison between foot-ground forces calculated via contact model optimization and using force plate measurements reveals that the NRMSE obtained for the normal force F_Z (NRMSE=8,58 %), is significantly smaller than those obtained for the tangential components, F_X, F_Y (NRMSE=36,66 % and NRMSE 21,23 %, respectively). As a result, the sharing problem is only solved for the moments in the horizontal plane and for the vertical force. The characterization of the presented model using the typical motion capture system (based on capturing the evolution of a set of markers attached to the body) does not seem to be the most appropriate path to follow. The skin motion artifact has a high impact in the quality of the results.

The results obtained via the forward dynamic optimization approach adequately reproduce the foot kinematics and the contact wrench for the normal force and the horizontal components of the torque. As in the first approach, the tangential force has a lower degree of agreement with experimental data than the normal force. This second approach presents a smoother behaviour, and the slope discontinuities have been reduced.

As a conclusion, the good correlation of the results suggests that the proposed contact model could be useful in a forward dynamic analysis (using the whole-body model) in order to address the prediction of human walking motion (see future work section).

Finally, although each optimization approach leads to different results in the design variables, they have the same order of magnitude. It must be remarked that the use of the same model in both, forward and inverse analyses, is something new in the field of biomechanics of multibody systems.

7.2 Future Work

This section contains the main research lines that are identified for future developments.

- When specific details of the joint motion are the object of study, the kinematic structure used in the biomechanical models can not be enough. With the aim of

solving this problem, a detailed model of some joints (such as knee or ankle) can be integrated in the whole-body model introducing the geometry and the anatomical properties of the joints. Moreover, these changes in the joint definition can improve the accuracy of the results in inverse and forward dynamic simulations.

- The analysis of the input data uncertainties in an IDA reveals the importance of improving the kinematic data processing. In this way, another important development that can be introduced is a new methodology to improve estimates of segment kinematics from measured marker trajectories. With this aim, some different strategies are present in the literature such as the global optimization method, Kalman filter techniques or local marker estimation. However there is no agreement in the way to obtain the best kinematic procedure.

- Similarly, the high sensitivity of some errors to force plate data when this information is used as input data in an IDA, revelas that the acquisition procedure using these devices could be improved.

- Regarding the foot-ground contact model a new approach can be developed. Since the foot is formed by a large number of bones and soft tissues are present in the heel, a new approach based on a group of segments modelled as a flexible body would be an alternative modelling technique. This detailed description can be of great importance in the simulation of the foot impact since it could increase the accuracy and reliability of the model.

- The forward dynamic analysis performed in this thesis can be seen as a first step in the field of motion prediction. Therefore, the implementation of the whole-body model using the developed methodology is an imminent future work line. A tool allowing predicting the motion of real subjects under some virtual condition would be of great help to anticipate the results of surgery or to assist the design of prosthetic/orthotic devices.

- Both the inverse and forward dynamics problems have been addressed considering the actuation at joint level (torques and forces at the joints). However, the joint torques are the result of the neuro-muscular actuation. Therefore, the model can be improved including the muscles and tendons definition. This procedure involves the selection of the relevant muscles, the attachment points of the musculotendon units that actuate the human model and the selection of the mathematical model of the muscle (and its parameters).

- Since several muscles serve each joint of the skeletal system, muscle forces cannot be directly computed from joint moments. This is the well-known redundant actuator problem in biomechanics. In order to solve this problem, optimization procedures need to be implemented. Several optimization methods are available in the literature. Also, different choices can be found for the design variables (muscle forces, muscle activations, neural excitations) and for their mathematical description. Therefore, the different alternatives can be studied and the most appropriate ones considering the computational cost and the numerical robustness can be selected and implemented and the results can be

qualitatively compared using EMG signals (the calculated muscle activations and muscle forces can be contrasted with the measured and processed muscle activations).

- Since the presented 3D model is developed using a generic multibody formulation, it can be used to study different human motions other than walking. In this way, the application of the methodology in different tasks such as running, jumping, dancing, etc. can be developed. Moreover, the human model can be also used in different areas of study such as ergonomics, biomedical design or physical rehabilitation.

Appendix A

Definition of Local Unit Vectors and Joint Positions

This Appendix contains the analytical expressions used to calculate the joint positions and the segment unit vectors from the captured marker positions. Figure A.1 shows the marker's and the joint's identification and Figure A.2 shows the segment unit vectors. Finally, Table A.1 contains the mathematical expressions for both, joint positions and segments unit vectors.

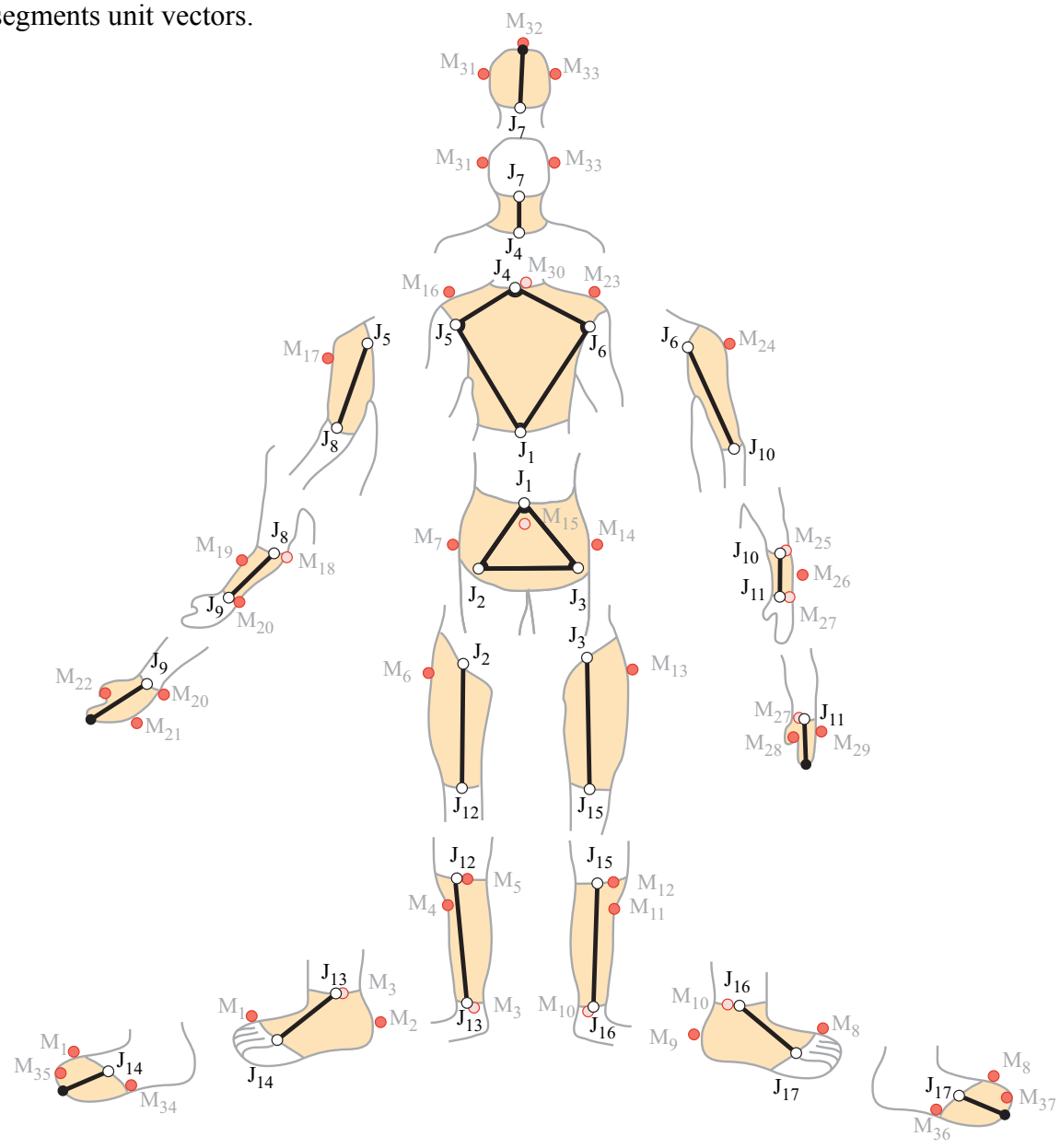

Figure A.1 Human body model Segments, joints and markers identifications.

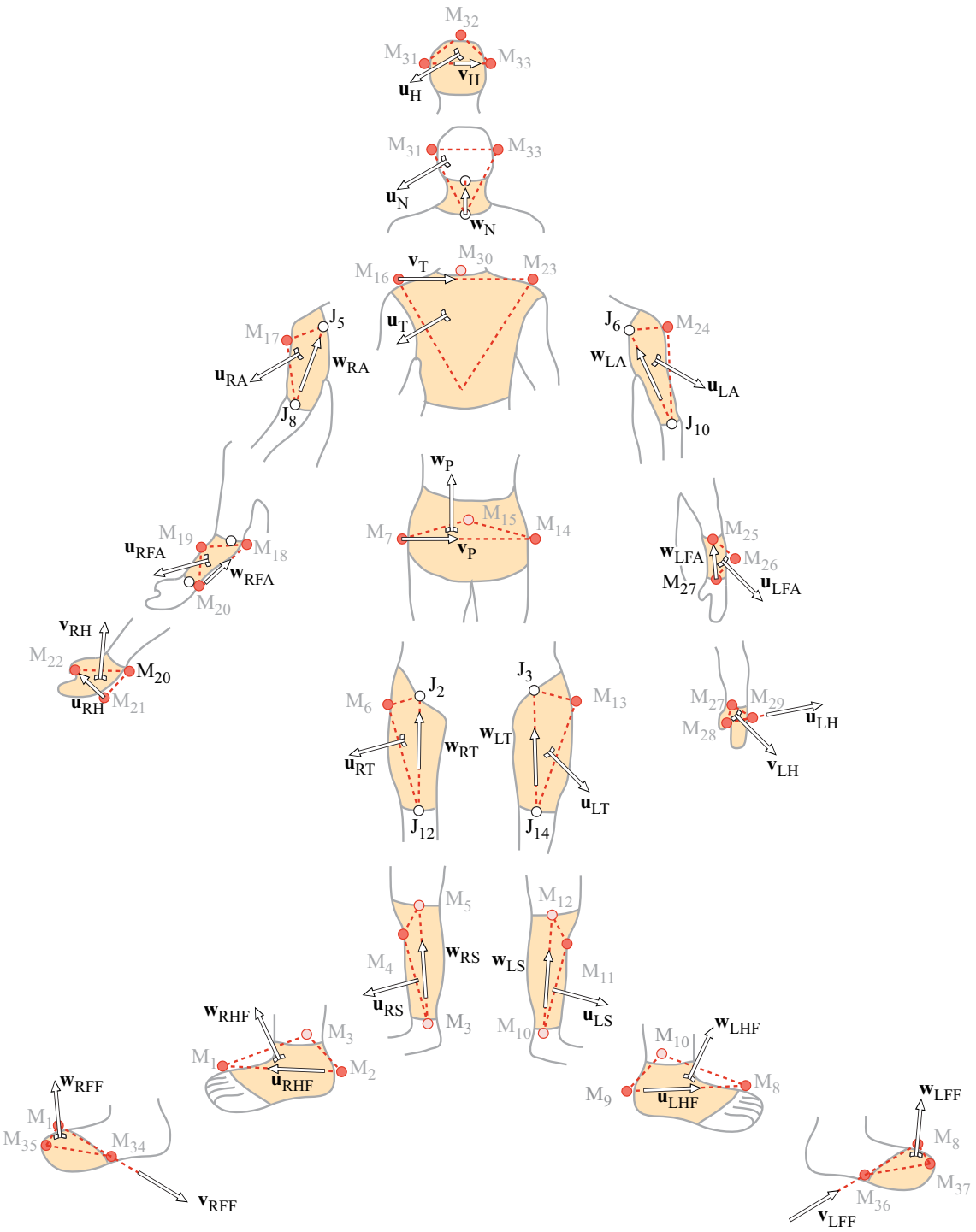

Figure A.2 Unit vectors of the segments.

Right forefoot (RFF)

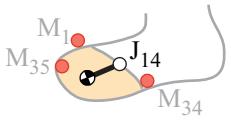

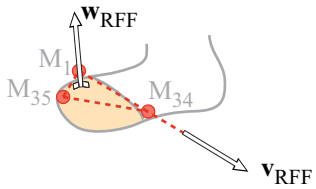

$$\mathbf{r}_{J14} = 0,95\mathbf{r}_{M34} + 0,05\mathbf{r}_{M1} - 0,015\mathbf{w}_{RFF}$$

$$\mathbf{u}_{RFF} = \mathbf{v}_{RFF} \wedge \mathbf{w}_{RFF} \qquad \mathbf{v}_{RFF} = (\mathbf{r}_{M34} - \mathbf{r}_{M1}) / |\mathbf{r}_{M34} - \mathbf{r}_{M1}|$$

$$\mathbf{w}_{RFF} = (\mathbf{r}_{M35} - \mathbf{r}_{M1}) \wedge (\mathbf{r}_{M34} - \mathbf{r}_{M1}) / |(\mathbf{r}_{M35} - \mathbf{r}_{M1}) \wedge (\mathbf{r}_{M34} - \mathbf{r}_{M1})|$$

Right hindfoot (RHF)

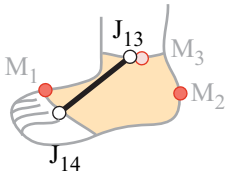

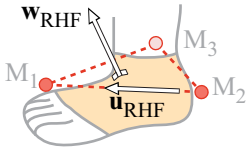

$$\mathbf{r}_{J13} = \mathbf{r}_{M3} - 0,008A_{13}\mathbf{u}_{RHF} + \\ + 0,393A_{15}\mathbf{v}_{RHF} + 0,706A_{17}\mathbf{w}_{RHF}$$

$$\mathbf{u}_{RHF} = (\mathbf{r}_{M1} - \mathbf{r}_{M2}) / |\mathbf{r}_{M1} - \mathbf{r}_{M2}| \qquad \mathbf{v}_{RHF} = \mathbf{w}_{RHF} \wedge \mathbf{u}_{RHF}$$

$$\mathbf{w}_{RHF} = (\mathbf{r}_{M1} - \mathbf{r}_{M3}) \wedge (\mathbf{r}_{M2} - \mathbf{r}_{M3}) / |(\mathbf{r}_{M1} - \mathbf{r}_{M3}) \wedge (\mathbf{r}_{M2} - \mathbf{r}_{M3})|$$

Right shank (RS)

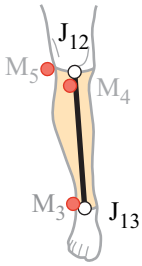

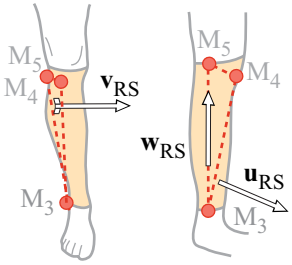

$$\mathbf{r}_{J12} = \mathbf{r}_{M5} + 0,423A_{11}\mathbf{u}_{RS} + 0,406A_{11}\mathbf{v}_{RS} - \\ - 0,198A_{11}\mathbf{w}_{RS}$$

$$\mathbf{v}_{RS} = (\mathbf{r}_{M4} - \mathbf{r}_{M5}) \wedge (\mathbf{r}_{M3} - \mathbf{r}_{M5}) / |(\mathbf{r}_{M4} - \mathbf{r}_{M5}) \wedge (\mathbf{r}_{M3} - \mathbf{r}_{M5})|$$

$$\mathbf{w}_{RS} = (\mathbf{r}_{M5} - \mathbf{r}_{M3}) / |\mathbf{r}_{M5} - \mathbf{r}_{M3}| \qquad \mathbf{u}_{RS} = \mathbf{v}_{RS} \wedge \mathbf{w}_{RS}$$

Left forefoot (LFF)

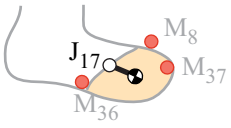

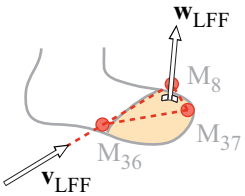

$$\mathbf{r}_{J17} = 0,95\mathbf{r}_{M36} + 0,05\mathbf{r}_{M8} - 0,015\mathbf{w}_{LFF}$$

$$\mathbf{u}_{LFF} = \mathbf{v}_{LFF} \wedge \mathbf{w}_{LFF} \qquad \mathbf{v}_{LFF} = (\mathbf{r}_{M8} - \mathbf{r}_{M36}) / |\mathbf{r}_{M8} - \mathbf{r}_{M36}|$$

$$\mathbf{w}_{LFF} = (\mathbf{r}_{M36} - \mathbf{r}_{M8}) \wedge (\mathbf{r}_{M37} - \mathbf{r}_{M8}) / |(\mathbf{r}_{M36} - \mathbf{r}_{M8}) \wedge (\mathbf{r}_{M37} - \mathbf{r}_{M8})|$$

Left hindfoot (LHF)

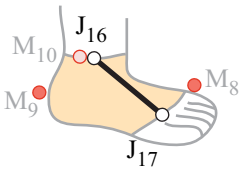

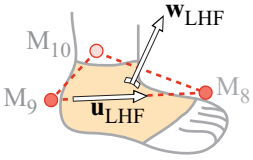

$$\mathbf{r}_{J16} = \mathbf{r}_{M10} - 0,008A_{14}\mathbf{u}_{LHF} + 0,393A_{16}\mathbf{v}_{LHF} - \\ - 0,706A_{18}\mathbf{w}_{LHF}$$

$$\mathbf{v}_{LHF} = \mathbf{w}_{LHF} \wedge \mathbf{u}_{LHF} \qquad \mathbf{u}_{LHF} = (\mathbf{r}_{M8} - \mathbf{r}_{M9}) / |\mathbf{r}_{M8} - \mathbf{r}_{M9}|$$

Left shank (LS)

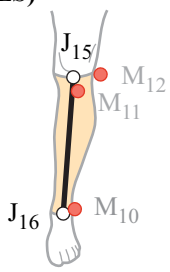

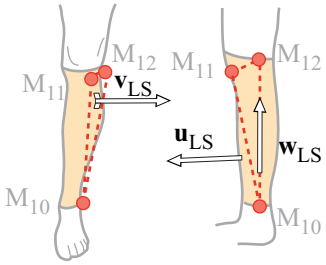

$$\mathbf{r}_{J15} = \mathbf{r}_{M12} + 0,423A_{12}\mathbf{u}_{LS} - 0,406A_{12}\mathbf{v}_{LS} - 0,198A_{12}\mathbf{w}_{LS}$$

$$\mathbf{v}_{LS} = (\mathbf{r}_{M11} - \mathbf{r}_{M12}) \wedge (\mathbf{r}_{M10} - \mathbf{r}_{M12}) / \left| (\mathbf{r}_{M11} - \mathbf{r}_{M12}) \wedge (\mathbf{r}_{M10} - \mathbf{r}_{M12}) \right|$$

$$\mathbf{w}_{LS} = (\mathbf{r}_{M12} - \mathbf{r}_{M10}) / |\mathbf{r}_{M12} - \mathbf{r}_{M10}| \qquad \mathbf{u}_{LS} = \mathbf{v}_{LS} \wedge \mathbf{w}_{LS}$$

Pelvis (P)

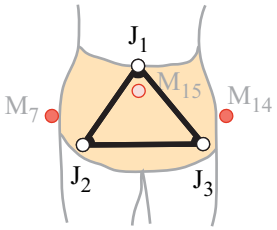

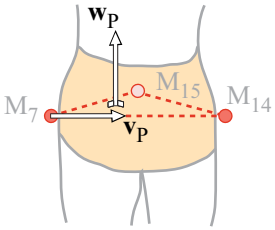

$$\mathbf{r}_{J1} = \frac{\mathbf{r}_{J2} + \mathbf{r}_{J3}}{2} - 0,01\mathbf{u}_P + 0,275\mathbf{w}_P$$

$$\mathbf{r}_{J2} = \mathbf{r}_{M15} + 0,598A_2\mathbf{u}_P + -0,344A_2\mathbf{v}_P - 0,290A_2\mathbf{w}_P$$

$$\mathbf{r}_{J3} = \mathbf{r}_{M15} + 0,598A_2\mathbf{u}_P + +0,344A_2\mathbf{v}_P - 0,290A_2\mathbf{w}_P$$

$$\mathbf{u}_P = \mathbf{v}_P \wedge \mathbf{w}_P \qquad \mathbf{v}_P = (\mathbf{r}_{M14} - \mathbf{r}_{M7}) / |\mathbf{r}_{M14} - \mathbf{r}_{M7}|$$

$$\mathbf{w}_P = (\mathbf{r}_{M7} - \mathbf{r}_{M15}) \wedge (\mathbf{r}_{M14} - \mathbf{r}_{M15}) / \left| (\mathbf{r}_{M7} - \mathbf{r}_{M15}) \wedge (\mathbf{r}_{M14} - \mathbf{r}_{M15}) \right|$$

Right thigh (RT)

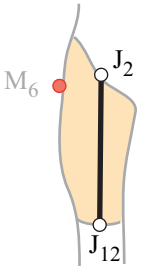

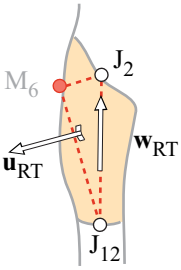

$$\mathbf{u}_{RT} = (\mathbf{r}_{M6} - \mathbf{r}_{J2}) \wedge (\mathbf{r}_{J12} - \mathbf{r}_{J2}) / \left| (\mathbf{r}_{M6} - \mathbf{r}_{J2}) \wedge (\mathbf{r}_{J12} - \mathbf{r}_{J2}) \right|$$

$$\mathbf{v}_{RT} = \mathbf{w}_{RT} \wedge \mathbf{u}_{RT} \qquad \mathbf{w}_{RT} = (\mathbf{r}_{J2} - \mathbf{r}_{J12}) / |\mathbf{r}_{J2} - \mathbf{r}_{J12}|$$

Left thigh (LT)

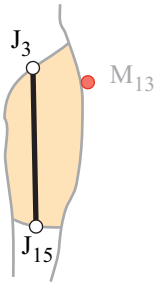

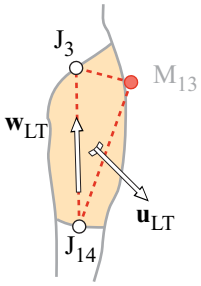

$$\mathbf{u}_{LT} = (\mathbf{r}_{J14} - \mathbf{r}_{J3}) \wedge (\mathbf{r}_{M13} - \mathbf{r}_{J3}) / \left| (\mathbf{r}_{J14} - \mathbf{r}_{J3}) \wedge (\mathbf{r}_{M13} - \mathbf{r}_{J3}) \right|$$

$$\mathbf{v}_{LT} = \mathbf{w}_{LT} \wedge \mathbf{u}_{LT} \qquad \mathbf{w}_{LT} = (\mathbf{r}_{J3} - \mathbf{r}_{J14}) / |\mathbf{r}_{J3} - \mathbf{r}_{J14}|$$

Right hand (RH)

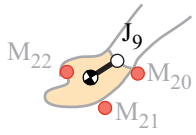

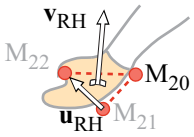

$$\mathbf{r}_{J9} = \mathbf{r}_{M20} + 0,025\mathbf{u}_{RH} + 0,015\mathbf{v}_{RH}$$

$$\mathbf{u}_{RH} = (\mathbf{r}_{M22} - \mathbf{r}_{M21}) / |\mathbf{r}_{M22} - \mathbf{r}_{M21}| \qquad \mathbf{w}_{RH} = \mathbf{u}_{RH} \wedge \mathbf{v}_{RH}$$

$$\mathbf{v}_{RH} = (\mathbf{r}_{M20} - \mathbf{r}_{M21}) \wedge (\mathbf{r}_{M22} - \mathbf{r}_{M21}) / |(\mathbf{r}_{M20} - \mathbf{r}_{M21}) \wedge (\mathbf{r}_{M22} - \mathbf{r}_{M21})|$$

Right forearm (RFA)

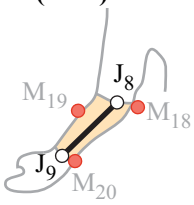

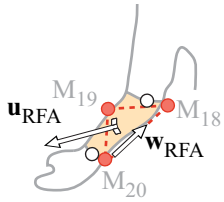

$$\mathbf{r}_{J8} = \mathbf{r}_{M18} + 0,0455\mathbf{u}_{RFA} + 0,035\mathbf{v}_{RFA}$$

$$\mathbf{u}_{RFA} = \mathbf{v}_{RFA} \wedge \mathbf{w}_{RFA} \qquad \mathbf{w}_{RFA} = (\mathbf{r}_{M18} - \mathbf{r}_{M20}) / |\mathbf{r}_{M18} - \mathbf{r}_{M20}|$$

$$\mathbf{v}_{RFA} = (\mathbf{r}_{M19} - \mathbf{r}_{M18}) \wedge (\mathbf{r}_{M20} - \mathbf{r}_{M18}) / (\mathbf{r}_{M19} - \mathbf{r}_{M18}) \wedge (\mathbf{r}_{M20} - \mathbf{r}_{M18})$$

Right arm (RA)

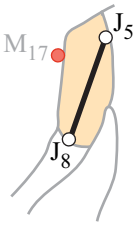

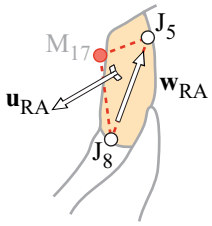

$$\mathbf{u}_{RA} = (\mathbf{r}_{M17} - \mathbf{r}_{J5}) \wedge (\mathbf{r}_{J8} - \mathbf{r}_{J5}) / |(\mathbf{r}_{M17} - \mathbf{r}_{J5}) \wedge (\mathbf{r}_{J8} - \mathbf{r}_{J5})|$$

$$\mathbf{v}_{RA} = \mathbf{w}_{RA} \wedge \mathbf{u}_{RA} \qquad \mathbf{w}_{RA} = (\mathbf{r}_{J5} - \mathbf{r}_{J8}) / |\mathbf{r}_{J5} - \mathbf{r}_{J8}|$$

Left hand (LH)

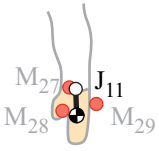

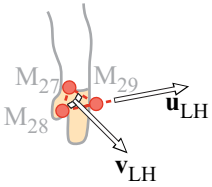

$$\mathbf{r}_{J11} = \mathbf{r}_{M27} + 0,025\mathbf{u}_{LH} - 0,015\mathbf{v}_{LH}$$

$$\mathbf{u}_{LH} = (\mathbf{r}_{M29} - \mathbf{r}_{M28}) / |\mathbf{r}_{M29} - \mathbf{r}_{M28}| \qquad \mathbf{w}_{LH} = \mathbf{u}_{LH} \wedge \mathbf{v}_{LH}$$

$$\mathbf{v}_{LH} = (\mathbf{r}_{M27} - \mathbf{r}_{M28}) \wedge (\mathbf{r}_{M29} - \mathbf{r}_{M28}) / |(\mathbf{r}_{M27} - \mathbf{r}_{M28}) \wedge (\mathbf{r}_{M29} - \mathbf{r}_{M28})|$$

Left forearm (LFA)

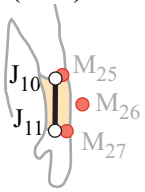

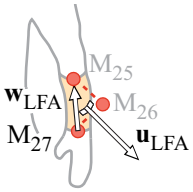

$$\mathbf{r}_{J10} = \mathbf{r}_{M25} + 0,0455\mathbf{u}_{LFA} - 0,035\mathbf{v}_{LFA}$$

$$\mathbf{u}_{LFA} = \mathbf{v}_{LFA} \wedge \mathbf{w}_{LFA} \qquad \mathbf{w}_{LFA} = (\mathbf{r}_{M25} - \mathbf{r}_{M27}) / |\mathbf{r}_{M25} - \mathbf{r}_{M27}|$$

$$\mathbf{v}_{LFA} = (\mathbf{r}_{M26} - \mathbf{r}_{M25}) \wedge (\mathbf{r}_{M27} - \mathbf{r}_{M25}) / |(\mathbf{r}_{M26} - \mathbf{r}_{M25}) \wedge (\mathbf{r}_{M27} - \mathbf{r}_{M25})|$$

Left arm (LA)

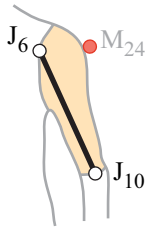

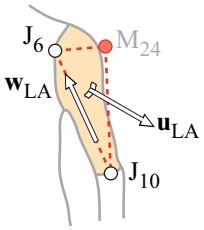

$$\mathbf{u}_{LA} = (\mathbf{r}_{J10} - \mathbf{r}_{J6}) \wedge (\mathbf{r}_{M24} - \mathbf{r}_{J6}) / \left| (\mathbf{r}_{J10} - \mathbf{r}_{J6}) \wedge (\mathbf{r}_{M24} - \mathbf{r}_{J6}) \right|$$

$$\mathbf{v}_{LA} = \mathbf{w}_{LA} \wedge \mathbf{u}_{LA} \qquad \mathbf{w}_{LA} = (\mathbf{r}_{J6} - \mathbf{r}_{J10}) / |\mathbf{r}_{J6} - \mathbf{r}_{J10}|$$

Head (H)

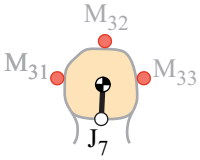

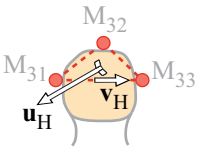

$$\mathbf{r}_{J7} = 0,5(\mathbf{r}_{M31} + \mathbf{r}_{M33}) - 0,04\mathbf{u}_H - 0,1\mathbf{w}_H$$

$$\mathbf{u}_H = (\mathbf{r}_{M31} - \mathbf{r}_{M32}) \wedge (\mathbf{r}_{M33} - \mathbf{r}_{M32}) / \left| (\mathbf{r}_{M31} - \mathbf{r}_{M32}) \wedge (\mathbf{r}_{M33} - \mathbf{r}_{M32}) \right|$$

$$\mathbf{v}_H = (\mathbf{r}_{M33} - \mathbf{r}_{M31}) / |\mathbf{r}_{M33} - \mathbf{r}_{M31}| \qquad \mathbf{w}_H = \mathbf{u}_H \wedge \mathbf{v}_H$$

Neck (N)

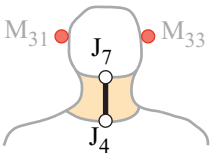

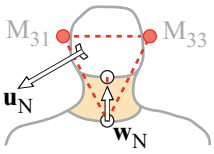

$$\mathbf{u}_N = (\mathbf{r}_{M33} - \mathbf{r}_{M31}) \wedge \mathbf{w}_N / \left| (\mathbf{r}_{M33} - \mathbf{r}_{M31}) \wedge \mathbf{w}_N \right|$$

$$\mathbf{v}_N = \mathbf{w}_N \wedge \mathbf{u}_N \qquad \mathbf{w}_N = (\mathbf{r}_{J7} - \mathbf{r}_{J4}) / |\mathbf{r}_{J7} - \mathbf{r}_{J4}|$$

Torso (T)

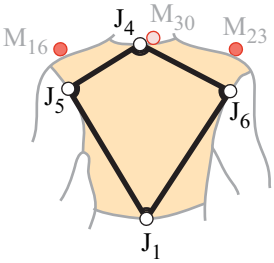

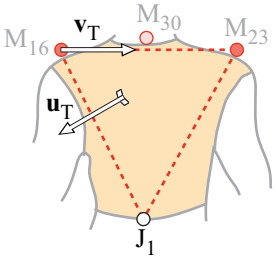

$$\mathbf{r}_{J5} = \mathbf{r}_{M16} - 0,02\mathbf{v}_T - 0,05\mathbf{w}_T$$

$$\mathbf{r}_{J6} = \mathbf{r}_{M23} + 0,02\mathbf{v}_T - 0,05\mathbf{w}_T$$

$$\mathbf{r}_{J4} = 0,5\mathbf{r}_{M30} + 0,25(\mathbf{r}_{J5} + \mathbf{r}_{J6})$$

$$\mathbf{u}_T = (\mathbf{r}_{M23} - \mathbf{r}_{J1}) \wedge (\mathbf{r}_{M16} - \mathbf{r}_{J1}) / \left| (\mathbf{r}_{M23} - \mathbf{r}_{J1}) \wedge (\mathbf{r}_{M16} - \mathbf{r}_{J1}) \right|$$

$$\mathbf{w}_T = \mathbf{u}_T \wedge \mathbf{v}_T \qquad \mathbf{v}_T = (\mathbf{r}_{M23} - \mathbf{r}_{M16}) / |\mathbf{r}_{M23} - \mathbf{r}_{M16}|$$

Table A.1 Definition of the joint positions and the segments unit vectors.

Appendix B

Calculation of the Actual Joint Torques and External Contact Wrenches from IDA Results

As seen in Chapter 4, since the independent coordinates **z** are the position of the lumbar joint (J1) and the orientation angles of all the bodies with respect to the ground, the components of the generalized forces $\mathbf{Q}_m$ do not correspond to the actual external wrenches (acting on the feet) and the joint torques. The procedure to obtain their values involves three steps:

1. Transform the generalized forces $\mathbf{Q}_m$ into an equivalent set of external wrenches $\tilde{\mathbf{G}}$ and internal torques $\tilde{\mathbf{T}}_m$. $\tilde{\mathbf{G}}$ is a 6×1 vector containing the force acting on the lumbar joint (three components) and an absolute torque acting between the pelvis and the ground (also three components). The tilde grapheme denotes that the external wrench does not act at its actual location, i.e., the contacting foot/feet.

2. Translate the external wrench $\tilde{\mathbf{G}}$ from the lumbar joint to the feet. This requires the solution of the double support problem, that is, how the total external wrench $\tilde{\mathbf{G}}$ is shared between both feet $\mathbf{G}_1, \mathbf{G}_2$. This step is explicitly developed in Section 4.5.

3. Use the obtained ground reactions $\mathbf{G}_1, \mathbf{G}_2$ to calculate the actual internal torques $\mathbf{T}_m$.

The results are obtained by equating the vector of generalized forces due to the set of forces and torques calculated when the external wrench acts on the pelvis, and the vector of generalized forces due to the forces and torques when the external wrench acts on its actual location.

The independent coordinate vector $\mathbf{z} = \{\mathrm{J1_X}, \mathrm{J1_Y}, \mathrm{J1_Z}, \alpha_1, \beta_1, \gamma_1, \alpha_2, \beta_2, \gamma_2, ..., \alpha_{18}, \beta_{18}, \gamma_{18}\}^T$ contains the driver variables. As seen in Section 3.4.1, $\alpha_S, \beta_S, \gamma_S$ are angular variables that define the orientation of the rigid body *S* with respect to the ground using sequential absolute rotations (firstly α_S, secondly β_S and finally γ_S). As seen in Eq. (3.92) the angular velocity of the rigid body with respect to the global reference frame can be written as:

$$\boldsymbol{\Omega}_S = \begin{bmatrix} \cos\beta_S \cos\gamma_S & -\sin\gamma_S & 0 \\ \cos\beta_S \sin\gamma_S & \cos\gamma_S & 0 \\ -\sin\beta_S & 0 & 1 \end{bmatrix} \begin{Bmatrix} \dot{\alpha}_S \\ \dot{\beta}_S \\ \dot{\gamma}_S \end{Bmatrix} \Rightarrow \mathbf{T}_S \equiv \begin{bmatrix} \cos\beta_S \cos\gamma_S & -\sin\gamma_S & 0 \\ \cos\beta_S \sin\gamma_S & \cos\gamma_S & 0 \\ -\sin\beta_S & 0 & 1 \end{bmatrix} \tag{B.1}$$

which can be assimilated to three Euler rotations, being α_S the third Euler rotation, β_S the second one and γ_S the first one.

Each component of $\mathbf{Q}_m$ is the generalized force related to the corresponding component of the virtual velocity $\dot{\mathbf{z}}_m^*$. The first three components of $\mathbf{Q}_m$ are related to a force acting on the lumbar joint of the pelvis, and as a result, it can be demonstrated that:

$$\mathbf{F}_{J1} = \{Q_{m1}, Q_{m2}, Q_{m3}\}^T \tag{B.2}$$

which are the three force components of the external contact wrench $\tilde{\mathbf{G}}$.

The other components of $\mathbf{Q}_m$ are torques between the ground and each segment that need to be expressed in the absolute global reference frame. It can be demonstrated that:

$$\mathbf{\Gamma}_S = \mathbf{T}_S^{-T} \mathbf{Q}_{mS} \tag{B.3}$$

where $\mathbf{T}_S$ is defined in Eq. (B.1), and $\mathbf{Q}_{mS}$ are the three components of $\mathbf{Q}_m$ related to the segment *S*. Note that the three last components of the contact wrench $\tilde{\mathbf{G}}$ are calculated using Eq. (B.3) for the pelvis segment.

At this point, the external contact wrench $\tilde{\mathbf{G}}$ (at the lumbar joint) and the external torques $\mathbf{\Gamma}_S$ are obtained. The next step is to calculate the internal torques $\tilde{\mathbf{T}}_m$. The principle of virtual power establishes a linear relationship between the torques $\mathbf{\Gamma}_S$ and the set of equivalent internal torques $\tilde{\mathbf{T}}_m$. Figure B.1 shows these two sets of torques for the lower limbs. Note that the segments *S* are defined according to the segment numeration (Figure 3.1) and internal torques are enumerated according to the joint's numeration (Figure 3.5 (b)).

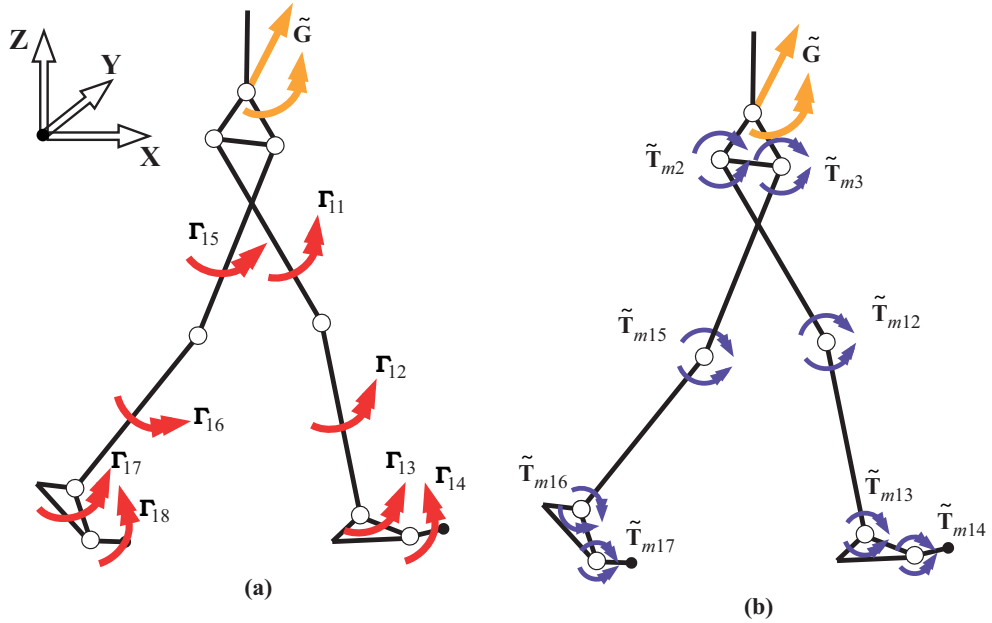

Figure B.1 Scheme of the lower limbs. (a) Absolute torques $\mathbf{\Gamma}_S$ and contact wrench acting on the lumbar joint $\tilde{\mathbf{G}}$. (b) Relative torques calculated using the pelvis as a support segment $\tilde{\mathbf{T}}_m$.

As an example, for the right leg, the internal torques $\tilde{\mathbf{T}}_m$ can be calculated as:

$$\tilde{\mathbf{T}}_{m14} = \mathbf{\Gamma}_{14} \tag{B.4}$$

$$\tilde{\mathbf{T}}_{m13} = \boldsymbol{\Gamma}_{13} - \tilde{\mathbf{T}}_{m14} \tag{B.5}$$

$$\tilde{\mathbf{T}}_{m12} = \boldsymbol{\Gamma}_{12} - \tilde{\mathbf{T}}_{m13} \tag{B.6}$$

$$\tilde{\mathbf{T}}_{m2} = \boldsymbol{\Gamma}_{11} - \tilde{\mathbf{T}}_{m12} \tag{B.7}$$

In a similar way, these equations can be written for each human body branch (i.e., for upper and lower extremities). As a result, all the internal joint torques can be determined. However, an absolute wrench remains between the ground and the pelvis segment $\left(\tilde{\mathbf{G}}\right)$.

This wrench corresponds to the contact forces applied to the multibody system, which appear actually at the foot-ground interface. Therefore, the external wrench $\tilde{\mathbf{G}}$ needs to be translated to the actual contact points at the feet. This step is explained on Section 4.5.

Assuming as known how the total external wrench $\tilde{\mathbf{G}}$ is shared between both feet $\mathbf{G}_1 = \{\mathbf{G}_{F1}, \mathbf{G}_{M1}\}$ $\mathbf{G}_2 = \{\mathbf{G}_{F2}, \mathbf{G}_{M2}\}$, (where subscript F and M indicate forces and moment components, respectively) the actual internal torques $\mathbf{T}_m$ can be determined applying the same principle. Again, for the right leg (see Figures B.1 and B.2):

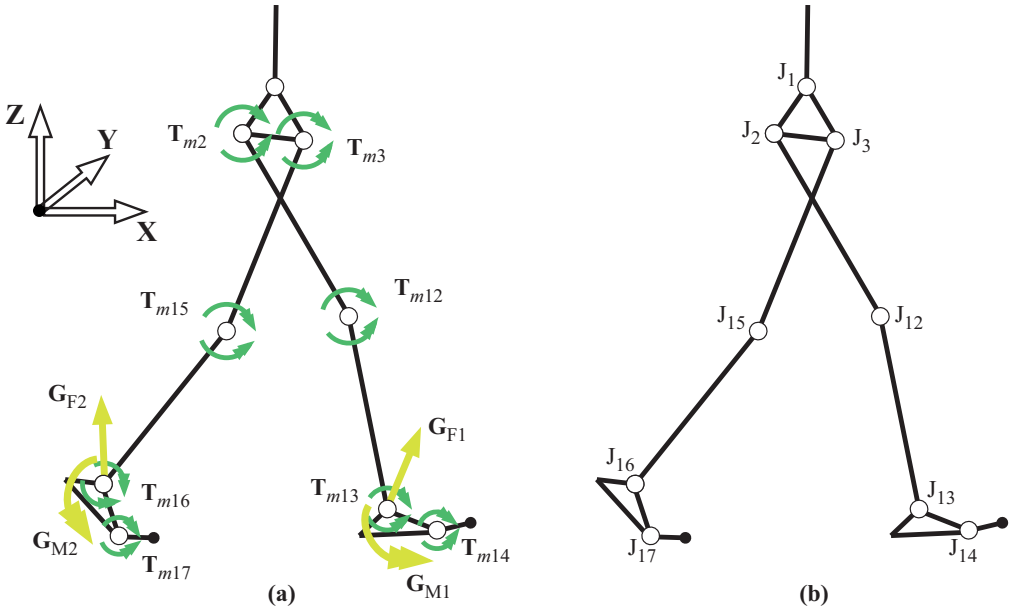

Figure B.2 Scheme of the lower limbs (a) Actual joint torques and contact forces. (b) Joints numeration.

$$\mathbf{T}_{m2} = \tilde{\mathbf{T}}_{m2} - \mathbf{G}_{M1} + (\mathbf{r}_{J2} - \mathbf{r}_{J13}) \wedge \mathbf{G}_{F1} \tag{B.8}$$

$$\mathbf{T}_{m12} = \tilde{\mathbf{T}}_{m12} - \mathbf{G}_{M1} + (\mathbf{r}_{J12} - \mathbf{r}_{J13}) \wedge \mathbf{G}_{F1} \tag{B.9}$$

$$\mathbf{T}_{m13} = \tilde{\mathbf{T}}_{m13} - \mathbf{G}_{M1} \tag{B.10}$$

$$\mathbf{T}_{m14} = \tilde{\mathbf{T}}_{m14} \tag{B.11}$$

where $\mathbf{r}_{J_i}$ is the position of the joint J_i in the absolute coordinate system.

Similarly, the actual joint torques belonging to each human body branch can be calculated, and the set of actual torques and wrenches acting on the biomechanical model can be finally determined.

Appendix C

Use of Bézier Curves to Define the Evolution of the Independent Coordinates

As seen in Chapter 5, Bézier Curves are used to define the analytical expressions of the 16 independent coordinates used in the bidimensional model $\mathbf{z}=\{x_1, z_1, \alpha_1, ..., \alpha_{14}\}$ (see Figure 5.1).

To obtain these expressions, $n+1$ control points $\mathbf{b}_j$ need to be defined for each curve [Cardona and Clos 2001]:

$$\mathbf{b}_j = \{ j/n,\, b_j \}, \qquad j = 0,...,n \tag{C.1}$$

The ordinate values b_j (also known as Bézier coefficients) of these control points are obtained via an optimization procedure which minimizes the difference between the actual measured curve and the one obtained using the Bézier expression. This process guarantees that the RMSE between the experimental curve $z_i^{\exp}$ and the analytical curve expression z_i^{bez} is lower than a chosen tolerance ε:

$$\sqrt{\frac{1}{N}\sum_{k=1}^{N}\left(z_i^{\exp}(k) - z_i^{bez}(k)\right)^2} \le \varepsilon \tag{C.2}$$

where index i refers to the index of the independent coordinates $(i = 1,...,16)$, k is the index of the time instants $(t_k = (k-1)\Delta t,\ \text{being}\ \Delta t = 1\,\text{ms})$ and N is the number of time steps of the simulation.

The order of the Bézier curves (n) is different for each independent coordinate z_i : n has the minimum value to guarantee that the RMSE between the two curves is lower than $\varepsilon = 10^{-4}$ rad for angular variables and lower than $\varepsilon = 10^{-4}$ m for the ankle position.

Bézier Curves are defined in a unit domain (u). Therefore, a linear change of variable needs to be applied:

$$u = \frac{t - t_1}{t_N - t_1}; \qquad t \in [t_1, t_N] \tag{C.3}$$

where t_1 and t_N are the initial and final time instants, respectively. The n-order Bernstein polynomial $b_i(u)$ for each independent coordinate can be expressed as a combination of Bernstein basis polynomials $\mathrm{B}_j^n(u)$ as:

$$b_i(u) = \sum_{j=0}^{n} b_j \mathrm{B}_j^n(u) \qquad u \in [0,1] \tag{C.4}$$

where the $n+1$ coefficients b_j are the Bézier coefficients. In a unit domain, the Bernstein basis polynomials of degree *n* are defined as:

$$\mathrm{B}_j^n(u) = C_n^j u^j (1-u)^{n-j} \qquad j = 0,...,n \tag{C.5}$$

where $C_n^j = n!/(j!(n-j)!)$. Therefore, using Eqs. (C.4) and (C.5), the analytical expression $b_i(u)$ can be calculated and, by means of the linear change of variable, Eq. (C.3), the time domain expression $z_i^{bez}[k]$ can be determined for each independent coordinate.

Then, the velocities and acceleration of the independent coordinates can be calculated as the first and second time derivatives of $b_i(u)$, respectively. Using the Bernstein basis, the Bézier coefficients b_j' (coefficients of the time derivative expression) depend on the known values b_j:

$$b_j' = n(b_{j+1} - b_j) \qquad j = 0,...,n-1 \tag{C.6}$$

Therefore, using both, the new Bézier coefficients b_j' and the Bernstein basis polynomials of degree n' $(n' = n-1)$, the first time derivative expression $b_i'(u)$ can be calculated (Eqs. (C.5) and (C.6)). For the second time derivative, a similar procedure needs to be applied obtaining a Bernstein polynomial of degree n'' $(n'' = n'-1)$. Finally, the time domain expressions $(\dot{z}_i^{bez}[k]$ and $\ddot{z}_i^{bez}[k])$ can be calculated using Eq. (C.3).

Appendix D

Extended Kalman Filter Formulation

The original formulation of the Kalman filter (KF) is intended only to linear systems. The multibody system used along this thesis is a nonlinear system, therefore the process and measurement models of the KF have to be approximated in some way. There are different types of algorithms based on the KF for nonlinear systems, in this thesis the extended Kalman filter (EKF) formulation has been used.

The EKF is applied as a controller for the forward dynamic analysis in Chapter 6, therefore, in this appendix, the implemented method and the combination with the matrix-R formulation are described.

Kalman Filter

The equations for the system dynamics and the measurement model are presented below. Consider a linear stochastic system dynamics (plant) given by a first order ODE with independent states:

$$\dot{\mathbf{x}}(t)=\mathbf{f}\left(\mathbf{x}(t),t\right)+\boldsymbol{\delta}(t) \tag{D.1}$$

$$\mathbf{y}(t)=\mathbf{h}\left(\mathbf{x}(t)\right)+\boldsymbol{\varepsilon}(t) \tag{D.2}$$

where $\mathbf{x}$ is the (unknown) state vector, $\dot{\mathbf{x}}$ its time derivative, and $\mathbf{y}$ is the measurement vector. $\mathbf{f}$ is the system dynamics function and $\mathbf{h}$ is the function defining the relationship between the state of the dynamic system and measurements that can be made. The process noise $\boldsymbol{\delta}$ and the measurement noise $\boldsymbol{\varepsilon}$ are considered zero-mean Gaussian noises with covariances $\mathcal{Q}(t)$ and $\mathcal{R}(t)$, respectively. The differential equation for the recursive estimation of the states $\hat{\mathbf{x}}$ is given (for the KF) by:

$$\dot{\hat{\mathbf{x}}}(t)=\mathrm{E}\left[\mathbf{f}\left(\hat{\mathbf{x}}(t),t\right)+\boldsymbol{\delta}(t)\right]+\bar{\mathbf{K}}(t)\left[\mathbf{y}(t)-\hat{\mathbf{y}}(t)\right]=\mathbf{F}(t)\hat{\mathbf{x}}(t)+\bar{\mathbf{K}}(t)\left[\mathbf{y}(t)-\hat{\mathbf{y}}(t)\right] \tag{D.3}$$

where E is the expectation, $\bar{\mathbf{K}}$ is the Kalman gain matrix, $\hat{\mathbf{x}}$ is the estimated state vector, $\hat{\mathbf{y}}$ are the predicted measurements and $\mathbf{F}$ is the matrix of a continuous linear differential equation defining a dynamic system (obtained as the Jacobian of $\mathbf{f}$). Note that $\mathbf{f}\left(\mathbf{x},t\right)=\mathbf{F}\mathbf{x}(t)$ as $\mathbf{f}\left(t\right)$ is linear in this case. Moreover:

$$\bar{\mathbf{K}}(t)=\mathbf{P}(t)\mathbf{H}^{T}(t)\mathcal{R}^{-1}(t) \tag{D.4}$$

$$\hat{\mathbf{y}}(t)=\mathrm{E}\left[\mathbf{h}\left(\hat{\mathbf{x}}(t),t\right)+\boldsymbol{\varepsilon}(t)\right]=\mathbf{H}(t)\hat{\mathbf{x}}(t) \tag{D.5}$$

$$\dot{\mathbf{P}}(t)=\mathbf{F}(t)\mathbf{P}(t)+\mathbf{P}(t)\mathbf{F}^{T}(t)-\mathbf{P}(t)\mathbf{H}^{T}(t)\mathcal{R}^{-1}(t)\mathbf{H}(t)\mathbf{P}(t)+\mathcal{Q}(t) \tag{D.6}$$

where $\mathbf{H}$ is the measurement sensitivity matrix (defined as the Jacobian of $\mathbf{h}$) and, since $\mathbf{h}$ is linear, $\mathbf{h}(t,\mathbf{x})=\mathbf{H}\mathbf{x}(t)$. $\mathbf{P}$ is the covariance of the state-estimation error. The main feature of the KF is its optimality: it minimizes the covariance $\mathbf{P}$. In some cases (as in this thesis) $\mathbf{f}$ and $\mathbf{h}$ can be nonlinear. In this case, the employed methodology is known as the extended Kalman filter.

Extended Kalman Filter

Unlike in the KF, now $\mathbf{f}$ and $\mathbf{h}$ can be nonlinear functions. The EKF approach approximates Eqs. (D.3), (D.5) and (D.6), respectively, by:

$$\dot{\hat{\mathbf{x}}}(t)=\mathrm{E}\left[\mathbf{f}\left(\hat{\mathbf{x}}(t),t\right)+\boldsymbol{\delta}(t)\right]+\bar{\mathbf{K}}(t)\left[\mathbf{y}(t)-\hat{\mathbf{y}}(t)\right]\simeq\mathbf{f}\left(\hat{\mathbf{x}}(t)\right)+\bar{\mathbf{K}}(t)\left[\mathbf{y}(t)-\hat{\mathbf{y}}(t)\right] \tag{D.7}$$

$$\hat{\mathbf{y}}(t)=\mathrm{E}\left[\mathbf{h}\left(\hat{\mathbf{x}}(t),t\right)+\boldsymbol{\varepsilon}(t)\right]=\mathbf{h}\left(\hat{\mathbf{x}}(t)\right) \tag{D.8}$$

$$\dot{\mathbf{P}}(t)\simeq\mathbf{F}(t)\mathbf{P}(t)+\mathbf{P}(t)\mathbf{F}^{T}(t)-\mathbf{P}(t)\mathbf{H}^{T}(t)\mathcal{R}^{-1}(t)\mathbf{H}(t)\mathbf{P}(t)+\mathcal{Q}(t) \tag{D.9}$$

Eq. (D.7) shows that the derivative of the state vector is function of the state vector and in Eq. (D.8) it can be seen that the predicted measurements are function of the estimates. The covariance matrix of state estimation uncertainty $\mathbf{P}$ is solved using the fixed point iteration as in [Pastorino 2012]. The Kalman gain is obtained, as previously, using Eq. (D.4) and the covariance matrix of the state estimation uncertainty using Eq. (D.6).

As explained in Chapter 3, the dynamics of the multibody system is described by the constrained Lagrangian equations

$$\begin{cases}\mathbf{M}\ddot{\mathbf{q}}+\boldsymbol{\Phi}_{\mathbf{q}}^{T}\boldsymbol{\lambda}=\mathbf{Q}\\ \boldsymbol{\Phi}=\mathbf{0}\end{cases} \tag{D.10}$$

In order to adopt the form of the Eq. (D.1) required for application of the EKF, the second order system of Eq. (D.10) is written as a first order one doing:

$$\mathbf{x}^{T}=\left\{\mathbf{q}^{T}\quad\mathbf{v}^{T}\right\} \tag{D.11}$$

where $\mathbf{v}=\dot{\mathbf{q}}$ (and, therefore, $\dot{\mathbf{v}}=\ddot{\mathbf{q}}$). Using Eqs. (D.10) and (D.11)

$$\dot{\mathbf{v}}=\mathbf{M}^{-1}\left(\mathbf{Q}-\boldsymbol{\Phi}_{\mathbf{q}}^{\mathrm{T}}\boldsymbol{\lambda}\right) \tag{D.12}$$

which can be written as

$$\begin{Bmatrix}\dot{\mathbf{q}}\\ \dot{\mathbf{v}}\end{Bmatrix}=\begin{Bmatrix}\mathbf{v}\\ \mathbf{M}^{-1}\left(\mathbf{Q}-\boldsymbol{\Phi}_{\mathbf{q}}^{\mathrm{T}}\boldsymbol{\lambda}\right)\end{Bmatrix}\Rightarrow\dot{\mathbf{x}}=\mathbf{f}(\mathbf{x}) \tag{D.13}$$

In order to convert the equations of motion into an ODE system the matrix-R procedure is used. As the EKF is used in a forward dynamic analysis, rheonomic equations are not present in the equations of motion. Therefore, the dependent velocities $\dot{\mathbf{q}}$ can be expressed as a function of the independent velocities $\dot{\mathbf{z}}$ as:

$$\dot{\mathbf{q}} = \mathbf{R}\dot{\mathbf{z}} \tag{D.14}$$

and the generalized acceleration vector is defined as:

$$\ddot{\mathbf{q}} = \mathbf{R}\ddot{\mathbf{z}} + \dot{\mathbf{R}}\dot{\mathbf{z}} \tag{D.15}$$

Then, the equations of motion described in Eq. (D.10) case be rewritten as:

$$\ddot{\mathbf{z}} = \left(\mathbf{R}^T\mathbf{M}\mathbf{R}\right)^{-1}\left[\mathbf{R}^T\left(\mathbf{Q} - \mathbf{M}\dot{\mathbf{R}}\dot{\mathbf{z}}\right)\right] \equiv \tilde{\mathbf{M}}^{-1}\tilde{\mathbf{Q}} \tag{D.16}$$

where $\tilde{\mathbf{M}} = \mathbf{R}^T\mathbf{M}\mathbf{R}$ and $\tilde{\mathbf{Q}} = \mathbf{R}^T\left(\mathbf{Q} - \mathbf{M}\dot{\mathbf{R}}\dot{\mathbf{z}}\right)$.

As the states are defined as:

$$\mathbf{x}(t) = \begin{bmatrix} \mathbf{z}(t) \\ \mathbf{w}(t) \end{bmatrix} \tag{D.17}$$

the following equations can be written:

$$\dot{\mathbf{x}}(t) = \begin{bmatrix} \dot{\mathbf{z}}(t) \\ \dot{\mathbf{w}}(t) \end{bmatrix} = \begin{bmatrix} \mathbf{w}(t) \\ \tilde{\mathbf{M}}^{-1}\tilde{\mathbf{Q}} \end{bmatrix} \equiv \begin{bmatrix} \mathbf{w} \\ \left(\mathbf{R}^T\mathbf{M}\mathbf{R}\right)^{-1}\left[\mathbf{R}^T\left(\mathbf{Q} - \mathbf{M}\dot{\mathbf{R}}\dot{\mathbf{z}}\right)\right] \end{bmatrix} = \mathbf{f}\left(\mathbf{x}(t), t\right) \Rightarrow \dot{\mathbf{x}} = \mathbf{f}\left(\mathbf{x}\right) \tag{D.18}$$

where $\mathbf{w}(t) = \dot{\mathbf{z}}(t)$. And taking into account Eq. (D.7):

$$\begin{bmatrix} \dot{\hat{\mathbf{z}}} \\ \dot{\hat{\mathbf{w}}} \end{bmatrix} = \begin{bmatrix} \hat{\mathbf{w}} \\ \left(\mathbf{R}^T\mathbf{M}\mathbf{R}\right)^{-1}\left[\mathbf{R}^T\left(\mathbf{Q} - \mathbf{M}\dot{\mathbf{R}}\hat{\mathbf{w}}\right)\right] \end{bmatrix} + \begin{bmatrix} \bar{\mathbf{K}}^{\mathrm{Z}} \\ \bar{\mathbf{K}}^{\mathrm{W}} \end{bmatrix}\left(\mathbf{y} - \hat{\mathbf{y}}\right) \tag{D.19}$$

Where $\bar{\mathbf{K}}^{\mathrm{Z}}$ and $\bar{\mathbf{K}}^{\mathrm{W}}$ are two blocks of $\bar{\mathbf{K}}$ associated to vectors $\mathbf{z}$ and $\mathbf{w}$, respectively. Note that Eq. (D.19) perfectly matches to Eq.(D.1) and, therefore, the EKF in Eqs. (D.7) – (D.9) can be straightforwardly applied.

In order to obtain the Kalman gain $\bar{\mathbf{K}}$, the covariance matrix $\mathbf{P}$ needs to be calculated (Eq. (D.9)). For this purpose, matrices **F** and **H** need to be calculated:

$$\mathbf{H}(t, \mathbf{x}) \equiv \frac{\partial \mathbf{h}(t, \mathbf{x})}{\partial \hat{\mathbf{x}}} = \begin{bmatrix} \dfrac{\partial \mathbf{h}(t)}{\partial \hat{\mathbf{z}}} & \dfrac{\partial \mathbf{h}(t)}{\partial \hat{\mathbf{w}}} \end{bmatrix} = \begin{bmatrix} \mathbf{H}^{\mathrm{Z}} & \mathbf{H}^{\mathrm{W}} \end{bmatrix} \tag{D.20}$$

$$\mathbf{F}(t) \equiv \frac{\partial \mathbf{f}(t)}{\partial \mathbf{x}} = \begin{bmatrix} 0 & \mathbf{I} \\ \dfrac{\partial\left(\tilde{\mathbf{M}}^{-1}\tilde{\mathbf{Q}}\right)}{\partial \mathbf{z}} & \dfrac{\partial\left(\tilde{\mathbf{M}}^{-1}\tilde{\mathbf{Q}}\right)}{\partial \mathbf{w}} \end{bmatrix} \tag{D.21}$$

which can be approximated as:

$$\mathbf{F}(t)=\begin{bmatrix} \mathbf{0} & \mathbf{I} \\ \tilde{\mathbf{M}}^{-1}\mathbf{R}^T\left(\mathbf{K}\mathbf{R}+2\mathbf{M}\mathbf{R}_{\mathbf{q}}\mathbf{R}\dot{\mathbf{w}}\right) & -\tilde{\mathbf{M}}^{-1}\mathbf{R}^T\left(\mathbf{C}\mathbf{R}+\mathbf{M}\dot{\mathbf{R}}\right) \end{bmatrix} \tag{D.22}$$

The resulting equations have to be integrated. Using the trapezoidal rule, the discrete-time integration can be expressed as:

$$\begin{bmatrix} \dot{\hat{\mathbf{z}}}_{k+1} \\ \dot{\hat{\mathbf{w}}}_{k+1} \end{bmatrix}=\frac{2}{\Delta t}\begin{bmatrix} \hat{\mathbf{z}}_{k+1}-\hat{\mathbf{z}}_k \\ \hat{\mathbf{w}}_{k+1}-\hat{\mathbf{w}}_k \end{bmatrix}-\begin{bmatrix} \dot{\hat{\mathbf{z}}}_k \\ \dot{\hat{\mathbf{w}}}_k \end{bmatrix} \tag{D.23}$$

where the subscript indicates the time step. Finally, using Eqs. (D.19) and (D.23)

$$\begin{bmatrix} \frac{2}{\Delta t}\left(\hat{\mathbf{z}}_{k+1}-\hat{\mathbf{z}}_k\right)-\dot{\hat{\mathbf{z}}}_k \\ \frac{2}{\Delta t}\left(\hat{\mathbf{w}}_{k+1}-\hat{\mathbf{w}}_k\right)-\dot{\hat{\mathbf{w}}}_k \end{bmatrix}=\begin{bmatrix} \hat{\mathbf{w}}_{k+1} \\ \left(\mathbf{R}^T\mathbf{M}\mathbf{R}\right)^{-1}\left[\mathbf{R}^T\left(\mathbf{Q}-\mathbf{M}\dot{\mathbf{R}}\hat{\mathbf{w}}_{k+1}\right)\right] \end{bmatrix}+\begin{bmatrix} \bar{\mathbf{K}}^{\mathrm{Z}}_{k+1} \\ \bar{\mathbf{K}}^{\mathrm{W}}_{k+1} \end{bmatrix}\left(\mathbf{y}-\hat{\mathbf{y}}\right) \tag{D.24}$$

which can be rewritten as:

$$\mathbf{g}\left(\hat{\mathbf{x}}_{k+1}\right)=\begin{bmatrix} \left(\hat{\mathbf{z}}_{k+1}-\hat{\mathbf{z}}_k\right)-\frac{\Delta t}{2}\left[\dot{\hat{\mathbf{z}}}_k-\mathbf{w}_{k+1}-\bar{\mathbf{K}}^{Z}_{k+1}\left(\mathbf{y}_{k+1}-\mathbf{h}\left(\hat{\mathbf{x}}_{k+1}\right)\right)\right] \\ \tilde{\mathbf{M}}\hat{\mathbf{w}}_{k+1}-\tilde{\mathbf{M}}\hat{\mathbf{w}}_k-\frac{\Delta t}{2}\left[\tilde{\mathbf{M}}\dot{\hat{\mathbf{w}}}_k-\tilde{\mathbf{Q}}_{k+1}-\tilde{\mathbf{M}}\bar{\mathbf{K}}^{\mathrm{W}}_{k+1}\left(\mathbf{y}_{k+1}-\mathbf{h}\left(\hat{\mathbf{x}}_{k+1}\right)\right)\right] \end{bmatrix}=0 \tag{D.25}$$

where $\mathbf{g}$ is a nonlinear function that can be solved using the Newton-Raphson method:

$$\mathbf{g}\left(\hat{\mathbf{x}}^{j+1}\right)\simeq\mathbf{g}\left(\hat{\mathbf{x}}^{j}\right)+\frac{\partial\mathbf{g}\left(\hat{\mathbf{x}}^{j}\right)}{\partial\hat{\mathbf{x}}}\left(\hat{\mathbf{x}}^{j+1}-\hat{\mathbf{x}}^{j}\right)=\mathbf{0} \tag{D.26}$$

$$\hat{\mathbf{x}}_{k+1}=\hat{\mathbf{x}}^{j+1}\ \text{ when }\ \left(\hat{\mathbf{x}}^{j+1}-\hat{\mathbf{x}}^{j}\right)\simeq\mathbf{0} \tag{D.27}$$

where *j* is the iteration index. Eq. (D.26) represents an iterative process that can be used until the norm of the residual $\left(\hat{\mathbf{x}}^{j+1}-\hat{\mathbf{x}}^{j}\right)$ is less than a specified tolerance.

The tangent matrix can be approximated as [Cuadrado *et al.* 2009]:

$$\begin{aligned} \frac{\partial\mathbf{g}\left(\hat{\mathbf{x}},t\right)}{\partial\hat{\mathbf{x}}}&=\begin{bmatrix} \frac{\partial\mathbf{g}\left(\hat{\mathbf{x}}\right)}{\partial\hat{\mathbf{z}}} & \frac{\partial\mathbf{g}\left(\hat{\mathbf{x}}\right)}{\partial\hat{\mathbf{w}}} \end{bmatrix} \\ &\simeq\begin{bmatrix} \mathbf{I}+\frac{\Delta t}{2}\bar{\mathbf{K}}^{Z}\mathbf{H}^{Z} & \frac{\Delta t}{2}\left(-\mathbf{I}+\bar{\mathbf{K}}^{Z}\mathbf{H}^{\mathrm{W}}\right) \\ \mathbf{R}^T\mathbf{K}\mathbf{R}+\tilde{\mathbf{M}}\bar{\mathbf{K}}^{\mathrm{W}}\mathbf{H}^{Z} & \mathbf{M}+\frac{\Delta t}{2}\left(\mathbf{R}^T\left(\mathbf{C}\mathbf{R}+\mathbf{M}\dot{\mathbf{R}}\right)+\mathbf{M}\bar{\mathbf{K}}^{\mathrm{W}}\mathbf{H}^{\mathrm{W}}\right) \end{bmatrix} \end{aligned} \tag{D.28}$$

where, as previously, $\mathbf{K} = -\frac{\partial \mathbf{Q}}{\partial \mathbf{z}}$ and $\mathbf{C} = -\frac{\partial \mathbf{Q}}{\partial \mathbf{w}}$.

At this point the correction provided by the EKF must be calculated and the estimation of the system state can be determined at each time step.

References

Ackermann M., Schiehlen W., (2006). Dynamic analysis of human gait disorder and metabolical cost estimation. *Archive of Applied Mechanics*, Vol. 75, 569–594.

Ackermann M., Van den Bogert A.J., (2010). Optimality priciples for model-based predic-tion of human gait. *Journal of Biomechanics*, Vol. 43, 1055–1060.

Adham R.I., Shihab S.A., (1999). Discrete wavelet transform: a tool in smoothing kinematic data. *Journal of Biomechanics*, Vol. 32, 317–321.

Agulló Batlle J., (2002). Mecànica de la partícula i del sòlid rígid. *Publicacions OK Punt*, Barcelona.

Alexander E.J., Andriacchi, T.P., (2001). Correcting for deformation in skin-based marker systems. *Journal of Biomechanics*, Vol. 34, 355–361.

Alonso F.J., (2005). Tratamiento de señales cinemáticas y de masas de tejido blando en el análisis dinámico inverso de modelos biomecánicos esqueletares. *Phd Thesis,* Universidad de Extremadura, Spain.

Alonso F.J., Cuadrado J., Lugris U., Pintado P., (2010). A Compact Smoothing-Differentiation and Projection Approach for the Kinematic Data Consistency of Biomechanical Systems, *Multibody System Dynamics*, Vol. 24 (1), 67–80.

Alonso F.J., Del Castillo J.M., Pintado P., (2005). Application of singular spectrum analysis to the smoothingof raw kinematic signals, *Journal of Biomechanics*, Vol. 38, 1085–1092.

Ambrósio J.A.C., Silva M., Abrantes J., (1999). Inverse dynamic analysis of human gait Using Consistent Data. *Proceedings of IV International Symposium on Computer Methods in Biomechanics and Biomedical Engineering*, Lisboa, Portugal

Ambrósio, J.A.C., Kecskeméthy A., (2007). Multibody dynamics of biomechanical models for human motion via optimization. *Computational Methods in Applied Sciences*, Vol. 4, 245–272.

Amirouche F.M.L., Ider S.K., Trimble J., (1990). Analytical method for the analysis and simulation of human locomotion. *Journal of Biomechanical Engineering*, Vol. 112, 379–386.

Anderson F.C., Pandy M.G., (1999). A dynamic optimization solution for vertical jumping in three dimensions. *Computer Methods in Biomechanics and Biomedical Engineering,* Vol. 2, 201–231.

Anderson F.C., Pandy M.G., (2001a). Dynamic optimization of human walking. *Journal of Biomechanical Engineering,* Vol. 123, 381–290.

Anderson F.C., Pandy M.G., (2001b). Static and dynamic optimization solutions for gait are practically equivalent. *Journal of Biomechanics*, Vol. 34, 153–161.

Anderson F.C., Pandy M.G., (2003). Individual muscle contributions to support in normal walking. *Gait Posture*, Vol. 17, 159–169

Andrews D., Dowling J.J., (1993). The contribution of below knee wobbling mass to the estimation of vertical knee joint forces following impact with the ground. *Journal of Biomechanics,* Vol. 26, 359.

Arnold A.S., Anderson F.C., Pandy M.G., Delp S.L., (2005). Muscular contributions to hip and knee extension during the single limb stance phase of normal gait: a framework for investigating the causes of crouch gait. *Journal of Biomechanics*, Vol. 38, 2181–2189.

Arnold A.S., Schwartz M.H., Thelen D.G., Delp S.L., (2007a). Contributions of muscles to terminal-swing knee motions vary with walking speed. *Journal of Biomechanics,* Vol. 40, 3660–3671.

Arnold A.S., Thelen D.G., Schwartz M.H., Anderson F.C., Delp S.L., (2007b). Muscular coordination of knee motion during the terminal-swing phase of normal gait. *Journal of Biomechanics,* Vol. 40, 3314–3324.

Ayoub M., Woldstad J., Lin C., Bernard T., (1998). A model to predict human motion during lifting, *SAE Digital Human Modeling for Design and Engineering Conference,* Dayton, Ohio.

Bandera C., Minen D., Manzilli G., (1990). Human walking dynamic model ssing ADAMS. An approach to miomechanics of the knee under dynamic loads. *Intl ADAMS conference.* Wiesbaden, Germany.

Barbosa I., Ambrósio J.A.C., Silva M.P.T., (2005). A foot contact model for the forward dynamics of human locomotion. *Proceedings of Multibody Dynamics 2005, ECCOMAS Thematic Conference,* (J.M. Goicolea, J.Cuadrado, J.C.García Orden, eds.), Madrid, Spain.

Barlett R., Force platforms and external force measurements (2007). *In R. Barlett (Ed), Introduction to sports biomechanics, E&FN SPON*, 206–227.

Bayo E., Ledesma R., (1996). Augmented Lagrangian and mass-orthogonal projection methods for constrained multibody dynamics. *Nonlinear Dynamics,* Vol. 9, 113–130.

Bernstein N.A., (1935) Studies of the Biodynamics of Locomotions (Normal Gait, Load and Fatigue). *Institute of Experimental Medicien*, Moscow, Russian.

Bhushan N., Shadmehr R., (1999). Computational nature of human adaptive control during learning of reaching movements in force fields. *Biological Cybernetics*, Vol. 81, 39–60.

Blount W.P. (1956). Don't throw away the cane. Journal of Bone and Joint Surgery. Vol. 38 (3), 695–708.

Bobbert M.F., Van Soest A.J., (1994). Effects of muscle strengthening on vertical jump height: a simulation study. *Medicine and Science in Sports and Exercise*, Vol. 26 (8), 1012–20.

Van den Bogert A.J., Blana D., Heinrich D., (2011). Implicit methods for efficient musculoskeletal simulation and ptimal control. *Symposium on Human Body Dynamics*, Procedia IUTAM, Vol. 2, 297–316.

Botto M.A., (2008). Controlo de Sistemas. *AEIST Press*, 1st ed. Lisbon, Portugal.

Bresler B., Frankel J.P., (1950). The forces and moments in the leg during level walking. *Transactions of the American Society of Mechanical Engineers*, Vol. 72, 27–36.

Buczek F.L., Cooney K.M., Walker M.R., Rainbow M.J., Concha M.C., Sanders J.O., (2006). Performance of an inverted pendulum model directly applied to normal human gait. *Clinical Biomechanics*, Vol. 21 (3), 288–296.

Cahouët V., Luc M., Amarantini D., (2002). Static optimal estimation of joint accelerations for inverse dynamics problem solution. *Journal of Biomechanics,* Vol. 35, 1507–1513.

Cappozzo A., Tommaso L., Pedotti A., (1975). A general computing method for the analysis of human locomotion. *Journal of Biomechanics,* Vol. 8, 307–320.

Cardona Foix S., Clos Costa D., (2001). Teoria de Màquines. *Edicions UPC*, Barcelona. Spain.

Celigüeta J.T., (1996). Multibody simulation of human body motion in sports. Proceedings of the *14th Symposium on Biomechanics in Sports*, Technical University of Lisbon, Portugal.

Cerveri P., Pedotti A., Ferrigno G., (2003). Robust recovery of human motion from video using Kalman filters and virtual humans. *Human Motion Science,* Vol. 22, 377–404.

Chao G.A., Rim L.S., (1973). Application of optimization principles in determining the applied moments in human leg joints during gait. *Journal of Biomechanics*, Vol. 6, 497–510.

Chèze L., (2000). Comparison of different calculations of three-dimensional joint kinematics from video-based system data. *Journal of Biomechanics,* Vol. 28, 879–884.

Chèze L., Fregly B.J., Dimnet J., (1995). A solidification procedure to facilitate kinematic analyses based on video system data. *Journal of Biomechanics,* Vol. 33, 1695–1699.

Chou L.S., Song S.M., Draganich L.F., (1995). Predicting the kinematics and kinetics of gait based on the optimum trajectory of the swing limb. *Journal of Biomechanics,* Vol. 28, 377–385.

Chow C.K., Jacobson D.H., (1971). Studies in human locomotion via optimal Programming. *Mathematical Biosciences*, Vol. 10, 239–306.

Chow C.K., Jacobson D.H., (1972). Further studies in human locomotion: Postural stability and control. *Mathematical Biosciences*, Vol. 15, 93–108.

Chung H.J., Xiang Y., Mathai A., Rahmatalla S., Kim J., Marler T., Beck S., Yang J., Arora J., Abdel-Malek K., (2007). A robust formulation for prediction of human running. Proceedings of the *2007 Digital Human Modeling for Design and Engineering Symposium,* Seattle, Washington.

Clause C.E., McConville J.T., Young J.W., (1969). Weight, volume and center of mass of segments of the human body. *AMRL-TR-69-70*. Aerospace Medical Research Laboratory, Wright-Patterson Air Force Base, Ohio, United States.

Collins S. H., Wisse M., Ruina A., (2001). A Three-Dimensional Passive-Dynamic Walking Robot with Two Legs and Knees. *International Journal of Robotics Research*, Vol. 20 (2), 607–615.

Cooney K.M., Sanders J.O., Concha M.C., Buczek F.L., (2006). Novel biomechanics demonstrate gait dysfunction due to hamstring tightness. *Clinical Biomechanics*, Vol. 21(1), 59–66.

Crosbie W.J., Nicol A.C., (1990). Biomechanical comparison of two paraplegic gait patterns. *Clinical Biomechanics*, Vol. 5 (2), 97–107.

Cuadrado J., Gutierrez R., Naya M.A., Morer P., (2001). A comparison in terms of accuracy and efficiency between a MBS dynamic formulation with stress analysis and a non-linear FEA code. *International Journal of Numerical Methods in Engineering*, Vol. 51 (9), 1033–1052.

Cuadrado J., Dopico D., Naya M.A., Gonzalez M., (2004). Penalty, semi-recursive and hybrid methods for MBS real-time dynamics in the context of structural integrators. *Multibody System Dynamics*, Vol. 12, 117–132.

Cuadrado J., Dopico D., Barreiro A., Delgado E., (2009). Real-time state observers based on multibody models and the extended kalman Filter. *Journal of Mechanical Science and Technology*, Vol. 23 (4), 894–900.

Davidson P.L., Wilson S.J., Wilson B.D., Chalmers D.J., (2008). Estimating subject-specific body segment parameters using a 3-dimensional modeller program. *Journal of Biomech*, Vol. 41, 3506–3510.

Davis B.L., Cavanagh P.R., (1993). Decomposition of superimposed ground reaction forces into left and right force profiles. *Journal of Biomechanics*, Vol. 26, 593–597.

Davis R.B., Ounpuu S., de Luca P.A., (1994). Joint Moments: Evaluation of ground reaction, inertial and segmental weight effects, *Gait and Posture*, Vol. 2(1), 58.

Dempster W.T., (1955). Space requirements of the seated operator. *WADC-55-159, AD-087–892*. Wright-Patterson Air Force Base, Ohio. United States.

Delp S., Loan P., Hoy M., Zajac F., Topp E., Rosen J., (1990). An interactive graphics-based model of the lower extremity to stydy orthopaedic surgical procedures. *IEEE Transactions on Biomedical Engineering*, Vol. 37 (8), 757–767.

Dinis P., Martins J., Pires E., (1999). Finite element simulation of the forarm flexion. *Proccedings of 4th International Symposium on Computer Methods in Biomechanics and Biomedical Engineering*, 295–300, Lisbon, Portugal.

Dopico D., (2004). Formulaciones semi–recursivas y de penalizaci´on para la din´amica en tiempo real de sistemas multicuerpo. *PhD thesis*, Universidad de la Coruña, Ferrol, Spain.

Dopico D., Luaces A., González M., Cuadrado J., (2011). Dealing with multiple contacts in a human–in–the–loop application. *Multibody System Dynamics* Vol. 25 (2), 167–183.

Dumas R., Nicol E., Chèze L., (2007a). Influence of the 3D inverse dynamic method on the joint forces and moments during gait. *Journal of Biomechanical Engineering.* Vol. 129(5), 786–790.

Dumas R., Chèze L. Verriest J.P., (2007b). Adjustments to McConville et al. and Young et al. body segment inertial parameters. *Journal of Biomechanics*, Vol. 40(3), 543–553. Corrigendum (2007), *Journal of Biomechanics* 40 (7), 1651–1652.

Eberhard P., Spagele T., Gollhofer A., (1999). Investigations for the dynamical analysis of human motion. *Multibody System Dynamics*, Vol. 3 (2), 1–20.

Elftman H. (1938). The measurement of the external force in walking. *Science*, Vol. 88 (2276), 152–153.

Elftman H. (1939). Forces and energy changes in the leg during walking. *American Journal of Physiology*, Vol. 125, 339–356.

Eng J.J., Winter D.A., (1994). Kinetic analysis of the lower limbs during walking: what information can be gained from a three-dimensional model?. *Journal of Biomechanics*, Vol. 28 (6), 753–758.

Fang A., Pollard N., (2003). Efficient Synthesis of Physically Valid Human Motion. *ACM Transactions on Graphics*, Vol. 22 (3), 417–426.

Fazel-Rezai R., Shwedyk E., (1998). Biomechanical signal filtering for dynamic analysis purpose: A quantitative comparison between different methods. Proceedings of the *11th Conference of the ESB*, Toulouse, France.

Flores P., Machado M., Silva M.P.T, Martins J., (2011). On the continuous contact force models for soft materials in multibody dynamics. *Multibody System Dynamics* Vol. 25 (3), 357–375.

Font-Llagunes J.M., Kövecses J., (2009). Efficient dynamic walking: Design strategies to reduce energetic losses of a compass walker at heel strike. *Mechanics Based Design of Structures and Machines,* Vol. 37 (3), 259–282.

Font-Llagunes J.M., Pàmies-Vilà R., Alonso F.J., Lugris U., (2011). Simulation and design of an active orthosis for an incomplete spinal cord injured subject. *IUTAM Symposium on Human Body Dynamics: From Multibody Systems to Biomechanics*, Procedia IUTAM, Vol. 2, 68–81, Waterloo, Ontario, Canada.

Forner-Cordero A., Koopman H.J.F.M., Van der Helm F.C.T., (2006). Inverse dynamics calculations during gait with restricted ground reaction force information from pressure insoles. *Gait and Posture,* Vol. 23 (2), 189–199.

Fregly B.J., Reinbolt J.A., Rooney K.L., Mitchell K.H., Chmielewski T.L., (2007). Design of patient-specific gait modifications for knee osteoarthritis rehabilitation. *IEEE Transactions on Biomedical Engineering*, Vol. 54 (9), 1687–1695.

Garcia, M. Chatterjee A., Ruina A., Coleman M., (1998). The simplest walking model: stability, complexity, and scaling. *Journal of Biomechanical Engineering*, Vol. 120 (2), 281–288.

García de Jalón J., Bayo E., (1994). Kinematic and dynamic simulation of multibody systems: the real-time challenge. *Springer-Verlag*, New York.

Georgiakis A., Stergioulas L.K., Giakas G., (2002a). Wigner filtering with smooth roll-off boundary for differentiation of noisy non-stationary signals. *Signal Processing*, Vol. 82, 1411–1415.

Georgakis A., Stergioulas L.K., Giakas G., (2002b). Automatic algorithm for filtering kinematic signals with impacts in the Wigner representation. *Medical and Biological Engineering and Computing*, Vol. 40, 625–633.

Giakas G., Stergioulas L.K., Vourdas A., (2000). Time-frequency analysis and filtering of kinematic signals with impacts using the Wigner function: accurate estimation of the second derivative. *Journal of Biomechanics*, Vol. 33, 567–574.

Gilchrist L.A., Winter D.A., (1996). A two-part, viscoelastic foot model for use in gait simulations. Journal of Biomechanics, Vol. 29 (6), 795–798.

Glaister B.C., Schoen J.A., Orendurff M.S., Klute G.K., (2009). A mechanical model of the human ankle in the transverse plane during straight walking: Implications for prosthetic design. *Journal of Biomechanical Engineering*, Vol. 131 (3), 034501-1–034501-5.

Goldberg A., (1997). IMPROV: a System for Real-time Animation of Behavior-based Interactive Synthetic Actors. Creating personalities for synthetic actors. *Lecture Notes in Computer Science*, Vol. 1195/1997, 58–73.

Goldsmith W., (1960). Impact, the theory and physical behaviour of colliding solids. *Edward Arnold Pub*., London, United Kingdom.

Gonthier Y., McPhee J., Piedboeuf J., Lange C., (2004). A regularized contact model with asymmetric damping and dwell-time dependent friction. *Multibody System Dynamics*, Vol. 11, 209–233.

Gordon D., Robertson E., Dowling J.J., (2003). Design and responses of Butterworth and critically damped digital filters, *Journal of Electromyography and Kinesiology*, Vol. 13, 569–573.

Grewal M.S., Andrews A.P., (2008). Kalman Filtering. Theory and Practice Using MATLAB. *John Wiley & Sons, Inc*. 3rd edition. New York, United States.

Groena B.E., Geurtsa M., Nienhuisa B., Duysensa J., (2012). Sensitivity of the OLGA and VCM models to erroneous marker placement: Effects on 3D-gait kinematics, *Gait and Posture* Vol. 35 (3) 517–521.

De Groote F., Van Campen A., Jonkers I., de Schutter J., (2010) Sensitivity of dynamic simulations of gait and dynamometer experiments to hill muscle model parameters of knee flexors and extensors. *Journal of Biomechanics* Vol. 43 (10) 1876–1883.

Gruber K., Denoth J., Ruder H., Stüssi E., (1991). Mechanics of joint stress. *Zeitschrift Fur Orthopadie Und Ihre Grenzgebiete*, Vol. 129 (3), 260–267.

Güller H.C., Berme N., Simon R.S., (1998). A viscoelastic sphere model for the representation of plantar soft tissue during simulations. *Journal of Biomechanics*, Vol. 31, 847–853.

Hansen A., Childress D., Miff S., Gard S., Mesplay K., (2004). The Human Ankle During Walking: Implications for Design of Biomimetic Ankle Prostheses and Orthoses. *Journal of Biomechanics*, Vol. 37 (10), 1467–1474.

Hansen N., (2006). The CMA evolution strategy: A comparing review. *Studies in Fuzziness and Soft Computing*, Vol. 192, 75–102.

Hardt D.E., Mann R.W., (1980). Technical note: Five body - Three dimensional dynamic analysis of walking. *Journal of Biomechanics*, Vol. 13, 455–457.

Hatze H., (1977). A complete set of control equations for the human musculo-skeletal system. *Journal of Biomechanics*, Vol. 10, 799–805.

Hatze H., (1980). The use of optimally regularized fourier series for estimating higher-order derivatives of noisy biomechanical data. *Journal of Biomechanics*, Vol. 14, 13–18.

Hatze H., (1981). A comprehensive model for human motion simulation and its application to the take-off phase of the long jump. *Journal of Biomechanics*, Vol. 14 (3), 135–142.

Hatze H., (1984). Quantitative analysis, synthesis, and optimization of human motion. *Human Movement Science*, Vol. 3, 5–25.

Hatze H., (2002). The fundamental problem of myoskeletal inverse dynamics and its implications. *Journal of Biomechanics,* Vol. 35, 109–115.

Hatze H., Venter A., (1981). Practical activation and retention of locomototion constraints in neuromusculoskeletal control system models. *Journal of Biomechanics*, Vol. 14, 873–877.

Hemami H., Stokes B.T., (1983). A qualitative discussion of mechanisms of feedback and feedforward control of locomotion *IEEE Transactions on Biomedical Engineering*, Vol. 30, 681–689.

Hemami H., Golliday C.L., (1977). The inverted pendulum and biped stability. *Mathematical Biosciences*, vol. 34 (1-2), 95–110.

Hemami H., Zheng Y.F., Hines M.J., (1982). Initiation of walk and tiptoe of a planar nine link biped. *Mathematics and Bioscience,* Vol. 61, 163–189.

Hertz, H., (1896). On the contact of solids- on the contact of rigid elastic solids and on hardness. *Miscellaneous Papers,* 146–183. MacMillan and Co., London, United Kingdom.

Herzog W. (2009), The biomechanics of muscle contraction: optimizing sport performance. *Sport-Orthopädie*, Vol. 25 (4), 286–293.

Hicks J., Arnold A., Anderson F., Schwartz M., Delp S., (2007). The effect of excessive tibial torsion on the capacity of muscles to extend the hip and knee during single-limb stance. *Gait and Posture*, Vol. 26, 546–552.

Hill A.V., (1938). The heat shortening and the dynamic constants of muscle Proceedings of the *Royal Society of London. Series B, Biological Sciences*, Vol. 126 (843), 136–195.

Hunt K.H., Crossley F.R.E. (1975). Coefficient of restitution interpreted as damping in vibroimpact. *Journal of Applied Mechanics,* Vol. 42 (2), 440–445.

Hurmuzlu Y., Moskowitz G.D., (1987a). Bipedal locomotion stabilized by impact switching: I. Two- and three-dimensional, three Element Models. *Dynamical Systems*, Vol. 2, 73–96.

Hurmuzlu Y., Moskowitz G. D., (1987b). Bipedal locomotion stabilized by impact switching: II. Structural stability analysis of four-element bipedal locomotion model. *Dynamical Systems*, Vol. 2, 97–112.

Jensen R.K., (1986). Body segment mass, radius, and radius of gyration proportions of children. *Journal of Biomechanics*, Vol. 19, 359–368.

Jensen R.K., (1993). Human morphology: its role in the mechanics of movement. *Journal of Biomechanics*. Vol. 26 (1), 81–94.

Jensen R.K., Fletcher P., (1994). Distribution of mass to the segments of elderly males and females. *Journal of Biomechanics*, Vol. 27 (1), 89–96.

Ju M., Mansour J.M., (1988). Simulation of the double limb support phase of human gait. *Journal of Biomechanical Engineering*, Vol. 110, 223–229.

Kadaba M.P., Ramakrishnan H.K., Wooten M.E., Gainey J., Gordon G., Cochran G. V.B., (1989). Repeatability of kinematic, kinetic, and electromyographic data in normal adult gait. *Journal of Orthopaedic Research*, Vol. 7, 849–860.

Kajita S., Kanehiro F., Kaneko K., Fujiwara K., Yokoi K., Hirukawa H., (2003). Biped Walking Pattern Generation by a Simple Threedimensional Inverted Pendulum Model. *Advanced Robotics*, Vol. 17, 131–147.

Kagawa T., Uno Y., (2010). Necessary condition for forward progression in ballistic walking. *Human Movement Science* Vol. 29, 964–976.

Kaplan M., (2000). Efficient optimal control of large-scale biomechanical systems. *PhD Thesis*, Stanford University, Stanford, California, Unitated States.

Kecskeméthy A., (2011). A novel cylinder–plane foot contact model for human gait otion reproduction. *Proceedings of Multibody Dynamics 2011, ECCOMAS Thematic Conference*, Brussels, Belgium.

Kim J.H., Abdel-Malek K., Yang J., Marler R.T., (2006). Prediction and analysis of human motion dynamics performing various tasks. *International Journal of Human Factors Modelling and Simulation*, Vol. 1 (1), 69–94.

Koopman B., Grootenboer H.J., de Jongh H.J., (1995). An inverse dynamics model forthe analysis, reconstruction and prediction of bipedal walking. *Journal of Biomechanics*, Vol. 28, 1369–1376.

Kuo A.D., (1998). A least squares estimation approach to improving the precision of inverse dynamics computations. *Journal of Biomechanical Engineering*, Vol. 120, 148–159.

Kuo A.D., (1999). Stabilization of lateral motion in passive dynamic walking. *The International Journal of Robotics Research*, Vol. 18 (9) 917–930.

Laananen D.H., Bolukbasi A.O., Coltman J.W., (1983). Computer simulation of an aircraft seat and occupant in a crash environment. Volume 1. Technical report. *US Department of Transportation, Federal Aviation Administration*, Atlantic City, New Jersey, United States.

Lafortune M.A., Lake M.J., Hennig E.M., (1996). Differential shock transmission response of the human body to impact severity and lower limb posture. *Journal of Biomechanics,* Vol. 29, 1531–1537.

Lankarani H.M., Nikravesh P.E. (1990). A contact force model with hysteresis damping for impact analysis of multibody systems. *Journal of Mechanical Design*, Vol. 112 (3), 369–376.

Leardini A., Chiari L., Della Croce U., Cappozzo A., (2005). Human motion analysis using stereophotogrammetry Part 2: Soft tissue artifact assesment and compensation. *Gait and Posture,* Vol. 21, 212–225.

Lee C.M., Jeong E.H., Freivalds A., (2001). Biomechanical effects of wearing high-heeled shoes. *International Journal of Industrial Ergonomics.* Vol. 28 (6), 321–326.

Lee S.H., Terzopoulos D., (2006). Heads Up! Biomechanical Modeling and Neuromuscular Control of the Neck. *Proceedings of ACM SIGGRAPH 2006 Conference*, 1188–1198, Boston, Massachusetts, United States.

Lee M.K., Le N.S., Fang A.C., Koh M.T., (2009). Measurement of body segment parameters using dual energy X-ray absorptiometry and three-dimensional geometry: An application in gait analysis. *Journal of Biomechanics*, Vol. 9;42(3) 217–22.

de Leva P., (1993). Validity and accuracy of four methods for locating the centre of mass of young male and female athletes. In: Bouisset, S., Métral, S. and Monod, H., Editors, 1993. Proceedings of the *14th International Society of Biomechanics Congress,* 318–319, Paris, France.

de Leva P., (1996). Joint centre longitudinal positions computed from a selected subset of Chandler's data. *Journal of Biomechanics*, Vol. 29 (9), 1231–1233.

Liu W., Nigg B.M., (2000). A mechanical model to determine the influence of masses and mass distribution on the impact force during running. *Journal of Biomechanics*, Vol. 33, 122–134.

Lu T.W., O'Connor J.J., (1999). Bone position estimation from skin marker coordinates using global optimisation with joint constraints. *Journal of Biomechanics,* Vol. 32, 129–134.

Manal K., McClay I., Richards J., Galinat B., Stanhope S., (2002). Knee moment profiles during walking: errors due to soft tissue motion of the shank and the influence of the reference coordinate system. *Gait and Posture,* Vol. 15, 10–17.

Marshall R.N., Wood G.A., Jennings L.S., (1989). Performance objectives in human movement: a review and application to the stance phase of normal walking. *Human Movement Science*, Vol. 8, 571–594.

Maurel W., Thalmann D., (1999). A computer model of the human shoulder including scapulo-thoracic constraints and joint sinus cones, *Proceedings of Fourth International Symposium on Computer Methods in Biomechanics and Biomedical Engineering*, 313–318, Lisboa, Portugal.

McCaw S.T., De Vita P., (1995). Errors in alignment of centre of pressure and foot coordinates affect predicted lower extremity torques. *Journal of Biomechanics,* Vol. 28 (8), 985–988.

McConville J.T., Churchille T.D. Kaleps I. Clauser C.E., Cuzzi J., (1980). *Anthropometric relationship of body and bodysegment moments of inertia*. *Report AFAMRL-TR-80-119*, Wright-Patterson Air Force Base, Ohio. United States.

McGeer T. (1990). Passive dynamic walking. *International Journal of Robotics Research*, Vol. 9 (2), 62–82.

Meglan D.A., (1991). Enhanced analysis of human locomotion. *PhD thesis*. The Ohio State University, Columbus, Ohio, United States.

Milne R.D, Davis J.P., (1992). The role of the shaft in the golf swing, *Journal of Biomechanics*, Vol. 25 (9), 975–983

Millard M. McPhee J., Kubica E., (2008). Multi-step forward dynamic gait simulation. Bottasso C.L. Editor, *Multibody Dynamics: Computational Methods in Applied Sciences*, Vol. 12, 25–43.

Millard M., (2011), Mechanics and Control of Human Balance. *Phd thesis*, Waterloo, Ontario, Canada.

Millard M., McPhee J., Kubica E., (2008). Multi-step forward dynamic gait simulation. In Bottasso C.L., Editor, *Multibody Dynamics: Computational Methods and Applications*, 25–43. Springer.

Millard M., Wight D., McPhee J., Kubica E., Wang D., (2009). Human foot placement and balance in the sagittal plane. *ASME Journal of Biomechanical Engineering*, 131(12), 2009.

Miller K., Chinzei K., (1997). Constitutive modelling of brain tissue: Experiment and theory. *Journal of Biomechanics*, Vol. 30 (11/12), 1115–1121.

Mirelman A., Patritti B.L., Bonato P., Deutsch J.E., (2010). Effects of virtual reality training on gait biomechanics of individuals post-stroke. *Gait and Posture*, Vol. 31 (4) 433–437.

Mochon S., McMahon T.A., (1980). Ballistic walking. *Journal of Biomechanics*, Vol. 13, 49–57.

Monnier G., Renard F., Chameroy A., Wang X., Trasbot J., (2006). A motion simulation approach integrated into a design engineering process. Proceedings of the *SAE International Conference and Exposition of Digital Human Modelling for Design and Engineering*. Lyon, France.

Morecki A., Ekiel J., Fidelus K., (1984). Cybernetic systems of limb motions in man, animals and robots. *Ellis Horwood Limited*, New York.

Moreira P., Silva M.P.T., Flores, P., (2009). Ground foot interaction in human gait: modelling and simulation. *Proceeding of 7th Euromech Solid Mechanics Conference,* Lisbon, Portugal.

Muybridge E., (1887). Animal locomotion. An electro-photographic investigation of consecutive phases of animal movements. *Photogravure company of New York*, University of Pennsylvania, New York, United States.

Murai A., Yamane K., Nakamura Y., (2008). Modeling and identification of human neuromusculoskeletal network based on biomechanical property of muscle. Proceedings of the *30th Annual International IEEE EMBS Conference*, Vancouver, Canada.

Nakamura Y., Yamane K., Murai A., (2006). Macroscopic modeling and identification of the human neuromuscular network. Proceedings of the *28th IEEE EMBS Annual International Conference*, 99–105, New York, United States.

Neptune R.R., Wright I.C., Van den Bogert A.J., (2000). A method for numerical simulation of single limb ground contact events: application to heel-toe running. *Computer Methods in Biomechanics and Biomedical Engineering,* Vol. 3, 321–324.

Neptune R.R., Kautz S.A., Zajac F.E., (2001). Contributions of the individual ankle plantar flexors to support, forward progression and swing initiation during walking. *Journal of Biomechanics*, Vol. 34, 1387–1398

Nigg B.M., Herzog W., (1995). Biomechanics of the musculo-skeletal system. *Chichester: John Wiley & Sons Inc*, New York, United States.

Nigg B.M., Liu W., (1999). The effect of muscle stiffness and damping on simulated impact force peaks during running. *Journal of Biomechanics*, Vol. 32, 849–856.

Nikolova G., Toshev Y., (2007). Estimation of male and female body segment parameters of the Bulgarian population using a 16-segmental mathematical model. *Journal of Biomechanics*, Vol. 40 (16), 3700–3707.

O'Connor C.M., Thorpe S.K., O'Malley M.J., Vaughan C.L., (2007). Automatic detection of gait events using kinematic data. *Gait and Posture*, Vol. 25 (3), 469–474.

Onyshko S., Winter D.A., (1980). A mathematical model for the dynamics of human locomotion. *Journal of Biomechanics,* Vol. 13, 361–368.

Pandy M., Zajac F., Sim E., Levine W., (1990). An optimal control model for maximum-height human jumping. *Journal of Biomechanics*, Vol. 23 (12), 1185–90.

Pandy M.G., (2003), Simple and complex models for studying muscle function in walking, *Philosophical Transactions of the Royal Society of London Biological Sciences*., Vol. 358, 1501–1509.

Pandy M.G., Berme N., (1988a). Model for the understanding of the ankle and knee during double support. Proceedings of *Modeling and Control Issues in Biomechanical Systems, ASME Winter Annual Meeting*, 89–102. Chicago, United States.

Pandy M.G., Berme N., (1988b). A numerical method for simulating the dynamics of human walking. *Journal of Biomechanics,* Vol. 21, 1043–1051.

Pandy M.G., Berme N., (1988c). Synthesis of human walking: A planar model for single support. *Journal of Biomechanics*, Vol. 21, 1053–1060.

Pandy M.G., Berme, N., (1989). Quantitative assesment of gait determinants during single stance via a three-dimensional model - Part I. Normal Gait. *Journal of Biomechanics,* Vol. 22, 717–724.

Pastorino R. (2012) Experimental validation of a multibody model for a vehicle prototype and its application to state observers. *PhD thesis.* Universidad de A Coruña, Spain.

Pearsall D.J., Costigan P.A., (1999). The effect of segment parameter error on gait analysis results. *Gait and Posture*, Vol. 9, 173–183.

Peasgood M., Kubica E., McPhee J., (2007). Stabilization of a dynamic walking gait simulation, *ASME Journal of Computational and Nonlinear Dynamics*, Vol. 2, 65–72.

Peasgood M., (2002), Energetics of prosthetic gait. *Master thesis*, University of Waterloo, Otario, Canada.

Perry J., (1992). Gait analysis: normal and pathological function. *SLACK Incorporated* 1st ed. Thorofare, New Jersey, United States.

Piazza S.J., Delp S.L., (2001). Three-Dimensional Dynamic Simulation of Total Knee Replacement Motion During a step-Up Task. *Journal of Biomechanical Engineering*, Vol. 123, 599–606.

Prasad P., (1984). An overview of the major occupant simulation models. *Mathematical Simulation of Occupant and Vehicle Kinematics, SAE Publication*, Vol. 146.

Psycharakis S., Miller S., (2006). Estimation of errors in force platform data, *Research Quarterly for Exercise and Sport*, Vol.77 (4), 514–518.

Ralston H.J., (1976). Energetics of Human Walking, *Neural Control of Locomotion*, 77–98. Herman R.M., Grillner S., Stein P.S.G., Stuart D.G., Editors. Plenum Press, New York.

Ramakrishnan H.K., Kadaba M.P., Wootten M.E., (1987). Lower extremity joint moments and ground reaction torque in adult gait. *Biomechanics of normal and prosthetic gait, Proceeedings of Winter Annual Meeting ASME*, 87–92, Boston, Massachusetts, United States.

Ramakrishnan H.K., Masiello G., Kadaba M.P., (1991). On the estimation of the three dimensional joint moments in gait. *ASME Biomechanics Symposium*, Vol. 120, 333–339.

Rao G., Amarantini D., Berton E., Favier D., (2006). Influence of body segments' parameters estimation models on inverse dynamics solutions during gait. *Journal of Biomechanics*, Vol. 39 (8), 1531–1536.

Rasmussen J., Vondrak V., Damsgaard M., de Zee M., Christensen S., Dostal Z., (2002). The AnyBody project – Computer analysis of the human body, Proceedings of the *International Congress of Biomechanics – Biomechanics of Man*, Cejkovice, Czech Republic

Reich J., Swoboda S., Steiner R., Daunicht W.J., (1999). BIOMEX 2 - An Environment for Complex Biomechanical Simulations", Proceedings of the *VIIth International Symposium on Computer Simulation in Biomechanics*, Calgary, Alberta, Canada.

Reinsch C.H., (1967). Smoothing by Spline Functions. *Numerische Mathematik* Vol.10, 177–183.

Reinbolt J.A., Fox M.D., Arnold A.S., Ounpuu S., Delp S.L., (2008). Importance of preswing rectus femoris activity in stiff-knee gait. *Journal of Biomechanics,* Vol. 41, 2362–2369.

Ren L., Jones R.K, Howard D., (2007). Predictive modelling of human walking over a complete gaitcycle. *Journal of Biomechanics*, Vol. 40 (7), 1567–1574.

Ren L., Jones R.K., Howard D., (2008). Whole body inverse dynamics over a complete gait cycle based only on measured kinematics. *Journal of Biomechanics*, Vol. 41, 2750–2759.

Remy C.D., Thelen D.G., (2009). Optimal estimation of dynamically consistent kinematics and kinetics for forward dynamic simulation of gait, *Journal of Biomechanical Engineering*, Vol. 131 (3), 031005-1–031005-9.

Ribeiro A., Rasmussen J., Flores P., Silva L.F., (2012). Modeling of the condyle elements within a biomechanical knee model. *Multibody System Dynamics*, Vol. 28, 181–197.

Riemer R., Hsiao-Wecksler E.T., Zhang X., (2008). Uncertainties in inverse dynamics solutions: a comprehensive analysis and an application to gait. *Gait and Posture*, Vol. 27 (4) 578–588.

Rodrigo S.E., Ambrósio J.A.C., Penisi O., (2007). Análisis dinámico inverso de modelos biomecánicos espaciales del cuerpo humano, Proceedings of the *8º Congreso Iberoamerciano de Ingenieria Mecanica,* Cusco, Perú.

Rodrigo S.E., Ambrósio J.A.C., Silva M.P.T. , Penisi O.H., (2008). Analysis of human gait based on multibody formulations and optimization tools, Mechanics Based Design of Structures and Machines, Vol. 36 (4), 446–477.

Rostami M., Bessonnet G., (2001). Sagittal gait of a biped robot during the single support phase. Part 2: optimal motion. *Robotica*, Vol. 19, 241–253.

Saha N., Mahadevan S., Midoun D., Yang J., (1993). A Finite element structure-dummy system model for side impact simulation. Automotive Design Engineering, 242–245.

Sauders J.B., Inman V.T., Eberhart H.D., (1952). The major determinants in normal and pathological gait. *Journal of Bone and Joint Surgery*, Vol. 35, 543–58.

Scovil C.Y., Ronsky J.L., (2006). Sensitivity of a Hill-based muscle model to perturbations in model parameters. *Journal of Biomechanics*, Vol. 39 (11) 2055–2063.

Senesh M., Wolf A., (2009). Motion estimation using point cluster method and Kalman filter. *Journal of Biomechanical Engineering,* Vol. 131 (5), 051008-1–051008-7.

Seth A., Sherman M., Reinbolt J.A., Delp S.L., (2011). OpenSim: a musculoskeletal modeling and simulation framework for in silico investigations and exchange. *Symposium on Human Body Dynamics.* Procedia IUTAM, Vol. 2, 212–232.

Shelburne K., Pandy M., (1997). A musculoskeletal model of the knee for evaluating ligament forces during isometric contractions, *Journal of Biomechanics*, Vol. 30 (2), 163–176.

Siegler S., Seliktar R., Hyman V., (1982). Simulation of human gait with the aid of a simple mechanical model. *Journal of Biomechanics*, Vol. 15, 415–425.

Silva M.P.T., Ambrósio J.A.C., (2002a). Kinematic data consistency in the inverse dynamic analysis of biomechanical systems. *Multibody System Dynamics*, Vol. 8(2), 219–239.

Silva M.P.T., Ambrósio J.A.C., (2002b). A multibody based methodology for the solution of the redundant nature of the muscle forces using static optimization, *Proceedings of V Congreso de Métodos Numéricos en Ingeniería*, Madrid, Spain.

Silva M.P.T., Ambrósio J.A.C., (2004). Sensitivity of the results produced by the inverse dynamic analysis of a human stride to perturbed input data. *Gait and Posture*, Vol. 19, 35–49.

Silva M.P.T., Ambrósio J.A.C., Pereira M.S., (1997). Biomechanical model with joint resistance for impact simulation. *Multibody System Dynamics*, Vol. 1 (1), 65–84.

Smak W., Neptune R.R., Hull M.L. (1999). The influence of pedaling rate on bilateral asymmetry in cycling. *Journal of Biomechanics*, Vol. 32 (9), 899–906.

Soest A.J., Casius L.J.R., (2000). Which factors determine the optimal pedaling rate in sprint cycling? *Medicine and Science in Sports and Exercise*, Vol. 32, 1927–1934.

Srinivasan S., Raptis I.A., Westervelt E.R. (2008). Low-dimensional sagittal plane model of normal human walking. *ASME Journal of Biomechanical Engineering*, Vol. 130, 051017-1–051017-11.

Stagni R., Leardini A., Cappozzo A., Grazia Benedetti M., Cappello A., (2000). Effects of hip joint centre mislocation on gait analysis results. *Journal of Biomechanics*, Vol. 33 (11), 1479–1487.

Taga G., (1995). A model of the neuro-musculo-skeletal system for human locomotion. *Biological Cybernetics*, Vol. 73, 97– 111.

Tayyari F., Smith J.L., (1997) Occupational Ergonomics. *Manufacturing Systems Engineering Series*, Vol. 3, ISBN 978-0-412-58650-7.

Tedrake R., Zhang T.W., Fong M., Seung H.S., (2004). Actuating a Simple 3D Passive Dynamic Walker . Proceedings of the *IEEE International Conference on Robotics and Automation (ICRA)*, Vol. 5, 4656–4661, New Orleans, Lousiana.

Thalmann D., (1999). Towards autonomous, perceptive, and intelligent virtual actors. *Lecture Notes in Artificial Intelligence*, 297–321, Springer-Verlag.

Thelen D.G., Anderson F.C., (2006). Using computed muscle control to generate forward dynamic simulations of human walking from experimental data. *Journal of Biomechanics*, Vol. 39(6) 1107–1115.

Towsend M.A., Seireg A., (1972). The synthesis of bipedal locomotion. *Journal of Biomechanics*, Vol. 5, 71–83.

Tsirakos D., Baltzopoulos V., Barlett R., (1997). Inverse Optimization: Functional and Physiological Considerations Related to the Force-Sharing Problem. *Critical Reviews in Biomedical Engineering,* Vol. 25, 371–407.

Tumer S., Engin A., (1993). Three-body segment dynamic model of the human knee. *Journal of Biomechanical Engineering*, Vol. 115, 351–356.

Valiant G.A., (1984). A determination of the mechanical characteristics of the human heel pad in vivo, *PhD thesis*. Pennsylvania State University, Pennsylvania, United States.

Vaughan, C.L., (1982). Smoothing and differentiation of displacement-time data: an application of splines and digital filtering. *International Journal of Bio-Medical Computing,* Vol. 13, 375–386.

Vaughan C.L., Davis B.L., O'Connor J.C., (1992). Dynamics of human gait. *Kiboho Publisher*, 2nd ed. Cape Town, South Africa.

Walker J.A., (1998). Estimating velocities and accelerations of animal locomotion: a simulation experiment comparing numerical differentiation algorithms. *The Journal of Experimental Biology,* Vol. 201, 981–995.

Wang L., Tan L., Ning H., Hu W., (2003). Silhouette analysis-based gait recognition for human identi cation, *IEEE Transactions on Pattern Analysis and Machine Intelligence*, Vol.25 (12), 1505–1518.

Williams R.J., Hansen A.H., Gard S.A., (2009). Prosthetic ankle-foot mechanism capable of automatic adaptation to the walking surface. *Journal of Biomechanical Engineering*. Vol. 131(3), 035002-1–035002-7.

Winter D.A, Sidwall H.G., Hobson D.A., (1974). Measurement and reduction of noise in kinematics of locomotion. *Journal of Biomechanics*, Vol. 7 (2), 157–159.

Winter D.A., (1990). Biomechanics and motor control of human motion, *John Wiley and Sons*. Hoboken, New York, United States.

Winter D.A., (1991). The biomechanics and motor control of human gait: Normal, elderly and pathological. *University of Waterloo Press*, Waterloo, Canada.

Winters J., (1995). Concepts in neuromuscular modeling, three-dimensional analysis of human motion, *Human Kinetics Publishers*, Champaign, Illinois, United States.

Wismans J.S.H.M, Janssen E.G., Beusenberg M., Koppens W.P., Lupker H.A., (1994), Injury biomechanics. *Course notes*. Faculty of Mechanical Univesity, Eindhoven University of Technology, Eindhoven, Netherlands.

Wismans J.S.H.M, (1996). Models in injury biomechanics for improved passive vehicle safety, *Crashworthiness of Transportation Systems: Structural Impact and Occupant Protection*. Proceedings of the *NATO Advanced Study Institute, Troia, Portugal*. J. Ambrósio, M. Pereira and F. Silva, eds., *Kluwer Academic Publishers*, Dordrecht.

Wojtyra M., (2003). Multibody Simulation Model of Human Walking, *Mechanics Based Design of Structures and Machines*, Vol. 31 (3), 357–379.

Wu G., Ladin Z., (1993). The effect of inertial load on human joint force and moment during locomotion. Proceedings of the *Second International Symposium on Three-Dimensional Analysis of Human Movement*, 106–107, Poitiets, France.

De Wit B., De Clercq D., Aerts P., (2000) Biomechanical analysis of the stance phase during barefoot and shod running. *Journal of Biomechanics*, Vol. 33 269–278.

Xiang Y., Chung H.J., Mathai A., Rahmatalla S., Kim J., Marler T., Beck S., Yang J., Arora J.S., Abdel-Malek K., (2009). Optimization-based dynamic human walking prediction. *International Journal for Numerical Methods in Engineering*, Vol. 79 (6), 667–695.

Yang J., Marler R.T., Kim H.J., Arora J.S., Abdel-Malek K., (2004). Multi-objective optimization for upper body posture prediction. Proceedings of the *10th AIAA/ISSMO Multidisciplinary Analysis*, Albany, New York, United States.

Yamaguchi G.T., Zajac F.E., (1990). Restoring unassisted natural gait to paraplegics via fuctional neuromuscular stimulation: A computer simmulation study. *IEEE Transactions on Biomedical Engineering*, Vol. 37, 886–902.

Yamaguchi G.T., Green J.I., Moran D.W., (1992). Development of a subject-specific, dynamic model of pathological gait. Proceedings of the *Second North American Congress of Biomechanics*, 399–400, Chicago, Illinois, United States.

Yamaguchi G.T., (2001). Dynamic modelling of muscle-skeletal motion. *Kluwer Academic Publisher*, Boston, United States.

Young J.W., Chandler R.F., Snow C.C., Robinette K.M., Zehner G.F., Lofberg M.S., (1983). Anthropometric and mass distribution characteristics of the adults female. *Technical Report FA-AM-83-16*, FAA Civil Aeromedical Institute, Oklaoma City, Oklaoma, United States.

Zajac F.E., (1989). Muscle and tendon: properties, models, scaling and applications to biomechanics and motor control. *Critical Reviews in Biomechanical Engineering*, Vol. 17 (4), 359–411.

Zatsiorsky V.M. Seluyanov V., (1985). Estimation of the mass and inertia characteristics of the human body by means of the best predictive regressions equations. *Biomechanics IX-B*, 233–239. Edited by Winter D.A., Norman R.W., Wells R.P., Hayes K.C., Patla A.E. Champaign, Ilinois, United States.

Zatsiorsky V.M., (1990a). In vivo body segment inertial parameters determination using a gamma-scanner method. *Biomechanics of human movement: applications in rehabilitation, sports and ergonomics*. 186–202. Edited by Berme N., Cappozzo A. Bertec Corporation, Worthington, Ohio, United States.

Zatsiorsky V.M., Seluyanov V.N., Ychugunova L.G., (1990b). Methods of determining mass-inertial characteristics of human body segments. *Contemporary problems of Biomechanics*. 272–291. Edited by Chernyi G.G., Regirer S.A. CRC Press. Boca Raton, Florida, United States.